İSTANBUL TECHNICAL UNIVERSITY ★ INSTITUTE OF SCIENCE AND TECHNOLOGY

MATHEMATICAL MODELING AND SIMULATION OF PHOTOPOLYMERIZATION PROCESS

Ph.D. Thesis by
Gökçen Alev ALTUN-ÇİFTÇİOĞLU, M.Sc.

Department : Chemical Engineering

Programme : Chemical Engineering

JUNE 2008

İSTANBUL TECHNICAL UNIVERSITY ★ INSTITUTE OF SCIENCE AND TECHNOLOGY

MATHEMATICAL MODELING AND SIMULATION OF PHOTOPOLYMERIZATION PROCESS

Ph.D. Thesis by
Gökçen Alev ALTUN-ÇİFTÇİOĞLU, M.Sc.

(506032003)

Date of submission : **21 April 2008**

Date of defence examination : **19 June 2008**

Supervisor (Chairman):	**Prof.Dr. Ayşegül ERSOY-MERİÇBOYU**
Members of the Examining Committee	**Prof.Dr. Melek TÜTER (İ.T.U.)**
	Prof.Dr. M. A. Neşet KADIRGAN (M.U.)
	Prof.Dr. Ayşen ÖNEN (İ.T.U.)
	Prof.Dr. Sabriye PİŞKİN (Y.T.U.)

JUNE 2008

İSTANBUL TEKNİK ÜNİVERSİTESİ ★ FEN BİLİMLERİ ENSTİTÜSÜ

FOTOPOLİMERİZASYON SÜRECİNİN MATEMATİKSEL MODELLENMESİ VE SİMULASYONU

Doktora Tezi
Y. Müh. Gökçen Alev ALTUN-ÇİFTÇİOĞLU
(506032003)

Tezin Enstitüye Verildiği Tarih : 21 Nisan 2008
Tezin Savunulduğu Tarih : 19 Haziran 2008

Tez Danışmanı :	**Prof.Dr. Ayşegül ERSOY-MERİÇBOYU**
Diğer Jüri Üyeleri	**Prof.Dr. Melek TÜTER (İ.T.Ü.)**
	Prof.Dr. M. A. Neşet KADIRGAN (M.Ü.)
	Prof.Dr. Ayşen ÖNEN (İ.T.Ü.)
	Prof.Dr. Sabriye PİŞKİN (Y.T.Ü.)

HAZİRAN 2008

ACKNOWLEDGEMENT

The dissertation would not have been possible without the help of so many people. I would like to take this opportunity to express my deep appreciation to you all.

First of all, I would like to take this opportunity to express my sincerest gratitude and appretiation to my advisor Prof. Dr. Ayşegül ERSOY-MERİÇBOYU for taking me as her student, for her advise and guidance during this research. She has always encouraged me and provided endless help. In each phase of this research, she provided invaluable support. It has been a great pleasure to work with her and I feel very lucky to have her as my advisor.

I am very greatful to Assoc. Prof. Dr. Clifford L. HENDERSON for inviting me to Georgia Institute of Techology in Atlanta, to conduct part of my PhD research in summers of 2005, 2006, and 2007 in his laboratory. Many thanks to Assist. Prof. Dr. Martha GALLIVAN, and Assist. Prof. Dr. Victor BREDVEELD for providing valuable suggestions during this work. I very much appreciate the financial support given by TUBITAK for my studies abroad in summer 2007.

I am also very thankful to Prof. Dr. M. A. Neşet KADIRGAN, who pays attention to students' academic growth, from which I benefit a lot, and for showing me understanding, giving me many valuable advice through out my undergraduate and graduate studies.

I would like to thank Prof. Dr. Sabriye PİŞKİN for accepting to be in my commitee. She has always been a great support to us through my undergraduate studies. I want to thank to Prof Dr. Melek TÜTER and Prof. Dr. Ayşen ÖNEN for taking their valuable time to review my dissertation.

I appreciate the opportunity to work in both Henderson's and Bredveeld's research groups at Georgia Institute of Technology. I owe many thanks to Dr. Yanyan TANG for the stereolithography apparatus training, Dr. Ryan SLOPEK for the help with microrheology studies and Dr. Santosh RAHANE for sharing his experience in FTIR studies. I would like to thank to Dr. Greg REYNOLDS for valuable discussions. I want to thank to İlhan YAVUZ (MSc.) and Dr. Yelda ÖZEL for helping me to put my thesis in order.

I want to thank my family because without them this thesis wouldn't be possible. The most important support has come from my father, Prof. Dr. Zikri ALTUN, and my dear mother, Aynur ALTUN, who have always stood beside me in difficult times. I am very grateful to my sister, Dr. Gülşah ALTUN, who supported me through out all my life. Finally, I want to thank to my husband Hüseyin ÇİFTÇİOĞLU, for his love, patience and understanding, for believing in me, and for being my best friend and my two year old son Orhun ÇİFTÇİOĞLU, for making my life very enjoyable.

April, 2008 Gökçen Alev ALTUN-ÇİFTÇİOĞLU

CONTENTS

ABBREVIATIONS **vii**
TABLE LIST **viii**
FIGURE LIST **ix**
NOMENCLATURE **xiv**
ÖZET **xviii**
SUMMARY **xx**

1. INTRODUCTION **1**

2. PHOTOPOLYMERIZATION **4**

2.1 Photoinitiators **5**

2.1.1. Unimolecular photoinitiators (type I) 5
2.1.2. Bimolecular photoinitiators (type II) 6

2.2. Monomers **7**

2.3. Additives **9**

2.4. Photopolymerization Kinetics **11**

2.4.1. Initiation reaction mechanism 11
2.4.2. Propagation reaction mechanism 16
2.4.3. Termination reaction mechanism 18
2.4.4. Rates and rate constants of propagation and termination reactions 19

2.5. Inhibition of Photopolymerization **24**

2.6. Applications of Photopolymerization **25**

2.7. Measurement Techniques of Photopolymerization **27**

2.7.1. Spectroscopy techniques 27
2.7.2. Calorimetry techniques 28
2.7.3. Rheology techniques 29

3. STEREOLITHOGRAPHY AND MICRORHEOLOGY **31**

3.1. Stereolithography 31

3.1.1. Applications of stereolithography 35
3.1.2. Research on stereolithography 35

3.2. Microrheology 38

3.2.1. Theory of passive microrheology 38
3.2.2. Determination of the gel point 42

4. EXPERIMENTAL STUDIES 47

4.1. Materials Used in the Experimental Studies 47

4.2. Stereolithography Experiments 50

4.3. Microrheology Experiments 51

4.3.1. Sample preparation 51
4.3.2. Experimental setup 52
4.3.3. Experimental work 56

4.4. FTIR Experiments 57

4.5. DSC Experiments 59

5. RESULTS AND DISCUSSION 61

5.1. Deterministic Model Development for Simulation of Photopolymerization Process Conducted in SLA 61

5.1.1. Simulation of photopolymerization process conducted in SLA 69
5.1.2. Results of experiments 79
5.1.3. Comparison of experimental and simulation results 81

5.2. Simulation of Microrheology Measurements 83

5.2.1. Modification of PDE model for microrheology measurements 83
5.2.2. Effect of UV light penetration depth on the gelation time and simulation of the results 85
5.2.3. Effect of UV light wavelength and intensity on the gelation time and simulation of the results 88
5.2.4. Effect of photoinitiator loading concentration and oxygen inhibition on the gelation time and simulation of the results 91

5.3. Model Development for the Simulation of Deoxygenated Microrheology Measurements by using Ordinary Differential Equations 99

5.3.1. Comparison of experimental, 1-D PDE and ODE model simulation results 103

5.4. Simulation of Deoxygenated Microrheology Measurements by Stochastic Monte Carlo Model 106

5.4.1. Stochastic Monte Carlo model 106
5.4.2. Application of stochastic Monte Carlo model to photopolymerization process 114
5.4.3. Conversion of deterministic rate constants to stochastic rate constants 119
5.4.4. Comparison of stochastic Monte Carlo simulations and experimental results 121
5.4.5. Comparison of the deterministic (1-D PDE and ODE) and stochastic simulation results 126

5.5. Validation of Stochastic Monte Carlo Model 130

5.5.1. Validation by FTIR measurements 130
5.5.2. Validation by DSC measurements 135

6. CONCLUSIONS AND RECOMMENDATIONS 139

6.1. Conclusions 139

6.2. Recommendations 145

REFERENCES 147

APPENDIX 156

CURRICULUM VITEA 180

ABBREVIATIONS

CAD : Computer Aided Design
CCD : Charge-Coupled Device
DMPA : 2,2-Dimethoxy-1,2-Diphenylethanone
DSC : Differential Scanning Calorimeter
FTIR : Fourier Transform Infrared
GPC : Gel Permeation Chromatography
IR : Infrared
MSD : Mean-Squared Displacement
ODE : Ordinary Differential Equations
OSA : Optical Stress Analysis
PA : Peak Area
PDE : Partial Differential Equations
PDSC : Photodifferential Scanning Calorimetry
SEM : Scanning Electron Microscopy
SL : Stereolithography
SLA : Stereolithography Apparatus
SMCM : Stochastic Monte Carlo Model
SR256 : 2(2-ethoxyethoxy) Ethyl Acrylate
SR272 : Triethylene Glycol Diacrylate
SR351 : Trimethylolpropane Triacrylate
SR494 : Ethoxylated Pentaerythritol Tetraacrylate
SSA : Stochastic Simulation Algorithm
UV : Ultraviolet
1-D : One Dimensional
2-D : Two Dimensional
3-D : Three Dimensional

TABLE LIST

Page No

Table 4.1 Physical and Chemical Properties of the Monomers........................... 48
Table 5.1 The Parameters Used to Simulate Photopolymerization Conducted in Stereolithography Apparatus 70
Table 5.2 Dimensions of the Fabricated Parts Obtained in Stereolithography Apparatus at Different Scanning Speeds................ 80
Table 5.3 Experimental and Model Results for the Part’s Dimensions 82
Table 5.4 Grouping of the Polymeric Radical Chain Length for ODE Model Simulation.. 103

FIGURE LIST

Page No

Figure 2.1 : Cleavage Mechanism of Unimolecular Photoinitiator Free-Radical Generation 6
Figure 2.2 : Hydrogen Abstraction Mechanism of Unimolecular Photoinitiator 6
Figure 2.3 : General Bimolecular Photoinitiator Free-Radical Generation Mechanism 6
Figure 2.4 : Molecular Structure of a Generalized Acrylate Monomer and Its Corresponding Polymer Repeat Unit; The R_1 Side Group May Vary 8
Figure 2.5 : Generalized Reaction Scheme for an Unsaturated Polyester System 9
Figure 2.6 : Absorption of Light by the Resin 14
Figure 2.7 : Network Formation During Polymerization of Multifunctional Monomers 17
Figure 2.8 : Diffusion and Reaction Steps During Termination of Two Polymer Radicals 21
Figure 3.1 : Schematic Diagram of Stereolithography 31
Figure 3.2 : Stair Stepping Effects 34
Figure 3.3 : Principles of Particle Tracking Microrheology; from Particle Motion to Sample Rheology 40
Figure 3.4 : Particle Tracking Microrheology Enables the Linear Viscoelasticity of Low Modulus Materials to be Extracted from the Fluctuation Spectrum. (a) Trajectory of the Probe Particle is Measured, (b) The Average Fluctuation Spectrum as a Function of Time *t* is Calculated, and (c) The Linear Viscoelasticity as a Function of Frequency ω can then be Found 45
Figure 3.5 : Steady Shear Viscosity and Equilibrium Modulus of a Cross-Linking Polymer as a Function of Reaction 46
Figure 4.1 : UV Visible Absorption Spectra of Irgacure 651 at Different Concentrations in Acetonitrile 49
Figure 4.2 : The SLA 250/50 Model Apparatus 50
Figure 4.3 : Schematic of the Experimental Setup Used in Microrheology Experiments 52
Figure 4.4 : Spectral Irradiance of 1000 W Hg(Xe) Arc Lamp 53
Figure 4.5 : Schematic of a Fabricated Sample Chamber Loaded with Sample 54
Figure 4.6 : Transmission Spectrum of Glass Cover Slip and Microscope Slide 55
Figure 4.7 : Bruker Brand FTIR Spectrometer 57

Figure 4.8 : The KBr Sample Chamber Used in FTIR Experiments 58
Figure 4.9 : UV Transmittance of the KBr Disc 58
Figure 4.10 : IR Spectra of the KBr Disc 59
Figure 4.11 : TA Instruments Q1000 Model Differential Scanning Calorimeter...60
Figure 5.1 : A Schematic Display of the PDE Model 62
Figure 5.2 : Parabolic Slice Representing the Cured Shape in The *y*-*z* Plane. The Rectangle Represents the Infinite Heat Reservoir Outside the Curing Region...65
Figure 5.3 : Contour Plot of Monomer Conversion for the Scanning Speed of $2.72x10^{-2}$ m/s...72
Figure 5.4 : Contour Plot of Monomer Conversion for the Scanning Speed of $1.18x10^{-2}$ m/s...72
Figure 5.5 : Contour Plot of Monomer Conversion for the Scanning Speed of $2.72x10^{-2}$ m/s...73
Figure 5.6 : Monomer Conversion Versus Time for the Scanning Speed of $2.72x10^{-2}$ m/s 74
Figure 5.7 : Monomer Conversion Versus Time for the Scanning Speed of $2.72x10^{-2}$ m/s 74
Figure 5.8 : Contour Plot of Photoinitiator Concentration for the Scanning Speed of $2.72x10^{-2}$ m/s 75
Figure 5.9 : Contour Plot of Photoinitiator Concentration for the Scanning Speed of $1.18x10^{-2}$ m/s..76
Figure 5.10 : Intensity Versus Time for the Scanning Speed of $2.72x10^{-2}$ m/s...76
Figure 5.11 : Radical Concentration Versus Time for the Scanning Speed of $2.72x10^{-2}$ m/s 77
Figure 5.12 : Temperature Change by Time for the Scanning Speed of $2.72x10^{-2}$ m/s..77
Figure 5.13 : Temperature Change by Time for the Scanning Speed of $1.18x10^{-2}$ m/s..78
Figure 5.14 : Temperature Change by Time for the Scanning Speed of $2.72x10^{-2}$ m/s..78
Figure 5.15 : SEM Micrographs of Fabricated Part for the Scanning Speed of $2.72x10^{-2}$ m/s 79
Figure 5.16 : SEM Micrographs of Fabricated Part for the Scanning Speed of $1.18x10^{-2}$ m/s 80
Figure 5.17 : Geometry for Gelation Time Simulations....................................84
Figure 5.18 : Effect of UV Light Penetration Depth on Gelation Time for Three Different Multifuntional Monomers and Comparison of Experimental and PDE Model Results ($[S]_0$=5wt%) 87
Figure 5.19 : Effect of UV Light Penetration Depth on the Gelation Time of SR494 for Different Wavelengths and Comparison of Experimental and PDE Model Results ($[S]_0$=5wt%) 88

Figure 5.20 : Effect of UV Light Penetration Depth on the Gelation Time of SR494 for 100% And 90% UV Light Transmissions and Comparison of Experimental and PDE Model Results ($[S]_0$=5wt%) 89
Figure 5.21 : Effect of UV Light Penetration Depth on the Gelation Time of SR494 68% and 10% UV Light Transmissions and Comparison of Experimental and PDE Model Results ($[S]_0$=5wt%) 90
Figure 5.22 : Effect of Photoinitiator Loading Concentration on the Gelation Time and Comparison of Experimental and PDE Model Results for Oxygenated and Deoxygenated Photopolymerization of SR494 92
Figure 5.23 : Effect of Photoinitiator Loading Concentration on the Gelation Time and Comparison of Experimental and PDE Model Results for Oxygenated Photopolymerization of SR494 94
Figure 5.24 : Effect of Photoinitiator Loading Concentration on the Gelation Time and Comparison of Experimental and PDE Model Results for Deoxygenated Photopolymerization of SR494 94
Figure 5.25 : Effect of Photoinitiator Loading Concentration on the Gelation Time and Comparison of Experimental and PDE Model Results for Oxygenated Photopolymerization of SR351 95
Figure 5.26 : Effect of Photoinitiator Loading Concentration on the Gelation Time and Comparison of Experimental and PDE Model Results for Deoxygenated Photopolymerization of SR351 96
Figure 5.27 : Effect of Photoinitiator Loading Concentration on the Gelation Time and Comparison of Experimental and PDE Model Results for Oxygenated Photopolymerization of SR272 97
Figure 5.28 : Effect of Photoinitiator Loading Concentration on the Gelation Time and Comparison of Experimental and PDE Model Results for Deoxygenated Photopolymerization of SR272 97
Figure 5.29 : Effect of Photoinitiator Loading Concentration on the Gelation Time and Comparison of Experimental and PDE Model Results for Oxygenated Photopolymerization of SR256 98
Figure 5.30 : Effect of Photoinitiator Loading Concentration on the Gelation Time and Comparison of Experimental and PDE Model Results for Deoxygenated Photopolymerization of SR256 98
Figure 5.31 : Effect of Photoinitiator Loading Concentration on the Gelation Time and Comparison of Experimental, PDE and ODE Models Results for Deoxygenated Photopolymerization of SR494 104

Figure 5.32 : Effect of Photoinitiator Loading Concentration on the Gelation Time and Comparison of Experimental, PDE and ODE Models Results for Deoxygenated Photopolymerization of SR351 104
Figure 5.33 : Effect of Photoinitiator Loading Concentration on the Gelation Time and Comparison of Experimental, PDE and ODE Models Results for Deoxygenated Photopolymerization of SR272 105
Figure 5.34 : Effect of Photoinitiator Loading Concentration on the Gelation Time and Comparison of Experimental, PDE and ODE Models Results for Deoxygenated Photopolymerization of SR256 105
Figure 5.35 : Effect of Photoinitiator Loading Concentration on the Gelation Time and Comparison of Experimental and SMCM Results for Deoxygenated Photopolymerization of SR494.......... 123
Figure 5.36 : Effect of Photoinitiator Loading Concentration on the Gelation Time and Comparison of Experimental and SMCM Results for Deoxygenated Photopolymerization of SR351.......... 124
Figure 5.37 : Effect of Photoinitiator Loading Concentration on the Gelation Time and Comparison of Experimental and SMCM Results for Deoxygenated Photopolymerization of SR272.......... 125
Figure 5.38 : Effect of Photoinitiator Loading Concentration on the Gelation Time and Comparison of Experimental and SMCM Results for Deoxygenated Photopolymerization of SR256.......... 125
Figure 5.39 : Comparison of Experimental, Deterministic and Stochastic Models Results for Deoxygenated Photopolymerization of SR494 127
Figure 5.40 : Comparison of Experimental, Deterministic and Stochastic Models Results for Deoxygenated Photopolymerization of SR351 127
Figure 5.41 : Comparison of Experimental, Deterministic and Stochastic Models Results for Deoxygenated Photopolymerization of SR272 128
Figure 5.42 : Comparison of Experimental, Deterministic and Stochastic Models Results for Deoxygenated Photopolymerization of SR256 128
Figure 5.43 : FTIR Spectrum of Cured and Uncured SR256 Resin ($[S]_0$=5%) 131
Figure 5.44 : Monomer Conversion as a Function of Reaction Time for SR256 ($[S]_0$=5%)..........132
Figure 5.45 : Comparison of Experimental and Predicted Conversion Values of SR256 Resin For 1% Photoinitiator Loading Concentration 133
Figure 5.46 : Comparison of Experimental and Predicted Conversion Values of SR256 Resin For 5% Photoinitiator Loading Concentration 133

Figure 5.47 : Comparison of Experimental and Predicted Conversion Values of SR256 Resin for 10% Photoinitiator Loading Concentration 134
Figure 5.48 : DSC Curves Obtained for the Photopolymerization of SR494 at 303K, 343 K, 383 K, and 403 K 135
Figure 5.49 : Comparison of Experimental and Predicted Conversion Values of SR494 Resin Photopolymerized at 303 K 136
Figure 5.50 : Comparison of Experimental and Predicted Conversion Values of SR494 Resin Photopolymerized at 343 K 137
Figure 5.51 : Comparison of Experimental and Predicted Conversion Values of SR494 Resin Photopolymerized at 383 K 137
Figure 5.52 : Comparison of Experimental and Predicted Conversion Values of SR494 Resin Photopolymerized at 403 K 138

NOMENCLATURE

I^*	: Photoinitiator Free Radical
a	: Tracer Particles Radius, (m)
A_0	: Maximum Intensity at the Center of the Laser Beam, (W/m^2)
A_{in}	: Amount of Radiation Incident on the Surface of the Resin, (W/m^2)
A_{out}	: Amount of Radiation Transmitted out of the Resin Volume, (W/m^2)
A_p	: Parameter for the Propagation Rate Constant
A_t	: Parameter for Termination Rate Constant
$A(z)$	: Total Amount of Radiation Absorbed in the Resin Volume
$A(x,y,z)$	: Intensity of Laser Light, (W/m^2)
$A(x,y,0)$	: Intensity of Laser Light at the Surface, (W/m^2)
A_{Ep}	: Pre-exponential Factors for the Propagation Reactions, (m^3/mol·s)
A_{Et}	: Pre-exponential Factors for the Propagation Reactions, (m^3/mol·s)
a_μ	: Propensity Function
C_d	: Cured Depth, (m)
C_{PM}	: Heat Capacity of Monomer, (J/kg·K)
C_{PP}	: Heat Capacity of Polymer, (J/kg·K)
C_P	: Heat Capacity of Photopolymerising System, (J/kg·K)
c	: Speed of Light, (m/s)
c_μ	: Stochastic Reaction Constant, (1/s)
C_1	: Fitting Parameter
D	: Diffusion Coefficient, (m^2/s)
d	: Characteristic Dimension of the System
D_M	: Monomer Diffusion Coefficient, (m^2/s)
D_R	: Polymeric Radical Diffusion Coefficient, (m^2/s)
D_S	: Photoinitiator Diffusion Coefficient, (m^2/s)
D_O	: Oxygen Diffusion Coefficient, (m^2/s)
$[DP_j]$	: Concentration of Dead Polymer Chain Length of j, (mol/m^3)
D_p	: UV Light Penetration Depth, (m)
dt	: Next Infinitesimal Time Interval, (s)
d_i	: Diameters of the Species, (m)
e_s	: Scaling Exponent for Short Chain Lengths
e_L	: Scaling Exponent for Long Chain Lengths
E_{max}	: Maximum Center Line Laser Exposure, (J/m^2)
E_c	: Critical Laser Exposure, (J/m^2)
E_p	: Activation Energies for the Propagation Reactions, (J/mol)
E_t	: Activation Energies for the Termination Reactions, (J/mol)
E_μ	: Activation Energy of the Reaction, (J/mol)
f	: Monomer Functionality

G : Elastic Modulus, (N/m^2)
G^* : Complex Shear Modulus, (N/m^2)
$G'(\omega)$: Storage Modulus, (N/m^2)
$G''(\omega)$: Shear Modulus, (N/m^2)
$\tilde{G}(s)$: Laplace Transform Shear Modulus, (N/m^2)
$G(t)$: Time Dependent Shear Modulus, (N/m^2)
$G^*(\omega)$: Frequency Dependent Complex Shear Modulus, (N/m^2)
G_∞ : Equilibrium Modulus, (N/m^2)
ΔH : Heat Flow, (W/g)
ΔH_p : Heat of Photopolymerization, (J/mol)
h : Planck's Constant, (J·s)
h_{air} : Air-Resin Heat Transfer Coefficient, (W/m^2·K)
i_c : Critical Chain Length
$i_{1/2}$: Fitting Parameter
k : Thermal Conductivity of the Curing System, (W/m·K)
k_{in} : Kinetic Rate Constant for Inhibition, (m^3/mol·s)
k_B : Boltzman's Constant, (J/K)
k' : Rate Constant for the Initiation Step, (m^3/mol·s)
k_i : Initiation Rate Constant, (1/s)
k_{p0} : Arrhenius Constants for the Propagation Reactions, (m^3/mol·s)
k_{t0} : Arrhenius Constants for the Termination Reactions, (m^3/mol·s)
k_p : Kinetic Rate Constant for Propagation, (m^3/mol·s)
k_{tc} : Kinetic Rate Constant for Termination by Combination, (m^3/mol·s)
k_{td} : Kinetic Rate Constant for Termination by Disproportionation, (m^3/mol·s)
k_{tp} : Kinetic Rate Constant for Termination by Photoinitiator Free Radicals, (m^3/mol·s)
k_t : Kinetic Rate Constant for Termination, (m^3/mol·s)
k_{fp} : Polymer Chain Transfer Kinetic Constant, (m^3/mol·s)
$k_{t,i,j}$: Chain-Length Dependent Termination Kinetic Constant, (m^3/mol·s)
k_μ : Deterministic Rate Constant, (m^3/mol·s)
$k_t^{i,i}$: Self-termination Rate Constant, (m^3/mol·s)
$k_t^{i,j}$: Bimolecular Deterministic Termination, (m^3/mol·s)
$k_p^{\ i}$: Propagation Rate Coefficient for an *i*-meric radical, (m^3/mol·s)
k^S : Stochastic Rate Constant, (1/s·molecules)
k^D : Deterministic Rate Constant, (m^3/mol·s)
M : Monomer Molecule
$[M]_0$: Initial Concentration of Monomers, (mol/m^3)
$[M]$: Monomer Concentration, (mol/m^3)
MW_S : Molecular Weight of the Photoinitiator, (kg/mol)
MW_M : Molecular Weight of the Monomer, (kg/mol)
MW_X : Molecular Weight of the Species, (kg/mol)
Δn_1 : Probable Number of Photoinitiators Decomposed
N_{Av} : Avogadro's Number, (molecules/mol)
N_{tot} : Initial Number of Total Molecules
N_{S0} : Initial Number of Photoinitiator Molecules
N_{M0} : Initial Number of monomers
n : Relaxation Exponent

N_x : Number of Species x
$[O_2]$: Concentration of Oxygen Molecules, (mol/m^3)
P_L : Laser Power, (W)
$P(\tau,\mu)$: Reaction Probability Density Function
$\langle p_{12} \rangle$: Average Probability of a Collision Between Molecules S_1 and S_2
R_1^* : Primary Radical Molecule
R_i : Initiation Rate, (mol/m^3·s)
$[R^*]_{tot}$: Total Radical Speices Concentration, (mol/m^3)
R_{abs} : Photon Absorption Rate, (W/m^2)
R_2^* : Polymer Radical of 2 Monomer Units
R_n^* : Polymeric Radical Chain of n Monomer Units
R_n : Polymer Molecule with Chain Length of n Monomer Units
R_p : Propagation Rate (Rate of Photopolymerization), (mol/m^3·s)
R_{rd} : Reaction Diffusion Constant, (m^3/mol)
R : Universal Gas Constant, (J/mol·K)
$\vec{r}(t)$: d-Dimensional Position Vector, (m)
$\langle \Delta\vec{r}^2(t) \rangle$: MSD, (m^2)
$\langle \Delta\tilde{r}^2(s) \rangle$: Unilateral Fourier Transform of the MSD, (m^2)
R_t : Termination Reaction Rate, (mol/m^3·s)
R_{in} : Inhibition Reaction Rate, (mol/m^3·s)
$[R_1^*]$: Concentration of Primary Radicals, (mol/m^3)
$[R_i^*]$: Concentration of Polymeric Radicals of Chain Length i, (mol/m^3)
R_μ : Reaction Channels
r_1 : Random Number
r_2 : Random Number
S : Photoinitiator Molecule
$[S]$: Concentration of Photoinitiator Molecules, (mol/m^3)
$[S]_0$: Initial Concentration of Photoinitiators, (mol/m^3)
s : Laplace Frequency Space
S_G : Gel Strength
s_s : Strain Strain, (m)
s_a : Strain Amplitude, (m)
S_i : Chemical Species
t_1 : Time when the Last Initiation Occured, (s)
t_2 : Time when the Last Reaction Occured, (s)
t_0 : Initial Time, (s)
T_{inf} : Temperature in the SLA, (K)
t_e : Characteristic Exposure Time, (s)
T : Temperaure, (K)
T_a : Chamber Temperature, (K)
T_b : Bath Temperature, (K)
$T_{g,i}$: Glass Transition Temperature of Component I, (K)
t : Reaction Time, (s)
u_{abs} : Rate of UV Absorption by the Resin Per Unit Time, (W/m^3)
v_f : Fractional Free Volume
v_{fct} : Critical Fractional Free Volume for Termination
v_s : Laser Scanning Speed, (m/s)
$v_{g,i}$: Fractional Free Volume of Component i, (K)
ν_{fcp} : Critical Fractional Free Volume for Propagation

v_M : Specific Volume of the Monomer, (m^3/kg)
v_P : Specific Volume of the Polymer, (m^3/kg)
V : Reaction Volume, (m^3)
ΔV_{coll} : Collision Volume, (m^3)
v_{12} : Relative Speed Between Molecules S_1 and S_2, (m/s)
$\langle v_{12} \rangle$: Average Relative Speed Between Molecules S_1 and S_2, (m/s)
w_0 : Gaussian Half-width, (m)
X : Conversion
$X_i(t)$: Species Number at any Given Time t
x_1 : Molecular Concentration of Reacting Specie S_1, (mol/m^3)
x_2 : Molecular Concentration of Reacting Specie S_2, (mol/m^3)
z : Depth of the Resin, (m)
Z : Inhibitor Molecule
Z^* : Inhibitor Radical Molecule
ε : Molar Absorptivity, (m^3/mol$\cdot$m)
ε_V : Volume Fraction Contraction Factor
δt : Small Time Interval, (s)
δ : Phase Angle
λ : Wavelength of the UV Light Irridiating the Resin Surface, (nm)
ϕ : Quatum Yield
ϕ_P : Volume Fraction of the Polymer
ϕ_M : Volume Fraction of the Monomer
α_i : Thermal Expansion Coefficient of Component i, (1/K)
α_c : Critical Degree of Conversion
v_f : Equilibrium Free Volume
ρ_M : Specific Density of the Monomer, (kg/m^3)
ρ_P : Specific Density of the Polymer, (kg/m^3)
η : Viscosity, (kg/m$\cdot$s)
$\sigma(t)$: Time Dependent Stress Response
σ : Induced Stress
τ : Waiting Time, (s)
ω : Frequency Applied of the Shearing Force, (1/s)
v : Frequency of the Light, (1/s)
∇^2 : 2-D Laplacian

FOTOPOLİMERİZASYON PROSESİNİN MATEMATİKSEL MODELLENMESİ VE SİMULASYONU

ÖZET

Stereolitografi, bilgisayarda tasarımı yapılmış karmaşık geometriye sahip herhangi bir cismin istenilen kalitede üretimini sağlayan bir yöntemdir. Stereolitografi yöntemi ile üretim serbest radikal fotopolimerizasyon tepkimesi ile gerçekleştirilmektedir. Bunun için bilgisayar kontrollü ultraviyole (UV) ışın kaynağı kullanılarak sıvı reçine kısa sürede istenilen geometride cisme dönüştürülür. Bu yöntem elektronik, tıp, uzay ve ulaşım gibi çok farklı sahalardaki uygulamalarıyla ekonomik büyüklüğü milyar dolarlara varan bir endüstri olma yolunda hızla ilerlemektedir. Ancak, stereolitografi ile üretimin temel süreci olan fotopolimerizasyon tepkimesi henüz tam olarak anlaşılmış değildir. Bu nedenle, günümüzde ilgi çekici bir araştırma konusu olarak karşımıza çıkmaktadır. Bu çalışmanın temel amacı fotopolimerizasyon tepkime kinetiğinin anlaşılmasını sağlayan ve bu süreçle ilgili doğru tahminler ile sürecin simulasyonunu yapabilen matematiksel modeller geliştirmektir. Bu amaçla geliştirilen, birinci modelde iki boyutlu kısmi diferansiyel denklemler kullanılmış ve başlatma, yayılma, sonlanma ve yavaşlatma gibi temel fotopolimerizasyon tepkimelerine ilave olarak ısı ve kütle aktarımı etkileri de gözönüne alınmıştır. İkinci modelde ise tepkime ortamında bulunabilecek farklı polimerik moleküllere ait derişimlerin belirlenmesi amacıyla bir boyutlu lineer olmayan adi diferansiyel denklemler kullanılmıştır. Bu modelde ayrıca, sonlanma tepkimeleri için kullanılan hız sabitleri tepkimeye giren polimerik moleküllerin monomer sayılarına bağlı olacak şekilde tanımlanarak difüzyonun tepkime kinetiğine etkisi hem yayılma hem de sonlanma hız sabitlerinin türetilmesinde göz önüne alınmıştır.

Stereolitografi cihazında gerçekleştirilen deneylerde dört fonksiyonel grup içeren etoksilenmiş pentaeritritol tetraakrilit (SR494) olan monomere uygun foton soğurma kapasitesine sahip başlatıcı madde %2 oranında katılarak, sıvı reçine yüzeyi bilgisayar kontrollü hareket edebilen bir UV ışın kaynağı ile aydınlatılmış ve farklı tarama hızlarında fotopolimerizasyon ile elde edilmiş katı cisimlerin boyutlarında meydana gelen değişim ölçülmüştür. Üretimi yapılan cisimlerin boyutları iki boyutlu kısmi diferansiyel denklemlerin kullanıldığı model kullanılarak hesaplanmış ve bulunan değerlerin deneysel sonuçlarla uyumlu olduğu belirlenmiştir.

Fotopolimerizasyon sürecinde jelleşme noktası, sıvı reçinenin vizkozitesinde hızlı bir artışın görüldüğü ve katılaşmanın başladığı nokta; bu noktaya ulaşmak için geçen süre de jelleşme zamanı olarak tanımlanmaktadır. Jelleşme zamanının belirlenmesi stereolitografi tekniğinin kullanıldığı üretimler için çok önemlidir. Bu çalışmada, reçine cinsinin, ışığa hassas başlatıcı madde derişiminin, UV ışınının özelliklerinin (dalga boyu ve şiddeti) ve UV ışınının reçine içine nüfuz etme derinliğinin jelleşme zamanına etkisi pasif mikroreoloji deneyleri yapılarak araştırılmıştır. Bu deneylerde,

farklı sayıda fonksiyonel gruplar içeren ve isimleri etoksilenmiş pentaeritritol tetraakrilit (SR494), trimetilpropan triakrilit (SR351), trietilen glikol diakrilit (SR272) ve 2(2-etoksietoksi) etil akrilit (SR256) olan dört monomere, çalışılan ışın frekansında yüksek oranda foton soğurma kapasitesine sahip ve isimi 2,2-dimetoksi 1,2-difeniletanon olan başlatıcı madde değişik oranlarda ilave edilerek hazırlanan reçine karışımları kullanılmıştır.

Birinci grup mikroreoloji deneylerinde, reçinedeki ışığa hassas başlatıcı madde derişimi sabit tutularak, UV ışınının reçine içine nüfuz etme derinliğine bağlı olarak jelleşme zamanındaki değişim belirlenmiştir. Bu deneyler oksijen varlığında gerçekleştirilmiş; ayrıca, UV ışını dalga boyunun ve şiddetinin jelleşme zamanına etkiside incelenmiştir. İkinci grup deneylerde ise, UV ışınının reçine içindeki sabit nüfuz etme derinliği için, jelleşme zamanının başlatıcı madde derişimine bağlı olarak değişimi incelenmiştir. Oksijenin yavaşlatıcı (inhibitör) etkisini gözlemek amacıyla bu deneyler oksijenli ve oksijensiz ortamlarda ayrı ayrı yapılmıştır.

Mikroreoloji deneyleri ile elde edilen sonuçların simulasyonu öncelikle bir boyuta indirgenen kısmi diferansiyel denklemlerden oluşan model ile yapılmıştır. Oksijenli ortamda gerçekleştirilen deney sonuçları ile bu koşullar için elde edilen simulasyon sonuçlarının birbirleri ile oldukça uyumlu olduğu gözlenmiştir. Ancak bu modelin oksijensiz ortamda yapılan deney sonuçlarının simulasyonunda aynı başarıyı gösteremeyerek yetersiz kaldığı belirlenmiştir. Bu nedenle, söz konusu simulasyon bir boyutlu lineer olmayan adi diferansiyel denklemlerin kullanıldığı model ile yapılmaya çalışılmış; ancak, bu modelin çözülmesi ile bulunan simulasyon sonuçlarıda deneysel veriler ile uyum göstermemiştir.

Süreklilik ve deterministik yaklaşıma dayanan bu modellerin oksijensiz ortamda yapılan deney sonuçlarını tahmin etmekteki yetersizlikleri yeni bir model geliştirilmesini zorunlu kılmıştır. Fotopolimerizasyon tepkimelerinin rastgele ve kesikli olmaları dikkate alınarak, yeni model stokastik Monte Carlo yaklaşımı temel alınarak oluşturulmuştur. Stokastik Monte Carlo yaklaşımına dayanan bu model ile elde edilen simulasyon sonuçları ile oksijensiz ortamda elde edilen deneysel sonuçların birbirleri ile uyumunun oldukça iyi olduğu gözlenmiştir. Son olarak, FTIR ve DSC teknikleri uygulanarak elde edilen fotopolimerizasyon tepkime dönüşüm değerleri ile stokastik Monte Carlo yaklaşımı ile hesaplanan dönüşüm değerleri karşılaştırılarak birbirlerine çok yakın olduğu belirlenmiş ve bu yeni modelin geçerliliği ispatlanmıştır.

MATHEMATICAL MODELING AND SIMULATION OF PHOTOPOLYMERIZATION PROCESS

SUMMARY

Stereolithography is a method which produces any object of complex geometry with desired qualities from its computer aided design. The production in stereolithography method is realized by the free-radical photopolymerization reaction. Therefore, a computer controlled ultraviolet (UV) light source is used to turn a liquid resin into a solid object of desired geometry in relatively short time. This method is rapidly growing into a multibillion dollar industry with applications in many fields such as electronics, medicine, aerospace, and transportation. However, the photopolymerization as the fundamental process of stereolithography production is not yet well understood. For this reason it is continuing to be an interesting active research subject today. The main purpose of this study is to develop mathematical models to contribute to the understanding of the reaction kinetics of the photopolymerization process and to make reliable simulations of the process. For this purpose, the first model was developed by using a system of two-dimensional partial differential equations to describe the heat and mass transfer effects in addition to the basic polymerization reactions: initiation, propagation, termination, and inhibition. The second model used one-dimensional coupled nonlinear ordinary differential equations describing the change in the concentration of various polymeric species in the reaction volume. The rate constants used for the termination reactions in this model is determined by considering the chain-length of the polymeric species involved in the reactions. The effects of the free volume and the diffusion on the reaction kinetics in this model are taken into account via both the propagation and termination rate constants.

In experiments conducted in stereolithography, the resin was prepared from four functional ethoxylated pentaerythritol tetraacrylate (SR494) monomer mixing with high absorbance capacity photoinitiator molecule of 2% by weight. The liquid resin surface was illuminated by the UV light source moving under the control of the computer in experiments conducted in stereolithography apparatus and the change in the dimensions of the solid objects produced with different UV light scanning speeds were measured. The dimensions of these solid objects were calculated by solving the model based on the two-dimensional partial differential equations and the results found were determined to be in good agreement with the experimental results.

Gelation point in photopolymerization process is referred to as the point where the liquid resin begins to cure or solidify, causing the resin viscosity to increase rapidly. The time elapses for the photopolymerization process to reach to this point is called the gelation time. The determination of the gelation time is very important for productions using stereolithography technique. In this study, the effects of the resin type, the concentration of photoinitiator, and the properties of UV light (wavelength

and intensity) and the penetration depth of the UV light into the resin on the gelation time were studied by passive microrheology experiments. Four different monomers that are with names ethoxylated pentaerythritol tetraacrylate (SR494), trimethylolpropane triacrylate (SR351), triethylene glycol diacrylate (SR272), and 2(2-ethoxyetoxy) ethyl acrylate (SR256) were used in these experiments. Resins were prepared from these four different monomers (SR494, SR351, SR272, and SR256) with different number of functional groups by mixing them with various amount of 2,2-dimethoxy 1,2-diphenylethanone photoinitiator molecule with high absorption coefficient at the frequency of UV light used in these experiment.

The concentration of the photoinitiator molecules in the first set of microrheology experiments was kept constant and the dependence of the gelation time on the penetration depth of the UV light into the resin was determined. These experiments were conducted in the presence of oxygen; in addition, the effect of the wavelength and the intensity of the UV light on the gelation time were studied. The dependence of gelation time on the photoinitiator loading concentration at the fixed penetration depth of the UV light into the resin were studied in the second set of microrheology experiments. In order to study the inhibition effect of oxygen, these experiments were conducted in the presence and in the absence of oxygen in the reaction volume.

The simulations of the results obtained from microrheology experiments were first carried out with the model based on the one-dimensional partial differential equations. The results from the experiments conducted in the presence of oxygen and the results of the simulations done under the same conditions were found to be in good agreement with each other. However, this model failed to show the same success in predicting the results of experiments conducted in the absence of oxygen. For this reason, the same simulations were repeated using the model based on the one dimensional coupled nonlinear ordinary differential equations; but, the simulation results from the solution of this model did not agree with the experimental data.

These failures of these models based on the deterministic and continuous approaches in predicting the results of experiments performed in the absence of oxygen in the reaction volume led to the development of a new theoretical model. The new model is based on the stochastic Monte Carlo approach in order to account for the inherently random and discrete nature of the photopolymerization reactions. The results from the simulations of this model based on the stochastic Monte Carlo approach and the results from the experiments performed in the absence of oxygen in reaction volume were determined to be in quite good agreement with each other. Finally, the photopolymerization reaction conversion values measured by the experiments conducted using the FTIR and DSC techniques and the conversion values obtained from the stochastic Monte Carlo approach were compared with each other and the close agreement between these results were determined; thus, the validation of this new model was proved.

1. INTRODUCTION

Photopolymerization, which is the underlying basic reaction mechanism of stereolithography (SL) has a wide range of applications such as: creating decorative and protective coatings, fabricating biomedical prostheses, contact lenses, and dental restorations, manufacturing electronic components, and making fiber optic coatings. Photopolymerization has been extensively studied due to its importance in so many fields. The absorption of light by the photoinitiator molecules mixed into the resin creates highly reactive radicals, and these radicals interact with the functional groups of monomers that compose the resin. This, in turn, converts the monomers into radicals and starts a chain reaction, which causes a large percentage of the monomers in the resin to ultimately become entangled in a highly cross-linked polymeric network. Another key advantage of using light-induced photopolymerization is that such processes tend to be less damaging to the environment; they generally use smaller amounts of solvents and less energy overall than polymerization processes that are activated by thermal means. Using photopolymerization also gives one a high degree of control over how the reaction proceeds as a function of both space and time in many applications such as SL.

SL is one of the most widely used and cost-effective method for creating three-dimensional (3-D) objects from thin layers of hardened (cured) liquid polymers. Generally, an intense ultraviolet (UV) light source is used to solidify these liquid polymers, which are also known as resins, from a series of consecutive two-dimensional (2-D) cross sections. Often data from computer-aided design (CAD) software is used to control the precise movements of the UV light source as it builds the object. The resulting product may serve as a prototype for engineering designs before its mass production and for low-volume manufacturing applications.

Stereolithography coupled with particle-tracking microrheology allows one to determine the rheological properties of the burgeoning polymeric product during the process of photopolymerization. Having such precise control over the rheological properties of an evolving product could have a paramount effect on its final quality and extend its ability to be used in different applications of high sensitivity.

Over the last few decades, a considerable literature has accumulated for the purpose of understanding the kinetics of the photopolymerization process [1-4]. The most important parameters which govern the photopolymerization process are the temperature, the UV light penetration depth, UV light source properties (wavelength and intensity), the functionality and reactivity of the monomer, and initial concentration and reactivity of the photoinitiator. The kinetics studies mainly measured and simulated double bond conversion and determined the effect of the parameters just mentioned on the overall double bond conversion. The effect of these parameters on the cure depth of the sample and photoinitiator loading concentration, in contrast, has not been nearly as well studied.

In this thesis, the effect of the scanning speed of the UV light source on the photopolymerization process is studied. These speeds were chosen so that the resulting fabricated polymerized products would have measurably different degrees of polymerization with scans done at these two speeds; additionally, if a speed much faster than the higher speed was used, the critical gel point was never achieved. This process was modeled using deterministic systems of two-dimensional (2-D) Partial Differential Equations (PDE).

This thesis also places a great deal of emphasis on understanding the effect of the UV light penetration depth, the photoinitiator loading concentration and oxygen inhibition on the final cured resin. Experimental gel points were determined using a passive particle-tracking microrheological technique; in these studies the random, thermally caused Brownian motion of embedded micron-sized fluorescent tracer particles is examined under videomicroscopy to determine the rheological properties of the resin.

First experiments were conducted to examine the dependence of the gelation time on the penetration depth of the UV light source. This process was modeled using both deterministic systems of one-dimensional (1-D) Partial Differential Equations (PDE) and ordinary differential equations (ODE) to represent the reaction rate equations; these deterministic simulations adequately predicted the trend of the experimental data. Another set of experimental measurements showed a nonlinear dependence on the gelation time in the absence of oxygen as a function of the photoinitiator loading concentration. The deterministic 1-D PDE and ODE modeling studies, though, failed to predict this trend of the experimental results accurately. Because of the failure of the deterministic and continous approach, a new probabilistic approach based on a discrete and stochastic Monte Carlo model (SMCM) was applied to the photopolymerization process; this stochastic model succeeded in capturing the inherent nonlinearity of the relationship between the gelation time and the photoinitiator loading concentration [5].

The dependence of the gelation time on the number of functional groups per monomer was studied both experimentally and via stochastic Monte Carlo model simulations. Confirming well-known conclusions in the literature, the speed of photopolymerization was found to be critically dependent on the functionality of the monomers. This nonlinear dependence of the gelation time on photoinitiator loading concentration becomes more obvious as the number of functional groups per monomer increases.

Fourier Transform Infrared Spectroscopy (FTIR) and Differential Scanning Calorimeter (DSC) experiments were performed to measure the rate of double bond conversion to further validate the SMCM.

2. PHOTOPOLYMERIZATION

Photopolymerization is a light-induced reaction that converts a liquid monomer into a solid polymer. The use of light, rather than heat, to drive the reactions leads to a variety of advantages, including solvent-free formulations, very high reaction rates at room temperature, spatial control of the polymerization, low energy input, and chemical versatility since a wide variety of resins composed of different types of monomers and photoinitiator molecules can be polymerized photochemically. Indeed, photopolymerization is one of the most rapidly expanding processes for materials production, with more than 15% annual growth projected for the next several years. Well over 50 billion kilograms of polymer are produced each year in the world, and it is expected that this figure will significantly increase in the coming years as higher-strength plastics and composite materials replace metals in automobiles and other products [6]. Therefore, photopolymerization is one scientific domain that offers both a wealth of fascinating fundamental challenges and a variety of practical applications that warrant further investigation.

Photopolymerization systems usually contain three main components: photoinitiators, monomers, and additives used to impart desired properties. The photopolymerization process is initiated by a reactive species produced from photoinitiator when light is absorbed. The reactive species, which may be either free radicals, cations or anions, adds to a monomer molecule by opening the π-bond to form a new radical, cation, or anion [7]. The process of breaking double bonds is repeated as additional monomer molecules are added to the many growing polymeric radicals in the reaction volume. Linear polymer chains result when the reacting monomer species contain a single double bond; multifunctional monomers, i.e., monomers with multiple double bonds, can react to form a densely cross-linked network of polymer chains. Such polymeric networks are relatively insoluble in organic solvents and resistant to heat and mechanical treatments [8, 9]. Because of these unique properties, these polymers have a large and growing number of practical applications in many fields including electronics, optics, video disc coatings, asperical lenses, biomaterails, and drug delivery [1, 2, 10, 11].

2.1 Photoinitiators

Most of the commonly used resins do not produce free radicals when exposed to UV light [2]. Thus, it is necessary to mix the resin with properly selected photoinitiator molecules so that they initiate the photopolymerization process by producing free radicals upon exposure to UV light. Upon absorption of UV light with a specific frequency, the photoinitiator molecule is promoted from the ground electronic state to either a singlet or triplet excited electronic state. These excited molecules then undergo cleavage or react with another molecule to produce initiating free radicals [12]. The photoinitiator is critically important because it controls the rate of initiation and its absorption of UV light limits the penetration of the incident light into the sample and, therefore, the cure depth [10]. The most commonly used photoinitiators are classified as unimolecular (Type I) and bimolecular (Type II) photoinitiators.

2.1.1 Unimolecular photoinitiators (type I)

With unimolecular photoinitiators, only a single molecular species interacts with the light and produces free radicals. One class of unimolecular photoinitiators produces radicals through the cleavage of the photoinitiator molecule as shown in Figure 2.1 [10]. This class of photoinitiators consists mostly of aromatic carbonyl compounds and the double bond cleavage may take place at either the α or β position with respect to the carbonyl group. When the bond adjacent to the carbonyl is broken to produce two free radicals—one benzoyl and one fragment radical—the process is called α-cleavage [12, 13]. In this case, the benzoyl radical is the predominant initiating species; the fragment radical may not contribute to the initiation [13]. β-cleavage occurs mostly in photoinitiators with a benzoyl chromophore which possess adjacent carbon-sulfur bond or carbon-oxygen bonds [12, 13].

A second class of unimolecular photoinitiators forms biradicals through intramolecular hydrogen abstraction as shown in Figure 2.2 [13]. Ketones often photodissociate via this mechanism; the products of this pathway are a ketyl radical, which participates in the termination of the photopolymerization process, and another radical that starts the propagation of the polymer chain.

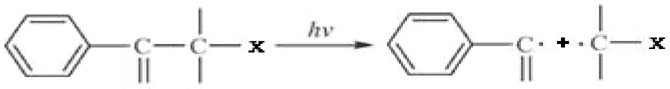

Figure 2.1: Cleavage Mechanism of Unimolecular Photoinitiator Free Radical Generation

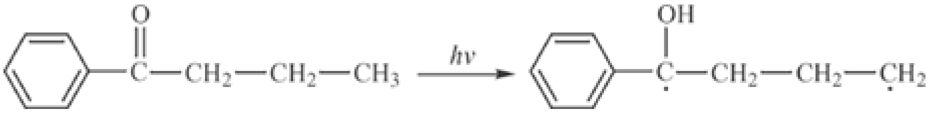

Figure 2.2: Hydrogen Abstraction Mechanism of Unimolecular Photoinitiator

2.1.2 Bimolecular photoinitiators (type II)

Bimolecular photoinitiator systems produce radicals by a bimolecular reaction wherein one photoinitiator molecule in an electronically excited state interacts with a second co-initiating molecule as shown in Figure 2.3 [13]. The photoinitiator in its excited state generally receives a hydrogen atom or an electron from the co-initiator, which is generally an ether or an alcohol. The transfer of an electron or hydrogen produces one or more free radicals, and it is these free radicals that actually begin the photopolymerization process. Benzophenone derivatives, thioxanthones, camphorquinones, benzyls, and ketocoumarins are all bimolecular photoinitiators [10, 13].

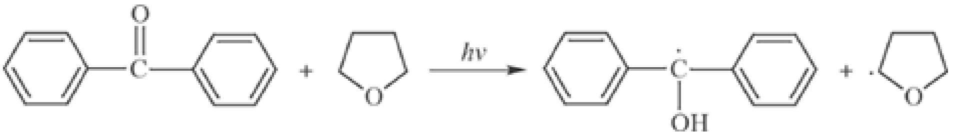

Figure 2.3: General Bimolecular Photoinitiator Free-Radical Generation Mechanism

The wavelength of the radiation needed to produce free radicals via bimolecular photoinitiatiation is generally longer (i.e., uses lower energy) than in unimolecular photoinitiator systems. Thus, the free radicals that are produced in the resins with bimolecular photoinitiators are less energetic than those produced by unimolecular photoinitiators. Because they have less kinetic energy, these free radicals diffuse less rapidly than in unimolecular photoinitiator systems [12, 13].

In the bimolecular systems described above, the co-initiator molecules do not absorb light to initiate polymerization. In contrast, photosensitizers that are able to absorb light are often used enhance the photopolymerization. Photosensitizers are used when a monomer or pigment absorbs light of similar frequencies as the photoinitiator; they allow one to use a frequency of light to which the monomer is transparent to initiate the photopolymerization process [12, 13]. Photosensitizers can increase the efficiency of the photoinitiation process by absorbing photons from the light source that the photoinitiator absorbs with low efficiency, or does not absorb at all [10]. The photosensitizers and photoinitiators interact by two mechanisms: energy transfer and electron transfer. In the energy transfer mechanism, the photosensitizer absorbs the light and transfers the energy to the photoinitiator in order to generate the free radicals that start the photopolymerization. In the more common electron transfer mechanism, the photosensitizer becomes electronically excited when illuminated and forms an excimer (excited dimer) with the photoinitiator; this excimer then facilitates electron transfer from the photoinitiator to the photosensitizer, and produces two free radicals [12].

2.2 Monomers

Unsaturated monomers containing carbon-carbon double bonds are extensively used in free-radical photopolymerization processes. The free radical active center on the growing polymeric radical reacts with the unsaturated monomer by opening the carbon-carbon double bond and adding the monomer unit to its chain. Acrylate and methacrylate, thiol-ene, and unsaturated polyesters are the three most commonly used monomers in photopolymerization processes [2].

Acrylate and methacrylate monomers are the most widely used in photopolymerization processes [10]. These resins are extensively employed in photopolymerization due to their high reactivity and ability to form a large variety of cross-linked polymers with tailor-made properties such as color, flexibility and surface characteristics. The generalized structures of acrylate and methacrylate monomers and of their corresponding polymer are shown in Figure 2.4.

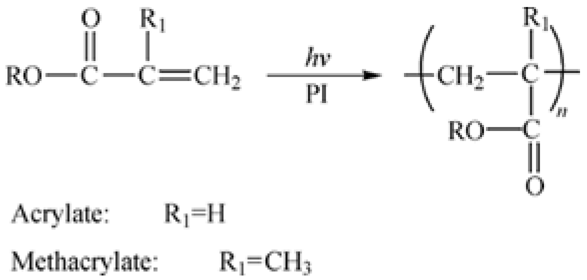

Figure 2.4: Molecular Structure of a Generalized Acrylate Monomer and Its Corresponding Polymer Repeat Unit; The R_1 Side Group May Vary

Studies have shown that acrylates have faster reaction rates than methacrylate counterparts [14]. The functionality of acrylate monomers is critical in its influence on the rheological properties of the burgeoning polymeric species and on the curing speed; monomers with more double bonds have a higher viscosity and, thus, a faster curing speed [15]. Linear acrylates are generally used as reactive diluents to reduce the viscosity of the unpolymerized liquid for ease of processing. In contrast, multifunctional acrylates increase the mechanical strength and solvent resistance of the polymer product by forming cross-linked networks rather than linear polymer chains [10, 13].

Acrylate and methacrylate monomers, despite their popularity, have several drawbacks; for example, they exhibit relatively large polymerization shrinkage and some methacrylate and acrylate monomers are highly toxic. In general, a methacrylate monomer is less toxic and volatile than the corresponding acrylate monomer [16]. Shrinkage, which is occurred as the covalent bonds formed between monomer molecules, produces stress in the resulting polymer parts; this stress can ultimately reduces the quality of these parts. Covalent bonds decrease the distance between monomer molecules by approximately half with respect to two separated molecules experiencing van der Waal's forces. Shrinkage results in a 5-25% loss in volume, which corresponds to 2-8% loss in linear dimensions [13, 16]. Thus, shrinkage can bring in additional financial costs for industries that use acrylate and methacrylate monomeric resins as the raw material. Oligomeric acrylates, which contain 1 to 12 repeat units formed via step-growth polymerization, are often used to reduce shrinkage in the final polymeric product [10, 13, 16, 17].

Systems that combine thiols with ene co-monomers, such as alkyl ethers or acrylates were originally developed in the 1970's, but were later abandoned for acrylate systems because of unpleasant odor of the sulfur byproducts [13]. In these systems, the thiol group functions as a photoinitiator by producing a thiyl and a hydrogen radical pair through a sulfur-hydrogen bond cleavage when exposed to UV light. Thiol-ene systems, therefore, require little or no photoinitiator in order to polymerize [10, 13-15]. Since photoinitiators are often the most expensive chemicals in a photopolymerization system, the production costs associated with thiol-ene systems are consequently reduced [14]. This has led to greater interest in these systems recently. Thiol-ene systems also are inhibited less by the presence of oxygen and experience less volume shrinkage compared to acrylate systems [13]. However a potential disadvantage of thiol-ene systems is that they have comparatively slow cure rates relative to conventional acrylate systems [10, 13].

Some of the first resins used in large scale free radical photopolymerization applications consisted of unsaturated polyester dissolved in styrene [10]. When exposed to UV light, the carbon-carbon double bond in the unsaturated polyester and styrene copolymerize to form a cross-linked network [12]. The generalized copolymerization reaction for an unsaturated polyester molecule with styrene is shown in Figure 2.5 [12].

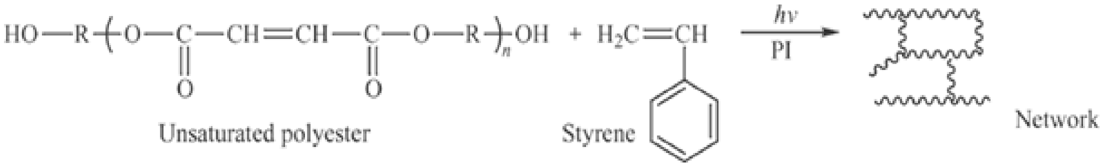

Figure 2.5: Generalized Reaction Scheme for an Unsaturated Polyester System

The unsaturated polyester-styrene copolymerization system has not been used widely due to its relatively slow curing rate, coupled with the high volatility of the reagents and the few types of different unsaturated polyester monomers that are commercially available. Currently unsaturated polyesters are chiefly used in the wood finishing industry because of their relatively low material cost [10, 13].

2.3 Additives

In photopolymerization process, additives are used for changing mechanical, chemical, surface, aesthetic, processing, and heat properties of final product [18]. The most commonly used additives are chain transfer agents, crosslinkers, plasticizers, pigments, aesthetic odorants, polymerization and polymer property modifiers, stabilizers, and surfactants.

Plasticizers are mainly used to increase the flexibility of the final product. Lubricants are commonly used to modify the surface properties. Plasticizers and lubricants are also frequently used to enhance the processing properties.

Pure polymers are often too rigid to be used as flexible films. A common example of this is the poly(vinyl chloride) or PVC. PVC in the pure state is a prohibitively rigid for many applications; thus, only when this polymer is softened by the addition of liquids, such as phthalate esters, it can be used as a flexible-film or Tygon tubing. Such liquid additives like phthalate esters are classified as plasticizers [18].

Antioxidants are additives used to prevent a material from degradation due to reaction with ambient oxygen. Odorants, deodorants, dyes and pigments are additives which are frequently used to enhance the appearance and smell of a product. Pigments are coloring additives and can be inorganic, such as Aluminium flakes, or organic, such as isoindolines, quinacridones, and dioxazines, in composition [19].

Dyes are another category of coloring additives. Typically dyes are organic liquids that exhibit a high degree of solubility in a wide range of common solvents. Because they are liquids, it is also simple to disperse them throughout most polymer samples. The most widely used dyes by the polymer industry are azo and anthraquinone dyes.

Mixing an unpolymerized or partially polymerized resin with specific chemicals called crosslinkers results in a chemical reaction that forms a cross-linked polymer network. Crosslinkers also exert a strong influence on the physical and rheological properties of the resulting polymer network. Some of the commercially available crosslinkers are bisphenol ethoxylate, diurethane dimethacrylate, divinylbenzene, trimethylolpropane ethoxylate, and polycarbodimide.

A chain transfer agent is an additive which changes the chain lengths of the polymeric radical and thereby the propagation rate of the photopolymerization process. Chain transfer agents shift the polymeric radical distribution towards a shorter average chain lengths. The high mobility of these shorter radicals in the reaction volume increases the rate of termination; which in turn decreases the overall rate of photopolymerization [20]. Common chain transfer agents include Isooctyl 3-mercaptopropionate, 4,4′-Thiobisbenzenethiol, and Pentaerythritol tetrakis(3-mercaptopropionate) [21].

2.4 Photopolymerization Kinetics

The chemistry and kinetics of photopolymerization are described in detail in many review articles and published books [2-4, 7, 18, 22-25]. Here, a concise description of the photopolymerization kinetics is given.

There are three primary reaction mechanisms in the photopolymerization process: initiation, propagation, and termination. In the following discussion, these primary reactions are discussed along with other features associated with photopolymerization kinetics.

2.4.1 Initiation reaction mechanism

The initiation step starts when photoinitiator molecules absorb photons to form photoinitiator free radicals, I^*. The fragmentation of an photoinitiator molecule into its free radicals is represented by the following reaction.

$$S \overset{k_i}{\rightarrow} 2I^* \tag{2.1}$$

Here S represents the photoinitiator molecule and k_i is the initiation rate constant for the dissociation of photoinitiator molecules via photon absorption. Photoinitiator free radicals then attack monomers to form primary radicals. This reaction step is represented by Eq. (2.2).

$$I^* + M \overset{k'}{\rightarrow} R_1^* \tag{2.2}$$

where M represents a monomer molecule, R_1^* represents the primary radical and k' represents the kinetic rate constant for the initiation step.

The rate of the reaction given in Eq. (2.1) depends on the intensity of the UV light shining on the resin. The amount of photoinitiator converted to free radicals is a function of both the intensity of the UV light and the time of exposure. These two factors determine the amount of free radicals produced as a function of the UV light penetration depth into the resin and the radial distance from the center of the UV light beam. At any depth, the UV light intensity obeys a Gaussian distribution in the plane normal to the surface with radial symmetry from the center of the UV light source.

The intensity reduction of the UV light source as it penetrates into the resin is due to the absorption of UV photons by photoinitiator molecules contained therein. It is well-known that, when light passes through an absorbing medium, its intensity as a function of penetration depth obeys the Beer-Lambert Law [24]. Since the resin contains UV-absorbing photoinitiator molecules, the intensity of the UV light as it penetrates through the resin may thus be treated via application of the Beer-Lambert Law. According to this law, the amount of radiation absorbed by the resin may be defined as the logarithm of the ratio of the intensity of the incident radiation on the surface of the resin to the intensity of radiation transmitted out of the resin volume.

If A_{in} represents the amount of radiation incident on the surface of the resin and A_{out} represents the amount of radiation transmitted out of the resin volume at a depth z from the surface, then the total amount of radiation, $A(z)$, absorbed can be given by Eq. (2.3).

$$A(z) = \log_{10}(\frac{A_{in}}{A_{out}}) \tag{2.3}$$

The total amount of radiation absorbed is also linearly related to the concentration of the photoinitiator molecules, which is expressed as [20],

$$A(z) = \varepsilon z[S] \tag{2.4}$$

where ε is the molar absorptivity, z is the light path length traveled by the UV light within the resin, and $[S]$ is the concentration of photoinitiator molecules. Absorptivity is the inherent ability of a chemical species to absorb light, which is constant at a given wavelength. During the absorption process, energy is transferred from a photon to a molecule; which causes electrons to be promoted from the lowest energy level to higher energy levels called excited states. The energy difference between the two electronic states is equal to the energy of the incident photon which is absorbed in the process. Combining Eqs. (2.3) and (2.4) gives,

$$\frac{A_{out}}{A_{in}} = e^{-2.303\varepsilon[S]z} \tag{2.5}$$

This equation is another formulation of the Beer-Lambert Law [24, 25]. According to Figure 2.6, the intensity of the UV light within the resin as a function of depth maybe written as:

$$A_{out} = A_{in} e^{-2.303\varepsilon[S]z} \tag{2.6}$$

The factor $2.303\,\varepsilon[S]$ in the exponential can be shown to be the absorption rate of the UV light by the resin per unit distance normal to the resin surface. This can be obtained via the following limit which measures the fraction of photons absorbed per unit volume of the resin. The rate of UV light absorption by the resin per unit volume, u_{abs}, is defined by the following limit based on the infinitesimal resin volume shown in Figure 2.6 [25].

$$u_{abs} = \lim_{\Delta x, \Delta y, \Delta z \to 0} \frac{A_{in}\Delta x \Delta y - A_{out}\Delta x \Delta y}{\Delta x \Delta y \Delta z} \tag{2.7}$$

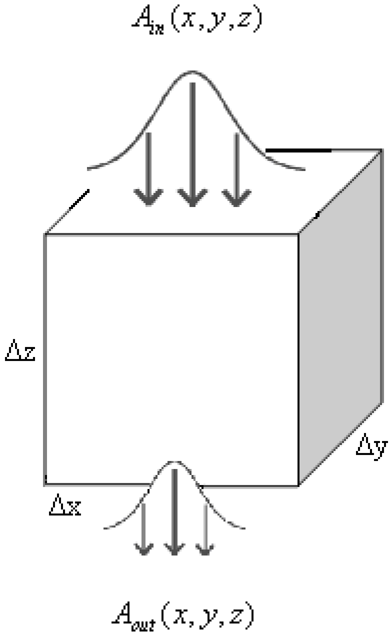

Figure 2.6: Absorption of Light by the Resin [25]

Assuming that the resin obeys the Beer-Lambert Law, the limit in Eq. (2.7) can be calculated using Eq. (2.6):

$$u_{abs} = \lim_{\Delta x,\Delta y,\Delta z\to 0} \frac{A_{in}\Delta x\Delta y - A_{in}e^{-2.303\varepsilon[S]\Delta z}\Delta x\Delta y}{\Delta x\Delta y\Delta z} \tag{2.8}$$

$$u_{abs} = \lim_{\Delta x,\Delta y,\Delta z\to 0} \frac{A_{in}(1-e^{-2.303\varepsilon[S]\Delta z})\Delta x\Delta y}{\Delta x\Delta y\Delta z} \tag{2.9}$$

Since the volume in Figure 2.6 has the same upper and lower bounding surfaces, the factors $\Delta x\Delta y$ in the numerator and denominator cancel out:

$$u_{abs} = \lim_{\Delta z\to 0} \frac{A_{in}(1-e^{-2.303\varepsilon[S]\Delta z})}{\Delta z} \tag{2.10}$$

Before taking the limit above, the exponential term may be expanded into a Taylor series to give

$$1-e^{-2.303\varepsilon[S]\Delta z}=2.303\varepsilon\left[S\right]\Delta z-\frac{(2.303\varepsilon\left[S\right]\Delta z)^2}{2!}+\frac{(2.303\varepsilon\left[S\right]\Delta z)^3}{3!}-+..... \qquad \textbf{(2.11)}$$

In stereolithography and microrheology applications, the value of the term $2.303\varepsilon\left[S\right]\Delta z$ is much less than 1.0. Therefore, Eq. (2.11) can be written using only terms to first order in Δz as:

$$1-e^{-2.303\varepsilon[S]\Delta z}=2.303\varepsilon\left[S\right]\Delta z \qquad \textbf{(2.12)}$$

Substituting Eq. (2.12) into Eq. (2.10) and canceling the factors of Δz in the numerator and denominator gives Eq. (2.13), which describes the rate of UV photons absorbed per unit distance of penetration into the resin in *z*-direction.

$$u_{abs}=2.303\varepsilon\left[S\right]A_{in} \qquad \textbf{(2.13)}$$

If *z* represents the depth of the reaction volume then the UV light absorption rate can be written as

$$R_{abs}=2.303\varepsilon\left[S\right]A_{in}z \qquad \textbf{(2.14)}$$

To get the initiation rate, R_i, in units of mol/(m^{3}s) Eq. (2.14) must be divided first by $N_{Av}hc/\lambda$, where N_{Av} is the Avogadro's number, *h* is the Planck's constant, *c* is the speed of light, and λ is the wavelength of the UV light irridiating the resin surface.

Since not all absorbed photons contribute to the photopolymerization initiation reaction, there is a need to introduce the concept of a quantum yield. The quantum yield is represented by ϕ and is defined as the fraction of absorbed photons that initiate photopolymerization. Thus, the rate of initiation in units of mol/(m^{3}s) is given by

$$R_i=\frac{2\phi\lambda R_{abs}}{N_{Av}hc} \qquad \textbf{(2.15)}$$

Photocleaving of each initiator molecule results in two initiator radicals and this is the reason how the factor 2 was introduced into Eq. (2.15) [26].

It is more convenient to express the conversion as a function of the thickness of the resin [7]. Thus, in writing the time derivative of the photoinitiator concentration (or equivalently the photon absorption rate), R_{abs} in Eq. (2.13) is multiplied by the depth of the reacting system, z [20].

$$\frac{d[S]}{dt}=-\frac{R_i}{2\phi}=-\frac{2.303\varepsilon[S]\lambda A_{in}z}{N_{Av}hc} \tag{2.16}$$

This equation gives the time derivative of the photoinitiator concentration when solved simultaneously with the other coupled nonlinear differential equations describing the reactions among monomers, photoinitiator radicals, and polymeric radicals.

2.4.2 Propagation reaction mechanism

During propagation, primary radical molecules, R_1^*, formed at the initiation step continue to add monomer molecules in a chain-like fashion to form macro radicals of different molecular weight. The propagation reaction between a free radical and a monomer molecule can be represented by the following equation.

$$R_1^*+M\xrightarrow{k_p}R_2^* \tag{2.17}$$

The resulting polymer radical R_2^* propagates by Eq. (2.18) and this process continues as indicated in Eq. (2.19).

$$R_2^*+M\xrightarrow{k_p}R_3^* \tag{2.18}$$

$$\vdots$$

$$R_{n-1}^*+M\xrightarrow{k_p}R_n^* \tag{2.19}$$

where R_n^* represents a growing polymeric radical chain of n monomer units and k_p is the kinetic rate constant for propagation. The rate of propagation depends on the functionality of the monomers. The photopolymerization of monomers with one double bond results in linear chains while the photopolymerization of multifunctional monomers produces highly cross-linked polymeric networks. During the propagation step, multifunctional monomers are added successively into polymer chains as units containing pendent double bonds. As the propagation reaction continues, these pendent double bonds are attacked by radical sites either on the same chain or on different chains. The propagation reaction which takes place between a pendent double bond and a radical site, both of which are on the same growing polymer radical, is called a primary cyclization reaction.

The propagation reaction which takes place between a pendent double bond on one growing polymer radical and a radical site on a different growing polymer radical is called an intermolecular interaction. Both cyclization and intermolecular reactions are cross-linking reactions and can only occur in the polymerization of multifunctional monomers. Figure 2.7 shows how these reactions may lead to a highly cross-linked network [2].

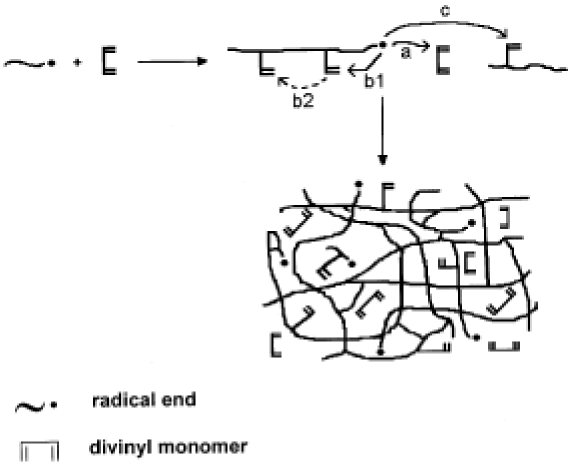

Figure 2.7: Network Formation During Polymerization of Multifunctional Monomers [2]

The cyclization reactions are assumed to be very effective from the beginning of the photopolymerization process. This is because the radical site would see a greater concentration of pendent double bonds in the vicinity of its own molecule than of monomer double bonds on the other species to attack. As discussed extensively by

Andrzejewska, such interactions lead to compact structures called microgels at the very early stages and cause a delay in the actual gel point conversion [2]. Macrogelation occurs by forming chemical bonding between the microgel particles. The formation of microgels is the reason for network inhomogeneity, and this can lead to a significant reduction in the mechanical strength of the polymer network when compared to a homogeneous network [27, 28].

2.4.3 Termination reaction mechanism

Termination reaction takes place by either coupling of two growing polymer radicals to form a single dead polymer of chain length equal to the sum of the chain lengths of combining radicals. This reaction is represented by Eq. (2.20) and is commonly called termination by combination [7].

$$R_n^* + R_m^* \xrightarrow{k_{tc}} R_{n+m} \tag{2.20}$$

where k_{tc} represents the kinetic rate constant for termination by combination. Radical termination may also occur as a result of an atom transfer from one growing polymer radical to another. This type of termination reaction is called termination by disproportionation and leads to two different types of dead polymer molecules, as shown in Eq. (2.21).

$$R_n^* + R_m^* \xrightarrow{k_{td}} R_n + R_m \tag{2.21}$$

where k_{td} represents the kinetic rate constant for termination by disproportionation. Termination can also take place by the reaction of an initiator radical with a growing polymer radical as shown in Eq. (2.22).

$$R_n^* + I^* \xrightarrow{k_{tp}} R_n \tag{2.22}$$

where k_{tp} represents the kinetic rate constant for termination by photoinitiator radicals.

Although there are two distinct rate constants for termination by combination and termination by disproportionation, it is a common practice in deterministic modeling of photopolymerization to use a single rate constant to describe both termination mechanisms [2, 16, 20]. Therefore throughout this thesis, the kinetic rate constants for termination by combination and for termination by disproportionation are assumed to be identical in this discussion and from now on k_{tc} and k_{td} will be represented by a common value k_t. Before giving the detailed mathematical expressions for the propagation and termination rate constants, a formula for the rate of initiation will be derived.

Termination reactions are heavily influenced by network formation. The reacting species's mobility through center of mass diffusion dramatically decreases as the size of the network gets larger. This leads to a reduced termination rate. This decreased rate of termination leads to an increase in radical concentration. The greater radical concentration then causes the photopolymerization rate to increase, which leads to autoacceleration. Even if the center of mass diffusion of polymer radicals becomes severely limited, the radicals can still approach each other either through segmental diffusion or by propagation. As the reaction proceeds and the crosslink density increases, the movement of radical sites by propagation reactions becomes much faster compared to segmental diffusion. Thus, diffusion becomes the dominating termination mechanism of reaction even at relatively low degrees of conversion.

2.4.4 Rates and rate constants of propagation and termination reactions

The rate of photopolymerization may be written as the time derivative of the monomer concentration. The monomer concentration decreases as function of time due the initiation and propagation reactions. Since most monomer molecules are involved in the propagation step, it is possible to neglect the rate of initiation in writing the time derivative of the monomer concentration. Thus, the rate of photopolymerization is defined as propagation rate, R_p, which is proportional to the product of the instantaneous monomer concentration [M] and the total concentration of all the radical species [R^*] in the reaction volume:

$$R_p = k_p[M][R^*] \tag{2.23}$$

From Eq. (2.23) one might conclude that the rate of propagation decreases as long as the photopolymerization proceeds since the monomer concentration $[M]$ decreases. However, in reality, the opposite of this expectation is often seen. Similar equations to Eq. (2.23) may easily be written in for the rates of termination and inhibition in terms of the concentrations of the species involved in the reaction.

Termination is considered as always being diffusion controlled from the onset of the photopolymerization [3, 29]. Benson and North first described the diffusion-controlled termination between two polymer radicals as a reaction taking place in three consecutive stages as illustrated in Figure 2.8 [3, 30, 31]. First, two polymer radicals must come into contact as a result of center-of-mass or translational diffusion. In the second step, a segmental reorientation of two polymer radicals must take place to bring the reactive chain ends in close proximity to form a radical-radical encounter pair. In the third step, the actual termination reaction occurs either by combination or disproportionation. As conversion increases, the polymer chains and the macroradicals begin to form entanglements leading to a highly cross-linked network as shown in Figure 2.7. As a result, both translational and segmental diffusion are significantly retarded. The continuing increase in the radical sizes as a result of propagation as a function of the reaction time further limits the mobility of the polymeric radicals. This mobility limitation of the growing polymer radicals due to the increased viscosity causes the rate of termination to decrease. This phenomenon is known as the gel effect or the Trommsdorf effect. The consequence of the Trommsdorf effect is that the termination rate coefficient not only depends on temperature and pressure as all rate coefficients do, but also on many other parameters that can have an influence on the diffusion of the growing polymer radicals. Some of these parameters are the polymer weight fraction, the resin viscosity, and the chain lengths of the macroradicals. There have been many models to include the diffusion control on the reaction through the propagation and termination constants [3].

Marten and Hamielec and Bowman and Peppas related the kinetic constants k_p and k_t directly to the diffusion coefficients of the monomeric and polymeric radicals, respectively [32-34]. Marten and Hamielec assumed that distinct regions exist for reaction- and diffusion-controlled polymerization, and divided the course of reaction into three conversion intervals to evaluate k_p and k_t [32, 33].

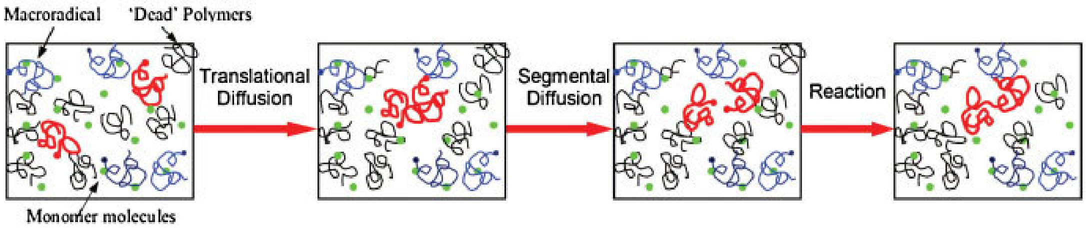

Figure 2.8: Diffusion and Reaction Steps During Termination of Two Polymer Radicals [3]

Bowman and Peppas adopted the same idea and coupled these intervals with volume relaxation during polymerization [34]. Anseth and Bowman developed a model for k_p and k_t by considering critical free volumes [4]. They defined a critical fractional free volume, v_{fcp} , which represents the volume in which the transition occurs from reaction to diffusion-control propagation. The formula for k_p developed by Anseth and Bowman is given in Eq. (2.24) [4].

$$k_p = \frac{k_{p0}}{1+e^{A_p(1/v_f - 1/v_{f_{cp}})}} \tag{2.24}$$

where A_p is a parameter that determines the rate at which the propagation rate constant decreases in the diffusion-controlled region, v_f is the fractional free volume of the curing system, $v_{f_{cp}}$ is the critical fractional free volume for propagation [3, 35].

Anseth and Bowman considered translational, segmental and reaction diffusion as diffusion resistance and developed a formula for the termination constant, k_t, as given in Eq. (2.25) [4].

$$k_t = \frac{k_{t0}}{1+\dfrac{1}{R_{rd}k_p[M]/k_{t0} + e^{-A_t(1/v_f - 1/v_{f_{ct}})}}} \tag{2.25}$$

where A_t is the parameter that determines the rate at which the termination rate constant decrease in the diffusion-controlled region, $v_{f_{ct}}$ is the critical fractional free volume for termination, and R_{rd} is the reaction diffusion constant. The rate constants

k_{p0} and k_{t0} in Eqs. (2.24) and (2.25) represent the Arrhenius constants for the propagation and termination reactions, which are given in Eqs. (2.26) and (2.27), respectively [11, 35]. The Arrhenius constants represent the effect of the temperature increase in the reacting system due to the heat released during the polymerization process.

$$k_{p0} = A_{Ep} e^{-E_p / RT} \tag{2.26}$$

$$k_{t0} = A_{Et} e^{-E_t / RT} \tag{2.27}$$

where the pre-exponential factors, A_{Ep} and A_{Et}, corresponds to the propagation and termination reactions in the absence of diffusion limitations, respectively; E_p and E_t are activation energies for the propagation and termination reactions, respectively; R is the universal gas constant; and T is the local temperature.

As can be seen from Eqs. (2.24) and (2.25), the propagation and termination rate constants are obtained from the free volume theory. According to this theory, the free volume of a component i in the polymerizing resin is given by the following relation [4, 34-39]:

$$v_{f,i} = v_{g,i} + \alpha_i (T - T_{g,i}) \tag{2.28}$$

where α_i is the thermal expansion coefficient of component i, $T_{g,i}$ is the glass transition temperature of component i, and $v_{g,i}$ is the fractional free volume of component i. If one assumes that the fractional free volume at the glass transition temperature associated with the monomer and polymer can be added ideally and that the free volume varies linearly with the temperature above the glass transition temperature, then the equilibrium free volume v_f may be written as [4]:

$$v_f = 0.025 + \alpha_M (T - T_{g,M})(1 - \phi_P) + \alpha_P (T - T_{g,P}) \phi_P \tag{2.29}$$

where ϕ_P is the volume fraction of the polymer and T is the reaction temperature. The subscripts M and P refer to monomer and polymer components of the system, respectively. The volume fraction of the polymer as a function of the conversion, *X*, can be calculated from Eq. (2.30).

$$\phi_P = \frac{X(1-\varepsilon_V)}{1-X\varepsilon_V} \tag{2.30}$$

where ε_V is the volume fraction contraction factor defined by Eq. (2.31).

$$\varepsilon_V = \frac{v_M - v_P}{v_M} \tag{2.31}$$

where v_M is the specific volume of the monomer and v_P is the specific volume of the polymer. Using Eqs. (2.29)-(2.31), the volume fraction of monomer can be easily obtained:

$$\phi_M = 1-\phi_P = \frac{1-X}{1-X\varepsilon_V} = \frac{1-X}{1-X(1-\frac{v_P}{v_M})} \tag{2.32}$$

Eq. (2.32) may also be written in terms of the specific densities of the monomer and the polymer:

$$\phi_M = \frac{1-X}{1-X(1-\frac{\rho_P}{\rho_M})} \tag{2.33}$$

The equilibrium free volume can also be expressed in terms of ϕ_M as shown in the following equation:

$$v_f = 0.025 + \alpha_M(T-T_{g,M})\phi_M + \alpha_P(T-T_{g,P})(1-\phi_M) \tag{2.34}$$

2.5 Inhibition of Photopolymerization

An important phenomenon in photopolymerization is inhibition. Inhibition happens when oxygen or other molecules such as hydroquinone react with either initiator radicals or polymeric radicals in the resin and thus prevent them from participating in further growth of the polymer. Oxygen interacting with the photopolymerizing resin at the initiation and propagation stages will cause inhibition and result in only partial conversion [8, 9]. The inhibition causes problems particularly in thin-film and coating applications where oxygen diffusion plays a significant role in increasing cure times. The free radicals formed by the photolysis of the initiator are rapidly scavenged by O_2 molecules to yield peroxy radicals. The peroxy radicals are not reactive towards the double bounds on the monomers, and therefore they can neither initiate nor participate in any polymerization reaction. These peroxy radicals usually abstract hydrogen molecule from the polymer backbone to generate hydroperoxides. The interactions of oxygen molecules with primary radicals is shown in Eq. (2.35).

$$R_1^* + O_2 \xrightarrow{k_{in}} R_1 - O - O^* \tag{2.35}$$

The interactions of oxygen molecules with growing polymer radicals can be represented as:

$$R_n^* + O_2 \xrightarrow{k_{in}} R_n - O - O^* \tag{2.36}$$

In this reaction, oxygen effectively acts as a chain terminator and reduces the rate of photopolymerization until all oxygen in the system has been consumed [12]. The oxygen dissolved in the resin, as well as the atmospheric oxygen diffusing into the system during the UV exposure, must be all consumed in order to obtain tack-free coatings with acceptable mechanical properties. For a high-quality curing one must minimize the inhibition reactions or completely eliminate them if possible. There are several ways to minimize the inhibition reactions in photopolymerization. One way is by the addition of amines, which undergo readily a chain peroxidation reaction and thus consume the dissolved O_2 molecules present in the polymerizing resin [40]. Wax barrier coats or shielding films may also be used to prevent oxygen from entering the system. Exposing the resin to the UV light under water slows down the diffusion of atmospheric oxygen into the system. The experiment can also be done under inert conditions, where the system is blanketed with an inert gas such as nitrogen, carbon dioxide, or argon [12].

Other methods include adding oxygen scavengers, dye sensitizers, or antioxidants to capture oxygen and prevent it from reacting with the propagating polymeric chains. High concentrations of photoinitiator or increased light intensity may also be used to increase the production of free radicals in order to consume the oxygen within the system more rapidly. The last method, however, is ineffective close to the surface because it is difficult to consume the oxygen faster than it diffuses into the sample.

Beside O_2 molecules, there are other inhibitors, such as hydroquinone and hydroquinone monomethyl ether, which are used somewhat counterintuitively to promote process- and shelf-stability of highly reactive, acrylate monomer-based polymeric substances [41]. These inhibitors react with the initiating and propagating free radicals and convert them either to non-radical species or less reactive radicals that are unable to promote propagation by the following reactions:

$$R_n^* + Z \longrightarrow R_n + Z^* \qquad \textbf{(2.37)}$$

In this reaction, the inhibitor Z transfers one of its hydrogen atoms to R_n^* and becomes a radical itself.

$$R_n^* + Z \longrightarrow R_n Z^* \qquad \textbf{(2.38)}$$

The reaction between the radical R_n^* and the inhibitor produces a less reactive radical species that is unable to promote a propagation reaction, as shown in Eq. (2.39).

$$R_n Z^* + R_n \longrightarrow \text{No } R\text{eaction} \qquad \textbf{(2.39)}$$

2.6 Applications of Photopolymerization

Thin polymer coatings on the surface of many materials, such as wood, glass, metals, and plastics can be made by the photopolymerization process. The polymer coatings can change the optical, physical, and chemical properties of the material's surface in a desirable way. For instance, household appliances often have a photopolymer coating to resist scratches or corrosive chemicals and contact lenses might have a coating to alter their color. Additionally some photopolymers are used for their adhesive properties as they photopolymerize.

The spatial and temporal control coupled with the rapidity of the reaction rates make photopolymerization processes very attractive for biological applications. Hydrogels and cross-linked hydrophilic polymers are increasingly used in biotechnology and medicine because they exhibit excellent biocompatibility, causing minimal inflammatory responses, thrombosis, and tissue damage [42]. Photopolymerization is used to convert a liquid monomer or macromer to a hydrogel by a rapid free-radical polymerization with spatial and temporal control under ambient or physiological conditions. Blood pumps, scaffolding for bone and tissue transplants, adhesives for suturing wounds, matrices for cell cultures, and microchips that perform biochemical analysis are examples of biological materials produced by photopolymerization reactions. Polymers can also be used to manufacture many other types of biomedical devices including prosthetic blood vessels, heart valves, skeletal joints, and kidneys. Photopolymerized hydrogels have recently become popular in drug-delivery systems and as coatings for biosensors [43-45].

The cross-linked networks resulting from photopolymerization of multifunctional monomers can also be used as a coating for optical fibers, optical discs, and for many applications in microelectronics. Current microelectronic applications range from fabricating chips, integrated circuits, sensors, and electrochromic displays [18, 46]. Photopolymerization of properly selected multifunctional monomers can provide a fast, easy, and economic way of making the vitally important devices mentioned above.

Stereolithography is a rapid prototyping technique that translates CAD files into 3-D solid objects one layer at a time by tracing a laser beam or ultraviolet light on the surface of a volume of liquid photopolymer. The resin solidifies wherever it is exposed to light, resulting in a solid layer. The process is repeated, layer-by-layer, until the 3-D object is completely built. Further details of stereolithography as used in this thesis are given in the next chapter.

Another increasingly important application of photopolymerization of multifunctional monomers is the manufacture of microfluidic devices in various disciplines. The need for such devices is growing in such fields as engineering, physics, chemistry, and biotechnology. Microfluidic devices have found pivotal applications in the field of molecular biology such as studying large-scale protein functions and structures, DNA analysis, and enzymatic analysis [18].

The photopolymerization process provides a means for reducing the hardening time of adhesive materials used in a variety of practical applications; for example, the importance of keeping the harding time of photopolymeric dental fillings to a minimum is self-evident. In short, the everyday, modern world is increasingly dominated by products developed from polymers of many different kinds.

2.7 Measurement Techniques of Photopolymerization

The progress of photopolymerization processes can be measured by varies techniques. These techniques, which are based on reaction kinetics, are spectroscopy and calorimetry, on the other hand rheology is based on changes in mechanical properties during photopolymerization.

2.7.1 Spectroscopy techniques

Spectroscopy referred to a branch of science concerned with the production, measurement, and interpretation of electromagnetic spectra arising from the interaction between radiation and various substances. Two methods namely, Infrared (IR) and Raman spectroscopy have been well established in studying photopolymerization [47-51]. IR and Raman spectroscopy both measure the vibrational energies of molecules and can be used to obtain both conversion and rate of photopolymerization. These two methods rely on different selection rules for spectral information [49, 51]. Peaks in the spectra correlate to functional groups within a molecule. As monomer is converted to polymer, the height of peaks associated with the monomer specific bonds decreases. The conversion may then be calculated as the ratio of this peak area (or height) at any point in time to the initial peak area. The rate of polymerization is calculated by differentiating the conversion curve with respect to time [50].

Fourier transform infrared (FTIR) spectroscopy is one of the most commonly used IR analysis method for determining the composition of polymers. FTIR spectroscopy measures the vibrational energies of atoms or specific groups of atoms within a molecule as well as rotational energies. The FTIR spectroscopy technique identifies components by comparing the spectrum of a sample to reference spectra [51]. FTIR spectroscopy allows rapid multiple scanning of a sample; therefore, the technique has permitted real-time observation of changes in the spectra [49]. As a result, this method is commonly used to follow the cure reaction of photopolymerization [50].

Raman spectroscopy is based on the Raman Effect, which is the inelastic scattering of photons by molecules; therefore, it is an emission phenomenon as opposed to IR absorption, and results from vibrations caused by changes in polarizability [49, 51]. Raman spectroscopy is particularly useful when studying aqueous solutions, wet samples, or where differentiation between polymers with similar structures is necessary [50]. Raman spectroscopy has several advantages compared to FTIR spectroscopy, such as higher quantum efficiency, the ability to study lower frequency vibrations, and higher spatial resolution as a result of shorter excitation wavelengths [48]. The Raman technique has the disadvantages of being slower and more costly. IR and Raman spectroscopy are considered complementary techniques, because the selection rules are different [50].

2.7.2 Calorimetry techniques

Calorimetry, which measures heat flow into a material (endothermic) or out of a material (exothermic), is categorized as adiabatic calorimetry, covering the temperature range from 10 to 400 K, and differential scanning calorimetry (DSC), covering the temperature range from 200 to 1000 K [52]. Photodifferential scanning calorimetry (PDSC) is a standard technique for obtaining the rate of photopolymerization and conversion [50, 52]. The conversion of monomer carbon double bonds to polymer carbon single bonds is an exothermic reaction. The heat flow, ΔH, from the sample is directly proportional to the rate of photopolymerization [50]:

$$R_p = \frac{\rho_M \Delta H}{\Delta H_p} \tag{2.40}$$

where R_p is the rate of photopolymerization, ρ_M is the density of the monomer and ΔH_p is the heat of photopolymerization for the reactive group of the monomer. The double bond conversion of the resin is calculated by integrating the area under the rate of polymerization versus time curve [50]. Calorimetry is advantageous because it is not affected by cross-linking reactions and offers direct measurement of the polymerization rate [53]; however, this technique suffers from serious drawbacks such as a long response time of the calorimeter and a low thermal conductivity of most samples which greatly limits temporal resolution [54]. As a result, spectroscopy methods are preferred for performing real-time measurements.

2.7.3 Rheology techniques

Rheology is defined as the flow of fluids and deformation of solids under stress and strain. There has been significant attention devoted to the theoretical and experimental determination of rheological properties of polymers such as the elasticity, viscosity, and viscoelasticity and the shear modulus [55]. Ideal solids exhibit purely elastic behavior and, in the opposite limit, ideal fluids exhibit purely viscous behavior. Many important materials such as polymers exhibit a complex mixture of these two extremes, called viscoelasticity, which is generally dependent on the material's temperature and on amount of stress applied and the resulting strain. Monitoring and measuring the rheological properties of polymers during their production can contribute to the understanding of the fundamental physics of the photopolymerization process as well as have significant impact on the final product's quality.

The degree of photopolymerization can be measured via calorimetry or spectroscopy. But these methods do not provide information about the changes in the mechanical properties as a function of reaction time as the resin passes from a liquid phase to a highly cross-linked gel. To measure these changes, one must use rheological methods.

Rheological behavior can be investigated by a variety of methods, including simple capillary viscometers, extrusion rheometers, and rotational viscometers [55]. When using sample rheology to determine bond conversion rates, one often must rely extensively on model assumptions; these can adversely affect the predictive ability of the model. As a result, it is preferable to directly measure the mechanical properties of a photoresin during the photopolymerization process.

The methods and equipment employed by classical rheology require macroscopic samples (typically at least milliliters); many materials of interest, for example biological samples, are too expensive or difficult to produce in such quantities. Also standard rheological equipment cannot be used in, for instance, a biological sample because this equipment measures the responses of the system via mechanical fixtures. Even if such fixtures could fit inside a cell, they could potentially disrupt the structure of the cell and invalidate the resulting measurements.

In recent years, microrheological methods have been developed to treat microscopic systems [56, 57]. Microrheology uses microscopic mechanical probe particles embedded into the viscous fluid to measure the relationship between the stress applied through these probe particles on the viscous liquid and the resulting deformation of the liquid; the deformation of the medium is calculated by measuring the difference between the current positions of these probe particles and the original points where they were embedded into the system. From these measurements rheological properties of the viscous liquid can be obtained. The main advantage of microrheological techniques is that they require only a microscopic amount of material to perform a rapid and detailed characterization of local rheological properties of complex fluids, including living cells, proteins, hydrogels, and colloids near the glass transition.

3. STEREOLITHOGRAPHY AND MICRORHEOLOGY

3.1 Stereolithography

Stereolithography is a technique that uses the UV light source with well-defined intensity patterns which are then reflected in the shape of cured parts transferred to the photocurable monomer to get the shape of the desired pattern. Patented in 1986, stereolithography was the first rapid prototyping (RP) process and is still the most utilized of all types of RP [58].

The basic components of a Stereolithography Apparatus (SLA) consist of a UV laser or UV light source (often a helium/cadmium laser or a Hg(Xe) arc lamp), liquid resin and an elevator system capable of moving in very precise increments, and a computer-based controlling system as shown in Figure 3.1.

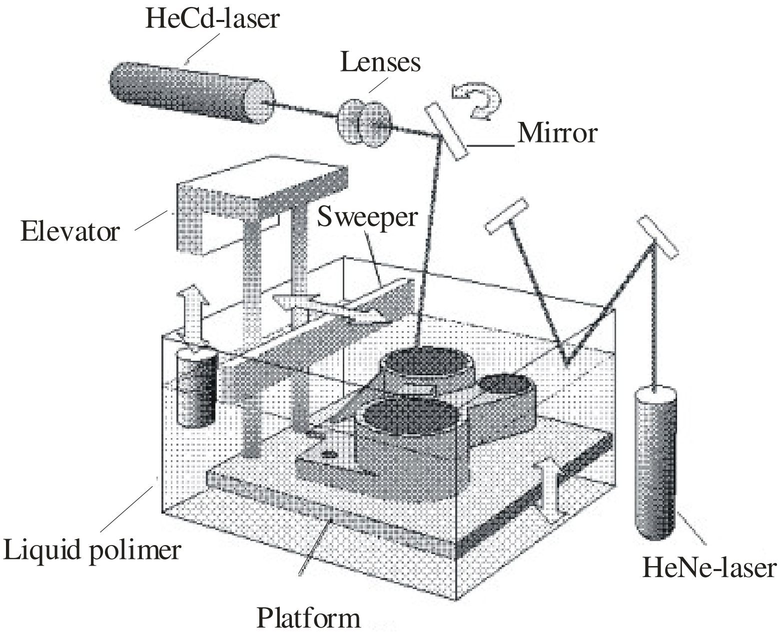

Figure 3.1: Schematic Diagram of Stereolithography [58]

A SLA is used to fabricate a predesigned object by photopolymerizing the resin layer by layer. For each layer in the part, the laser beam traces a cross-section pattern for the part on the surface of the liquid resin. Exposure to the UV light causes the resin to cure, or solidify, quickly in the shape of the pattern the light traces. Once the layer has been completely cured in the desired shape, it is lowered by a single layer thickness typically 50 µm to 150 µm into the liquid resin via an elevator system. Then, the curing process is repeated to form the second layer in the desired shape. There will be many molecules on the surface of each freshly cured layer with unbroken or pending double bonds. On top of each new cured layer, there is a layer of liquid resin with initiator molecules that can absorb photons from the UV light source. The resulting initiator radicals can attack the pending double bonds on the surface of the cured layer below; this creates polymeric radicals at the surface of the cured layer that can react with monomers or polymeric radicals in the liquid and connect the cured layer with the layer being formed out of the liquid. This process by which each layer bonds to its neighbors can be thought of as a self-adhesive property of the resin. As the process repeats, it causes the layers to eventually form the desired 3-D object [58-60].

During the curing process, the SLA also generates support structures from the resin to attach the part being built to the elevator platform; these support structures prevent the part from deflecting due to the force of gravity and also accurately hold the layers in place so that they resist lateral pressure. Many 3-D CAD software packages automatically generate support structures. Upon completion of the fabrication process, the object is elevated from the chamber and the support structures are cut off [59].

After being cured, the part is cleaned of excess resin by immersion in a chemical solvent bath and then it is more fully cured in an UV oven. The combination of higher temperature and longer wavelength UV light used in the oven breaks some of the unreacted double bonds and also cures the resin hidden in the crevices of the part, causing the part to harden [59].

The main benefits of SLA can be given as:

- It can build highly detailed objects with tolerances within 1 cm.

- It is a relatively fast process, allowing a part to be completed within a few days.

- Compared to traditional manufacturing, it is relatively cheap.

- It is suitable for prototyping, even for small production runs.

- Its prototypes can be easily changed to incorporate last-minute changes.

- It can create a physical object directly from a CAD model independent of its shape and complexity.

Operational parameters of SLA must be precisely defined prior to the start of the actual curing process. The most important of these parameters are the layer thickness, the hatch spacing, the hatch overcure, the border overcure, the hatch fill cure depth, the hatch style, the part orientation, and the blade gap. Optimizing these parameters to obtain durable cured products is currently the focus of intense research. Thus, it is useful to define these parameters in detail. Layer thickness is defined as the thickness of each slice being cured for the production of the part. In order to form a layer, the laser first traces the shape of its outline and then crosshatches the area within, according to the selected hatch pattern or hatch style. The distance between these parallel hatch vectors is called the hatch spacing. If the hatch spacing is very small, it will be comparable to the cross section of the UV light source, minimizing the amount of undercured resin in the layer and the need for post-cure UV light exposure to harden the object. Large hatch spacing, in contrast, causes pockets of liquid resin to be trapped inside crosshatching pattern, which thus must subsequently be further cured [61].

If the hatch spacing is relatively large, after the area is crosshatched, the resulting layer consists of a honeycomb pattern created by the solidified hatch vectors with small pockets containing uncured liquid resin. In this case, a second finer, but shallower pass over the layer is done with the laser. This second pass creates a thin upper film over the pockets of liquid resin. The thickness of this thin top layer is called the hatch fill cure depth. These pockets of liquid resin also have a thin, effective bottom layer because of the thin film that formed the top of the previous layer [61].

Hatch overcure is the depth into the previous layer (i.e., beyond the current layer thickness) which is exposed to the UV light source during a given pass of the laser along a hatch vector. Border overcure is the depth that the layer as a whole is cured past the actual thickness of the layer at the end curing of a single layer [61].

As mentioned above, when a layer is finished, the SLA elevator lowers it into the resin pool to coat it with fresh liquid. Sometimes the surface tension of the liquid resin causes vertical distortions of this liquid layer. To smooth the liquid surface, a recoater blade is used to spread the liquid evenly across the solid layer below. The vertical separation between the bottom of the recoater blade and the top of the previously cured layer, and thus the resulting thickness of the liquid resin layer after the recoater blade smoothens it, is called the blade gap [62].

Since the fabricated object is made up of discrete layers of cured resin, if the object has large changes in slope perpendicular to plane of the layers, there may be a noticeable stair-stepping effect along these slopes as shown in Figure 3.2.

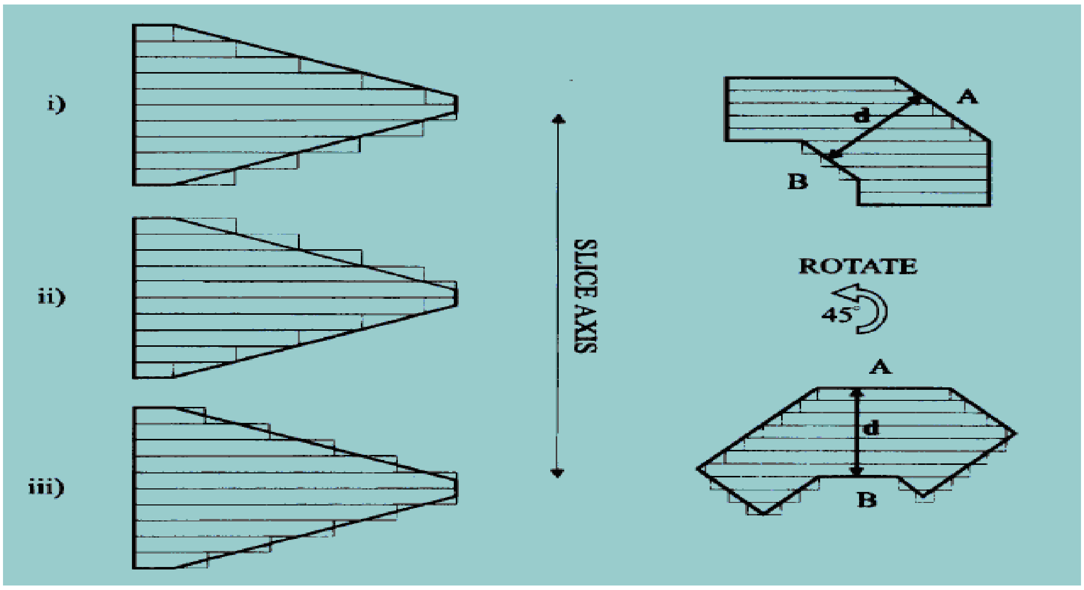

Figure 3.2 : Stair Stepping Effects [62]

Manually sanding or polishing away such effects can be the most labor-intensive phase of fabricating highly detailed objects. Reducing the layer thickness can decrease these effects but have the side effect of increasing the time and cost required to fabricate the object. Another strategy takes advantage of the fact that the surfaces of the parts in the plane of the layers which are perpendicular to the beam of the UV light source do not show such effects. Thus, the key part of the SL process is first deciding the most critical portions of the object and then choosing the appropriate layer thickness and the orientation of those portions with respect to the UV light source so that the part is produced to the correct tolerances with minimum cost [62].

3.1.1 Applications of stereolithography

SL is used in a variety of real-world applications in a wide range of fields from manufacturing decorative and protective coatings to biomedicine. SL allows a manufacturer to evaluate the feasibility, ease of manufacturing, ergonomics, and aesthetics of a proposed design before committing to a large-scale production. The SL model can also be placed in a wind tunnel to measure its aerodynamics and can be tested using Optical Stress Analysis (OSA) to study the effects of external loadings, torsion, tension, and pressure [62, 63]. The SL prototype can be used as a marketing tool since it allows customers to see, touch, and test a model of a product before the product is mass produced. Stereolithography has found a growing number of applications in the field of biomedical engineering. For instance, a surgeon can make a SL prototype of both a portion of a patient’s body and of a proposed implant to practice a delicate surgical procedure.

Some of the most common applications of stereolithography are found in the production of [20, 62-64]:

- Aesthetic and conceptual models,
- Parts requiring detail and accuracy,
- Master patterns for castings and secondary processes,
- Decorative and protective coatings,
- Optical disks and aspherical lenses, and
- Medical models.

3.1.2 Research on stereolithography

SL is a rapidly growing technology which involves the photopolymerization of monomer resins layer by layer to build complex prototypes using a UV light source. In recent years there have been extensive theoretical and experimental studies of the kinetics of the various reactions involved in photopolymerization of resins consisting of either single or multi-functional monomers [2-4, 15, 64]. These studies have illustrated that the most important parameters affecting the conversion in the photopolymerization process are the temperature, the UV light intensity, the monomer functionality, and the photoinitiator loading concentration. Most of the current theoretical models of photopolymerization assume that the extent of resin cure is only a function of the amount of the cumulative exposure to UV radiation [59, 65-67]. These modeling studies assume that any point in the resin will solidify as soon as the total amount of radiation received at that point passes a minimum critical value. Recent studies have shown that this is an oversimplification of the underlying physics of photopolymerization. A more realistic model must take into account the mass and heat transfer effects along with the conventional kinetic equations for the photopolymerization reactions [11, 20, 68-71].

The physical, mechanical, and thermal properties of photopolymerizing monomers and photoinitiators are essentials to produce durable objects using the SL technique [12, 15]. There is significant current research targeted on discovering new resins and initiators both to produce high-quality parts and also to diversify the range SL applications.

Eschl and coworkers tested and simulated the transient post-fabrication shrinkage of the parts produced in SLA. The effect of two resin material types, acrylate and epoxy, on the SL cure process [72]. They found that the epoxy resin produces more accurate parts because the stress due to shrinkage is smaller and the final stiffness is higher. Their methodology of studying material effects is based on an investigation of the built results rather than a direct study on the building process. This is a different perspective, however, which cannot address the curing dynamics or the heating issue in SL building process.

Another trend of contemporary investigation concerns optimizing the SLA operational parameters (e.g., the hatching space, curing depth, layer thickness, and part orientation relative to the UV light beam) and subsequent post-curing procedures (e.g., post-curing time, temperature, and UV light intensity) which directly affect the quality and strength of the produced object [62-64, 73-78].

Saito conducted experiments varying laser power and scanning speed in SLA, and claimed a relationship which is close to the power function between the cured depth and laser scanning speed on a semi-log plot [65]. Nagamori and coworkers performed SL curing tests to investigate how the laser power, laser beam diameter, and laser scanning speed affect the cured depth and width [66, 67]. They correlated the cured depth with the energy density (exposure) and found a linear relation on a semi-log graph. All these studies were trying to directly connect the laser exposure to the part dimensions, as in the exposure threshold model [59]. Hur and coworkers additionally studied the part deformation and the thermal stress formed in the built part when the laser is stationary and moves along one line [63].

There has been much research on the relationship between the SL operational parameters and the rheological properties, such as the tensile strength, of the resulting object. The main purpose of this ongoing research effort has been to find SL operational parameters that optimize the aspects of prototype production. For example, Schuab et al. identified layer thickness, part orientation, and over-cure depth as the key SL process parameters affecting accuracy and strength [78]. They then used the design of experiments and the analysis of variance technique to analyze and compare the significance of these variables, and concluded that layer thickness and part orientation have more effect on the part dimensional accuracy. Jacobs proposed that layer thickness, laser power, scanning velocity and orientation are the important process parameters affecting part strength and the mechanical properties of SL prototypes [59]. Banerjee et al. conducted a study on the mechanical strength of the prototypes made by an SL process [79]. They found that layer thickness, orientation and post-curing time are the most important SL process parameters expected to impart maximum influence upon the ultimate tensile strength of the prototype. Chockalingam et al. investigated the effects of layer thickness, hatch spacing, hatch style, hatch overcure, and hatch fill cure depth on the physical properties of the cured parts [80]. Recent studies have determined that layer thickness and orientation are the most important SL process parameters that influence the part strength [75].

Cho and coworkers also used a genetic algorithm-based methodology to determine an optimal value set for the SL process parameters, such as hatch spacing, hatch overcure, border overcure, hatch fill cure depth, and layer thickness, to minimize the error in SL part fabrication [81]. Onuh and Hon used the Taguchi method to design and conduct experiments concerning layer thickness, hatch spacing, hatch style, hatch overcure, and hatch fill cure depth. They analyzed the results and optimized these parameters to improve the surface finish of SL parts [62]. Onuh and Hon added two new hatch styles to their previous work and studied the effects of these styles on the dimensional accuracy [82]. Jayanthi and coworkers studied the influence of SL process parameters, such as layer thickness, hatch spacing, hatch overcure, and fill cure depth, on the resulting curl distortion of the cured part [83].

3.2 Microrheology

Microrheology employs two general categories of techniques which are passive and active. In the active techniques the motion of probe particles is controlled by external forces; whereas, passive techniques use thermal fluctuations to induce motion of the probes. Passive microrheology for viscoelastic materials is based on the Brownian motion of tracers embedded in the viscous fluid for example, a photopolymerizing resin. In such microrheological methods, there is no need for an external driving force hence, the name is passive. The thermal energy is the driving force behind the motion of the tracers in this case. Because the thermal driving force supplied by the ambient temperature is small, the sample is subjected to equilibrium thermal fluctuations only. Since these fluctuations are both random and small in magnitude, passive rheological methods probe only the linear viscoelastic response of the surrounding medium [56].

The thermal energy of an embedded probe particle is on the order of product of Boltzman's constant (k_B) and temperature of the probe particle (T), which can cause detectable particle motion only in relatively soft materials, such as polymer solutions and gels. Thus, applications of passive rheological measurements are considerably difficult in dense systems such as polymer melts and solids. Nevertheless, with recently developed modern particle tracking techniques, such measurements can be made; as a result, microrheology measurements can nowadays be performed on complex fluids with wide ranges of viscosities [57, 84, 85].

3.2.1 Theory of passive microrheology

The theoretical basis for passive microrheology is provided by considering the behavior of a spherical particle with a radius of a embedded in two limiting cases of media, which are purely viscous Newtonian liquid media and fully elastic network media. The motion of particles in a Newtonian liquid is diffusive and the diffusion coefficient can be determined from the well-known Stokes-Einstein relation [86]:

$$D = \frac{k_B T}{6\pi\eta a} \tag{3.1}$$

where k_B is Boltzman's constant, η is the viscosity of the photopolymerizing resin, a is the tracer particle radius, T is the temperature, and D is the diffusion coefficient. D is a measure of how rapidly particles execute thermally driven Brownian motion. Also, in deriving the above equation, it is assumed that embedded tracer particles are much larger in size than the molecules of the viscous fluid. In addition, it is also assumed that particles are rigid and no heterogeneities exist in the medium. Therefore, in microrheological applications, particle dynamics are related to the medium and probe properties and provide quantitative information about the local microenvironment.

The dynamics of particle motions are then revealed in the time-dependent position correlation function of individual tracer particles through the mean-squared displacement (MSD) [87]. For diffusive motion, the *d*-dimensional MSD and the diffusion coefficient are related by

$$D = \lim_{t\to\infty} \frac{1}{2td} \left\langle \Delta\vec{r}^{\,2}(t) \right\rangle \tag{3.2}$$

where d is the characteristic dimension of the system and $\left\langle \Delta\vec{r}^{\,2}(t) \right\rangle$ is the MSD of the individual particles undergoing thermal motions. $\left\langle \Delta\vec{r}^{\,2}(\tau) \right\rangle$ is simply the square of the net distance the tracer typically moves during a given time interval, τ, which in this context is called a waiting time (lag time) measured in second and is defined as:

$$\left\langle \Delta\vec{r}^{\,2}(\tau) \right\rangle = \left\langle \left| \vec{r}(t+\tau) - \vec{r}(t) \right|^2 \right\rangle = \frac{k_B T d}{3\pi\eta a}\tau \tag{3.3}$$

where the brackets denote averaging over all starting times t, and $\vec{r}(t)$ is the d-dimensional position vector. The Stokes-Einstein relation enables one to measure viscosity by observing the time-dependent MSD of a particle of known size. Also, the intrinsic stochastic nature of thermal energy requires one to collect a large amount of data as a function of waiting time, τ ; here the angled brackets indicate an average over both many starting times *t* and the ensemble of particles in the field of view in order to obtain consistent statistics. Figure 3.3 illustrates the principle steps of particle tracking microrheology.

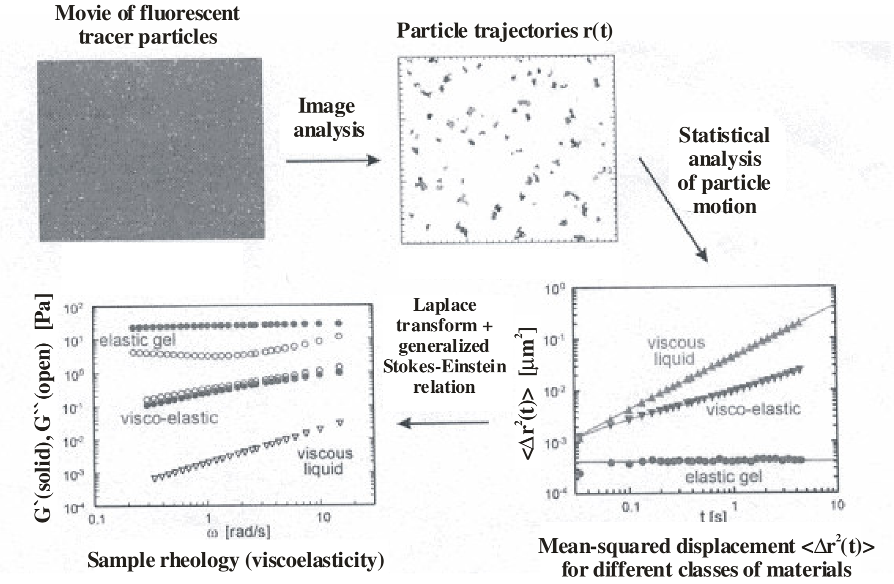

Figure 3.3: Principles of Particle Tracking Microrheology; from Particle Motion to Sample Rheology [64]

For a purely elastic material, the MSD will reach an average plateau value $\left\langle \Delta \vec{r}^{2} \right\rangle$ which is independent of waiting time and is determined by the elastic modulus of the material. Equating the thermal energy of a tracer particle of radius *a* to the elastic energy density of the network that is deformed by the displacement of the tracer particle gives:

$$\left\langle \Delta \vec{r}^{2} \right\rangle_{\tau \to \infty} = \frac{k_B T d}{3\pi G a} \qquad \textbf{(3.4)}$$

where *G* is the elastic modulus of the network. Most materials are viscoelastic; they both store and dissipate energy, with the relative proportions depending on frequency. These materials are characterized by the complex shear modulus, G^* :

$$G^*(\omega) = G'(\omega) + iG''(\omega) \tag{3.5}$$

The complex shear modulus is usually measured by applying a strain varying sinusoidally in time. The real part of complex shear modulus, $G'(\omega)$, represents the response in phase with the applied strain and measure the ability of the material to store energy. The imaginary part, $G''(\omega)$, represents the response out of phase with the applied strain and measure the ability to dissipate energy [88]. In other words, $G'(\omega)$ and $G''(\omega)$ represent the elastic and viscous response of the material [87]. For such material, the generalized Stokes-Einstein relation relates the MSD to the complex shear modulus. In the Laplace frequency space, s, it is written [57, 86, 87]:

$$\tilde{G}(s) = \frac{s}{6\pi a}\left[\frac{2k_B T}{s^2\left\langle \Delta\tilde{r}^2(s)\right\rangle} - ms\right] \tag{3.6}$$

where $\left\langle \Delta\tilde{r}^2(s)\right\rangle$ is a unilateral Fourier transform of the MSD given in Eq. (3.3). Within a valid frequency range, the inertial effect of the tracer particle, ms in the above equation, can be neglected, and Laplace-transformed complex shear modulus takes the form:

$$\tilde{G}(s) = \frac{k_B T d}{3\pi a s\left\langle \Delta\tilde{r}^2(s)\right\rangle} \tag{3.7}$$

The complex shear modulus can also be expressed in the frequency domain as shown in Eq. (3.8).

$$G^*(\omega) = \frac{k_B T d}{3\pi a(i\omega)\left\langle \Delta\tilde{r}^2(\omega)\right\rangle} \tag{3.8}$$

where ω is the frequency of the applied shearing force. The two moduli $G'(\omega)$ and $G''(\omega)$ obey the Kramers-Kronig relations; they are not two independent functions and both can be determined from the single, real function of $\tilde{G}(s)$. The derivation of Eq. (3.7) has been the seminal breakthrough for passive microrheology. Although originally derived on a rather ad hoc basis, the generalized Stoke's Einstein relation has since been shown to be an extremely valuable tool with a strong theoretical backing [56].

The frequency range where Eq. (3.8) remains valid is dependent on both the inertia and compressibility of the system, but includes the typical range of video microscopy, 0.1-60 Hz. Direct comparison with macroscopic rheological data has revealed excellent agreement, often beyond limits where it might be anticipated.

3.2.2 Determination of the gel point

An experimentally measurable characteristic of the transition from liquid to solid is the gel point, that is, the instant at which the connectivity of the polymeric network extends over the entire sample. The measurement of the gel point of a particular photopolymerizing compound is a material property of that compound and does not depend on the method used to measure it [85, 89]. Among the most common techniques used to measure the gel point are small amplitude oscillatory rheometry and light scattering.

As mentioned previously, the complex shear modulus of a viscoelastic material is given by Eq. (3.5). One method for calculating the gel point from the components of the shear modulus is by finding the time when the storage modulus $G'(\omega)$ and the loss modulus $G''(\omega)$ curves cross; there is a controversy in the literature, however, whether the gel point occurs exactly when these two curves intersect or merely somewhere near the intersection point [90]. A method proposed by Winter and Chambon for detecting the gel point in small amplitude oscillatory rheometry experiments is based on calculating the ratio $G''(\omega)/G'(\omega)$, which is constant over a wide range of frequencies at the gel point [89]. This method is based on the relation between the loss and storage moduli corresponding to a critical gel point given by the following equation:

$$\frac{G''(\omega)}{G'(\omega)} = \tan(\delta) \qquad \textbf{(3.9)}$$

In small amplitude oscillatory rheometry experiments, a shear strain, s_s, which results from a shear stress applied to a complex fluid under going photopolymerization reaction as a function of time *t,* can be calculated as follows [85]:

$$s_s = s_a \sin(\omega t) \tag{3.10}$$

where s_a is the strain amplitude (m) and ω is the frequency of the applied strain. The time dependent stress response, $\sigma(t)$, of the viscoeleastic media is given by

$$\sigma(t) = G'(\omega) s_a \sin(\omega t) + G''(\omega) s_a \cos(\omega t) \tag{3.11}$$

Using the phase angle δ defined in Eq. (3.9), the stress response can be written as:

$$G^* = \frac{\sigma_0}{s_a} \mathrm{e}^{i\delta} = G'(\omega) + iG''(\omega) \tag{3.12}$$

As the photopolymerization proceeds, the resin makes a transition from the elastic phase to the plastic phase, and hence, the shear modulus increases. The larger the shear modulus, the more rigid the material becomes since the same change in horizontal distance (strain) will require a larger force (stress). This is why the shear modulus is sometimes called the modulus of rigidity. From the ratio of $G''(\omega)/G'(\omega)$ at the gel point, the relaxation exponent *n* can be calculated. This result then may be used to determine the gel strength, S_G, through the following formula [91]:

$$G'(\omega) = \Gamma(1-n)\cos(\delta)\, S_G \omega^n \tag{3.13}$$

The value of the relaxation exponent *n* varies between 0 and 1. The phase angle, δ, between the sinusoidal stress and strain functions is independent of frequency but proportional to the relaxation exponent [91].

$$\delta = \frac{n\pi}{2} \tag{3.14}$$

The range of the power law in Eq. (3.13) has not been fully determined, although it is expected to predominate on length scales from as small as the prepolymer strand length up to the macroscopic sample dimension.

The validity of the Winter-Chambon method for accurately determining the gel point has been demonstrated in studies of various materials, including chemically and physically cross-linked gels [89, 92, 93].

Dynamic light scattering is another technique which can provide a nondestructive, real-time determination of both the gel point and the critical dynamics near the point of gelation [94]. Additionally, techniques such as spectroscopy and calorimetry can also be used to measure the critical degree of conversion at the gel point.

The procedure for calculating the complex shear modulus in Eq. (3.5) from the experimentally measured, time-dependent displacement vector is described in Figure 3.4 below. The trajectories of the embedded particles are recorded by the digital video camera built into the experimental apparatus and then the mean-square amplitude of these fluctuations as a function of time is calculated. This time-dependent MSD data is converted to the frequency (Laplace) domain via the transform shown in Eq. (3.7).

First solve Eq. (3.3) for the viscosity, η, as a function of the waiting time, τ, and take its Laplace transform so that it is now a function of the Laplace frequency s. Multiplying the Laplace-transformed viscosity by the Laplace frequency yields the Laplace transform of the shear modulus:

$$\tilde{G}(s) = s\eta(s) \tag{3.15}$$

Note that this is the same quantity as in Eq. (3.6). The inverse Laplace transform of Eq. (3.15) gives the time-dependent shear modulus $G(t)$, which is used as an intermediate step for obtaining the frequency-dependent complex shear modulus $G^*(\omega)$. The Fourier transform of $G(t)$ yields $G^*(\omega)$, which is the same quantity in Eq. (3.5).

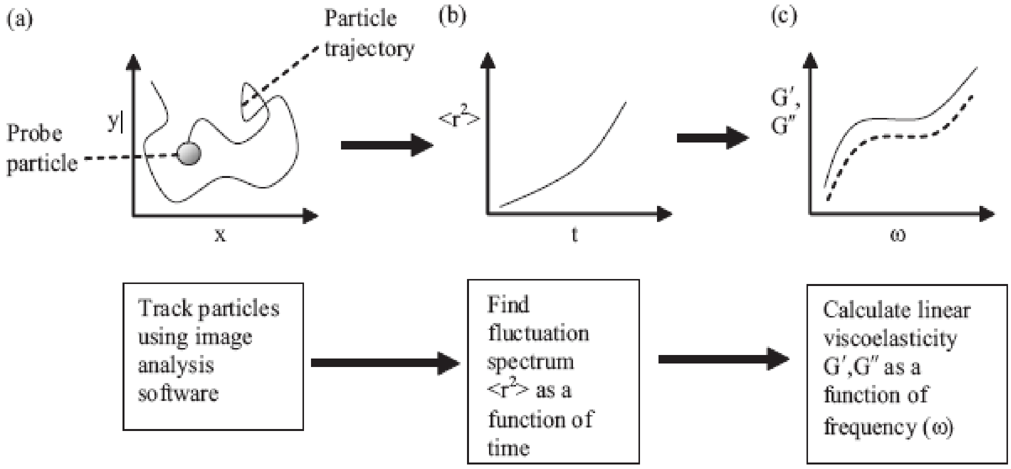

Figure 3.4: Particle Tracking Microrheology Enables the Linear Viscoelasticity of Low Modulus Materials to be Extracted from the Fluctuation Spectrum. (a) Trajectory of the Probe Particle is Measured, (b) The Average Fluctuation Spectrum as a Function of Time *t* is Calculated, and (c) The Linear Viscoelasticity as a Function of Frequency ω can then be Found [85]

The congruency of the loss and storage moduli can easily be inferred from Eqs. (3.9) and (3.15); this is expressed as $G'(\omega) \sim G''(\omega) \sim \omega^n$. This is also consistent with the Kramers-Kronig relation [89]. The relaxation exponent *n* here is generally equal to 0.5. The loss and storage modulus becoming equivalent is a unique rheological property of the gel point. As seen in Figure 3.4, the behavior of the shear viscosity and equilibrium modulus are also unique properties of the gel point. Therefore both set of these rheological properties can be used to determine the gel point.

Passive microrheology methods can be used to perform in situ monitoring of the liquid-to-gel transition during free-radical photopolymerization. A rapid increase in the viscosity of the polymerizing resin occurs prior to the liquid-to-solid transition at the point of gelation. Therefore, gelation can readily be detected with rheological techniques. Microrheology can monitor changes in sample rheological properties of UV-irradiated photoresin samples through Eq. (3.3) describing the MSD. The point at which the MSD first becomes independent of *t* can be used to define the gelation point. Before the liquid-to-solid transition, the MSD increases with increasing waiting times, characteristic of a viscous liquid. After the transition the MSD becomes independent of waiting time, which can be intrepted as the signature of an elastic gel.

The liquid-to-solid transition during the photopolymerization of the resin is marked by a point of gelation, which in the photopolymerization is the result of the formation of densely cross-linked polymer networks.

The stress in a polymerizing resin is time dependent due to the viscoelastic behavior and the changing chemical composition as the polymer network forms with time. As photopolymerization proceed, the steady shear viscosity of the liquid sample, η, rapidly increases and diverges to infinity at the point of gelation. This behavior of shear viscosity is illustrated in Figure 3.5, where the logarithm of shear viscosity is plotted against the reaction time [89]. The shear viscosity of a polymerizing resin is defined as its resistance to shear flow, which depends on time and temperature for non-Newtonian liquids like most polymerizing resins. The vertical axis in Figure 3.5 is double scaled to represent the behavior of the steady state modulus as a function of conversion beyond gel point in the same plot. Measurements for viscosity and steady state modulus, G_∞, for polymerizing resin and fully cured sample give reliable data away from gel point. The equilibrium modulus, G_∞, remains near zero because the stress in a deformed gel can still relax completely; however, beyond the point of gelation, the equilibrium modulus starts to monotonically increase. The rheological behavior at the point of gelation is unique in that infinite time is required for stress relaxation, which in a broad distribution of shorter self-similar modes.

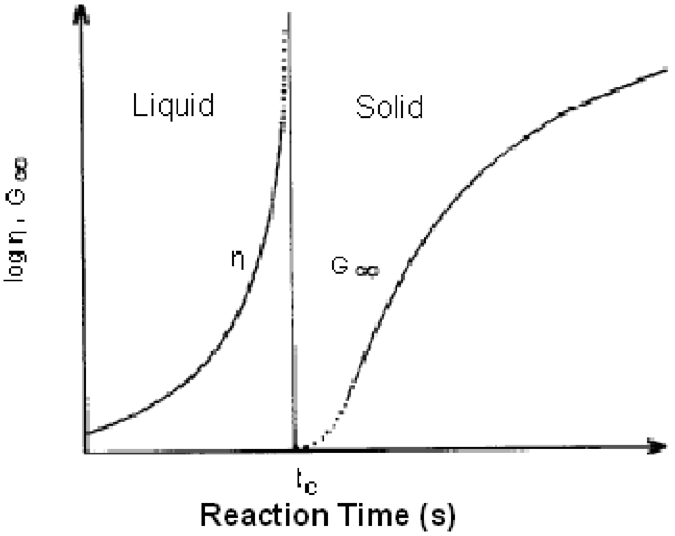

Figure 3.5: Steady Shear Viscosity and Equilibrium Modulus of a Cross-Linking Polymer as a Function of Reaction Time [89]

4. EXPERIMENTAL STUDIES

Experimental studies carried out in this thesis can be classified mainly in four groups as:

1. Stereolithography experiments,
2. Passive Microrheology experiments,
3. Frourier Transform Infrared Spectroscopy experiments
4. Differential Scanning Calorimetry experiments

4.1 Materials Used in the Experimental Studies

High reactivity and the ability to form a large variety of cross-linked polymers with tailored properties such as color, flexibility, and surface characteristics are determining factors in the choice of monomers composing the resins. In this study the particular monomers were selected as; 2(2-ethoxyethoxy) ethyl acrylate, triethylene glycol diacrylate, trimethylolpropane triacrylate, and ethoxylated pentaerythritol tetraacrylate which are known by the acronyms of SR256, SR272, SR351, and SR494, respectively. The chemical structures of these monomers are given below.

SR256 :

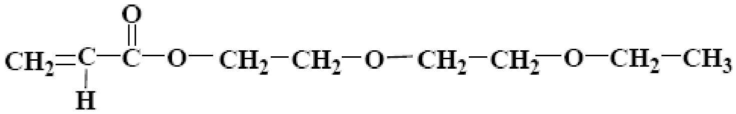

$$CH_2=\underset{H}{C}-\overset{\overset{O}{\|}}{C}-O-CH_2-CH_2-O-CH_2-CH_2-O-CH_2-CH_3$$

SR272 :

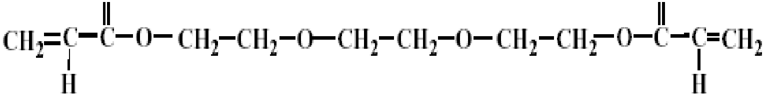

$$CH_2=\underset{H}{C}-\overset{\overset{O}{\|}}{C}-O-CH_2-CH_2-O-CH_2-CH_2-O-CH_2-CH_2-O-\overset{\overset{O}{\|}}{C}-\underset{H}{C}=CH_2$$

SR351 :

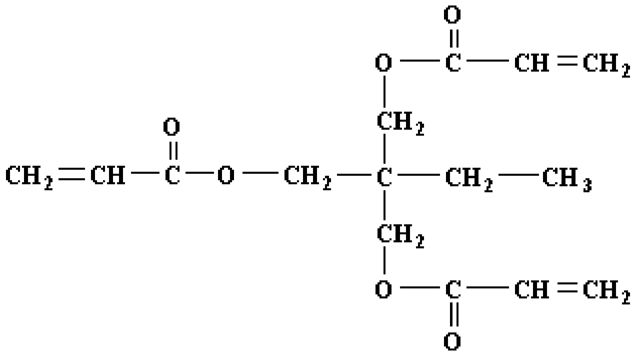

SR494 :

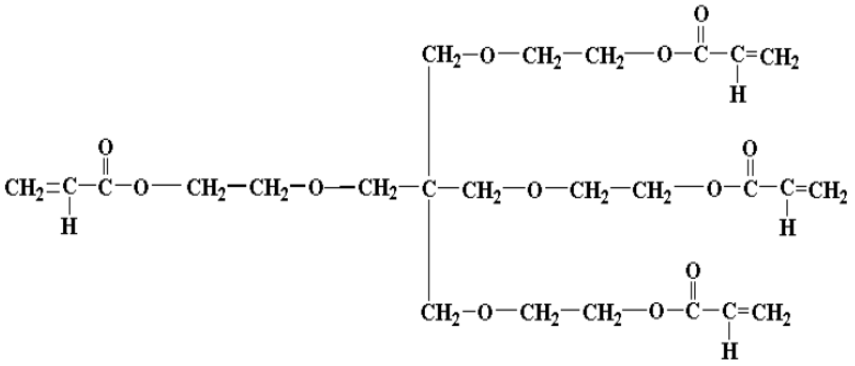

The physical and chemical properties of these monomers used in the experiments are given in Table 4.1, respectively.

Table 4.1: Physical and Chemical Properties of the Monomers [95]

Acronym	Name	Number of functional groups	Molecular Weight (kg/mol)	Specific Gravity at 25° C (kg/m^3)	Refractive Index at 25°C
SR256	2(2-ethoxyethoxy) ethyl acrylate	1	0.188	1.013	1.4366
SR272	Triethylene glycol diacrylate	2	0.258	1.109	1.461
SR351	Trimethylolpropane triacrylate	3	0.296	1.109	1.472
SR494	Ethoxylated pentaerythritol tetraacrylate	4	0.528	1.128	1.471

As mentioned in Chapter 2 photopolymerization reactions are driven by photoinitiators, which are chemicals that produce free radicals when exposed to specific wavelengths of light. A number of different photoinitiators, each with its unique absorption spectrum, is currently available. More varieties are continually being developed; so, one can easily obtain a photoinitiator that could have good absorption rate to the particular frequency of UV light used in an experiment. The UV light source used in these experimental studies has a strong emission peak at 365 nm. Thus, a suitable photoinitiator molecule for these experiments should have a strong absorbance at this wavelength and decompose efficiently into highly reactive radicals. It was found that 2,2-dimethoxy-1,2-diphenylethanone, also known as Irgacure 651 (DMPA), meets these requirements. The chemical structure of Irgacure 651 is given as follows:

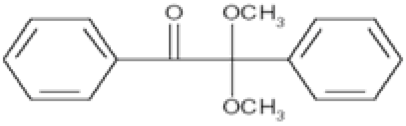

Figure 4.1 shows three UV visible absorption spectra of Irgacure 651 at different concentrations in acetonitrile. As can be seen from this figure, Irgacure 651 strongly absorbs UV light in the 320 to 380 nm wavelength range. Thus, Irgacure 651 was chosen as a photoinitiator molecule for this investigation not only its strong absorbance between 320-380 nm, but also its high efficiency in curing unsaturated acrylate monomers.

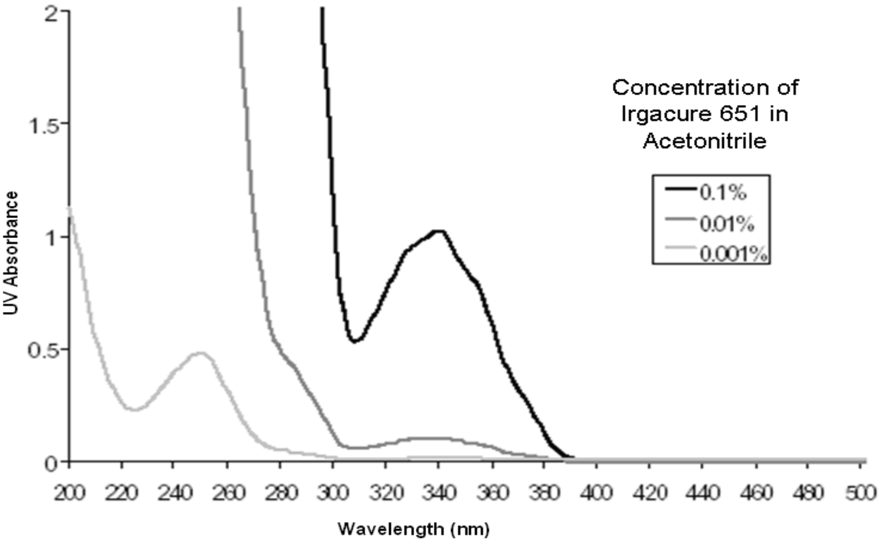

Figure 4.1: UV Visible Absorption Spectra of Irgacure 651 at Different Concentrations in Acetonitrile [96]

All the resins used in the experimental studies were purchased from Sartomer, and the photoinitiator was purchased from Ciba.

The micron-sized, inert fluorescent tracer particles used in the microrheology experiments to probe the rheological propertied of the resin as it polymerizes were provided as a courtesy by a research group at the University of Twente, the Netherlands. The silica-based tracer particles contained a type of red fluorescent dye (rhodamine) and had a diameter of 0.5 microns.

4.2 Stereolithography Experiments

Stereolithography experiments were performed by using a SLA 250/50 model apparatus shown in Figure 4.2. In these experiments effect of the scanning speed of the UV light source on the photopolymerization process was investigated. The monomer and photoinitiator chosen for these experiments were SR494 and Irgacure 651, respectively. Three scanning speeds (2.72×10^{-2} m/s, 1.18×10^{-2} m/s, and 2.72×10^{-1} m/s) for the UV light source were employed.

Figure 4.2: The SLA 250/50 Model Apparatus

The experiments were performed with a photocurable resin containing 2% photoinitiator by weight, under ambient conditions, which allowed oxygen to diffuse into the resin. The SLA was used here to do a single laser scan in a straight line across the resin at three different speeds mentioned above. In all experiments, the UV light source irradiated the resin for approximately 0.02 s.

After each laser scan was completed, the polymerized parts were taken out of the resin container after 30 min and drained on the platform for 30 min. The parts were then cleaned for 1 min in tri-propylene glycol monomethyl ether and for another 1 min in water at room temperature in a Branson 5210 cleaning system in ultrasonic mode. After cleaning, the parts were dried with compressed air, and then their dimensions were measured by Hitachi S800 FEG model scanning electron microscopy (SEM). The SEM measurements were calibrated using a standard grid with known dimensions. To ensure that the results were reproducible and statistically significant, each UV light scan part-fabrication process was repeated twenty times for each of the two different scanning speeds.

4.3 Microrheology Experiments

In this study the passive microrheology technique was used to investigate the effect of photoinitiator loading on photopolymerization of multifunctional monomers.

4.3.1 Sample preparation

At the beginning of sample preparation the micron-sized silica-based tracer particles were washed in ethanol several times before being embedded into the resin. For this purpose a small quantity of the ethanol/particle suspension was centrifuged at 3000 rpm for half a minute in an Eppendorf Mini Spin centrifuge. After centrifuging, the ethanol supernatant component was removed from the top of the centrifuge tubes, leaving a more concentrated suspension of tracers behind. The heavier tracer-particle component then was mixed with fresh ethanol for further washing, and then the solution was centrifuged again. This process was repeated two more times. Application of repeated washing process removes all impurities which will affect the photopolymerization process. At the end of washing process, the ethanol supernatant was removed and the tracer particles were mixed with pure monomer. This mixture were then washed three more times in pure monomer and centrifuged to remove the ethanol and obtain the final tracer particle suspension in pure monomer solution. The photoinitiator solution with desired concentration was prepared by weighing photoinitiator and then adding the appropriate weight of the pure monomer resin. The resulting photoinitiator-monomer solution was then mixed using first a Fisher Scientific Mini Vortexer and then a Fisher Scientific FS20H Sonicator.

4.3.2 Experimental setup

Microrheology experiments were performed using an experimental setup comprised of the following main components (Figure 4.3):

1. Microscope,
2. UV Lamp and Filter,
3. Sample Chamber,
4. Digital Camera with variable frame rate, and
5. Data Acquisition System.

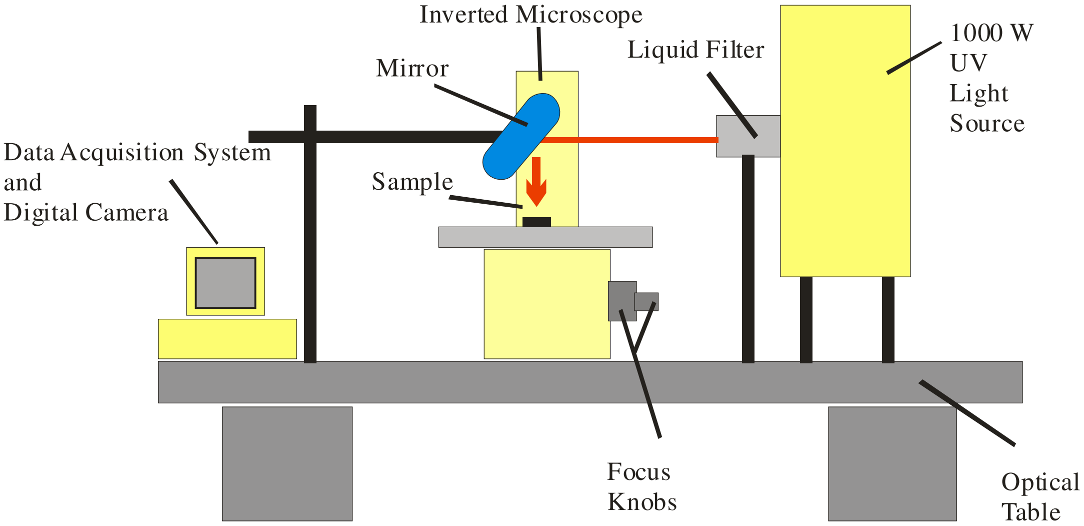

Figure 4.3: Schematic of the Experimental Setup Used in Microrheology Experiments

The experimental setup was designed around a Leica DM-IRB inverted microscope with four objectives lenses (100x, 63x, 40x, and 10x). The microscope was placed on a Newport optical table so that the experimental equipment could be easily and securely adjusted and to shield the experimental apparatus from ambient vibrations, which might adversely affect the tracking of the tracer particles. The system's microscope was used to track the motion of the micron-sized tracer particles. A Spectra-Physics arc lamp housing apparatus (model 66923) equipped with a 1000 watt Hg(Xe) UV lamp was used as the source of UV light in these experiments. Figure 4.4 shows the spectral irradiance of this lamp. The lamp housing was raised 0.1524 meters above the table and 0.1524 meters by optical posts to align the UV light beam with the microscope assembly. A Spectra-Physics liquid filter was mounted in the UV light path directly in front of a condensing lens. The filter absorbed most of the IR frequencies from the light, while allowing the transmission of visible and UV frequencies. A zero-aperture iris diaphragm was mounted to the front of the liquid filter to collimate the emitted UV light. A mirror coated with enhanced aluminum was mounted on the opposite side of the microscope, directly across from the condensing lens of the lamp assembly. This mirror was set at a 45° angle in order to reflect the UV light beam toward the sample reaction chamber in the microscope.

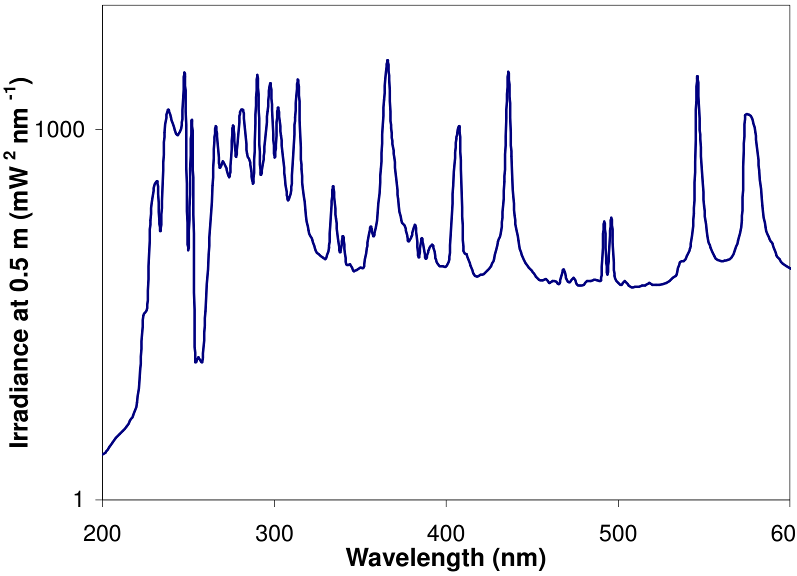

Figure 4.4: Spectral Irradiance of 1000 W Hg(Xe) Arc Lamp [64]

The small rectangular sample chamber was fabricated by using a Fisherbrand pre-cleaned microscope slide for its base. Two parallel strips of M laboratory brand parafilm were placed 1 mm apart on the slide and a cover glass with an index of 1.5 was centered over strips. The stack of materials was then heated, causing the parafilm to melt and adhere to both the cover slip and the glass slide, thereby creating a thin, open reaction chamber capable of holding approximately 2 μL to 3 μL of sample. Since these materials are all relatively inexpensive, new sample chamber was fabricated for each experiment performed.

The pre-prepared sample was loaded into the chamber using a micropipette, and then the chamber was sealed with vacuum grease to prevent evaporation. As the liquid monomer resin polymerizes into a solid, it shrinkages in volume. In order to minimize the effect of this shrinkage, a thin steel mask was employed to shield most of the reaction chamber from the UV lamp light; thus, since very little amount of the sample volume was exposed to the UV light and polymerized, the corresponding shrinkage was also very small. The mask had a narrow slit and was placed on the sample channel. Thus, the total sample area exposed to UV light was approximately one millimeter squared. In Figure 4.5 a diagram of the designed sample chamber loaded with a sample was illustrated. The transmission spectrum of the cover slide and the microscope slide measured by using HP 8453 spectrophotometer are shown in Figure 4.6.

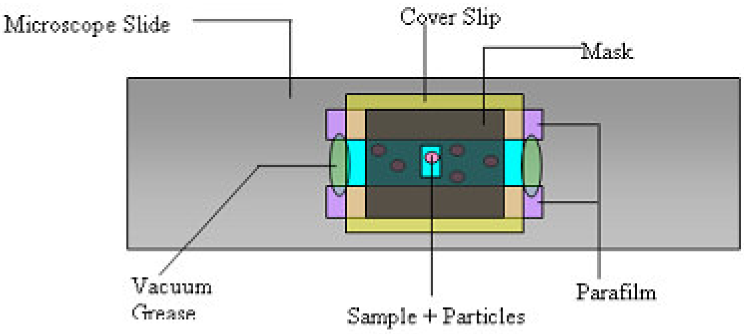

Figure 4.5: Schematic of a Fabricated Sample Chamber Loaded with Sample

In this study, two different wavelengths (248 nm and 356 nm) of UV light were used to drive the photopolymerization reaction. The wavelength of UV light was varied using UV bandpass filters. Both UV bandpass filters had a 30 nm bandwidth around their main transmission frequency. The 248 nm UV bandpass filter was purchased from Barr Associates and the 356 nm was purchased from Newport. Because the polymerization process was considerably slower even for the most reactive monomeric resin (SR494 with four double bonds per monomer) at 248 nm than at 356 nm, all the experiments were conducted with the longer wavelength (356 nm).

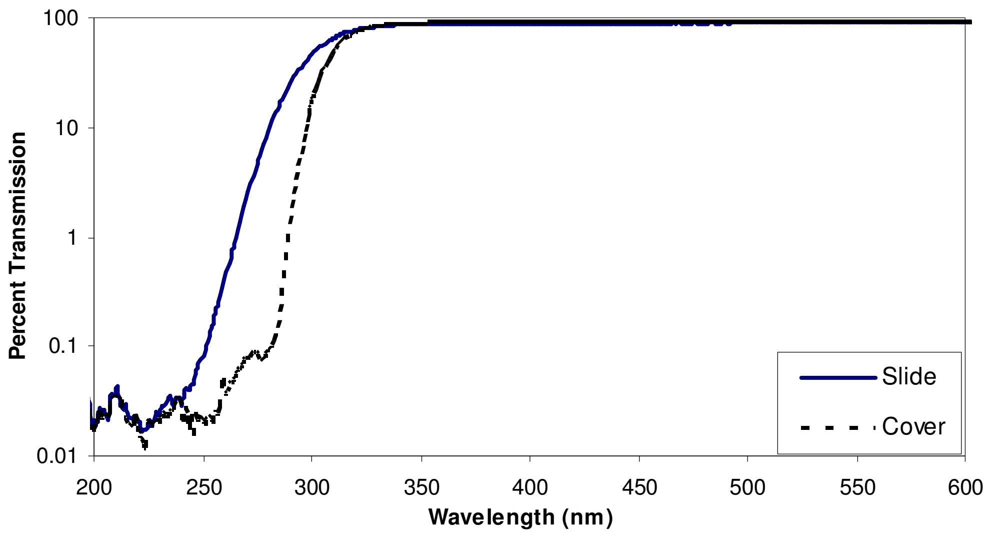

Figure 4.6: Transmission Spectrum of Glass Cover Slip and Microscope Slide

Two digital video cameras were used in the microrheology experiments to track the tracer particles. The first camera is an analog 640 x 480 pixel charge-coupled device (CCD) that has a frame rate of 30Hz (Cohu 4920). The second camera, a Hamamatsu Electron Multiply CCD Digital Camera C9100, has a variable frame rate, but was always used at 30 Hz.

Images of the fluorescent tracer particles were transferred to the computer and recorded in real time using a PXC-200, a precision frame grabber, and the OpenBox image-acquisition software. After a predetermined number of images were recorded, the iris diaphragm in the UV light path was opened and the polymerization process was initiated. After all the images were recorded, OpenBox was used to divide the video file into a series of image stacks for further analysis. Recorded video images of tracer particles in the photopolymerizing resin were recorded; then these images were converted into a digital format for analysis. The conversion was performed automatically by a dedicated frame-grabbing card. The digital images were then saved on a standard computer disk. The recorded data was processed by software written in IDL, a programming language optimized for visual data analysis. Through this software, the locations of particles on different frames were identified and the particle trajectories were computed as a function of time. Once the particle positions were identified in each frame, the MSD for a set of selected particles was calculated using various values for the waiting time parameter τ as a function of time. In this study, the time between successive frames was set to be 0.033 s (or equivalently 30 frames/s). The IDL software identified the particle positions in each frame and correlated these positions frame by frame to calculate the MSD as a function of time. The MSD information can be used in Eq. (2.3) to calculate the rheological properties as a function of time.

Note that τ can never be less than the time between successive images (0.033 s) since the experiment has no way of measuring precisely what happens to particles in the time between images.

In the current study, the tracer particles are embedded into the resin within a small reaction volume sandwiched between two glass plates, as shown in the apparatus in Figure 4.5. The MSD curve as a function of time can be transformed into the shear viscosity before gelation and into the shear modulus after gelation. From the complex shear modulus, the ratio of the loss and the storage moduli as basic rheological properties of the photopolymerizing material can be calculated. Thus, the photopolymerization process of the sample is examined as a function of depth and information about the various rheological properties are also expressed as a function of depth.

4.3.3 Experimental work

A set of experiments was performed with the SR494, SR351, and SR272 resins to study the effect of the UV light penetration depth on the gelation time where the photoinitiator loading concentration was set to 5% by weight. These experiments were conducted in the presence of oxygen. The wavelength of the UV light source used in these experiments was 356 nm.

To study the effect of the wavelength on the dependence of gelation time on the UV light penetration depth, the experiment for SR494 resin was repeated with a different UV light wavelength of 248 nm in the presence of oxygen.

To study the effect of the intensity on the dependence of gelation time on the UV light penetration depth, the experiment for SR494 resin was again repeated for four different UV light intensities in the presence of oxygen.

A final set of experiments was performed to study the effect of the photoinitiator loading concentration on the gelation time with and without the presence of oxygen in the ambient atmosphere for the SR494, SR351, SR272, and SR256 resins. For the SR494 resin, four different photoinitiator loading concentrations were used. For the SR351, SR272, and SR256 resins, nine different photoinitiator loading concentrations were used.

4.4 FTIR Experiments

To determine the double bond conversion of the resin as a function of the photoinitiator loading concentration a Bruker brand FTIR spectrometer was used (Figure 4.7).

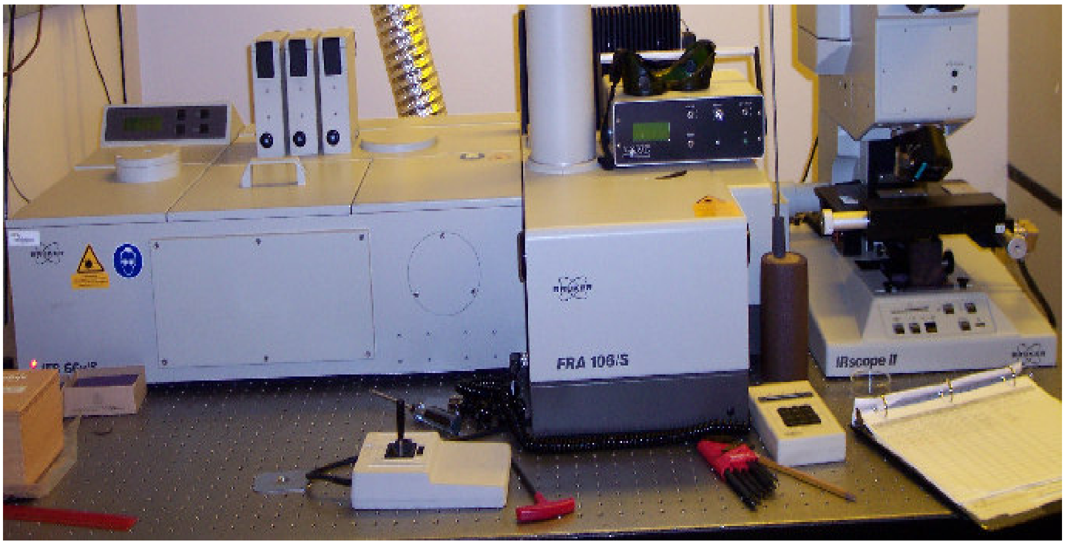

Figure 4.7: Bruker Brand FTIR Spectrometer

For this purpose, a specific sample chamber that allowed transmittance of both IR and UV wavelengths into the resin was fabricated. Since the FTIR measurements requires only a small amount of sample, a disposable sample chamber that is compatible with the sample holder of the spectroscope was designed. The fabrication began by grinding the FTIR spectrograde powder potassium bromide (KBr) salt purchased from Crystal Labs. A Graseby Specac Press was used to make the KBr pellets. Two teflon spacers, separated by a 1 mm gap, were placed in parallel on top of the KBr disc. The other KBr disc was then centered and placed over the gap between the Teflon pieces. The stack of materials was then fastened with metal clips. The gap of the chamber could hold approximately 2 μL to 3 μL of sample.

The sample was loaded into the chamber using a micropipette and then the chamber was sealed with vacuum grease when necessary to prevent evaporation. A diagram of the fabricated KBr disc and sample chamber is shown in Figure 4.8.

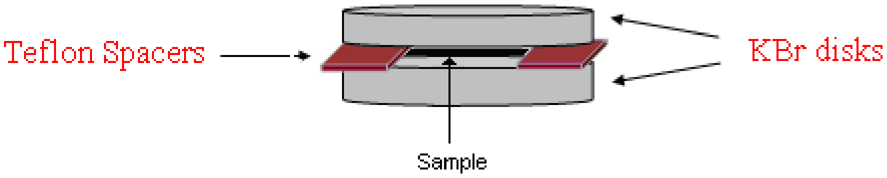

Figure 4.8: The KBr Sample Chamber Used in FTIR Experiments

The UV transmission spectrum of the KBr disc was taken by an HP 8453 UV-Visible spectrophotometer and is shown in Figure 4.9. While the transmission of UV wavelengths is not perfect, it was sufficiently large at 356 nm for the purposes of these experiments. The IR absorption spectrum of a KBr disc taken with a Bruker FTIR spectrometer is shown in Figure 4.10. As seen in Figure 4.10, KBr does not influence the IR spectrum in the wavenumber range between 4000 cm^{-1} and 400 cm^{-1} or wavelength range between 25000 nm to 2500 nm.

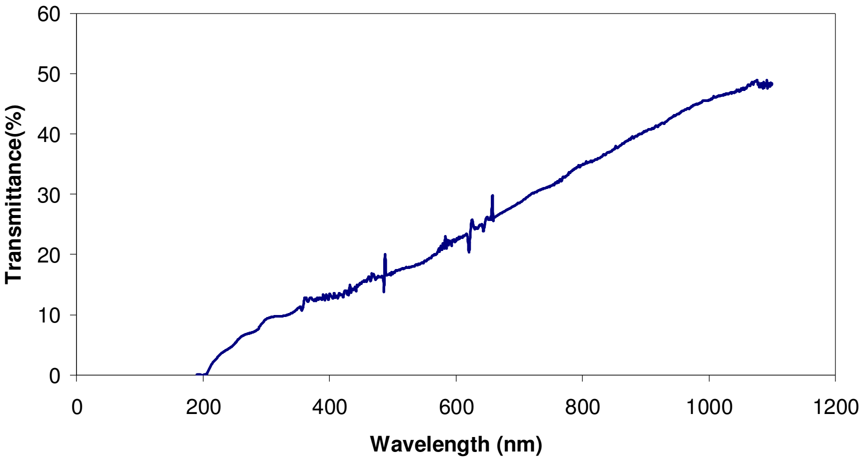

Figure 4.9: UV Transmittance of the KBr Disc

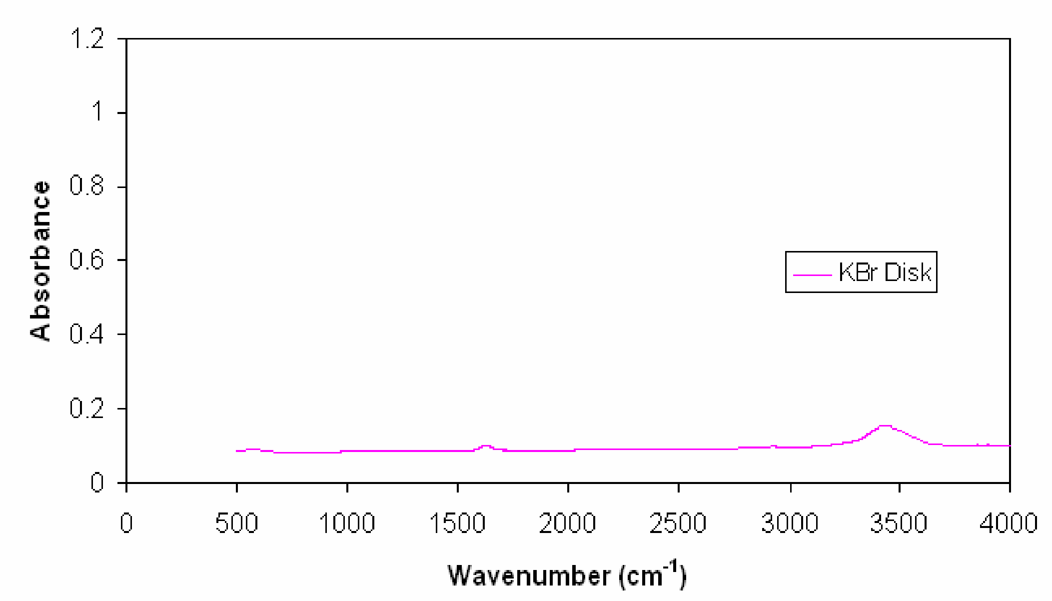

Figure 4.10: IR Spectra of the KBr Disc

The samples were loaded into the sample chamber and then placed with the sample holder in the FTIR spectrometer. The sample was then positioned so that the IR laser beam directly illuminated the center of the KBr disc.

The data was transferred to the computer and recorded by Opus software. After a blank spectrum of KBr disc was recorded, spectra for the uncured samples and cured samples were recorded one after another and the results were compared and correlated with each other. After the data acquisition, Opus programs were used to analyze the data further.

FTIR experiments were done with SR256 resin. The experiments were conducted using three different photoinitiator loading concentrations for a range of UV light exposure times (curing times).

4.5 DSC Experiments

The DSC experiments were conducted isothermally to study the double bond conversion as a function of temperature. For this purpose, approximately 1.16 mg of SR494 resin with 0.02% Irgacure 651 photoinitiator by weight percentage was put in an aluminum sample pan using a micropipette. A TA Instruments DSC Q1000 with photocalorimetric accessory was used to monitor the photopolymerization of the resin. An Exfo Photonic Solutions Novacure 2100 light source, which had source power of 0.06 mW, was used with a filter to produce 365 nm UV light. A continuous flow of nitrogen gas was passed through the DSC apparatus to prevent oxygen from inhibiting the photopolymerization process. In these experiments the normalized heat flow signal obtained from the DSC apparatus as a function of the reaction time was integrated to get the total heat generated by the photopolymerization reaction at four different reaction temperatures, which are 303 K, 343 K, 383 K, and 403 K.

Figure 4.11: TA Instruments Q1000 Model Differential Scanning Calorimeter

5. RESULTS AND DISCUSSION

This section provides a detailed discussion of both SL and microrheology experimental results. To determine the effect of the scanning speed of the UV light source on the curing process, the SL experiments were performed at three different scanning speeds. To simulate the experimental results, an advanced deterministic kinetic model was utilized. This model takes into account the conventional kinetics based on initiation, propagation and termination, and oxygen inhibition which are explained in Chapter 3. Additionally, heat and mass transfer effects were included in this model through a coupled system of differential equations which are second-order in spatial variation and first-order in time variation [11, 71].

To study the rheological properties of a photopolymerizing system, a set of passive microrheology experiments were performed to measure the gelation time as a function of both the UV light penetration depth, UV light properties (wavelength and intensity), and the photoinitiator loading concentration. Three different methods were used to model the results of the microrheology experiments. The first two methods were based on the same advanced deterministic kinetic model mentioned above. The third method was a stochastic Monte Carlo model based on the Gillespie algorithm [5].

5.1 Deterministic Model Development for Simulation of Photopolymerization Process Conducted in SLA

The UV laser-induced photopolymerization process of multifunctional monomers is the underlying reaction in SL. This chapter is focused on developing a computational model to predict the behavior of this process. An advanced deterministic model based on second-order partial differential equations derived from conventional kinetics based on initiation, propagation and termination, oxygen inhibition and mass and energy balances is investigated for this purpose. The heat and mass transfer effects that serve as the core of the model were also considered [2, 3, 11]. Since this model is mainly based on Partial Differential Equations, it will be referred as PDE model.

A schematic display of the PDE model approach used to simulate the SL photopolymerization process is shown in Figure 5.1.

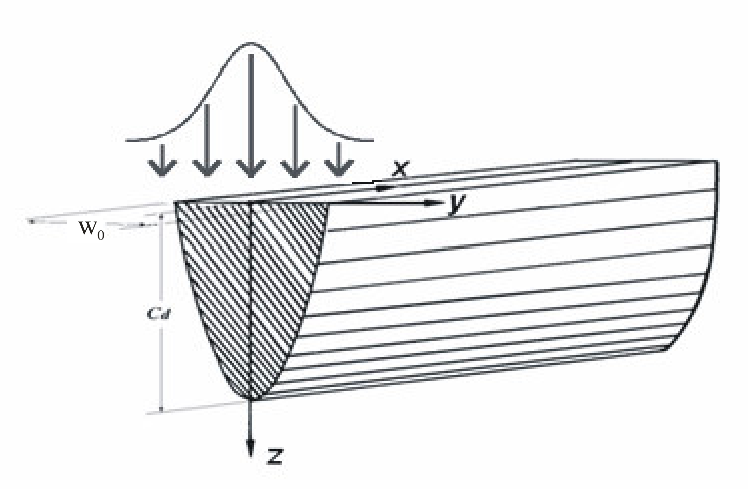

Figure 5.1: A Schematic Display of the PDE Model [59]

The UV laser light illuminating the surface of the resin is assumed to have a Gaussian profile, as shown in Figure 5.1. The energy of the laser beam is progressively absorbed by resin layers just below the area of incidence. Consequently, as the depth z increases, the energy content of the laser beam decreases. It is assumed that the UV curable resin is consisting of monomer and photoinitiator molecules only and the concentrations of these species are uniform throughout the resin. Besides, absorption of laser radiation within the resin obeys the Beer-Lambert Law along the z direction. According to Beer-Lambert Law, the intensity of laser light, $A(x, y, z)$, available at a depth $z > 0$ is related to the intensity at the surface ($z = 0$) in the following manner [59]:

$$A(x, y, z) = A(x, y, 0)e^{-z/D_p} \qquad \textbf{(5.1)}$$

Where D_p is the penetration depth defined as the depth of resin which results in a reduction in the intensity to $1/e$ of the surface intensity. It should be noted that, for a given laser wavelength, D_p is a characteristic of the resin. For a laser beam with a

Gaussian intensity distribution profile, the intensity at the surface can be written in terms of the radius from the center of the laser beam as,

$$A(x,y,0) = A(r,0) = A_0 e^{-2r^2/w_0^2} \tag{5.2}$$

where w_0 is defined as the Gaussian half-width at which the intensity reduces to $1/e^2$ of the maximum intensity at $r = 0$. A_0 is the maximum intensity at the center of the laser beam. Combining Eqs. (5.1) and (5.2) and substituting $r^2 = x^2 + y^2$ gives

$$A(x,y,z) = A_0 e^{-2\left(x^2+y^2\right)/w_0^2} e^{-z/D_p} \tag{5.3}$$

Since the laser beam is scanned in a straight line along x direction with a constant speed, v_s, the x coordinate can be written as a function of time

$$x = v_s(t - t_0) \tag{5.4}$$

Substituting Eq. (5.4) into Eq. (5.3) gives

$$A(t,y,z) = A_0 e^{-2\left((v_s(t-t_0))^2+y^2\right)/w_0^2} e^{-z/D_p} \tag{5.5}$$

Incorporating a time parameter t_0 in Eq. (5.4), causes the intensity of the laser light, A, to go through a maximum at $t = t_0$ and then to asymptotically approach zero as $t \to \infty$. As the laser moves from $-\infty$ to $+\infty$ along the x direction, the characteristic exposure time for any point on the surface is given as [59]

$$t_e = 4.3\frac{w_0}{v_s} \tag{5.6}$$

The characteristic exposure time t_e is the time during which any point on the surface receives 99.99% of its exposure to the incident light of the laser beam moving at constant velocity v_s.

In order to monitor the exposure as function of time at any point on the surface, t_0 in Eq. (5.4) has to be greater than the characteristic exposure time. When applying Eq. (5.5), the unit of intensity must be converted from A_0 (W/m^2) to mol (of photons)/(m^{2}s). The energy of a single UV photon can be expressed by using Planck's law as hv, where h is Planck's constant and v is the frequency of the light in Hz. This, in turn can be converted to units of energy per mole of UV photons by multiplying the energy of a single photon by Avagadro's number N_{AV} to give hvN_{AV}. It is more convenient, though, to work in wavelengths of UV light rather than frequencies. Thus, hvN_{AV} can be rewritten as hvN_{AV}/λ where c is the speed of light in a vacuum and the wavelength is measured in meters. Using standard values for the physical constants, hvN_{AV}/λ evaluates to 1.19x10^{-1} (J·m/mol)/λ(m). It is more conventional to measure the wavelength in nm, which changes this to 1.19x10^{-8} (J·nm/mol)/λ(m). Dividing A_0 by this factor will make the units of Eq. (5.5) compatible with the units of the underlying reaction rate equations of photopolymerization.

As the Gaussian laser beam scans the resin surface along the x direction as shown in Figure 5.2 portion of the resin takes the shape of a parabolic cylinder [59]. From Figure 5.1 the repetitive cure behavior along the x axis is obvious: the cure region is considered to be composed of consecutive parabolic planes, each of which represents the curing of the resin in the y-z plane. Heat and mass transfer along x direction is ignored due to the infinitely small differences in the experimentally measured properties of neighboring slices. With these assumptions, 3-D curing process is modeled as a 2-D problem in the y-z plane. A further simplification comes from the symmetry of the cured parabolic planes with respect to the z-axis. Because of this symmetry, the boundary conditions of the model are developed using only half of the cross section as shown in Figure 5.2.

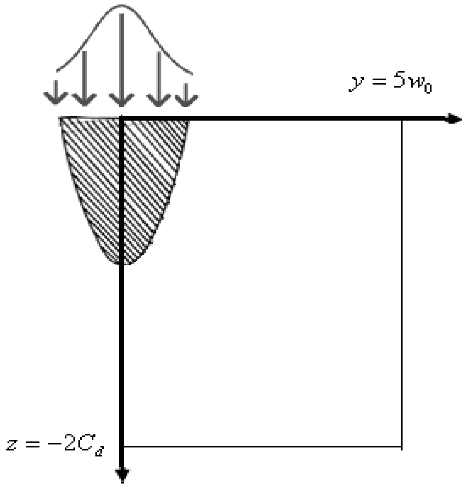

Figure 5.2: Parabolic Slice Representing the Cured Shape in the *y-z* Plane. The Rectangle Represents the Infinite Heat Reservoir Outside the Curing Region [59]

The shaded region in the *y-z* plane in Figure 5.2 inside the rectangle is where most of the curing reaction occurs and where the material properties change most significantly. The maximum cure depth during a single laser scan along a straight line as shown in Figure 5.2 is found to be [59]

$$C_d = D_p \ln(E_{\max} / E_c) \tag{5.7}$$

where $E_{\max}$ represents the maximum center-line laser exposure and E_c the critical laser exposure at which the liquid resin makes the transition to the solid phase. When z becomes $2C_d$, the laser intensity diminishes to about 13% of its original value; therefore, a rectangular area shown in Figure 5.2 with dimensions $5w_0$ and $2C_d$ in the y and negative z directions, respectively, should be sufficiently large to model the photopolymerization reaction accurately under ambient conditions [59].

The whole photopolymerization process can be divided into four basic steps to develop the model equations. These steps are initiation, propagation, termination, and inhibition. Since the photopolymerization process is exothermic, the associated heat transfer must be taken into account. The following heat transfer equation assumes internal energy conservation [97]:

$$\rho C_p \frac{\partial T}{\partial t} = k\nabla^2 T + \Delta H \frac{\partial [M]}{\partial t} \quad \textbf{(5.8)}$$

where ρ, C_p, k, and $[M]$ are the density, heat capacity, thermal conductivity, and molar concentration of monomers, respectively. ΔH is the total enthalpy change per mole of monomer molecules if all of the double bonds are broken during polymerization. ∇^2 is a 2-D Laplacian. The consumption of the monomer during the polymerization can be represented by the following equation [97]:

$$\frac{\partial [\mathrm{M}]}{\partial \mathrm{t}} = \nabla(\mathrm{D_M}\nabla[\mathrm{M}]) - \mathrm{R_p} \quad \textbf{(5.9)}$$

where D_M is the monomer diffusion coefficient, R_p is the propagation rate.

The Gaussian intensity profile of the laser beam illuminating the surface of the resin will cause a concentration gradient of photoinitiator molecules and polymer radicals during the curing process. Therefore, the mass transfer equations for both the polymeric radicals and photoinitiators must include the associated diffusion terms representing the motion of molecules from a high concentration region to a low concentration region. The mass transfer equation for polymeric radicals can be given as [97],

$$\frac{\partial \left[R^*\right]}{\partial t} = \nabla(D_R\nabla[R^*]) + R_i - R_t - R_{in} \quad \textbf{(5.10)}$$

where R_i, R_t, and R_{in} represent the initiation, termination, and inhibition reacrion rates, respectively, and D_R is the polymeric radical diffusion coefficient. Similarly, the mass transfer equation for photoinitiators can be given as [97],

$$\frac{\partial [S]}{\partial t} = \nabla(D_S\nabla[S]) - R_i / 2\phi \quad \textbf{(5.11)}$$

where [S] is the photoinitiator concentration, D_S is the photoinitiator diffusion coefficient, R_i is the initiation rate, and ϕ is the quantum yield, which is defined as the fraction of absorbed photons that initiate polymerization, respectively.

The mass transfer equation for inhibition of free radicals by oxygen molecules is represented by the following relation [97].

$$\frac{\partial[O_2]}{\partial t} = \nabla(D_O \nabla[O_2]) - R_{in} \qquad \textbf{(5.12)}$$

Here $[O_2]$ is the oxygen concentration, D_O is the oxygen diffusion coefficient, and R_{in} is the inhibition rate.

These 2-D partial differential equations Eqs. (5.8)-(5.12) are coupled with one another by initiation, propagation, termination, and inhibition rates. Hence, they must be solved simultaneously. These initiation, propagation, termination, and inhibition rates come from the solution of kinetic equations describing the reaction mechanism which are discussed in detail in Chapter 2.

It should be noted that Eq (5.8) takes into account the heat generated only by propagation reaction. This is justified because experimentally the heat generated by absorption of light was found to be on the order of 10 J/mol, while the heat generated by propagation reaction is found to be order of 10^5 J/mol [71].

In this study, Eqs. (5.8)-(5.12) are solved for the following boundary conditions using the multiphysics modeling and simulation software developed by COMSOL Group.

Initial and boundary conditions will be given for the rectangular region shown in Figure 5.2. To simplify writing the initial and boundary conditions, the concentrations $[M]$, $[R^*]$, $[S]$, and $[O_2]$ will be collectively represented by $[H]$.

$$[H]_{(t=0)} = [H]_0 \text{ at } 0 \le y \le 5w_0,\ -2C_d \le z \le 0 \qquad \textbf{(5.13)}$$

$$\frac{\partial[H]}{\partial y} = 0 \text{ at } y = 0,\ -2C_d \le z \le 0,\ t \ge 0 \quad \textbf{(5.14)}$$

$$[H]_{(t=0)} = [H]_0 \text{ at } y = 5w_0,\ -2C_d \le z \le 0 \quad \textbf{(5.15)}$$

$$\frac{\partial[H]}{\partial z} = 0 \text{ at } z = 0,\ 0 \le y \le 5w_0,\ t \ge 0 \quad \textbf{(5.16)}$$

$$[H]_{(t=0)} = [H]_0 \text{ at z} = -2C_d,\ 0 \le y \le 5w_0 \quad \textbf{(5.17)}$$

$$T_{(t=0)} = T_0 \text{ at } 0 \le y \le 5w_0,\ -2C_d \le z \le 0 \quad \textbf{(5.18)}$$

$$\frac{\partial T}{\partial y} = 0 \text{ at } y = 0,\ -2C_d \le z \le 0,\ t \ge 0 \quad \textbf{(5.19)}$$

$$T_{(t=0)} = T_0 \text{ at } y = 5w_0,\ -2C_d \le z \le 0 \quad \textbf{(5.20)}$$

$$T_{(t=0)} = T_0 \text{ at z} = -2C_d,\ 0 \le y \le 5w_0 \quad \textbf{(5.21)}$$

The size of the shaded region in the rectangle of Figure 5.2, which corresponds to the half cross section of the parabolic cylinder in the *y*-*z* plane in Figure 5.1, increases with time as heat conduction and/or molecular diffusion continues [69].

The resin inside the SLA chamber is in contact with air so that the heat transfer with the air must be incorporated into the simulation by the boundary condition for temperature.

$$k\frac{\partial T}{\partial z} = h_{air}\left(T_{\inf} - T\right) \text{ at } z = 0,\ 0 \le y \le 5w_0,\ t \ge 0 \quad \textbf{(5.22)}$$

where k is the thermal conductivity of the curing resin system, and h_{air} is the air-resin heat transfer coefficient and T_{inf} is temperature in the SLA chamber.

Taking into account the boundary conditions along the parabolic interface between the cured and uncured regions specifically would make the simulation intractable; thus, the whole cured region is approximated by the rectangular region in Figure 5.2. And the boundary conditions used in this simulation corresponds to this geometry.

The rectangular domain in Figure 5.2 is chosen to be large enough to ensure that the uncured liquid acts as a heat reservoir for the region where the reaction takes place. Thus, although significant nonlinear changes are taking place in the cured region during the photopolymerization process, immediately outside the cured region, the properties of the uncured liquid remain the same as they were prior to the start of the reaction. The boundary conditions (Eqs. 5.13-5.22) along with rate constants are provided as input to COMSOL for solving coupled PDEs given in Eqs. (5.8)-(5.12).

5.1.1 Simulation of photopolymerization process conducted in SLA

The 2-D PDE model described above is used to simulate the photopolymerization process conducted in SLA with the COMSOL package program. The rate constants, material properties, the SLA operation parameters, laser beam or UV light source propeties, and resin composition which are used as inputs to COMSOL are given in Table 5.1. The simulations were performed using the extended approximate geometry in Figure 5.2 and the boundary conditions given in Eqs. (5.13)-(5.22). The model was then solved using a time-dependent nonlinear solver in the COMSOL software package.

The UV light source, which scans along the resin surface in the *x* direction, is assumed to have a Gaussian intensity distribution in the *y* direction. Thus, in applying the 2-D PDE model, it is assumed that the photopolymerization takes place in the *y*-*z* plane as the photons penetrate into the resin. The simulations were performed at three different scanning speeds of $2.72\times10^{-2}\,\mathrm{m/s}$, $1.18\times10^{-2}\,\mathrm{m/s}$, and $2.72\times10^{-1}\,\mathrm{m/s}$.

Table 5.1: The Parameters Used to Simulate Photopolymerization Conducted in Stereolithography Apparatus [11, 71]

	Parameters	Symbols	Values	Units
Model Parameters	Parameter for propagation rate	A_{p}	6.1	-
	Parameter for termination rate	A_{t}	6.4	-
	Pre-exponential factor	A_{Ep}	28.4	$\mathrm{m^3/mol\text{-}s}$
	Pre-exponential factor	A_{Et}	8916	$\mathrm{m^3/mol\text{-}s}$
	Activation energy	E_{p}	1627	J/mol
	Activation energy	E_{t}	2103	J/mol
	Reaction diffusion constant	R_{rd}	0.013	$\mathrm{m^3/mol}$
	Laser scanning velocity	V_s	0.272/0.0272/0.018	m/s
	Bath temperature	T_{b}	304.55	K
	Thermal convection coefficient	h_{air}	4.18	$\mathrm{W/m^2\text{-}K}$
	Chamber temperature	T_{a}	300.48	K
Laser Parameters	Laser power	P_{L}	0.0288	W
	Wavelength	λ	325	nm
	Beam radius	w_o	$1.1\text{x}10^{-4}$	m
Material Properties	Thermal conductivity	k	0.142	W/m-K
	Heat of polymerization	ΔH_{P}	$2.85\text{x}10^{5}$	J/mol
	Absorptivity (initiator)	ε	19.9	$\mathrm{m^3/mol\text{-}m}$
	Initiation quantum yield	ϕ_i	0.6	-
	Diffusion coefficient (monomer)	D_{M}	$1\text{x}10^{-3}$	$\mathrm{m^2/s}$
	Diffusion coefficient (radical)	$D_{\mathrm{P.}}$	1	$\mathrm{m^2/s}$
	Diffusion coefficient (initiator)	D_{S}	1	$\mathrm{m^2/s}$
	Diffusion coefficient (oxygen)	D_{O}	$49\text{x}10^{-7}$	$\mathrm{m^2/s}$
	Coefficient of thermal expansion (monomer)	α_{M}	0.00177	1/K
	Coefficient of thermal expansion (polymer)	α_{P}	0.00012	1/K
	Glass transition temperature (monomer)	$T\mathrm{g_M}$	205.65	K
	Glass transition temperature (polymer)	$T\mathrm{g_P}$	488.35	K
	Heat capacity (monomer)	$C_{P,M}$	$C_{P,M} = 5.6 \times T(K) + 218.6$	J/kg-K
	Heat capacity (polymer)	$C_{P,P}$	$C_{P,P} = 9.1 \times T(K) - 1535.5$	J/kg-K
	Heat capacity (curing system)	C_P	$C_P = C_{P,M}(1-X) + C_{P,P}X$	J/kg-K
	Density (monomer)	ρ_{M}	$1128/(1+\alpha_M(T-298))$	$\mathrm{kg/m^3}$
	Density (polymer)	ρ_{P}	$1200/(1+\alpha_P(T-308))$	$\mathrm{kg/m^3}$
	Density (curing system)	ρ	$\rho = \rho_M\phi_M + \rho_P(1-\phi_M)$	$\mathrm{kg/m^3}$
Resin Composition	Monomer concentration	$[M]$	2136	$\mathrm{mol/m^3}$
	Initiator concentration	$[S]$	89.82	$\mathrm{mol/m^3}$
	Oxygen concentration	$[O_2]$	$1\text{x}10^{-3}$	$\mathrm{mol/m^3}$

As mentioned before during the experiments photons are only introduced into the system during this period of 0.02 s while the UV light source is shining. The total curing time in both the experiments and the simulations, though, is 31 minutes; thus, most of the photopolymerization, in fact, involves dark reactions—reactions involving the various polymeric radicals that were produced in the first 0.02 s. For all of the scanning speeds, since the UV light source shines for 0.02 s, the same amount of photons is introduced into the resin. The main difference is that, at higher scanning speeds, the photons are spread out over a larger portion of the resin's surface. Thus, the photoinitiator and monomer radicals produced encounter more ambient oxygen molecules that have diffused into the resin and then form peroxy radicals that inhibit the progress of the photopolymerization. Conversely, at lower scanning speeds, the photons are concentrated in a smaller area and thus the concentration of radicals produced by photoinitiation is higher. Therefore, the effect of oxygen inhibition will not be as dramatic; and, as a result, there will be a higher degree of photopolymerization. These trends are reflected in the monomer conversion contour plots as a function of depth and width shown in Figures 5.3, 5.4, and 5.5 corresponding to scanning speeds of $2.72\times10^{-2}\,\mathrm{m/s}$, $1.18\times10^{-2}\,\mathrm{m/s}$, and $2.72\times10^{-1}\,\mathrm{m/s}$, respectively. These figures are plotted at the end of the simulation time which is equal to time of exposure plus the waiting time of 30 minutes and represents the monomer conversion as a function of geometry of the reaction volume. In Figures 5.3 and 5.4 where contours indicating net photopolymerization can easily be seen.

However, Figure 5.5 dramatically demonstrates the effect of oxygen inhibition on photopolymerization. As can be seen from this figure, there are no contours visible which indicates that there is no solid phase present. This simulation was done with a laser scanning speed one order of magnitude higher than the scanning speeds used in the simulations in Figures 5.3 and 5.4.

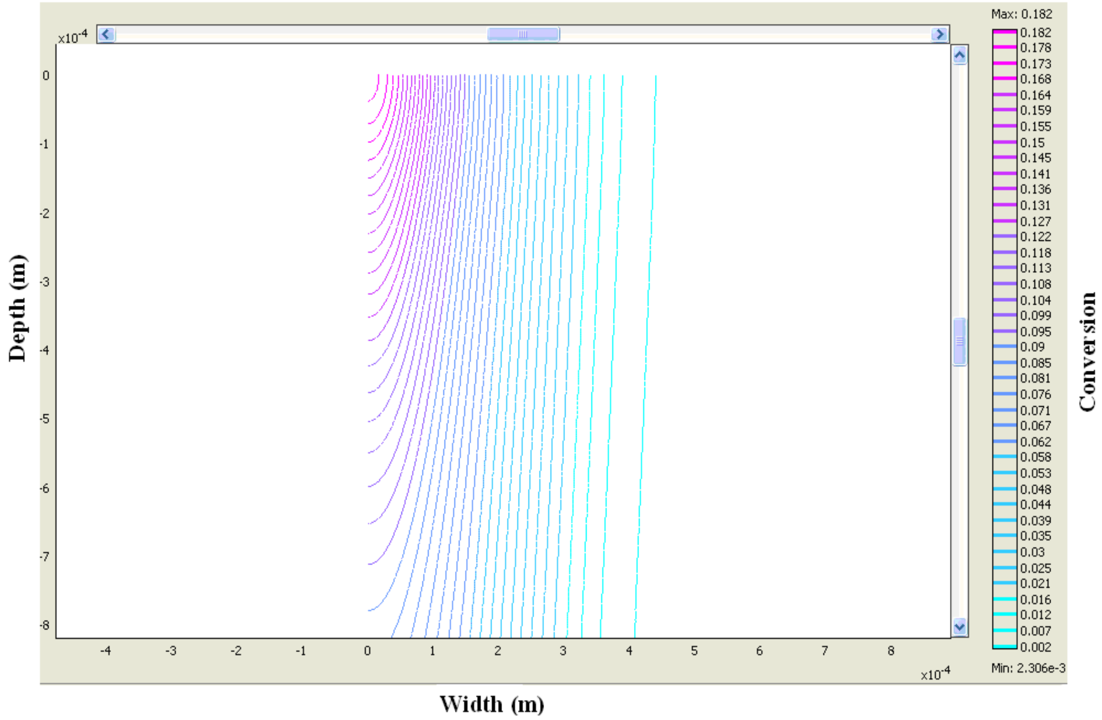

Figure 5.3: Contour Plot of Monomer Conversion for the Scanning Speed of $2.72\times10^{-2}\,m/s$

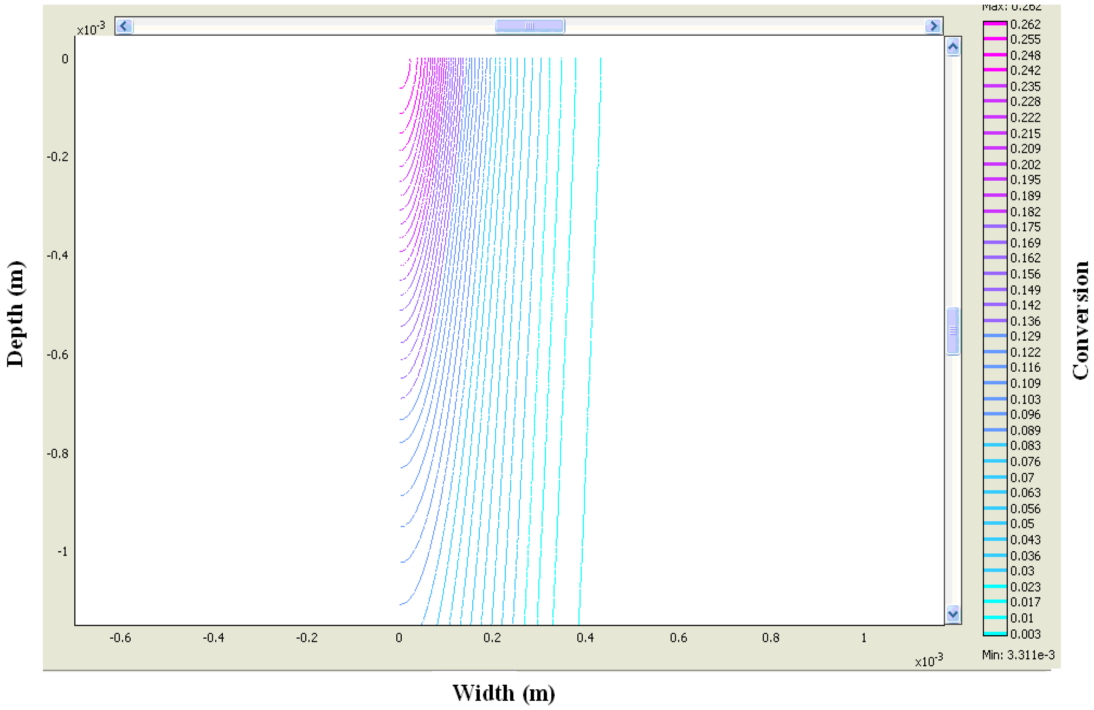

Figure 5.4: Contour Plot of Monomer Conversion for the Scanning Speed of $1.18\times10^{-2}\,m/s$

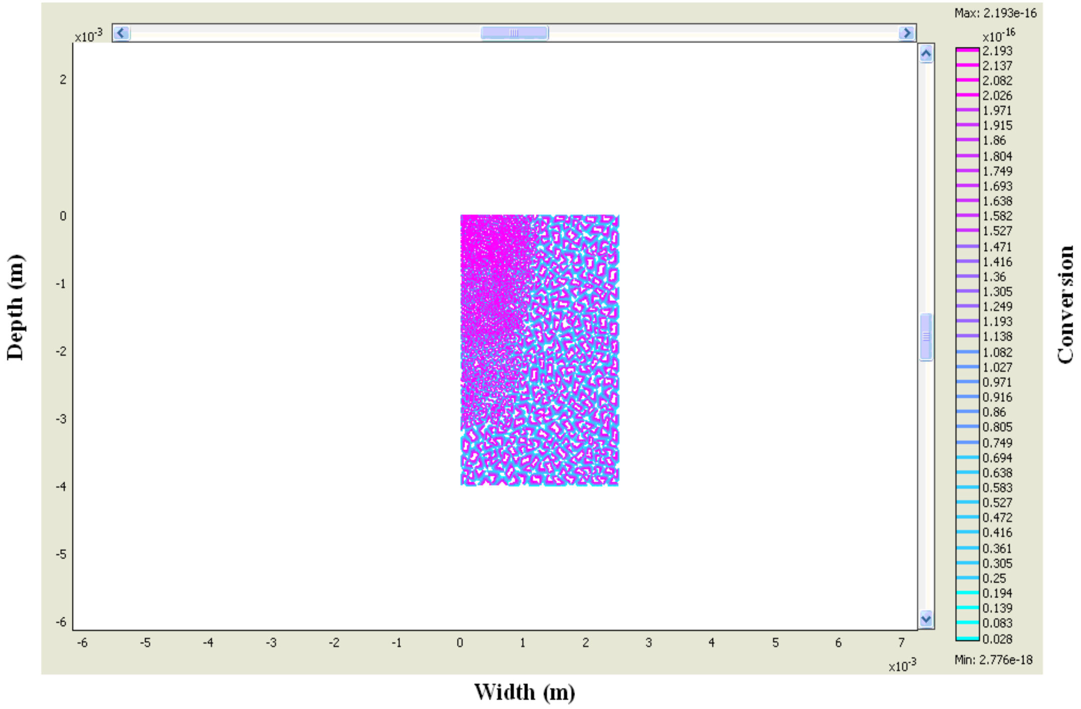

Figure 5.5: Contour Plot of Monomer Conversion for the Scanning Speed of $2.72\times10^{-1}\,\mathrm{m/s}$

Ambient oxygen in the SLA chamber diffuses into the acrylate resin and inhibits free radical photopolymerization by reacting with the photoinitiator and primary radicals and the growing polymer radicals to form peroxy radicals [98]. Since peroxy radicals are much less reactive than all the polymeric radicals directly participating in the photopolymerization reaction, the peroxy radicals do not readily reinitiate polymerization. Thus, the oxygen essentially retards the polymerization process by consuming free radicals. When the laser is turned on, photoinitiator molecules absorb photons from laser field and through a decomposition reaction proceed to form two photoinitiator radicals each. Diffused oxygen in the resin immediately starts scavenging these radicals. The photopolymerization reaction becomes competitive with the formation of peroxy radicals only after the concentration of oxygen molecules in the resin falls below the concentration of photoinitiator and polymeric radicals. Thus, if the UV light scanning speed is high, there may not be enough photoinitiator radicals produced to decrease the oxygen molecule concentration in the portion of the resin over which the laser scans to the point that polymerization can take over.

In Figures 5.6 and 5.7 the monomer conversion as a function of time is given. These figures clearly shows that most of the conversion takes place during the exposure time of 0.02 s.

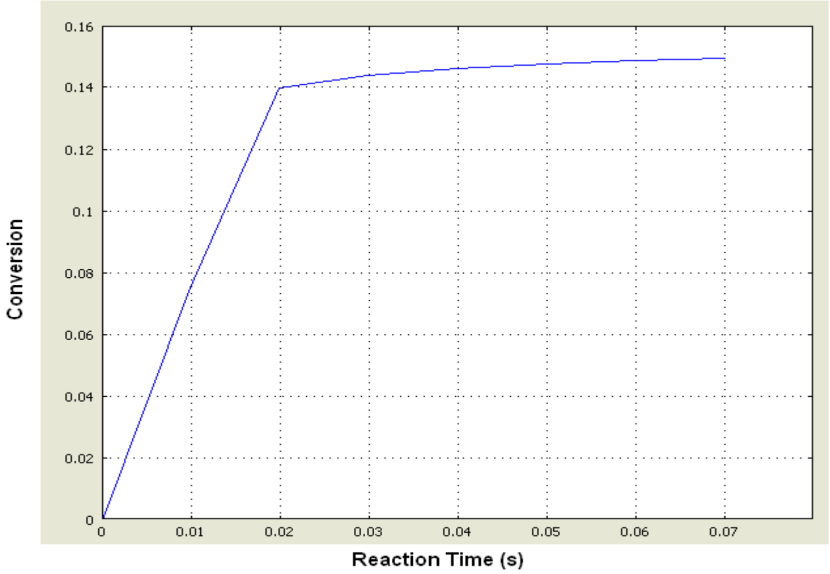

Figure 5.6: Monomer Conversion Versus Time for the Scanning Speed of $2.72\times10^{-2}\,\mathrm{m/s}$

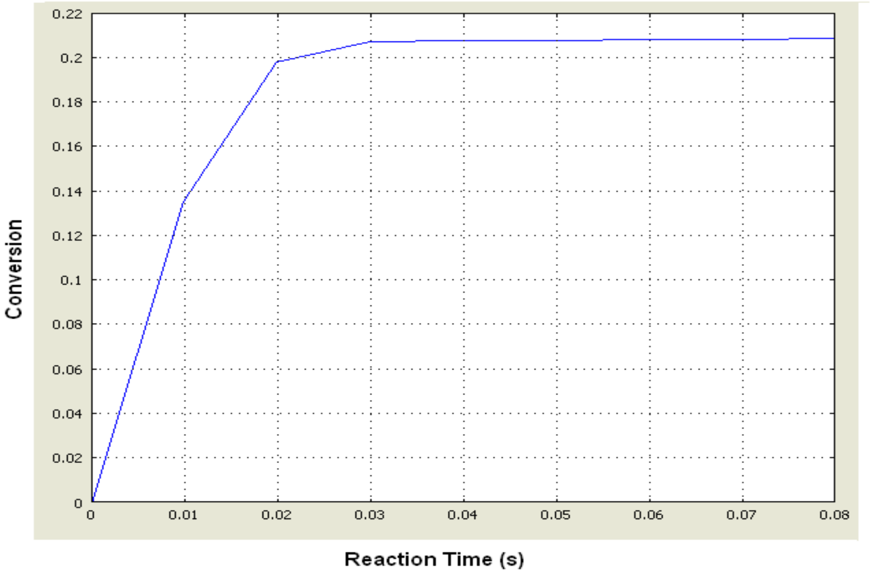

Figure 5.7: Monomer Conversion Versus Time for the Scanning Speed of $2.72\times10^{-2}\,\mathrm{m/s}$

Comparing Figure 5.6 and 5.7 which are obtained for the surface with Figure 5.3 and Figure 5.4, one can also see that most of the conversion as a function of the depth and width takes place at and immediately beneath to the surface. These figures also shows that almost 85% of the monomer conversion takes place during the laser exposure time of 0.02 s. The rest of the conversion corresponds to dark polymerization reactions – those that proceed without direct laser illumination.

Contour plots of the photoinitiator concentration change at the end of the simulation time (31 min) as a function of the depth and width corresponding to the laser scanning speeds of $2.72\times10^{-2}\,\mathrm{m/s}$ and $1.18\times10^{-2}\,\mathrm{m/s}$ are shown in Figures 5.8 and 5.9, respectively. Figures 5.8 and 5.9 clearly show that most of the photoinitiator concentration change takes place at and immediately beneath the surface.

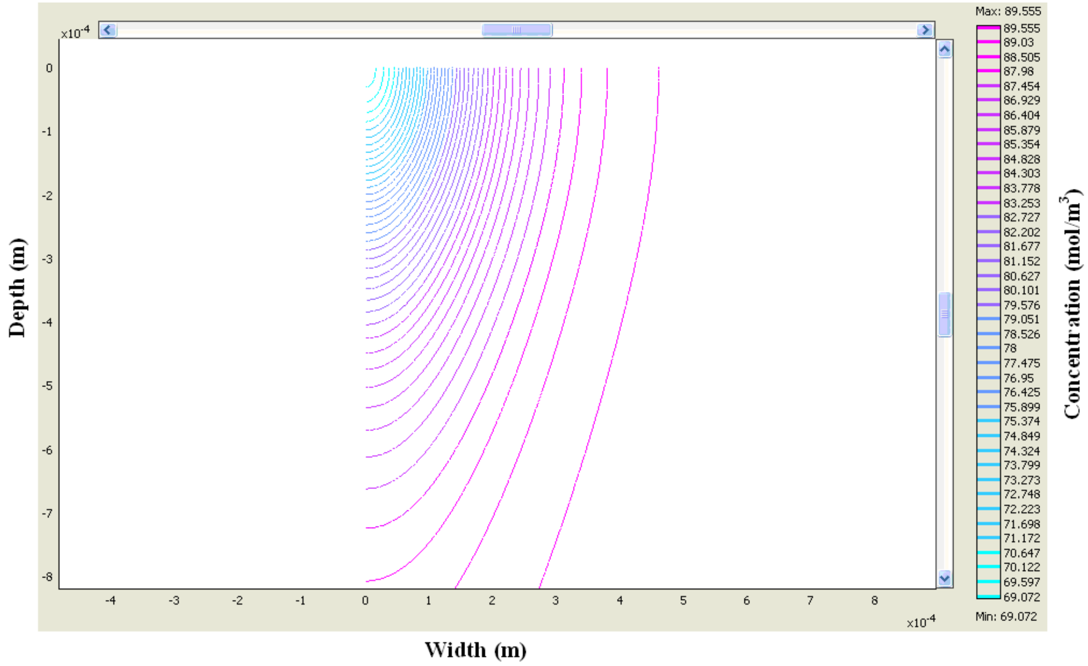

Figure 5.8: Contour Plot of Photoinitiator Concentration for the Scanning Speed of $2.72\times10^{-2}\,\mathrm{m/s}$

It should be emphasized that the paraboloid shape of the contours in all the contour plots results from the Gaussian distribution of the intensity of the incident light beam, which can be seen in Figure 5.10. Examining the radical concentration change in Figure 5.11, it is easy to see that almost all the radicals are produced during the laser exposure time of 0.02 s. However, a small amount of photoinitiator molecules that have absorbed photons persist in excited states when the laser is turned off. As they decay, they contribute a small number of new radicals into the system during the dark period. This is why there is a small, non-zero amount of radical production for several hundredths of a second after the laser is turned off. Eventually, after a time period which is longer than the lifetime of the photoinitiator excited state, all the excited photoinitiator molecules produced by the laser decay and the net production of radicals goes to zero. Figure 5.11 clearly shows this phenomenon.

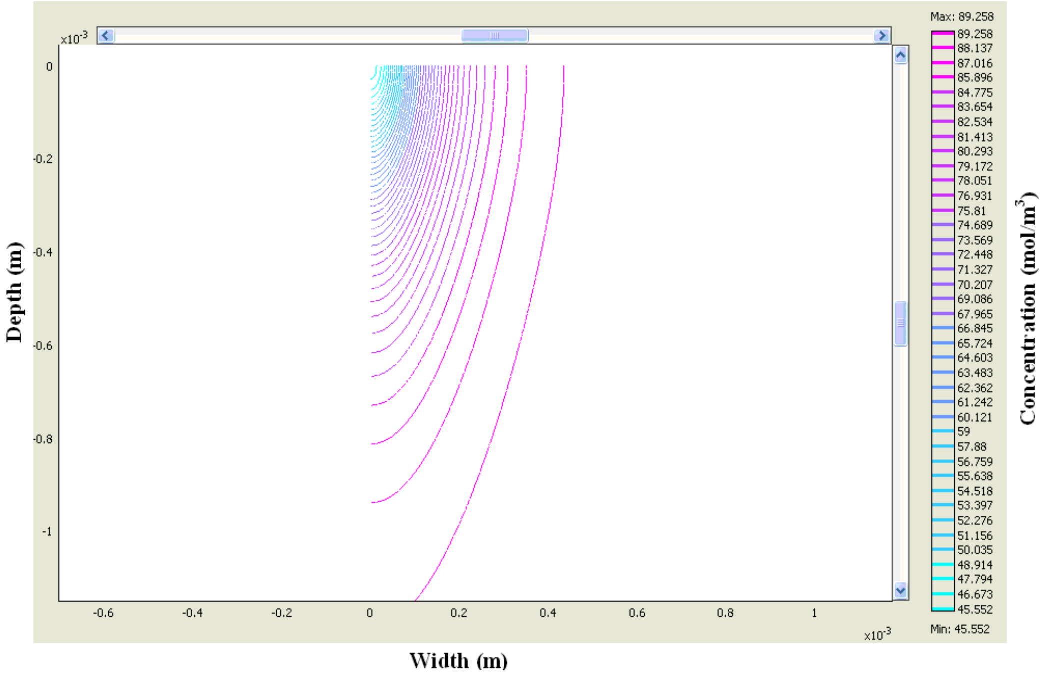

Figure 5.9: Contour Plot of Photoinitiator Concentration for the Scanning Speed of $1.18\times10^{-2}\,\mathrm{m/s}$

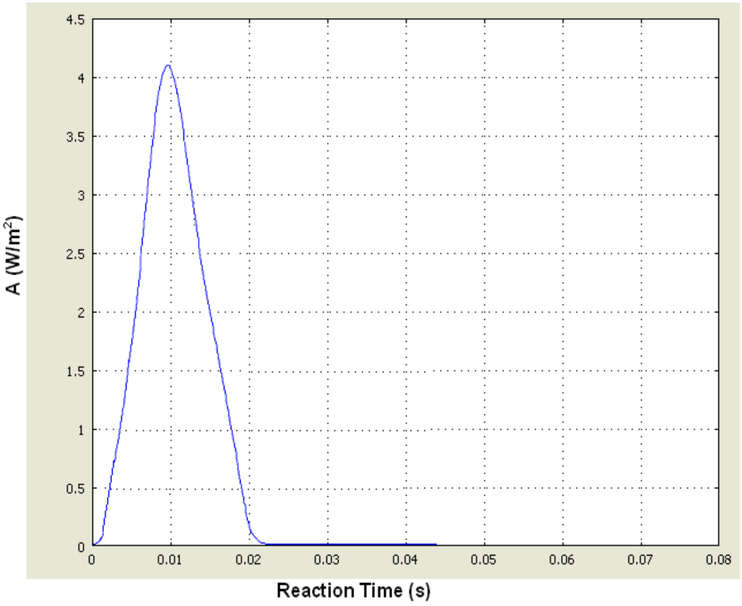

Figure 5.10: Intensity Versus Time for the Scanning Speed of $2.72\times10^{-2}\,\mathrm{m/s}$

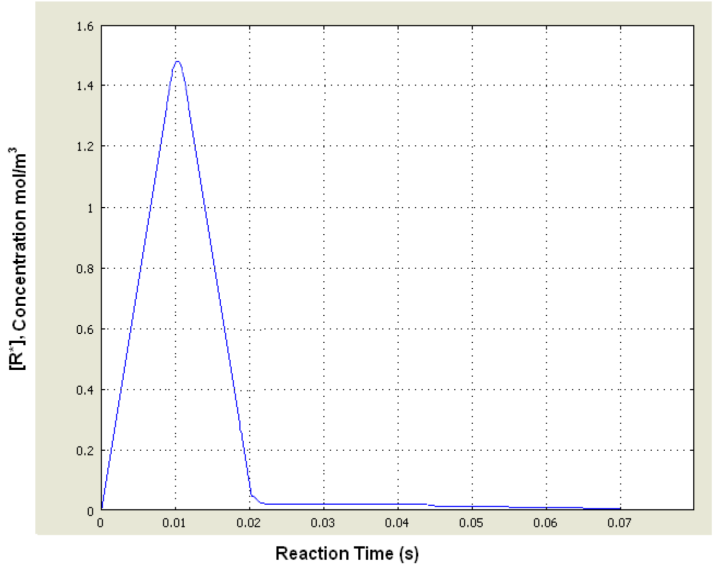

Figure 5.11: Radical Concentration Versus Time for the Scanning Speed of $2.72\times10^{-2}\,\mathrm{m/s}$

The progress of photopolymerization process can also be reflected by the temperature change by time. Figures 5.12, 5.13 and 5.14 show the temperature change as a function of time for laser scanning speeds of $2.72\times10^{-2}\,\mathrm{m/s}$, $1.18\times10^{-2}\,\mathrm{m/s}$, and $2.72\times10^{-1}\,\mathrm{m/s}$, respectively.

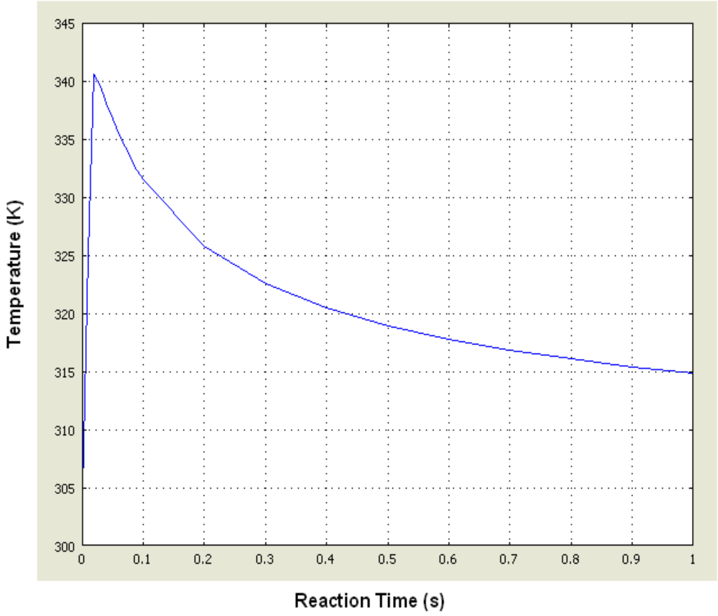

Figure 5.12: Temperature Change by Time for the Scanning Speed of $2.72\times10^{-2}\,\mathrm{m/s}$

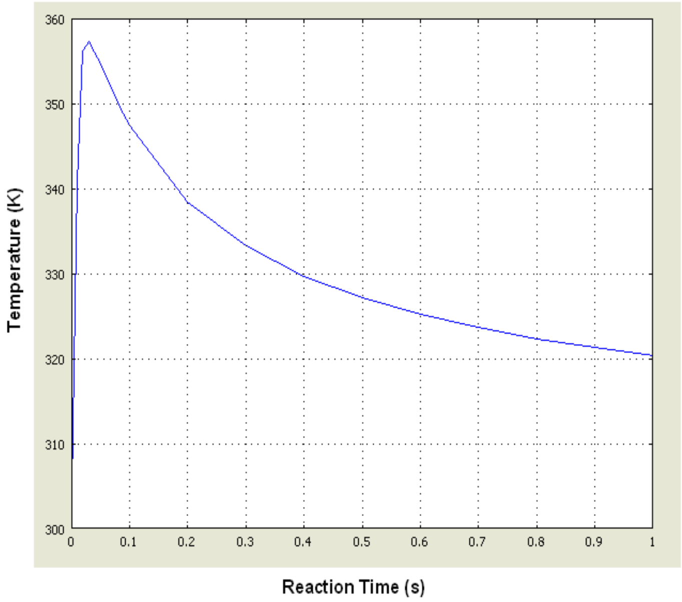

Figure 5.13: Temperature Change by Time for the Scanning Speed of $1.18\times10^{-2}\,\mathrm{m/s}$

The photopolymerization process is exothermic and these figures show that the higher temperature changes occur at the lower laser scanning speeds, which correspond to higher monomer conversion. The temperature rise is considerably less in Figure 5.14 since it results from the photopolymerization simulation that also produced the conversion contour plot in Figure 5.5, which shows that there is no net photopolymerized solid phase produced.

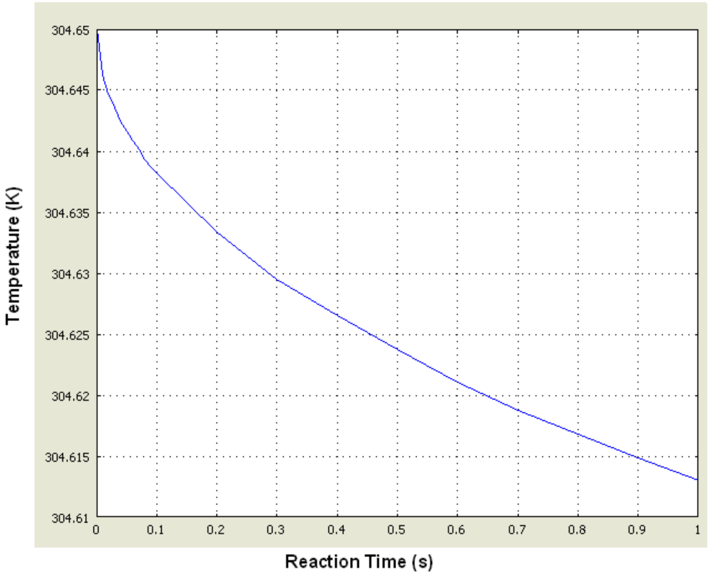

Figure 5.14: Temperature Change by Time for the Scanning Speed of $2.72\times10^{-1}\,\mathrm{m/s}$

5.1.2 Results of experiments

The maximum depth and widths of a 2-D cross section of the cured resin parts obtained in SL experiments were measured by the SEM device. Two examples of SEM micrographs of the fabricated parts at two different scanning speeds were given in Figures 5.15 and 5.16. These figures show how these measurements are made. Dimensions of fabricated parts obtained in SL at two different scanning speeds were summarized in Table 5.2. The experiments perfomed in SLA showed that the critical gelation time was never achieved with the highest scanning speed of $2.72\times10^{-1}\,\mathrm{m/s}$, which is in agreement with the simulation results (Figure 5.5). Thus, no dimension measurements for this speed is given.

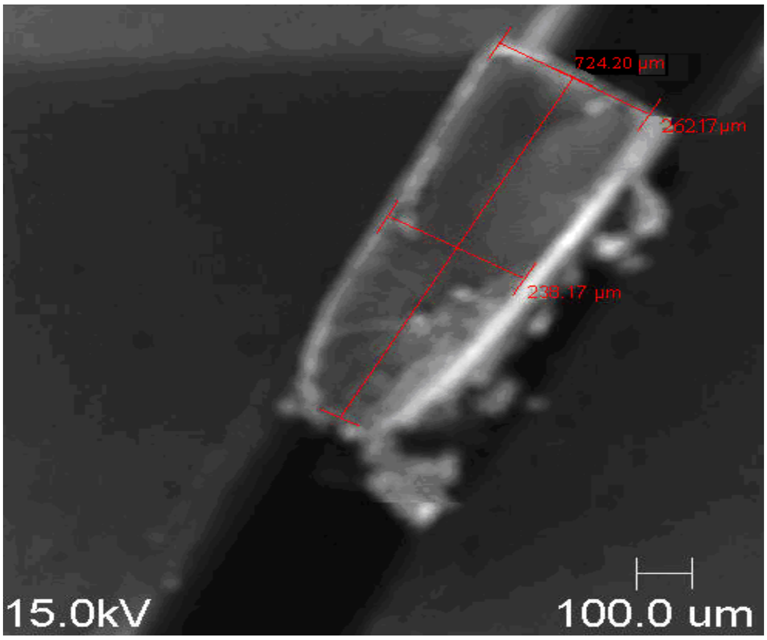

Figure 5.15: SEM Micrographs of Fabricated Part for the Scanning Speed of $2.72\times10^{-2}\,\mathrm{m/s}$

It can be seen from Table 5.2 that the parts built at UV light scanning speed of $1.18\times10^{-2}\,\mathrm{m/s}$ have larger widths and depths than those built at UV light scanning speed of $2.72\times10^{-2}\,\mathrm{m/s}$. This difference occurs because the UV exposure time at any point on the resin surface decreases as the scanning speed increases, thus reducing the degree of photopolymerization. As a result of the slower scanning speed, more photons from the UV light source are concentrated over a smaller surface area; this, in turn, creates more photoinitiator radicals in the volume below that surface area, causing a higher degree of photyopolymerization.

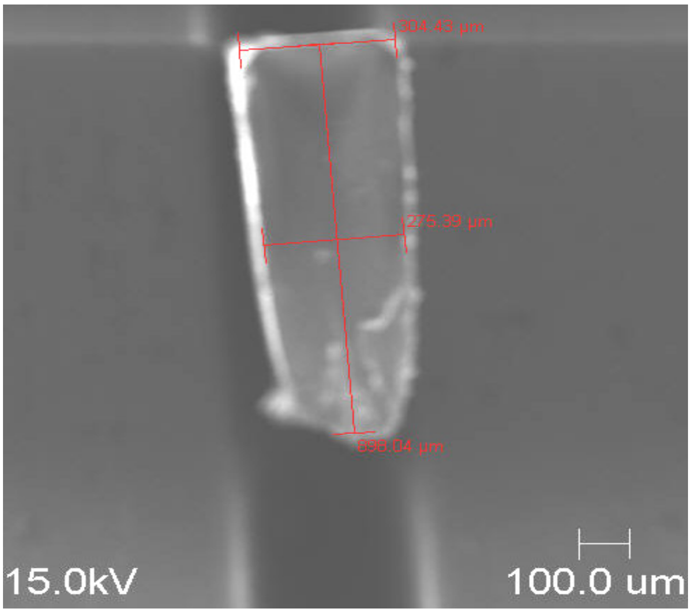

Figure 5.16: SEM Micrographs of Fabricated Part for the Scanning Speed of $1.18 \times 10^{-2}\,\mathrm{m/s}$

Table 5.2: Dimensions of the Fabricated Parts Obtained in Stereolithography Apparatus at Different Scanning Speeds

Scanning speed (v_s) (m/s)	2.72×10^{-2}		1.18×10^{-2}	
	Max Depth (µm)	**Max Full Width (µm)**	**Max Depth (µm)**	**Max Full Width (µm)**
	724	262	898	304
	703	275	945	309
	761	268	963	317
	738	266	922	311
	763	259	901	349
	762	265	956	272
	738	256	951	324
	727	268	980	329
	753	256	958	332
	741	267	988	277
	725	260	990	335
	727	267	978	333
	757	273	945	302
	759	261	907	316
	768	255	998	347
	757	275	972	331
	774	283	1008	334
	737	260	964	345
	730	250	938	328
	756	274	982	334
Average	745	265	957	322

As mentioned above, the width and the depth of parts produced by the SLA were measured at two different scanning speeds. To ensure that the results were reproducible and statistically significant, each single laser scan part-fabrication process in SLA was repeated twenty times for each of the two different laser scanning speeds under the same conditions and average dimensions were determined.

5.1.3 Comparison of experimental and simulation results

The average values for the part dimensions obtained experimentally are given in Table 5.3 with the same part dimensions estimated from 2-D PDE model simulations. Table 5.3 also lists the relative prediction error between the measurements and the simulations of the width and depth of the cured parts. The errors associated with the simulation results are calculated using the following formula:

$$\text{prediction error} = \frac{\text{simulated value} - \text{experimental value}}{\text{experimental value}} \times 100\% \qquad \textbf{(5.23)}$$

The simulation predictions for the part dimensions were obtained by reading the appropriate dimensions from the contour plots given in Figures 5.3 and 5.4 based on the overall part geometry for contours corresponding to monomer conversion values of 5%, 10%, and 15%. As can be seen from Table 5.3, the contours corresponding to 10% conversion value agree much better with the experimental part measurements than either those for 5% or 15% conversion values.

Two significant trends are apparent in the data given in Table 5.3. First, generally for three different conversion values, the error in the part dimensions predicted by the model decreases as the scanning speed of the UV light decreases. Second, the deterministic 2-D PDE model is capable for predicting the experimentally measured dimensions for two UV light scanning speed used.

Table 5.3: Experimental and Model Results for the Part's Dimensions

	Max Depth (µm)				Max Full Width (µm)			
V_s (m/s)	Exp. Value	Conversion	Simulation Value	Error (%)	Exp. Value	Conversion	Simulation Value	Error (%)
$2.72\text{x}10^{-2}$	***745***	5%	1180	58	***265***	5%	460	73
		10%	**640**	**-16**		**10%**	**265**	**0**
		15%	245	-67		15%	180	-32
$1.18\text{x}10^{-2}$	***957***	5%	1365	29	***322***	5%	470	45
		10%	**978**	**2**		**10%**	**334**	**3**
		15%	620	-35		15%	290	-10

Finally it should be noted that, as the resin photopolymerizes and the double bond conversion value increases, the polymerizing liquid resin solidifies. Thus, the conversion value reached at this point is known as critical conversion. Experimentally, the boundary for this region is the outermost surface of the fabricated part. For the simulations, however, there are just a set of contours corresponding to various conversion values for the resin as given in Figures 5.3 and 5.4. To determine the critical conversion value from the simulation results, one must examine different contours to find the contour with dimensions which minimize the relative error compared to the experimental measurements.

In Table 5.3, one can see that using lower conversion value (5%) as the critical conversion corresponds to larger part dimensions and leads to relative errors that are positive. As one increases the conversion value used as the critical conversion, the relative errors in the part dimension decrease and then become negative. Thus, the conversion value where the relative error in the predicted part dimensions is zero corresponds to the critical conversion value. From the deterministic 2-D PDE simulations, it can be concluded that critical conversion value of the SR494 resin is approximately 10%.

The qualitative agreement between the experimental and simulation results for the photopolymerization of SR494, which is a resin containing tetrafunctional monomers, stimulated further studies to validate the 2-D PDE model.

It is well-known that one of the most important parameters in the photopolymerization of multifunctional monomers is the gelation time. The point in time when a photopolymerizing resin undergoes a phase transition from liquid to solid at a critical extent of reaction during gelation is called the gel point [99]; the total reaction time required to reach the gel point is called the gelation time. Because at the gel point drastic changes occur in the rheological properties of a resin, any information about the gelation time will undoubtedly have practical value to industrial applications. For instance, the gelation time is critically important to the rapid prototyping industry for optimizing the building time and other parameters such as the scanning speed and the photoinitiator loading concentration. Because the gelation time is so practically important, the PDE model was used to predict the gelation time of the multifunctional monomers. To compare with the model's predictions, a series of passive microrheology experiments was performed for the photopolymerization of multifunctional monomers over a wide range of photoinitiator loading concentrations.

5.2 Simulation of Microrheology Measurements

In this section, a series of microrheology measurements was performed to determine the gelation times for the photopolymerization reaction of SR494, SR351, SR272, and SR256 resins. Then simulation of these measurements were made by using different theoritical models.

5.2.1 Modification of PDE model for microrheology measurements

Instead of the 2-D PDEs given in Section 5.1, the simulations of microrheology measurements were done using 1-D PDEs. The reason for this simplification was two-fold:

1. The lamp in these experiments was stationary and
2. The area of the resin's surface illuminated by the light beam was 1 mm^2, small enough to justify ignoring the variation in the x and y directions (Figure 5.1).

This approximation reduces the problem to a time dependent 1-D PDEs, which are given in Eqs (5.8)-(5.12). The parameters used as input for the simulation of microrheology measurements of SR494 resin is given in Table 5.1. The parameters used as input for the simulations of microrheology measurements of SR351, SR272, and SR256 resins are given in Tables A.1-A.3, respectively in Appendix A.

In all simulations, the 1-D PDE model is solved for the sample thickness only assuming insulation boundary conditions at both ends of the reaction thickness as shown in Figure 5.17.

Figure 5.17: Geometry for Gelation Time Simulations

The purpose of these simulations is to determine the gelation time as a function of the UV light penetration depth, UV light properties (wavelenght and intensity), and the photoinitiator loading concentration in the reaction volume. For the determination of the gelation time from the simulation results, the critical conversion values of the multifunctional monomers are predicted by using Flory criteria [100].

Flory showed that the weight average molecular weight of a polymeric molecule containing *f*-functional monomers can be determined from the following equation [100]:

$$\bar{M}_{\omega} = \frac{(1+\alpha)M_{A_f}}{1-\alpha(f-1)} \quad \textbf{(5.24)}$$

where M_{A_f} represents the molecular weight of a *f*-functional monomer and α is defined as the conversion value or the fraction of the *f*-functional monomers that have reacted. Flory defined the functionality, *f*, for a branching unit as the number of other molecules that can react with this network-forming species [100]. For example, a monomer with three double bond has the ability to bond with six other molecules. This is because each of the three double bonds when broken forms two radicals, and thus it can bind with two other molecules. Therefore, according to Flory, the monomer with three double bonds would have functionality $f = 6$. The bi-double bond acrylate molecule can connect with four molecules, and thus $f = 4$.

Also note that, in deriving Eq (5.24), it is assumed that all functional groups of the same type are equally reactive, all groups react independently of one another, and intramolecular condensation does not occur. Gelation is defined as the point when the weight average degree of polymerization or the weight average molecular weight diverges (becomes infinite). This happens when the denominator in Eq. (5.24) becomes zero. So the gelation point (the critical conversion) is

$$\alpha_c = \frac{1}{f-1} \tag{5.25}$$

By using Eq. (5.25) the critical conversion values of SR494, SR351, SR272, and SR256 resins are calculated as 0.14, 0.2, 0.33, and 1, respectively.

As mentioned before, during the photopolymerization process the photoresin remains a liquid polymer until to the point where the critical conversion occurs, which is theoretically equivalent to the gel point [92, 93]. Monomers with higher functionality form infinite cross-linked networks more rapidly than ones with lower functionality. As a result, monomers with higher functionality reach to the gel point at lower conversion values than those with lower functionality. Correspondingly, the polymerization of monomers with higher functionality reaches the critical convergence point in a considerably shorter time than those with lower functionality.

Eq. (5.25) can only be used for polymerizing resins composed of monomers that have a functionality value f greater than one. For resins consisting of monofunctional monomers, one must rely on experimental measurements of the resin's characteristic rheological properties such as viscosity to determine the critical conversion value.

5.2.2 Effect of UV light penetration depth on the gelation time and simulation of the results

To understand the dependence of the gelation time on the UV light penetration depth into the resin, experiments were performed using the SR494, SR351, and SR272 resins, which have four, three, and two double bonds per monomer, respectively. In each experiment, the photoinitiator loading concentration was 5% by weight percentage. To simulate these experimental results, a series of calculations were performed with the COMSOL software package.

During the simulation for each resin, COMSOL generates the double bond conversion values as a function of both the reaction time and the penetration depth of the UV light into the resin; thus, for each resin, at the penetration depths at which experimental measurements were performed, COMSOL was used to plot a graph of conversion values as a function of reaction time. As example, some of the COMSOL-generated graphs plotted at 60 µm UV light penetration depth, which is the half geometry used for gelation time simulations (Figure 5.17), for SR494, SR351, and SR272 resins are given in Appendix B.

From the conversion time curves obtained at different UV light penetration depths, the reaction time corresponding to critical conversion values of monomers was read. This reaction time is taken as the gelation time for a specific monomer at a specific penetration depth. These simulated gelation times as a function of penetration depth for the SR494, SR351, and SR272 are compared with the experimentally measured values in Figure 5.18.

Figure 5.18 shows the experimental and simulation results in three pairs of curves with similar behavior; each pair consists of the data obtained experimentaly (represented by a dashed line) and predicted by simulation (represented by a solid line) for the same monomer. It should be noted that the agreement between 1-D PDE model and experimenttal results of SR494 is quite remarkable. However, this agreement is acceptable for SR351 and SR272 resins.

As can be seen in all the curves in Figure 5.18, the gelation time increases as the penetration depth increases. This is expected from the Beer-Lambert law since the light intensity decreases as it penetrates through the resin [59].

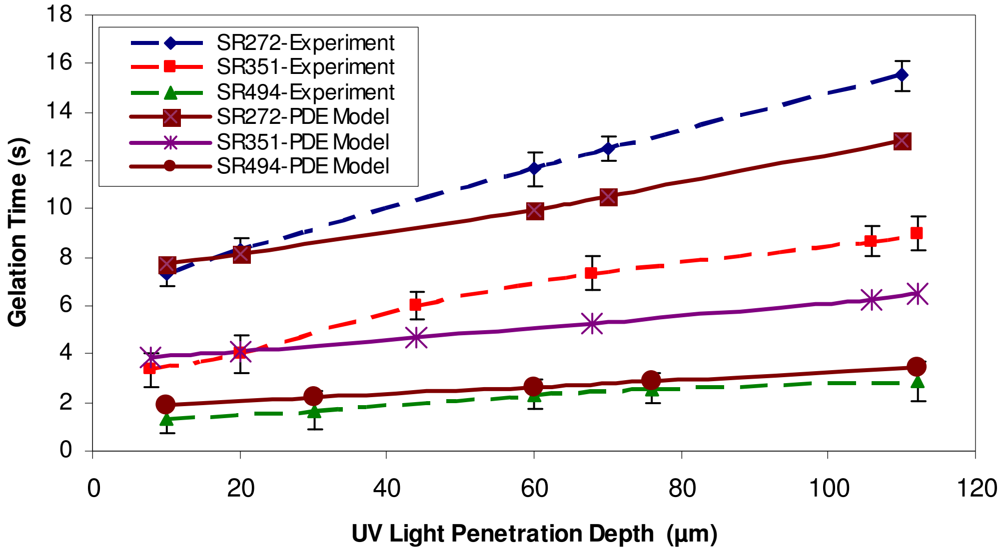

Figure 5.18: Effect of UV Light Penetration Depth on the Gelation Time for Three Different Multifuntional Monomers and Comparison of Experimental and PDE Model Results ($[S]_0$=5wt%)

Additionally, the gelation time is affected by the functionality of the monomer in two important ways. First, as the functionality of the monomer increases, the gelation time decreases at all penetration depths for SR494 resin. For example, for SR494, the monomer with the highest functionality, the gelation times for all penetration depths are significantly lower than for the gelation times for the other two monomers (Figure 5.18). Second, as the functionality of the monomer increases, the difference between the gelation times at minimum and maximum penetration depths decreases. The difference between the gelation times for SR494 at the minimum penetration depth and the maximum penetration depth is only approximately 1 second; in contrast, the corresponding differences in gelation times for the SR351 and SR272 are approximately 4 and 6 seconds, respectively (Figure 5.18). These trends are expected because a polymeric radical composed of higher functionality monomers has a higher probability of reacting with neighboring species. As a result, the mutual entanglement of the growing polymer chains will proceed faster.

5.2.3 Effect of UV light wavelength and intensity on the gelation time and simulation of the results

In order to understand the effect of the UV light wavelength on the relation between the gelation time and UV light penetration depth for SR494 resin, additional experiments were conducted by using a shorter wavelength of 248 nm. Figure 5.19 shows the experimentally measured and simulated gelation time data as a function of UV light penetration depth for two wavelengths of 356 nm and 248 nm.

As seen before experimental and simulation data obtained for the 356 nm wavelength are in reasonable agreement. Although the agreement between the experimental and simulation data obtained for the 248 nm wavelength is not as good for the last four points, the overall trends of the curves agree. Also, it should be noted that the scale here is half the size of that in Figure 5.18, which tends to magnify the difference in the 248 nm curves.

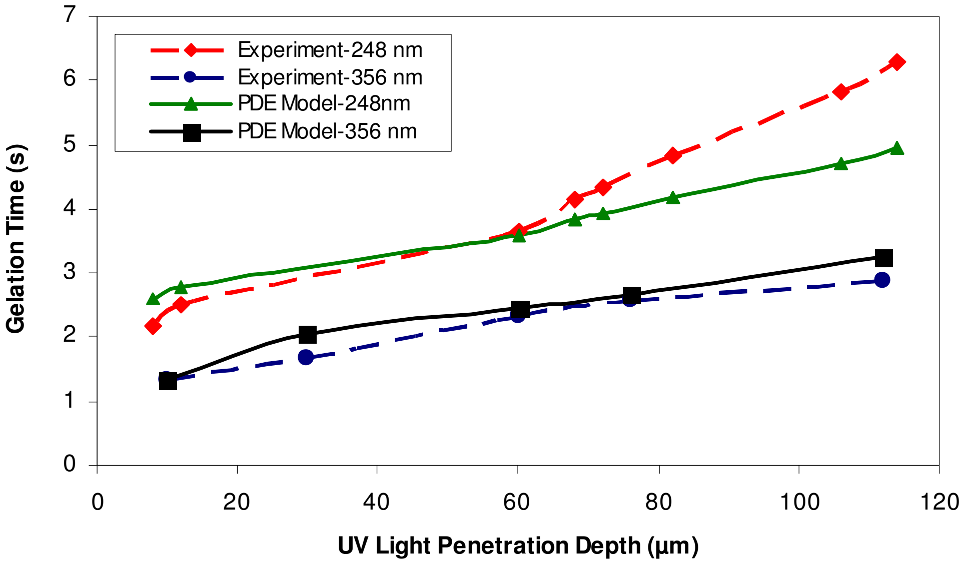

Figure 5.19: Effect of UV Light Penetration Depth on the Gelation Time of SR494 for Different Wavelengths and Comparison of Experimental and PDE Model Results ($[S]_0$=5wt%)

Another interesting trend is that, although the UV photons at 248 nm have more energy than those at 356 nm and could be thought to accelerate the photopolymerization process, the gelation times for all penetration depths are found longer for 248 nm light. The explanation of this phenomena might be the absorbance of Irgacure 651 photointiator molecules is much more strong in the 356 nm region than in the 248 nm region (Figure 4.1). Thus, although photons with a wavelength of 248 nm have significantly more energy than photons with a wavelength of 356 nm, such high energy photons are not efficient in producing photoinitiator radicals from Irgacure 651. This can be the main reason that the higher wavelength light results in lower gelation time.

The effect of the UV light intensity on the relation between the gelation time and UV light penetration depth for SR494 was studied by using three different filters to reduce the intensity of the incident UV light. The intensity of the 356 nm was reduced by 10%, 68% and 90% by using neutral density filters obtained from Newport. The experimental and simulation results obtained for different UV light intensities are shown in Figures 5.20 and 5.21.

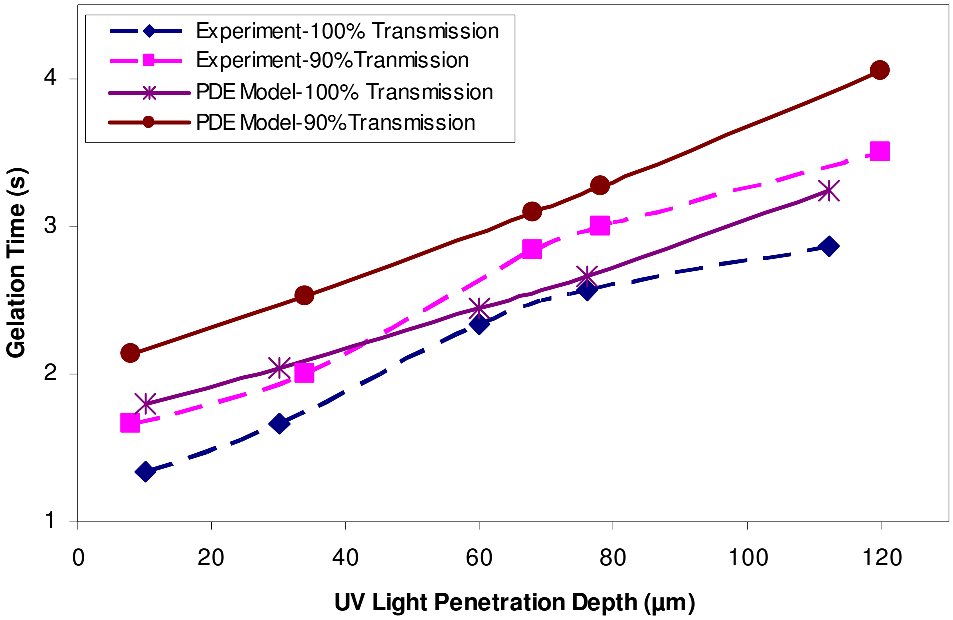

Figure 5.20: Effect of UV Light Penetration Depth on the Gelation Time of SR494 for 100% And 90% UV Light Transmissions and Comparison of Experimental and PDE Model Results ($[S]_0$=5wt%)

A general trend in both figures is that, as the transmission of UV light increases, the gelation time decreases. The explanation for this is clear; because, a higher transmission value means that more photons are reaching the resin and causing more photoinitiator molecules to photodissociate, thus speeding the photopolymerization reactions and reducing the gelation time.

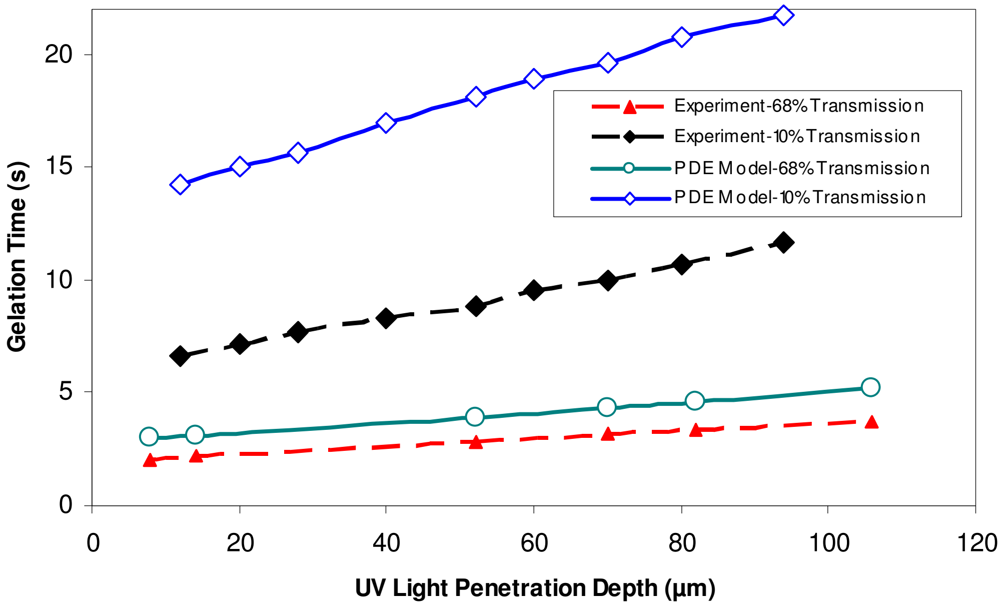

Figure 5.21: Effect of UV Light Penetration Depth on the Gelation Time of SR494 68% and 10% UV Light Transmissions and Comparison of Experimental and PDE Model Results ($[S]_0$=5wt%)

As can be seen from Figure 5.20, the overall agreement between theory and experiment is quite reasonable. Both simulation and experimental results show linear dependence of the gelation time on the penetration depth.

Figure 5.21 shows further results of the dependence of the gelation time on the UV light penetration depth under two lower UV light intensities than given in Figure 5.20. As can be seen, both simulation curves show the same general trends as the corresponding experimental curves. The agreement between theory and experiments worsened as a function of decreasing intensity of the UV light illuminating the surface of the resin. This trend became more prominent for SR494 resin as can be seen in Figure 5.21. The main reason behind this trend is that the oxygen inhibition reactions are more effective in the 1-D PDE model simulations than the corresponding experimental measurements. The 1-D PDE model is based on the concentration of species and do not accurately take into account the functionality of the monomers. The reactivity of the monomers increases as a function of double bonds. The increase in this reactivity is not included the 1-D PDE model. Thus the model over predicts the gelation time as a function of UV light intensity.

5.2.4 Effect of photoinitiator loading concentration and oxygen inhibition on the gelation time and simulation of the results

The gelation time of multifunctional monomers for different photoinitiator loading concentrations were determined experimentally for two different cases:

1. Allowing the ambient oxygen to diffuse into the resin, and
2. Deoxygenating the resin thoroughly by degassing it in a vacuum chamber.

The simulations of these experiments were done by using the modified 1-D PDE model. The simulation of the data obtained at deoxygenated conditions were made by eliminating Eq. (5.12) from the model. Both simulations and experiments were performed for the SR494, SR351, SR272, and SR256 resins at nine different photoinitiator loading concentrations of 0.25%, 0.5%, 1.0%, 2.0%, 3.0%, 4.0%, 5.0%, 6.5%, and 8.0% by weight percentage. The gelation times for the SR494 resin in the absence of oxygen at photoinitiator loading concentrations greater than 2.0% could not be experimentally measured; thus, the experiments and simulations for SR494 only use the four lowest photoinitiator loading concentrations.

For the oxygenated and deoxygenated cases, the COMSOL-generated graphs of conversion values as a function of reaction time for only 2% photoinitiator loading concentration at 60 μm UV light penetration depth for SR494, SR351, SR272 and SR256 resins are given in Appendix C as examples.

The experimental and simulation results obtained for the gelation time of the SR494 resin as a function of the photoinitiator loading concentration are shown in Figure 5.22. The upper curves with filled and empty diamonds represent the experimental and simulation results obtained in the presence of oxygen, respectively. The lower two curves with filled and empty squares represent the experimental and simulation results obtained in the absence of oxygen.

It is clear from Figure 5.22 that, if the photopolymerization occurs in the presence of oxygen, the rate of the decrease in the gelation time as a function of the photoinitiator loading concentration, is quite large initially; but, decreases considerably and becomes almost zero after the photoinitiator concentration reaches a value of approximately 4.0% by weight.

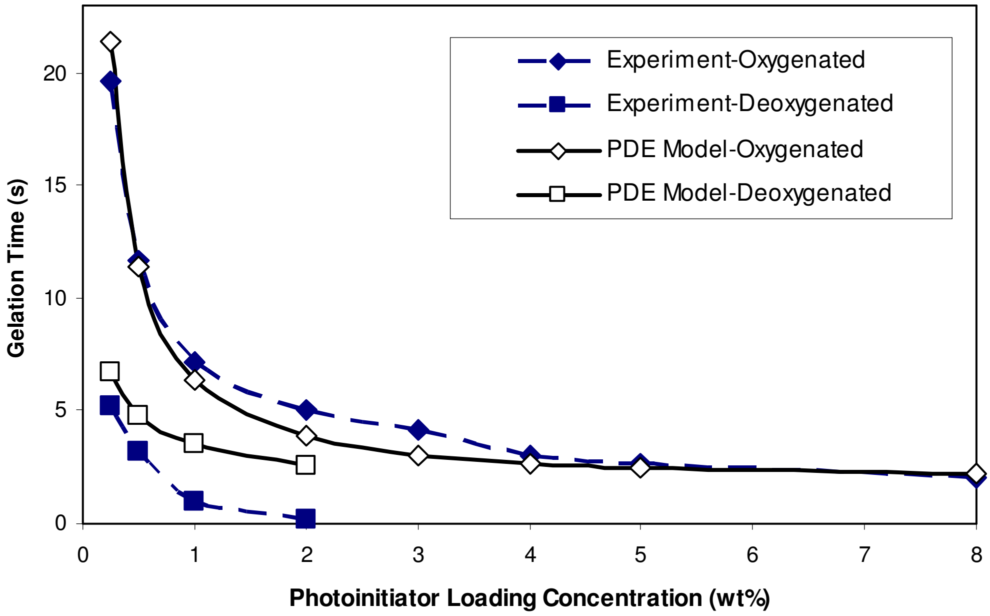

Figure 5.22: Effect of Photoinitiator Loading Concentration on the Gelation Time and Comparison of Experimental and PDE Model Results for Oxygenated and Deoxygenated Photopolymerization of SR494

This behavior of the rate of change of the gelation time as a function of the photoinitiator loading concentration can be understood in the following way. The number of photons emanating from the UV light source of fixed intensity during the fixed illumination time brings a certain number of photons into the resin. If the photoinitiator concentration is too low, many of these photons would not be absorbed by an photoinitiator. In this region, therefore, increasing the photoinitiator loading concentration will increase the number of photons absorbed, thus increasing the number of photoinitiator radicals in the resin. This in turn will increase the number of photopolymerization reactions occurring in the system, which will decrease the gelation time. Beyond a certain photoinitiator concentration, however, all the photons impinging on the system from the light source have already transformed photoinitiators into photoinitiator radicals; after this point, adding further photoinitiator molecules to the resin will not increase the total number of photoinitiator radicals and thus the gelation time will not be appreciably affected.

Figure 5.22 also shows that the photoinitiator loading concentration has the most dramatic effect for values between 0.25% and 2 % by weight, as expected. The agreement between simulation and experiment data obtained for photopolymerization in the presence of oxygen is quite reasonable and the simulation predictions are almost within the margin of error for all the experimental results. However, in the absence of oxygen the agreement between simulation and experimental results for the photopolymerization of SR494 resin is not as good. SR494 has four double bonds and this greatly increases the probability of any polymeric radical having multiple radical sites; this, in turn, greatly enhances the speed of the photopolymerization process.

This trend is clearly seen in Figure 5.22. In the absence of oxygen, the multiple radical and multifunctional sites of the reacting species in the reaction volume is the main reason for the rapid gelation of the SR494 resin. In contrast in the presence of oxygen, as photons produce photoinitiator radicals, the oxygen molecules scavenge a large number of these radicals, thus causing a considerable reduction in the initiating radical concentration. This reduction in the photoinitiator radical concentration decreases the nonlinearity of the photopolymerization process, therefore making it more suitable for modeling by deterministic 1-D PDEs. The 1-D PDE model predictions of the gelation time as a function of photoinitiator loading concentration for the photopolymerization of the SR494 resin in the absence of oxygen do not agree with the experimental data as good as its predictions for the same process in the presence of oxygen, as seen in Figure 5.22.

In Figures 5.23 and 5.24, the gelation time versus photoinitiator loading concentration for the photopolymerization of the SR494 resin in the presence of oxygen and in the absence of oxygen are shown in logarithmic scales on both axes, respectively. Where, solid lines indicate simulation results of the 1-D PDE model and dashed lines indicate experimental results.

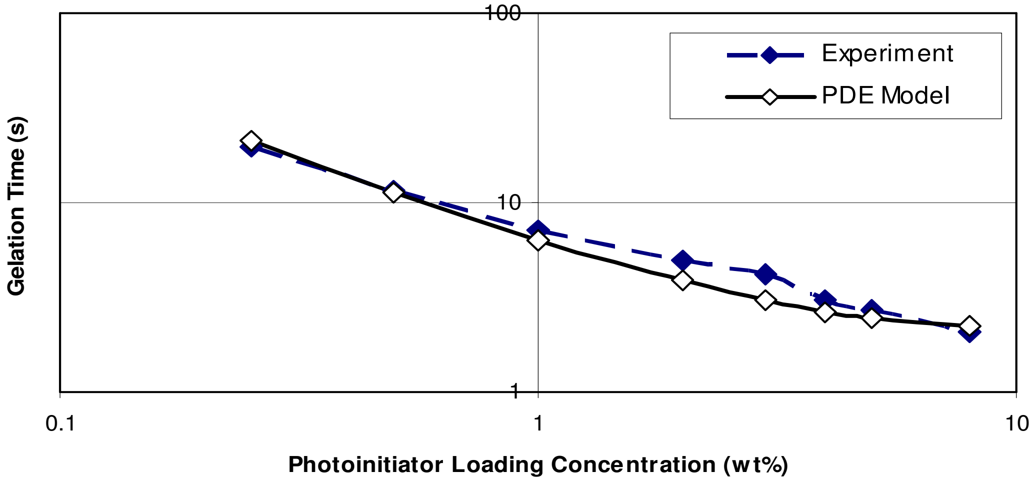

Figure 5.23: Effect of Photoinitiator Loading Concentration on the Gelation Time and Comparison of Experimental and PDE Model Results for Oxygenated Photopolymerization of SR494

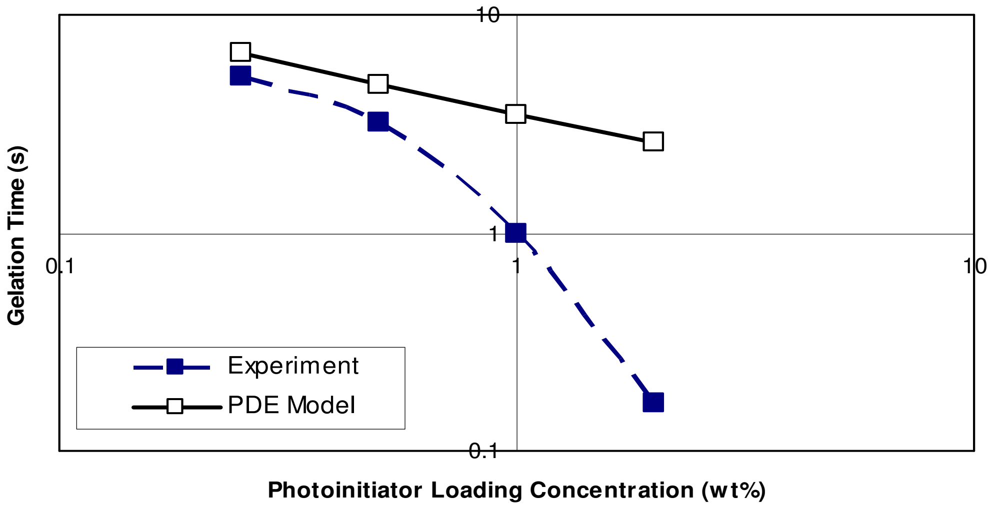

Figure 5.24: Effect of Photoinitiator Loading Concentration on the Gelation Time and Comparison of Experimental and PDE Model Results for Deoxygenated Photopolymerization of SR494

As seen from Figure 5.23, taking the logarithm of the both the gelation time and the photoinitiator concentration, the experimental and simulation data for the photopolymerization done in the presence of oxygen show a near linear relationship. A similar linear dependence with a somewhat different slope is seen for the logarithmic plot of the simulation predictions of the gelation time's dependence on the photoinitiator concentration in the deoxygenated case, represented by unfilled squares. In contrast, the experimental results for the deoxygenated case, represented by filled squares, shows pronounced nonlinearity in the logarithmic plot, as seen in Figure 5.24.

The dependence of the gelation time on the photoinitiator loading concentration for three different types of resin—SR351, SR272, and SR256—was further studied using the different photoinitiator loading concentrations of 0.25%, 0.5%, 1.0%, 2.0%, 3.0%, 4.0%, 5.0%, 6.5%, and 8.0%, as given above. The results of experimental measurements and the simulation predictions for the photopolymerization of these resins in the presence of oxygen and in the absence of oxygen are shown in Figures 5.25-5.30 as a logarithmic plot of the gelation time as a function of the photoinitiator loading concentration. In Figures 5.25-5.30 the experimental results are represented by dashed lines and the simulation results are represented by solid lines.

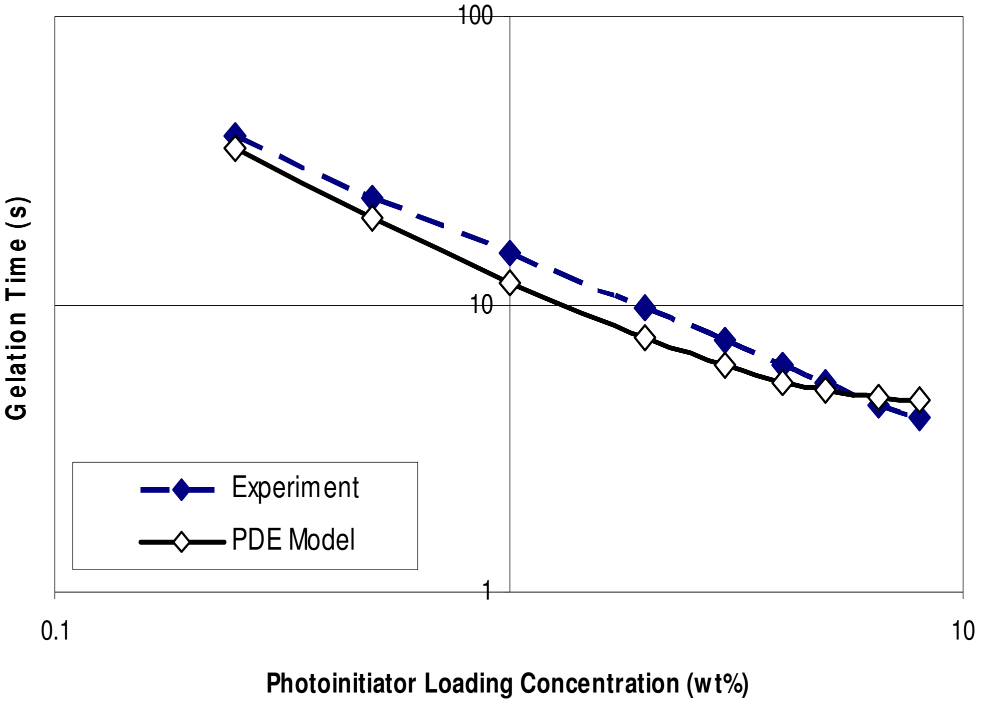

Figure 5.25: Effect of Photoinitiator Loading Concentration on the Gelation Time and Comparison of Experimental and PDE Model Results for Oxygenated Photopolymerization of SR351

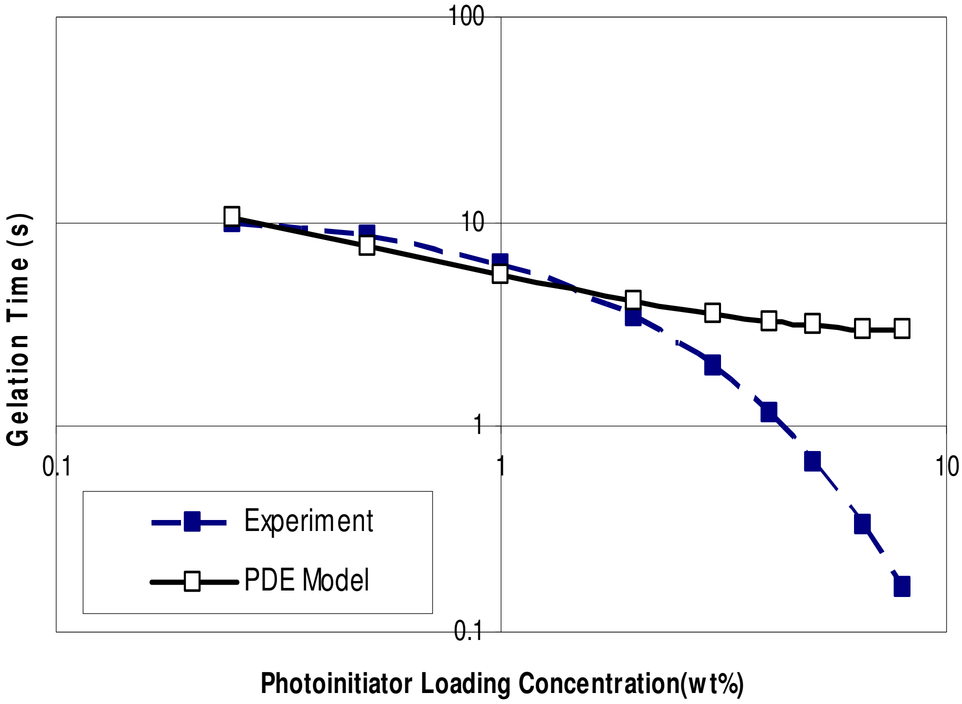

Figure 5.26: Effect of Photoinitiator Loading Concentration on the Gelation Time and Comparison of Experimental and PDE Model Results for Deoxygenated Photopolymerization of SR351

From Figures 5.25, 5.27, and 5.29, it can easily be seen that the experimental and simulation results agree both qualitatively and quantitatively. The experimental curves of the gelation time as a function of the photoinitiator loading concentration are all linear in plots with logarithmic scales on both axes and the associated simulations also produce very similar linear behavior.

Additionally, for the same photoinitiator loading concentrations the gelation time increases as the functionality of the monomers of the corresponding photopolymerizing resins decreases. The 1-D PDE simulations reproduce this linear behavior quite well and their predictions agree closely with the experimental measurements.

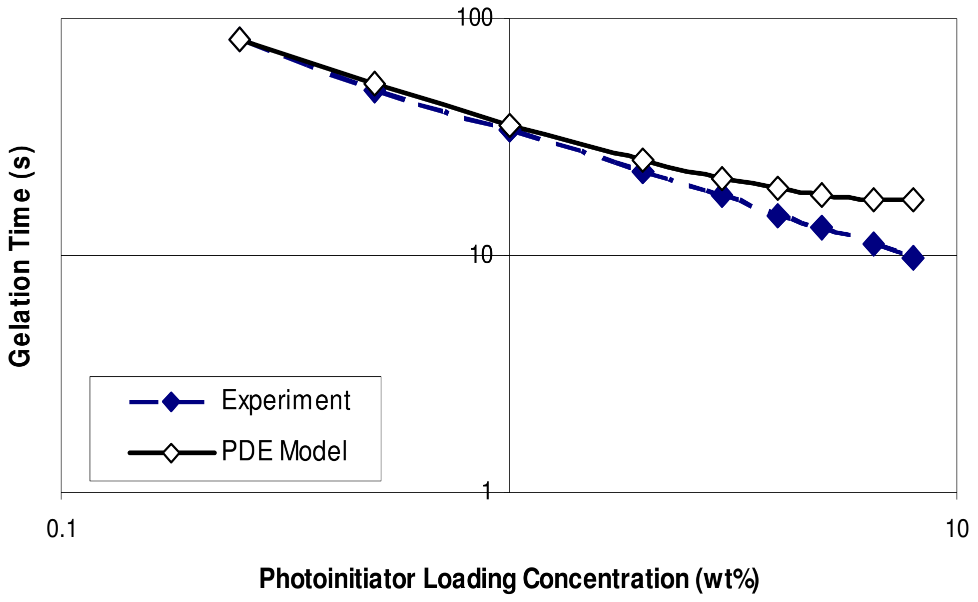

Figure 5.27: Effect of Photoinitiator Loading Concentration on the Gelation Time and Comparison of Experimental and PDE Model Results for Oxygenated Photopolymerization of SR272

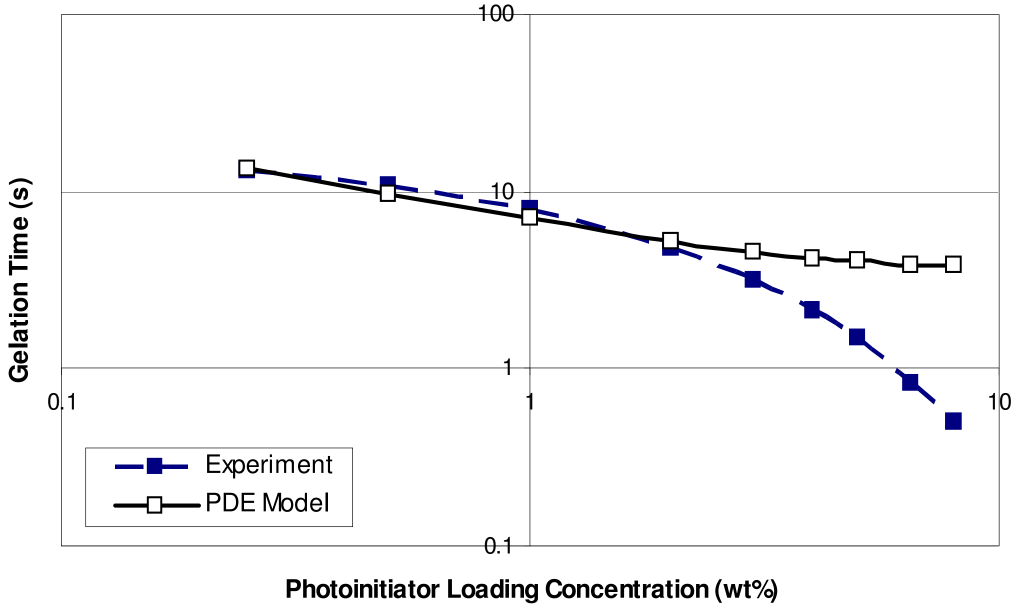

Figure 5.28: Effect of Photoinitiator Loading Concentration on the Gelation Time and Comparison of Experimental and PDE Model Results for Deoxygenated Photopolymerization of SR272

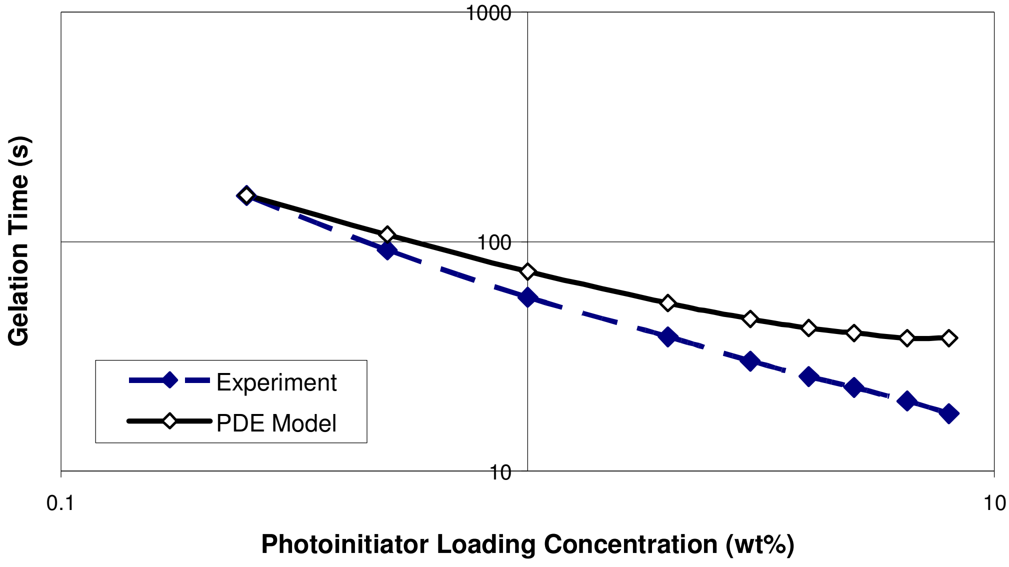

Figure 5.29: Effect of Photoinitiator Loading Concentration on the Gelation Time and Comparison of Experimental and PDE Model Results for Oxygenated Photopolymerization of SR256

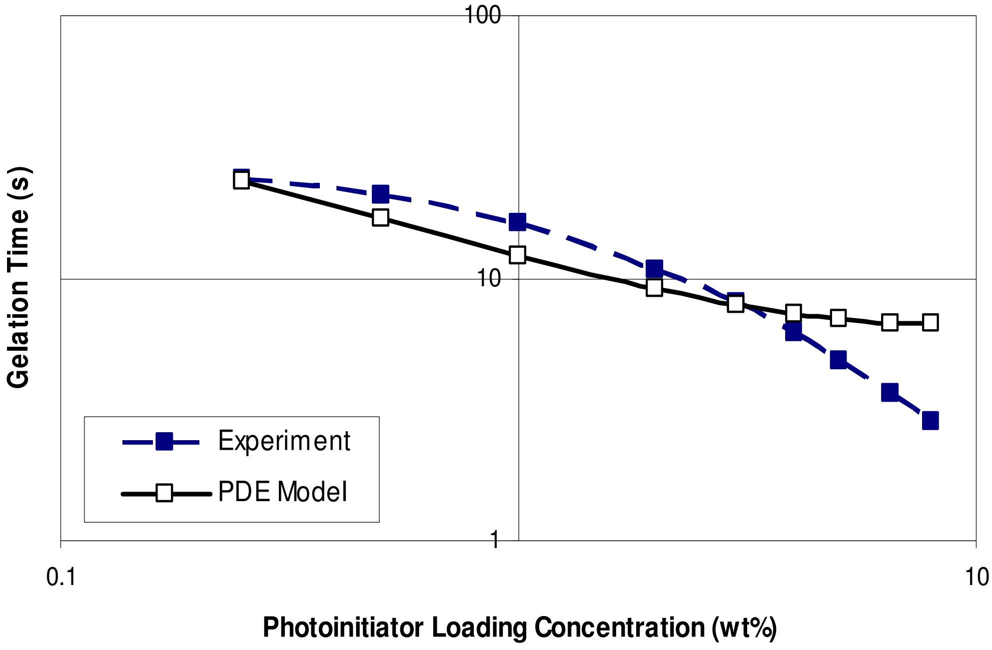

Figure 5.30: Effect of Photoinitiator Loading Concentration on the Gelation Time and Comparison of Experimental and PDE Model Results for Deoxygenated Photopolymerization of SR256

Experimental and theoretical studies relating the dependence of the gelation time on the photoinitiator loading concentration for SR351, SR272, and SR256 were then repeated in the absence of oxygen. The comparison of experimental measurements and simulation results for these resins are shown in Figures 5.26, 5.28, and 5.30. As can be seen in these three figures, there is considerable deviation between the predicted values obtained from the 1-D PDE model and the actual experimental results. These results clearly show that the 1-D PDE model is insufficient for the description of the photopolymerization process of the resins carried out in the absence of oxygen.

It is also clear that from Figures 5.26, 5.28, and 5.30 that the behavior of the experimental curves of the gelation time as a function of the photoinitiator loading concentration becomes increasingly nonlinear as the functionality of the monomers of the corresponding photopolymerizing resins increases. The increased functionality increases the number of residual double bonds on the growing polymeric molecules and contribute significantly to the formation of highly crosslinked polymer network. Therefore, the deviation between the simulation and experimental results is the greatest for SR494 resin. The gelation time again increases as the functionality of the monomers of the corresponding photopolymerizing resins decreases. The 1-D PDE model simulations also failed to predict this increasingly nonlinear behavior as a function of increasing monomer functionality.

5.3 Model Development for the Simulation of Deoxygenated Microrheology Measurements by using Ordinary Differential Equations

The failure of the deterministic 1-D PDE model in predicting the highly nonlinear behavior of the gelation time as function of the photoinitiator loading concentration in the absence of oxygen was the main motivation to search for other models for the simulation of photopolymerization process. For this purpose, another deterministic kinetic approach that involved solving a system of coupled first-order ordinary differential equations (ODEs) was employed. In what follows, this model is referred to as the ODE model.

This mathematical model is an adaptation of the method developed by Lovestead and Bowman to the photopolymerization process [20]. It is based on the basic photopolymerization reaction mechanisms of initiation, propagation, and termination. This model includes autoacceleration, autodeceleration, volume shrinkage, and reaction diffusion terms in both propagation and termination reaction constants. This model was further improved to include the chain-length dependence in termination reaction constant. The kinetic equations describe the time variation of the species concentrations such as the photoinitiator, monomer, polymeric radical, and dead polymer concentrations in the reaction volume.

The underlying elementary reaction mechanisms responsible for the variation of the species concentrations with time are discussed in Chapter 2. Applying the concept of mass balance to the reaction volume under these elementary reaction mechanisms leads to the reaction rate equations below for the photoinitiator molecule concentration, the double-bond-weighted monomer concentration, the concentrations of polymeric radicals and dead polymer molecules of every possible length. Thus, the rate equation for the photoinitiator concentration, [*S*], becomes

$$\frac{d[S]}{dt} = -2.303\varepsilon[S]A_{in}z \tag{5.26}$$

where A_{in} represents the amount of radiation on the surface of the resin at $t=0$, ε is the molar absorptivity coefficient in units of, and z is the depth of the resin. For the monomer concentration, [*M*], following rate equation can be written:

$$\frac{d[M]}{dt} = -k_p[M][R^*]_{tot} \tag{5.27}$$

where $[R^*]_{tot}$ represents the total concentration of polymeric radicals of all possible lengths in the reaction volume at any time, and k_p is the propagation constant given Eq. (2.24). The rate equation for the concentration of primary radicals, $[R_1^*]$, is then:

$$\begin{aligned}\frac{d[R_1^*]}{dt} = R_i - k_p[M][R_1^*] + k_{fp}[DP_1]\sum_{i=1}^{n}[R_i^*] - k_{fp}[R_1^*]\sum_{j=1}^{n} j[DP_j] \\ - k_{t,1,j}[R_1^*][R_j^*]\end{aligned} \tag{5.28}$$

where k_{fp} represents the polymer chain transfer kinetic constant, $[DP_j]$ is the concentration of dead polymer chain length of *j*, and $k_{t,i,j}$ is the chain-length-dependent termination kinetic constant for the termination of a polymer radical of length *i* by a polymer radical of length *j*. The mathematical expression for $k_{t,i,j}$ can be obtained from the modification of the termination kinetic constant given in Eq. (2.25) to include the chain-length dependence, as given below [32].

$$k_{t,i,j} = \frac{k_{t0}}{1+\left(\dfrac{1}{\dfrac{Rk_p[M]}{k_{t0}} + e^{-At(1/v_f - 1/v_{fct})}\dfrac{1}{2}\left(\dfrac{1}{i^{\gamma}}+\dfrac{1}{j^{\gamma}}\right)}\right)} \tag{5.29}$$

Similar to Eq. 4.28 for the concentration of polymeric radicals of length *i*, $[R_i^*]$, the rate equation can be written as:

$$\begin{aligned} \frac{d[R_i^*]}{dt} &= k_p[M]([R_{i-1}^*]-[R_i^*]) + k_{fp}i[DP_i]\sum_{j=1}^{\infty}[R_j^*] - k_{fp}[R_i^*]\sum_{j=1}^{\infty}j[DP_j], \quad \mathrm{i} \neq 1 \\ &\quad -\sum_{j=1}^{\infty}k_{t,i,j}[R_i^*][R_j^*] \end{aligned} \tag{5.30}$$

The rate equation for the concentration of dead polymers of length *i*, [*DP_i*], is given as:

$$\begin{aligned} \frac{d[DP_i]}{dt} &= k_{fp}[M][R_i^*] + k_{fp}\sum_{j=1}^{\infty}j[DP_j][R_i^*] - k_{fp}i[DP_i]\sum_{j=1}^{\infty}[R_j^*] \\ &\quad + k_{t,j,(i-j)}\sum_{j=1}^{i-1}[R_j^*][R_{(i-j)}^*] \end{aligned} \tag{5.31}$$

The ODE model described here is comprised of the coupled ordinary differential equations given in Eqs. (5.26)-(5.31). These equations are solved numerically by using an implementation of the 4th order Runga-Kutta method written in FORTRAN 90. The algorithm code of this program written for this study is given in Appendix D.

In applying the ODEs (Eqs. 5.26-5.31) to the SR494 resin composed of four functional monomers, it is assumed that the primary radical concentration, $[R_1^*]$, has one monomer, three double bonds, and one radical. The growing of primary radicals is assumed to take place in a chain-like fashion through the addition of monomers where only a single double bond on each added monomer is broken. The model assumes live and dead polymer molecules of every possible length are present in the reaction volume. The dead polymer concentration acts like a chain-transfer agent and helps the crosslinking of the growing polymeric molecules. Since the dead polymer concentration is used as a source for regenerating live polymers of every length, this mimics the crosslinking between polymer molecules.

The full ODE model requires the simultaneous solution of infinitely many coupled differential equations; obviously this is not feasible even with the supercomputers available today. To adequately describe the reaction volume, the size of the set of ODEs to be solved must be on the order of 10^5-10^6. Thus, some simplification of the full ODE model is required in order to make the problem computationally tractable. Thus, to reduce the number of ODEs and increase the computational efficiency, coarse graining approximations were used [101-103]. In the coarse graining approximation, not all of the concentrations of radicals of different chain lengths are treated independently; instead, the concentrations of certain sets of polymeric radicals are assumed to be equal and are thus governed by a single ODE. The size of these sets of equivalent radical concentrations varies as the chain length of the radicals increases. Thus, polymeric radicals with chain lengths less than 100 monomer units were represented by using a different ODE for each radical's concentration; that is the grain size was set to 1. For radicals with chain lengths between 101 and 600 monomer units, the grain size was set to 5. This meant that the concentrations of radicals with chain sizes between 101 and 105 monomer units were assumed to be equal and all of these radical concentrations were governed by a single ODE. In the end, the grain size was adjusted so that polymeric radicals with chain lengths up to 390600 monomer units could be described by a set of just 600 ODEs as given in Table 5.4.

Table 5.4: Grouping of The Polymeric Radical Chain Length for ODE Model Simulation

Polymeric Radical Chain Size	Number of Equations Grouped Together
1-100	1
101-600	5
601-3,100	25
3,101-15,600	125
15,601-78,100	625
78,100-390,600	3,125

5.3.1 Comparison of experimental, 1-D PDE and ODE model simulation results

The ODE model was solved to simulate the relation between the gelation time and photoinitiator loading concentration for the deoxygenated photopolymerization of multifunctional monomers. The relevant reaction parameters given in Tables 5.1, A.1-A.3 are used as input for solving the ODE model described by Eq. (5.26)-(5.31) above. From the simultaneous solutions of these coupled equations, the conversion defined by Eq. (5.32) below is calculated as a function of reaction time.

$$X(t) = \frac{[M]_0 - [M]_t}{[M]_0} \qquad \textbf{(5.32)}$$

The calculations were made for SR351, SR272, and SR256 resins for photoinitiator loading concentrations of 0.25%, 0.5%, 1.0%, 2.0%, 3.0%, 4.0%, 5.0%, 6.5%, and 8.0% by weight percentage. For SR494 resin, the calculations were repeated only for the lowest four photoinitiator loading concentrations. In Appendix E, the conversion time curves obtained from the ODE model for only 2% photoinitiator loading concentration for SR494, SR351, SR272, and SR256 are given as examples.

The gelation times corresponding to different photoinitiator loading concentrations were determined from simulated conversion time curves of 1-D PDE and ODE models for SR494, SR351, SR272, and SR256 resins and compared with experimental values as shown in Figures 5.31-5.34, respectively.

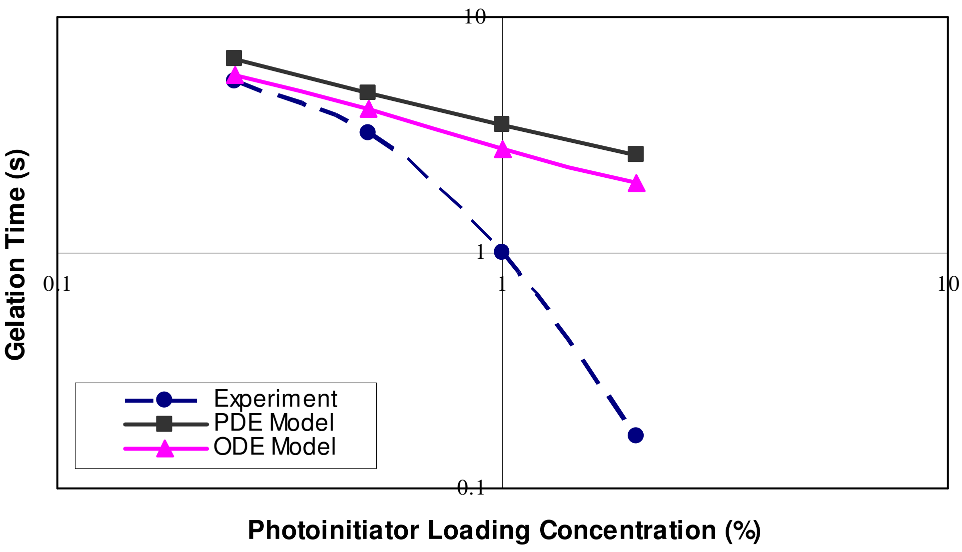

Figure 5.31: Effect of Photoinitiator Loading Concentration on the Gelation Time and Comparison of Experimental, PDE and ODE Models Results for Deoxygenated Photopolymerization of SR494

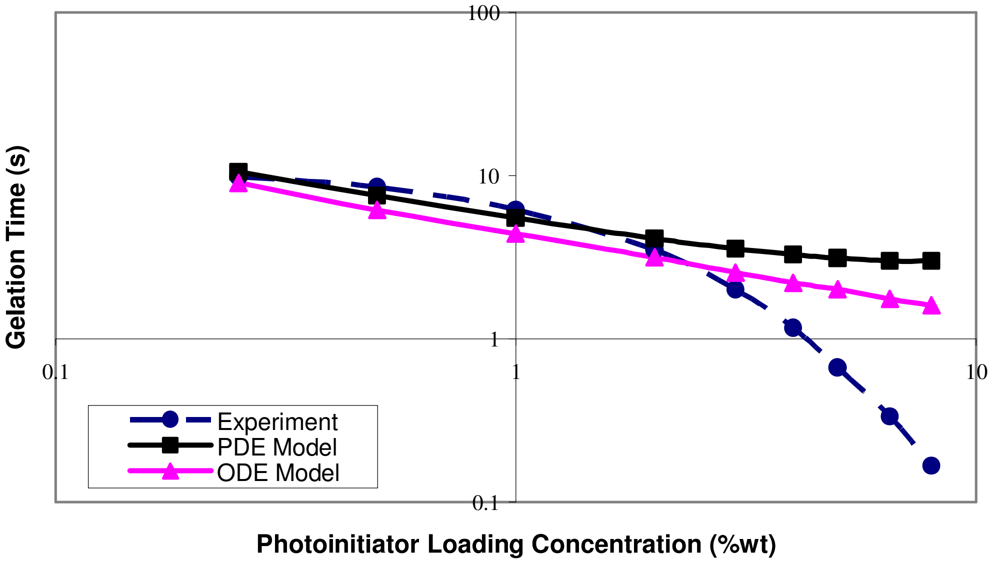

Figure 5.32: Effect of Photoinitiator Loading Concentration on the Gelation Time and Comparison of Experimental, PDE and ODE Models Results for Deoxygenated Photopolymerization of SR351

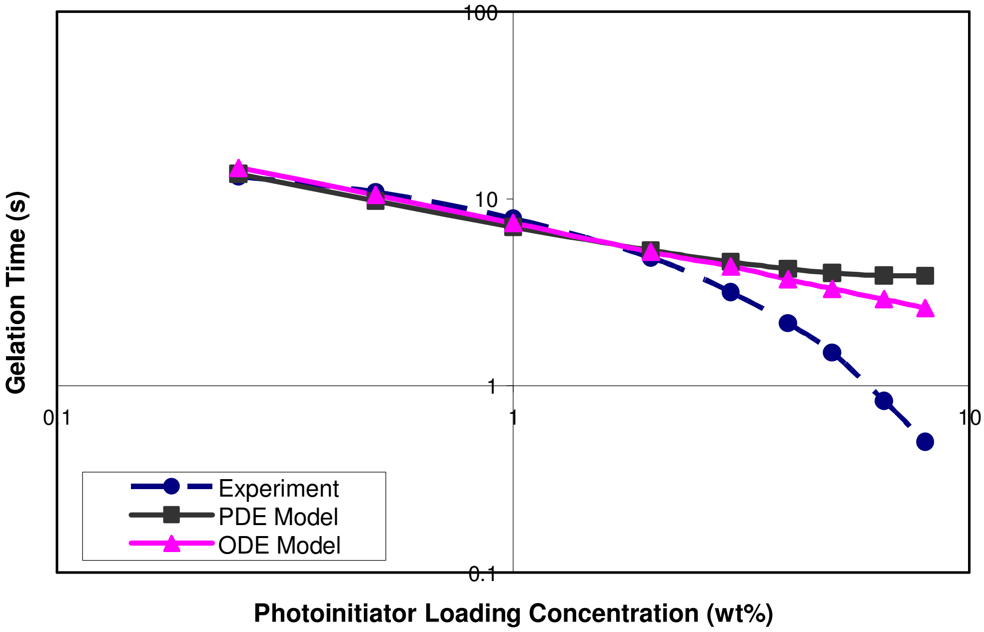

Figure 5.33: Effect of Photoinitiator Loading Concentration on the Gelation Time and Comparison of Experimental, PDE and ODE Models Results for Deoxygenated Photopolymerization of SR272

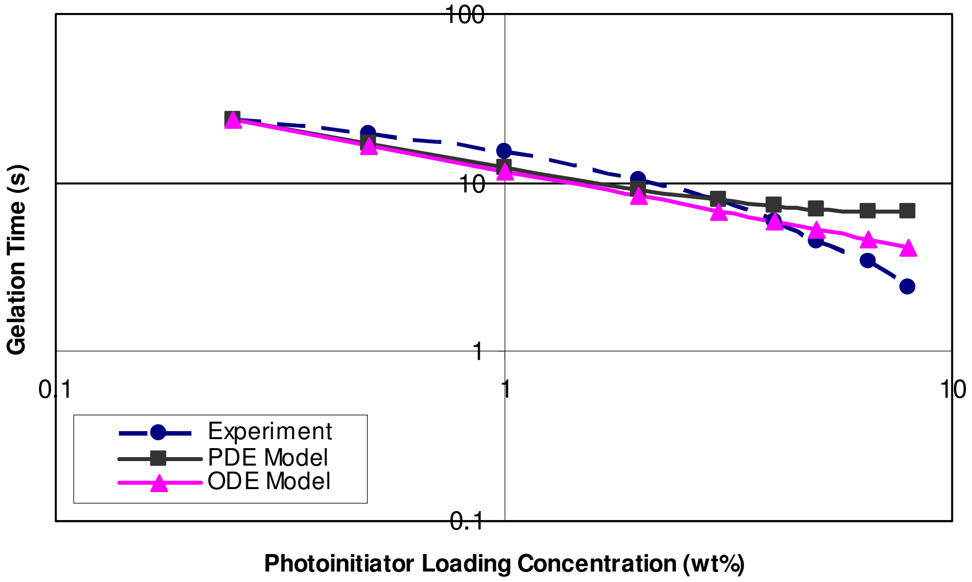

Figure 5.34: Effect of Photoinitiator Loading Concentration on the Gelation Time and Comparison of Experimental, PDE and ODE Models Results for Deoxygenated Photopolymerization of SR256

In this comparison 1-D PDE simulation and experimental gelation times corresponding to the values obtained at 60 μm UV light penetration depth, which is the half geometry used for gelation time simulations (Figure 5.17) and half depth of the sample chamber, is used. The upper solid curves with filled squares and triangles show the results of the 1-D PDE model and ODE model simulation of the deoxygenated photopolymerization process, respectively. The lower dashed curve with filled circles shows the experimental results for the deoxygenated photopolymerization process.

A similar linear dependence with somewhat different slopes is seen for the logarithmic plot of 1-D PDE and ODE models's predictions of the dependence of the gelation time on the photoinitiator loading concentration in the absence of oxygen inhibition. The results for experiments conducted in the absence of oxygen show that the deterministic 1-D PDE and ODE models was insufficient for the description of the behavior of photopolymerization process. While the experimental results showed pronounced nonlinear behavior in a logarithmic plot (Figures 5.31-5.34), the deterministic 1-D PDE and ODE models in contrast showed linear behavior.

5.4 Simulation of Deoxygenated Microrheology Measurements by Stochastic Monte Carlo Model

The considerable deviation between the actual experimental results and both the predictions of the deterministic 1-D PDE and ODE model in the absence of oxygen underscored the need for a new model that takes into account the noncontinuous, discrete nature of chemical reactions. For this purpose, a stochastic Monte Carlo model (SMCM), which is based on probabilistic approach, was developed to simulate these experimental data.

5.4.1 Stochastic Monte Carlo model

The traditional approach to chemical kinetics assumes the following preconditions:

1. The number of molecules of different species in the reaction volume can be represented by a continuous, single-valued function of time.

2. Chemical reactions can be regarded as a continuous rate process.

Using the above preconditions one can easily construct a set of coupled, first-order, ordinary differential equations for the concentration of each reacting species in terms of the concentrations of all others. These equations are called reaction rate equations. Solving these equations, with prescribed initial conditions, gives the concentration of each species in the reaction volume as a function of time. Although there are many important and useful applications of this deterministic approach to chemical kinetics in the literature one should be aware of its weakness as well [2, 3, 11, 20, 68-71]. The deterministic approach is based on the assumption that the time evolution of a chemically reacting system is both continuous and deterministic. However the time evolution of a chemically reacting system is not a continuous process, since the changes in the population numbers of various species in the system can obviously take place only by discrete integer amounts. Even if quantum effects are neglected and one assumes that molecules obey Newton's law of motion, it is impossible even in principle to predict the exact molecular population levels at some future time unless the positions and velocities of all molecules in the system are taken into account.

The time evolution of a chemically reacting system in many cases can be treated as a continuous and deterministic process to a high degree of accuracy. However, this deterministic approach becomes more difficult to apply and in some cases inapplicable for systems that involve complex macromolecules, long time scales, and interactions of several different molecule types. The free radical photopolymerization of multifunctional monomers is a highly nonlinear reaction and produces highly cross-linked networks. It is not possible to get adequate results from deterministic chemical kinetics for such nonlinear systems as observed in this study.

A powerful computational method was developed by Gillespie from premises which takes explicit account of the fact that the time evolution of spatially homogenous chemical system is a discrete and stochastic process [5, 104]. Gillespie named this method the Stochastic Simulation Algorithm (SSA).

In order to apply SSA to the simulation of a photopolymerization process, it will be assumed that the reaction mixture is spatially homogenous (well-mixed), where nonreactive collisions occur far more often than reactive collisions.

The SSA, describes the time evolution of an isothermal, well-mixed system of chemically reacting molecules contained in a fixed reaction volume of V. SSA can be applied to a variety of physical phenomena such as chemical reactions, diffusion, and radioactive decay. The common element in all these systems is their stochasticity, which arises from the inability to predict the either the order of events or which events will occur in a given time. In these systems, the variables describing the populations of different species as a function of time are random variables, the successive values of which are not independent from each other.

In brief and concise description of SSA, the reaction volume is assumed to contain molecules of N distinct chemical species S_i ($i = 1, 2, \ldots, N$) interacting via M reaction channels R_μ (μ=1, 2,…,M). The number of the species S_i, at any given time, t, in the reaction volume will be denoted by $X_i(t)$, thus, the main goal of SSA is to calculate the $X_i(t)$ values from their initial values $X_i(t_0)$ at initial time t_0. To achieve this goal, the following assumptions are made about the collision dynamics of the reaction volume [104]:

1. The overwhelming majority of the molecular collisions are elastic (nonreactive) collisions.
2. The dominant effect of nonreactive collisions is to separate the reactive collisions in time, thus making them occur essentially in a random manner.
3. The time evolution of the populations of the various species in the reaction volume takes place in thermal equilibrium.
4. The reaction volume is well-mixed or spatially homogenous for reactive collisions.

The stochastic formulation of chemical reaction kinetics is a direct consequence of the random manner in which reactive collisions occur in a system consisting of molecules in thermal equilibrium. Besides being an effective numerical algorithm, SSA is also a model for chemically reacting systems that takes into account the discreteness and finiteness of the molecular populations as a function of time as well as stochastic effects. SSA ignores the nonreactive molecular collisions, which if included in the molecular dynamics simulation would consume an overwhelming amount of the simulation time and computational effort; thus, by this approximation, SSA only explicitly treats reactions that change the interacting species number in the reaction volume. In addition, since SSA uses fewer modeling assumptions compared to deterministic ODEs, it is therefore closer to the models based on probabilistic approach.

The changes in the species populations are of course a consequence of the chemical reactions occurring among the species in the reaction volume. In a well-mixed reaction volume, each reaction channel R_μ is completely characterized by a propensity function a_μ as described by Gillespie [5, 104]. The propensity function a_μ can be calculated by using the stochastic reaction constants c_μ which characterizes a binary reaction R_μ taking place between a particular pair of chemical species in the reaction volume. This stochastic reaction constant is introduced into SSA by the following fundamental hypothesis [104]:

$$c_\mu \delta t = \begin{array}{l}\text{the average probability that a particular pair of molecules in} \\ \text{the reaction volume will react via the reaction channel } R_\mu \text{ in} \\ \text{the next small time interval } (\delta t)\end{array} \qquad \textbf{(5.33)}$$

This hypothesis was shown to be valid for any molecular system which is kept well-mixed either by direct stirring or by simply requiring that nonreactive molecular collisions occur much more frequently than reactive molecular collisions [5, 104].

To calculate the stochastic reaction constant for binary reactions, the following assumptions are made:

1. The molecules S_i are hard spheres with masses m_i and diameters d_i.
2. A collision between two molecules S_1 and S_2 will occur if the center-to-center distance between an S_1 and an S_2 molecule decreases to $d_{12}=(d_1+d_2)/2$.
3. In a small time interval δt the molecule S_1 sweeps out a collision volume, described by Eq. (5.34), relative to molecule S_2:

$$\Delta V_{coll} = \pi d_{12}^2 v_{12} \delta t \quad \textbf{(5.34)}$$

where v_{12} denotes the relative speed between the molecules S_1 and S_2.

4. If the center of molecule S_2 lies within ΔV_{coll}, then the molecules S_1 and S_2 will collide in the small time interval δt.

Using the assumptions above, the average probability that the molecular pair S_1 and S_2 will collide in the next small time interval δt can be expressed as:

$$\left\langle \frac{\delta V_{coll}}{V} \right\rangle = \frac{\pi d_{12}^2 \langle v_{12} \rangle}{V} \delta t \quad \textbf{(5.35)}$$

where $\langle v_{12} \rangle$ is the average relative velocity between S_1 and S_2 calculated using the Maxwell-Bolzmann velocity distribution at the temperature T of the reaction volume. From Eqs. (5.33) and (5.35), the average probability $\langle p_{12} \rangle$ of a collision in V at time t between $X_1(t)$ molecules of species S_1, and $X_2(t)$ molecules of species S_2 is then:

$$\langle p_{12} \rangle = \frac{\pi d_{12}^2 \langle v_{12} \rangle}{V} \quad \textbf{(5.36)}$$

$\langle p_{12} \rangle$ includes the probability of both reactive and nonreactive collisions. If every binary collision leads to an R_μ reaction, then the Eq. (5.36) corresponds exactly to the quantity c_μ in Eq. (5.33). Since, Eq. (5.36) includes also the probability of nonreactive collisions, it should be modified so that it corresponds to the probability of reactive collisions only. Reactive collisions will occur only when the kinetic energy due to the relative motion of the colliding molecules exceeds some prescribed value E_μ, the activation energy of the reaction. Thus, average probability of a reactive binary collision between S_1 and S_2 molecules can be obtained by multiplying the Eq. (5.36) by an Arrhenius factor as given in Eq. (5.37).

$$c_\mu = \frac{\pi d_{12}^2 \langle v_{12} \rangle}{V} e^{-E_\mu / kT} \quad \textbf{(5.37)}$$

SSA treats the reaction rates as reaction probabilities per unit time. The stochastic reaction constant c_μ can also be related to the more familiar reaction rate constant k_μ, which is used in the deterministic formulation of chemical kinetics. To illustrate this connection, the following binary reaction will be considered.

$$R_1: \qquad S_1 + S_2 \rightarrow S_3 \tag{5.38}$$

If, at time t, there are X_1 molecules of S_1 and X_2 molecules of S_2, then there will be X_1X_2 possible pairs, any one of which may react according to the R_1 reaction. If the average probability that a particular S_1S_2 pair reacts within the next infinitesimal time interval dt is c_1dt, then the probability of reaction R_1 occuring somewhere inside the reaction volume V in the next infinitesimal time interval $(t, t+dt)$ is $X_1X_2c_1dt$. From this result, it may be inferred that the average rate at which R_1 reaction occurs is $\langle X_1X_2\rangle c_1$, where the angular brackets denote an average taken over an ensemble of stochastically identical reacting systems. Dividing this result by the reaction volume gives the average reaction rate per unit volume. As shown in many basic chemical kinetics texts, the deterministic rate constant k_1 for the R_1 reaction may be defined by dividing this average reaction rate per unit volume by the product of the average densities of the reacting species S_1 and S_2. Hence, the equation connecting the stochastic (c_1) and deterministic rate constants (k_1) for R_1 reaction can be given as:

$$k_1 = \frac{\langle x_1x_2\rangle Vc_1}{\langle x_1\rangle\langle x_2\rangle} \tag{5.39}$$

Here x_1 and x_2 represent the molecular concentrations of reacting species S_1 and S_2, respectively. Since the deterministic approach does not distinguish the average of a product from the product of averages, Eq. (5.39) may easily be further simplified to Eq. (5.40) [104]:

$$k_1 = Vc_1 \tag{5.40}$$

Gillespie defined the propensity function a_μ for reaction pathway R_μ as the product of the stochastic rate constant c_μ and another factor h_μ, which is defined as the number of distinct molecular reactant combinations for the reaction R_μ present in the reaction volume at time *t* [104]. Then starting from the fundamental stochastic hypothesis given in Eq. (5.33), he developed a mathematical expression for the reaction probability density function $P(\tau,\mu)$ which is defined by:

$P(\tau,\mu)d\tau$ **=** probability at time *t* that the next reaction in the reaction volume *V* will occur in the infinitesimal time interval $(t+\tau, t+\tau+d\tau)$, and will be an R_μ reaction**.** **(5.41)**

Here *t* is the starting time of the reaction. In order to calculate $P(\tau,\mu)$ one must first define $P_0(\tau)$, which is the probability of having no interactions between time *t* and and $t+\tau$. Thus the probability for a reaction of the type R_μ will occur in the next infinitesimal time interval $(t+\tau, t+\tau+d\tau)$ can be given as:

$$\mathrm{P}(\tau,\mu)d\tau = \mathrm{P}_0(\tau)\mathrm{h}_\mu \mathrm{c}_\mu d\tau \qquad \textbf{(5.42)}$$

$P(\tau,\mu)$ is a joint probability density function of two variables namely, a continuous variable of τ $(0 \le \tau < \infty)$ (the waiting time) and discrete variable of μ $(\mu = 1,2,...,M)$. $P(\tau,\mu)$ can be related to a_μ by following equation.

$$P(\tau,\mu) = a_\mu e^{\left[-\sum_{\mu=1}^{M} a_\mu \tau\right]} \qquad \textbf{(5.43)}$$

where, as stated above,

$$a_\mu = h_\mu c_\mu \qquad \textbf{(5.44)}$$

is the propensity function. Integrating $P(\tau,\mu)$ of Eq. (5.43) from $0 \text{ to } \infty$ over waiting time τ gives:

$$\frac{a_\mu}{\sum_{i=1}^{M} a_\mu} = \text{total probability for an reaction occuring in time interval } (\tau,\infty) \qquad \textbf{(5.45)}$$

By answering the following questions, one can use Monte Carlo technique to make a simulation with the stochastic approach described by Eq. (5.43):

1. When will the next reaction occur?
2. What kind of reaction will it be?

Both of these questions must be answered probabilistically by generating a pair of random numbers, the probability density function of which is $P(\tau,\mu)$ given in Eq. (5.43). Such pairs of random numbers can easily be generated on any digital computer with a reliable “unit-interval uniform random number generator” function or subprogram. When the random number generating program is called, it calculates and returns two independent random numbers, r_1 and r_2 from the uniform distributions of numbers in the unit interval. If the unit-interval, uniform random number generator is called successively n times it will generate a set of n pseudorandom numbers. The random number generator needs an initial seed value. Every seed deterministically generates only one sequence of pseudorandom numbers. Thus, the seed must be changed to get a new sequence of pseudorandom numbers. The pseudorandom number generator should always be initialized with the user-chosen seed before it is called to generate any random numbers.

The variables τ and μ of the probability density functions $P(\tau,\mu)$ may now be determined by using the random numbers r_1 and r_2 as shown in Eqs. (5.46) and (5.47):

$$\tau = -\frac{\ln(r_1)}{a_{tot}} \qquad \textbf{(5.46)}$$

and

$$\sum_{i=1}^{j-1} a_i \leq r_2 a_{tot} < \sum_{i=1}^{j} a_i \tag{5.47}$$

where

$$a_{tot} = \sum_{\iota=1}^{M} a_{\mu} \tag{5.48}$$

Gillespie [104] gives a rigorous proof that the pair (τ, μ) determined according to Eqs. (5.43) and (5.45) may be regarded as having been drawn from the set of random pairs whose probability density function is $P(\tau, \mu)$ of Eq. (5.43). Eq. (5.45) determines which reaction will occur in the next infinitesimal time interval $d\tau$ following the waiting time τ.

5.4.2 Application of stochastic Monte Carlo model to photopolymerization process

In order to apply SMCM to photopolymerization process an algorithm in FORTRAN 90 was written for this study and it is given in Appendix F. In developing this algorithm the following concise explanations were considered. In the reaction volume, at any time, there are a number of competing reaction pathways that can be followed. Furthermore, the number and identities of the species in the reacting volume change as a function of time. Because of this, the number of possible reaction pathways likewise changes as a function of time. But for a given waiting time τ, although it is not known deterministically which particular pathway will be followed, the stochastic simulation method used in this study assumes that one of these possible reactions will definitely occur during the next infinitesimal time interval $d\tau$ following the waiting time τ. That is, the reaction does not start until the end of waiting time τ and it goes to completion within the next infinitesimal time interval $d\tau$ following the waiting time. Since there is no deterministic way for predicting which reaction path will be followed, the model employed here uses two generated pseudorandom numbers r_1 and r_2. Once r_1 and r_2 are determined, the waiting time τ and then the reaction pathway that will be followed in the next infinitesimal time interval $d\tau$ can be determined by solving Eqs. (5.46) and (5.47).

Once τ is calculated from Eq. (5.46), the reaction time is updated. The index of the reaction that will take place is determined from the inequality given in Eq. (5.47). Then, according to the result of this reaction, the reactant species number as well as the product species number are updated accordingly along with their double bond and radical numbers in this model. For example, if the reaction pathway chosen is represented by Eq. (5.38), then the species number of the product S_3 would be increased by one and the species number of the two reactants S_1 and S_2 would be decreased each by one. If no S_3 molecules existed before this reaction took place, S_3 would be added to the reaction volume. Similarly, if the reaction used up all of one or both of the reactant species S_1 and S_2, these would be removed from the reaction volume.

The propensities a_μ for all the reactions possible within a cycle are calculated based on the number of particular reaction pathways that could occur between the existing reactants in reaction volume. These propensities are used in Eqs. (5.46)-(5.48) to determine the waiting time and the index of the reaction that will occur following the waiting time. For instance, the propensity, a_μ, for the reaction shown in Eq. (5.38) is calculated by multiplying the number of unique S_1- S_2 pairs in the reaction volume with the stochastic rate constant, c_μ, given by Eq. (5.37).

If a binary reaction involves two molecules of the same type S_1, then the number of unique reactant pairs is $X_1(X_1 - 1)/2$, where X_1 is the species number of S_1, so that double counting is avoided.

In a primary cyclization reaction, a radical on a molecule attacks a double bond within the same molecule. The number of unique ways that this type of interaction may take place in a molecule is given by the product of its number of bonds and its number of radicals. Therefore, the propensity for a primary cyclization reaction is obtained by multiplying this number of radical-double bond combinations by the species number of the molecule undergoing primary cyclization. Because the propensity of primary cyclization is directly proportional to the number of double bonds in a polymeric radical, it will be increasingly important for resins composed of monomers with more functional units.

Because of the time dependence of both the number of species and the possible number of reaction pathways among these species, at the beginning of each reaction cycle, the propensities are recalculated for all reactant species within the reaction volume. To determine the waiting time for the next reaction and which reaction will occur within this updated new reaction volume, another pair of pseudorandom numbers r_1 and r_2 are generated and the whole simulation cycle is repeated until either there is no reaction pathway remaining or the simulation time expires.

Photon absorption has been shown to be a slow process relative to the time scale of polymer propagation and termination reactions [101, 105]. Thus, an exponential decay formula is used to determine when one photoinitiator molecule decays to two photoinitatior radicals. These photoinitiators then are assumed to attack instantaneously on a functional group to form radicals. If the function groups are on a monomer then the radicals formed are called primary radicals. At the beginning of the photopolymerization reaction, the process starts with only two primary radicals. This corresponds to the fact that one photoinitiator molecule is decomposed prior to the start of the photopolymerization reaction. It is assumed that the photopolymerization reaction actually starts as soon as the light photon is absorbed by one of photoinitiator molecules mixed into the resin.

At the beginning of photopolymerization simulation, the time is set to the elapsed time for a single photoinitiator molecule to decompose into two photoinitiator radicals upon photon absorption. This is because the attack of the photoinitiator radicals on monomers or any other functional groups in the reaction volume is assumed to be instantaneous.

As soon as the reaction time is increased by the waiting time τ, the program checks whether sufficient time has elapsed for one or more photoinitiator molecules to absorb photons and decompose. The probable number of photoinitiators that will have decomposed since the last time a photoinitiator molecule absorbed a photon and decomposed into two photoinitiator radicals, Δn, is calculated from

$$\Delta n = N_{S0}\left[e^{-k_i t_1} - e^{-k_i t_2}\right] \qquad \textbf{(5.49)}$$

Where N_{S0} is the initial number of photoinitiators, k_i is the initiation rate constant, t_1 is the time when the last initiation occurred and t_2 is equal to the time when the last reaction occurred, *t*, plus the current waiting time τ. Note that even though the same symbol τ is used to represent the waiting time for each iteration, its actual value in every reaction cycle is randomly chosen using Eq. (5.46). If $\Delta n \geq 1$, then t_1 is set to the value of t_2. In this manner, t_1 is reset in this manner so that, for future reaction cycles, the next time an photoinitiator absorbs a photon Eq. (5.49) will again produce a value $\Delta n \geq 1$. If $\Delta n \leq 1$, t_1 is left unchanged which implies that no new photoinitiators decomposed during the current reaction cycle.

In the initial reaction cycle, there are only monomers and photoinitiator molecules present in resin; therefore, the photoinitiator radicals can only interact with monomers. In later reaction cycles, however, there are other reactive species present in the resin with which the photoinitiator radicals can interact. Thus, after the initial reaction cycle, whenever Eq (5.49) indicates that one or more photoinitiator molecules have decomposed, the program generates random numbers to determine with which species present in the resin the resulting photoinitiator radicals will interact. The number of random numbers generated is twice the number of photoinitiator molecules that have decomposed. These random numbers are generated in a way that allows these newly created photoinitiator radicals to interact among themselves, however the probability of this happening is very small. After all the photoinitiator radicals interact with the species present in the reaction volume then the next photopolymerization cycle starts.

The time to decompose one photoinitiator molecule was calculated from the following rate equation.

$$\frac{dN_S}{dt} = -k_i N_S \tag{5.50}$$

where N_S is the total number of photoinitiator molecules at any time *t* in the reaction volume and k_i is the initiation rate constant. Representing the initial number of photoinitiator molecules by N_{S0}, the clock time, *t*, required to allow one photoinitiator molecule to decompose can easily be obtained from the solution Eq. (5.51).

$$t = \left(-\frac{1}{k_i} \right) \ln\left(\frac{N_{S0} - 1}{N_{S0}}\right) \tag{5.51}$$

Two free radicals are assumed to undergo propagation reactions instantaneously to form two primary radicals of equal reactivities. So, the first reaction cycle starts with two primary radicals at the this clock time *t*.

For the simulation algorithm of SMCM, the number of new species formed and the number of present species consumed during any reaction, a 3-D array is introduced. The indexes of this 3-D array are chosen to represent the monomer, double bond, and radical numbers of the species present in the reaction volume and it is updated as the reaction proceeds as will be discussed below.

When two molecules interact to form a new species, the species numbers of the two reactant molecules in 3-D array are immediately decreased by 1 to reflect their consumption during the reaction. Then, at the end of each reaction cycle, the 3-D array is updated to reflect the newly formed product species. If the species formed is present in the reaction volume, only the species number is updated. If the species was not present before in the reaction volume, an entry for this species is added to the 3-D array. Then all possible reactions among the various species in the reaction volume are recalculated and the process repeats.

Both for reaction times as well as for the type of reaction takes place among all possible reactions are determined using two random numbers generated by unix system's pseudorandom number generator. The reaction time and the index of the reaction were calculated from Eqs. (5.47) and (5.48), respectively. The first random number is used to set the time increment that passed between the end of the last reaction and start of this reaction. The second random number is used to determine which reaction pathway is chosen. Both of these processes comprise the SMCM described above.

5.4.3 Conversion of deterministic rate constants to stochastic rate constants

For the simulation of deoxygenated microrheology measurements by SMCM, both chain-length-independent and chain-length-dependent propagation and termination rate constants were used. For chain length independent simulation the propagation and termination rate constants given in Eq (2.24) and Eq (2.25) were used. To incorporate chain length dependence in the propagation and termination rate constants Eq. (5.52)-(5.55) were considered.

The chain length dependence of the propagation rate coefficient given by Smith and Russel is as follows [106]:

$$k_p^i = k_p^\infty \left\{ 1 + C_1 \exp\left(\frac{-\ln 2}{i_{1/2}} (i-1) \right) \right\} \tag{5.52}$$

where k_p^i represents the propagation rate coefficient for an i-meric radical adding to a monomeric molecule.

The termination rate constants are taken to be different according to the number of monomers present in the terminating polymeric radicals. Using the nomenclature of Smith, Russel, and Heuts, the self-termination rate —that is when two of the same polymeric radicals collide together and terminate— of a polymeric radical of length i (denoted by $k_t^{i,i}$) can be calculated from the monomeric radical self-termination rate (denoted by $k_t^{1,1}$) by one of two formulae depending on the chain length [106, 107]:

$$k_t^{i,i} = k_t^{1,1} i^{-e_S}, \qquad i \le i_c \tag{5.53}$$

$$k_t^{i,i} = k_t^{1,1} i_c^{-e_S + e_L} i^{-e_L}, \qquad i > i_c \tag{5.54}$$

Here i_c is termed a critical chain length—the dividing point between "short" and "long" polymeric radical chains—and is taken to be 100, e_S is the scaling exponent for short chain lengths and is taken to be 0.5, and e_L is the scaling exponent for long chain lengths and is taken to be 0.16. These scaling exponents as well as the value for the critical chain length are taken from Smith and Russell [106, 107]. The $k_t^{1,1}$ are Arrhenius rate constants of the form of Eq. (2.27).

To calculate the bimolecular deterministic termination rate constant $k_t^{i,j}$ between two species of different number of monomers *i* and *j*, the formula below was used:

$$k_t^{i,j} = \sqrt{k_t^{i,i} k_t^{j,j}} \tag{5.55}$$

This formula is known as the geometric mean model for the cross-termination rate coefficients.

All of the deterministic rate constants above are for bimolecular reactions and are thus in units of (m^3/mol·s). However, the unit of a bimolecular stochastic rate constant is (1/s·molecules). Thus, converting a deterministic bimolecular rate constant (k^D) to a stochastic bimolecular rate constant (k^S) is accomplished by dividing by a factor of Avogadro's number multiplied by the reaction volume:

$$k^S = \frac{k^D}{N_{AV} V} \tag{5.56}$$

The initial reaction volume V_x of a species *X* is calculated by dividing the number of molecules of that species N_x to the initial concentration of the species multiplied by Avogadro's number (N_{AV}):

$$V_X = \frac{N_X}{N_{AV}[X]} \tag{5.57}$$

The initial concentration of a molecule or radical is calculated by dividing its density ρ_x and its molecular weight (MW_x):

$$[X] = \frac{\rho_X}{MW_X} \tag{5.58}$$

At the beginning, the reaction volume consists of the monomer and the photoinitiator molecules. Conceptually, the total reaction volume can be taken as the sum of the volumes for each of these components:

$$V = V_S + V_M \tag{5.59}$$

or

$$V = \frac{N_{S0}}{[S]_0 N_{AV}} + \frac{N_{M0}}{[M]_0 N_{AV}} = \frac{[M]_0 N_{S0} + [S]_0 N_{M0}}{[S]_0 [M]_0 N_{AV}} \tag{5.60}$$

where N_{S0} and N_{M0} represent the initial number of photoinitiators and monomers, respectively; $[S]_0$ and $[M]_0$ represent the initial concentration of the photoinitiator and monomer molucules. Substituting Eq. (5.60) into Eq. (5.56) gives:

$$k^S = \frac{[S]_0 [M]_0 k^D}{[M]_0 N_{S0} + [S]_0 N_{M0}} \tag{5.61}$$

The initial number of initiator molecules can be calculated easily from Eq. (5.62) corresponding to a given photoinitiator weight percent.

$$N_{S0} = \frac{MW_S MW_M N_{tot}}{MW_S (1 - MW_S) + MW_S MW_M} \tag{5.62}$$

where MW_S and MW_M are the molecular weights of photoinitiators and monomers respectively and N_{tot} is the some of the initial number of photoinitiators and monomers present in the reaction volume.

5.4.4 Comparison of stochastic Monte Carlo simulations and experimental results

The SMCM simulations were first performed for binary propagation and termination reactions using chain-length-independent rate constants, then the simulations were repeated by using chain-length-dependent rate constants and allowing primary cyclization reactions. The calculations were done for four different resins of SR494, SR351, SR272, and SR256. The calculated conversion values for these resins as a function of reaction times were plotted and given in Appendix G (Figures G.1-G.4) for a set of different photoinitiator loading concentrations of 0.25%, 0.50%, 1.0%, 2.0%, 3.0%, 4.0%, 5.0%, 6.5%, and 8.0% by weight percentage.

As can be seen from Figures G.1-G.4, the double bond conversion becomes faster as the photoinitiator loading concentration increases for all the resins as expected. The effect of photoinitiator loading concentration on the speed of the photopolymerization process is stronger for the low photoinitator loading concentrations of 0.25%, 0.50%, and 1.0%. Above 1.0%, though, increasing the photoinitiator loading concentration has a much less pronounced effect on the speed of the photopolymerization.

From simulated conversion time curves critical gelation times corresponding to Flory predictions are determined and are plotted as a function of photoinitiator loading concentrations in Figures 5.35-5.38. The simulation data in Figures 5.35-5.38 were obtained with ten different runs with different seed values used to generate the pseudorandom numbers; the plotted gelation times are an arithmetic average of the gelation times predicted by the ten individual runs.

The results from the SMCM using chain-length-independent rate constants for both propagation and termination reactions displayed the same nonlinear behavior as the experimental results showed for the predictions of gelation times for lower photoinitiator loading concentrations (Figures 5.35-5.38). At higher photoinitiator loading concentrations, however, the predictions deviated somewhat from the experimental results. To remedy this, the model was altered to include the effect of the chain lenght dependence in propagation and termination rate constants as given in Eqs. (5.52)-(5.55) and to allow polymeric radicals to undergo primary cyclization reactions.

Cyclization is a unimolecular reaction; thus, its overall reaction rate is proportional to the species population. Propagation and termination, though, are bimolecular reactions; thus, their overall reaction rate is proportional to the product of the populations of the two reactant species. Therefore, as the reaction proceeds, and the population of species that can react via propagation and termination pathways grows, the reaction rates for propagation and termination quickly dominate the cyclization reaction rates because of the quadratic versus linear growth in the respective propensities. For this reason as mentioned above, the overall cyclization propensities were multiplied by an additional enhancement factor of ten to make these pathways more competitive with the propagation and termination pathways. It was observed that the exact value of this multiplicative enhancement factor for cyclization is not critical. For a value of 20, it noticeably makes the overall gel point versus photoinitiator loading concentration curve nonlinear, in agreement with experimental results. Increasing the value to 50, 100, or several hundred does make this nonlinearity somewhat more prominent, but does not affect the overall trend. The cyclization rate constant for a polymeric radical was assumed to be the same as the product of its propagation rate constant and this enhancement factor. In calculating the probabilities for the cyclization reactions, this enhancement factor was used as described by Wen et al. [105].

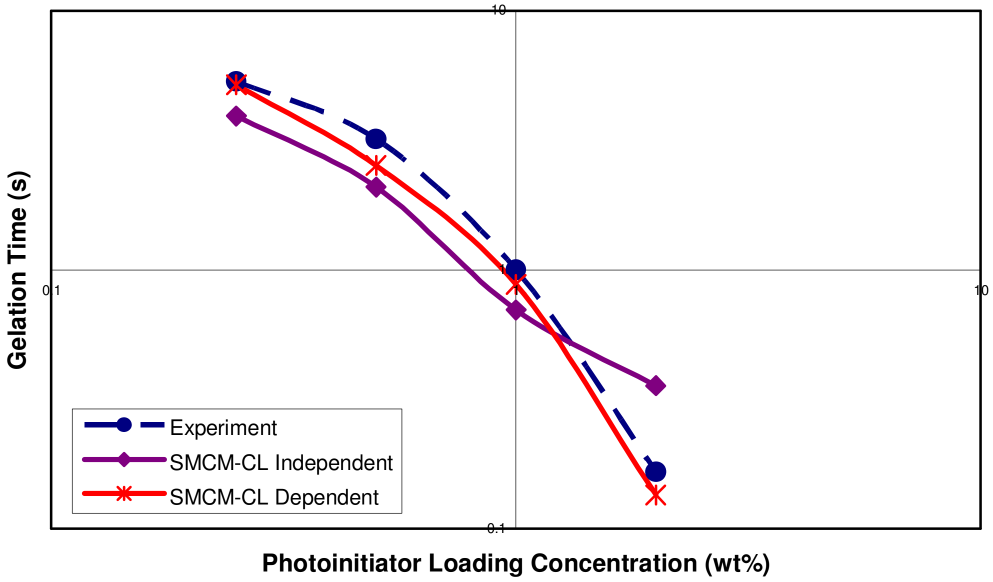

Figure 5.35: Effect of Photoinitiator Loading Concentration on the Gelation Time and Comparison of Experimental and SMCM Results for Deoxygenated Photopolymerization of SR494

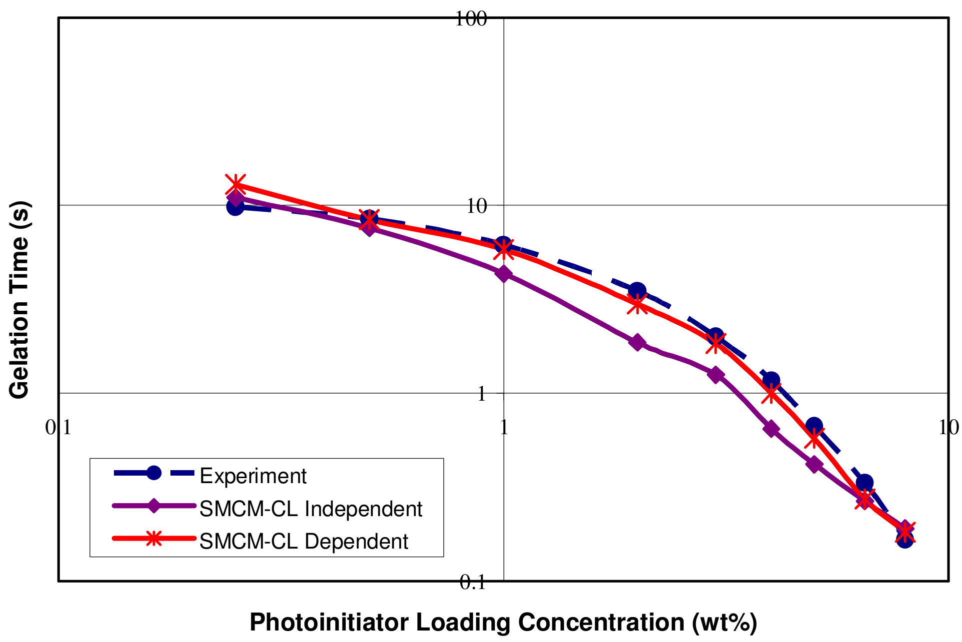

Figure 5.36: Effect of Photoinitiator Loading Concentration on the Gelation Time and Comparison of Experimental and SMCM Results for Deoxygenated Photopolymerization of SR351

The results of the SMCM simulations including chain-lenght dependence and primary cyclization reactions are also shown in Figures 5.35-5.38. As can be seen from these figures, using the chain-lenght dependent propagation and termination rate constants and allowing primary cyclization significantly increased the agreement between the simulation and experimental results. The Figures 5.35-5.38 show that the nonlinear dependence of the gelation time on the photoinitiator loading concentrations persist for every cases even for the photopolymerization of resin SR256 composed of monofunctional monomers.

The relatively good agreement between experimental results and the predictions of the current SMCM based on the SSA is mostly attributed to the fact that the time evolution of the photopolymerization process is treated probabilistically rather than deterministically. The rate constants used in the current stochastic approach are viewed as reaction probabilities rather than reaction rates.

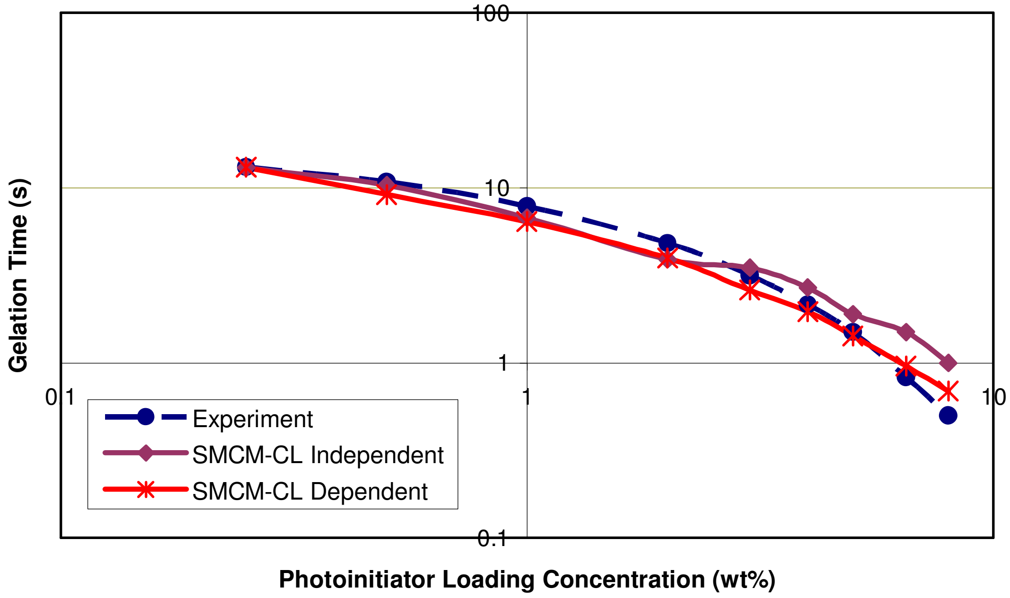

Figure 5.37: Effect of Photoinitiator Loading Concentration on the Gelation Time and Comparison of Experimental and SMCM Results for Deoxygenated Photopolymerization of SR272

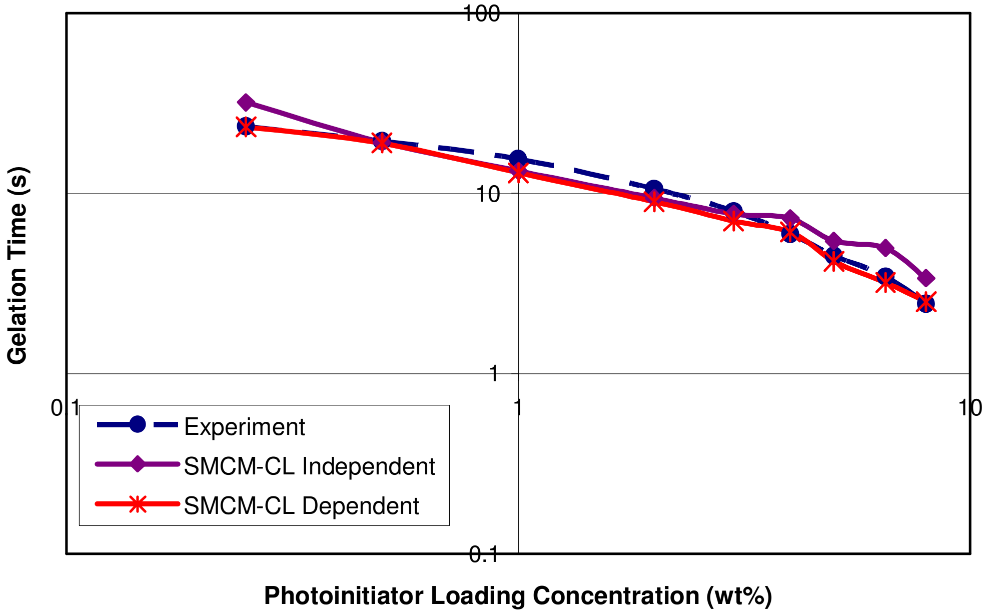

Figure 5.38: Effect of Photoinitiator Loading Concentration on the Gelation Time and Comparison of Experimental and SMCM Results for Deoxygenated Photopolymerization of SR256

Although the ampirical parameters used in the current stochastic simulations determined for methyl methacrylate system, using these for acrylate photopolymerization greatly improved the agreement between the simulation predictions and experimental results in this study [106].

5.4.5 Comparison of the deterministic (1-D PDE and ODE) and stochastic simulation results

Figures 5.39-5.42 compares both experimental and all simulation results for the deoxygenated photopolymerization of SR494, SR351, SR272, and SR256 resins used in this study. In Figures 5.39-5.42, the dashed line with circles represents the experimental data, the solid line with squares represents the results of the deterministic 1-D PDE model, and the solid line with triangles represents the results of the deterministic ODE model. Additionally the solid lines with astrices and diamonds represent the results of two sets of calculations using the SMCM based on the SSA; the line with astrices is from simulations that included chain length dependence in the stochastic rate constants and allowed primary cyclization reactions, the line with diamonds is for simulations that excluded both of these effects.

The dependence of the gelation times on the photoinitiator loading concentrations predicted by both the deterministic 1-D PDE and ODE models appears to be linear in this logarithmic scale. On the other hand, both sets of SMCM simulations predict at least the qualitatively correct behavior for this dependence. As can be seen, the stochastic model agrees far better with experiment than the other two deterministic models for SR494, SR351, SR272, and SR256 resins (Figures 5.39-5.42).

As can be seen from Figures 5.39-5.42, for all resins investigated in this study as the photoinitiator loading concentration increases, the stochastic model’s predictions agree with the trend of the experimental measurements. In contrast, with the deterministic 1-D PDE and ODE models the agreement worsens as the photoinitiator loading concentration increases.

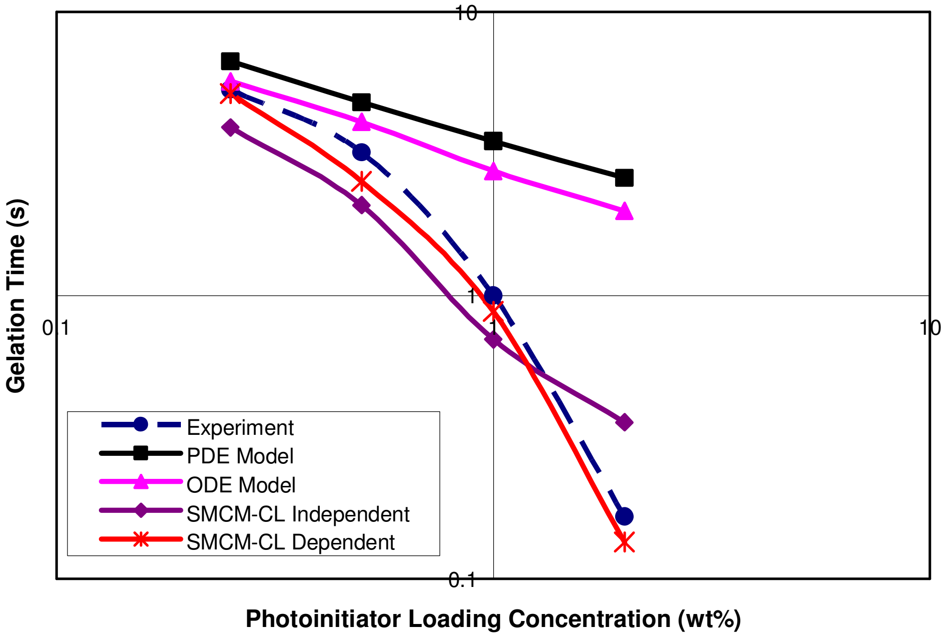

Figure 5.39: Comparison of Experimental, Deterministic and Stochastic Models Results for Deoxygenated Photopolymerization of SR494

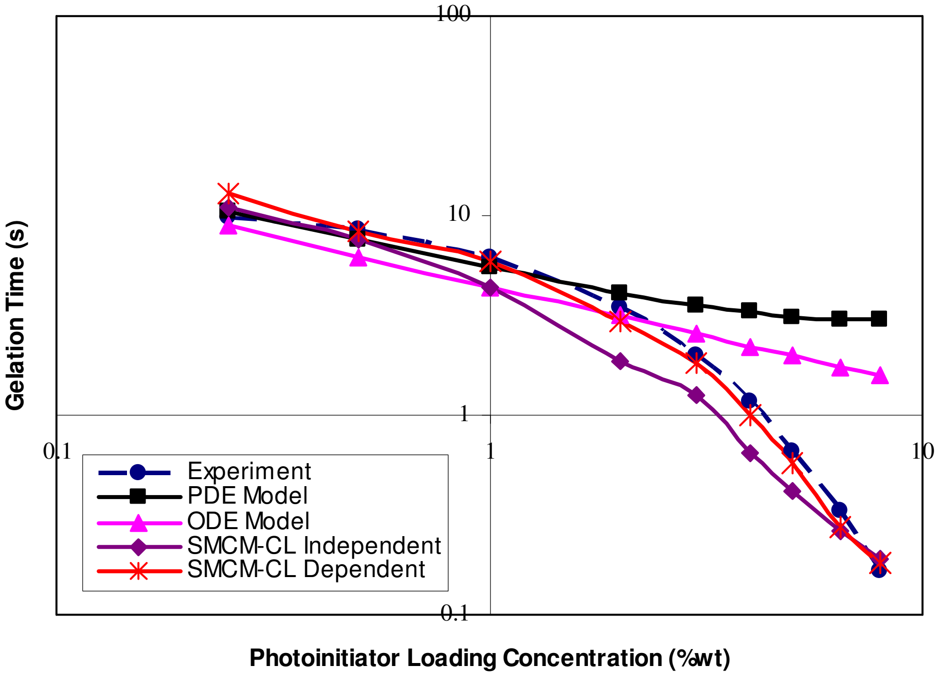

Figure 5.40: Comparison of Experimental, Deterministic and Stochastic Models Results for Deoxygenated Photopolymerization of SR351

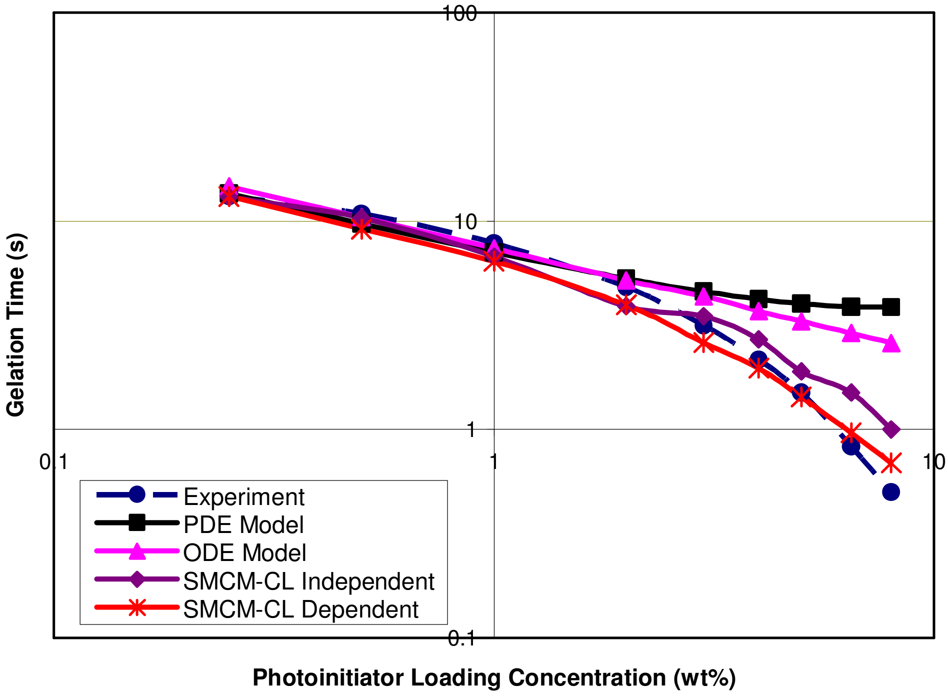

Figure 5.41: Comparison of Experimental, Deterministic and Stochastic Models Results for Deoxygenated Photopolymerization of SR272

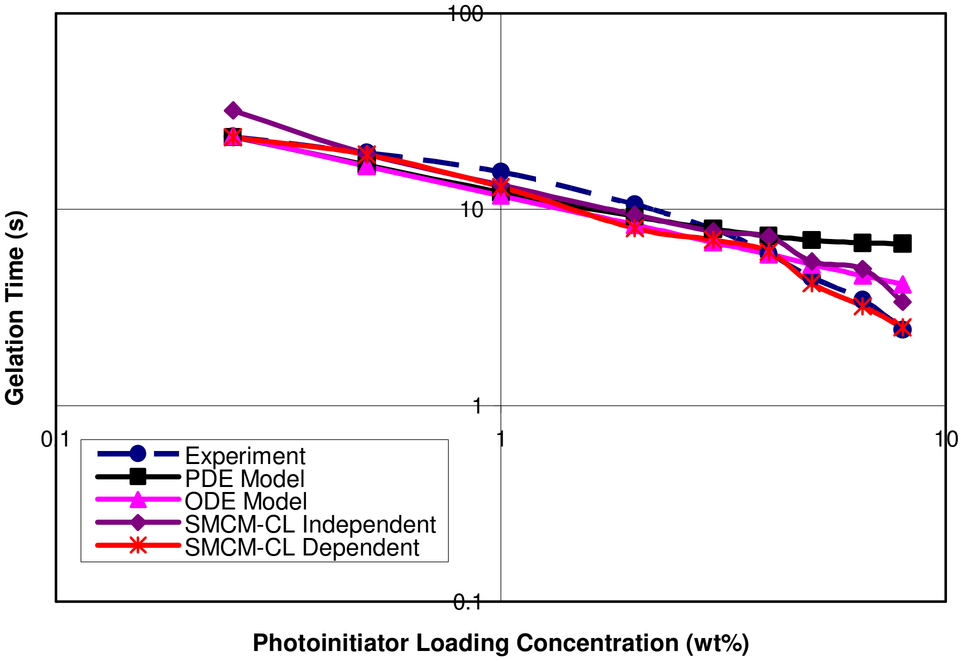

Figure 5.42: Comparison of Experimental, Deterministic and Stochastic Models Results for Deoxygenated Photopolymerization of SR256

The stochastic rate constants are determined by dividing the corresponding deterministic rate constants by the reaction volume; it is difficult, however, to measure the reaction volume accurately. This may account for some of the discrepancies between the current stochastic model's predictions and the experimental results.

The overall qualitative agreement between experiment and the deterministic 1-D PDE and ODE model simulation results is much better for SR351, SR272, and SR256 resins than for SR494 at lower photoinitiator loading concentrations (Figures 5.39-5.42). The nonlinear dependence of the gelation time on the photoinitiator loading concentration somewhat decreases as the functionality of monomers decreases. This explains the increase in the qualitative agreement of the simulations and the experimental measurements as a function of decreasing monomer functionality. However, as can be seen in Figures 5.39-5.42, the stochastic models do capture the nonlinear character of the photopolymerization process in every cases.

For SR351, SR272, and SR256 resins the gelation time values predicted by the deterministic 1-D PDE and ODE models decrease with the increasing photoinitiator loading concentrations up to the value of 4% by weight and then levels off and stays almost constant regardless of the increase in the photoinitiator loading concentration.

Thus, the deterministic 1-D PDE and ODE models compare well with the experimental results for the three lowest photoinitiator loading concentrations but fails to follow the experimental profile for higher concentrations. The SMCM simulation with chain-length independent rate constants and which excludes primary cyclization reactions displays similar nonlinear behavior as the experimental data, but the deviations from experiment become increasingly significant as the photoinitiator loading concentration inreases. The SMCM simulation with chain-length dependent rate constants and which permits primary cyclization reactions follow the experimental profile closely; it performs particularly well for lower photoinitiator loading concentrations, and qualitatively follows the experimental trend even at the highest photoinitiator loading concentrations.

The nonlinear dependence of gelation time on the photoinitiator loading concentration for SR256 resin is not as prominent as for higher multifunctional monomers; it occurs only for those reactions with the highest photoinitiator loading concentrations (Figure 5.42). Due to the decreasing nonlinearity in the experimental data for SR256, the curves for the linear deterministic 1-D PDE and ODE simulations agree reasonably with the experimental curve until the highest photoinitiator loading concentration values; and, even for the high photoinitiator loading concentration values, the deviations between the 1-D PDE and ODE simulations and experiment are relatively small.

Although the deterministic 1-D PDE and ODE models developed in this study do not accurately predict the nonlinear dependence of the gelation time on both the photoinitiator loading concentration and the functionality of the monomers in the absence of oxygen, the literature is full of successful applications of the deterministic approach to the chemical kinetics of polymerization of monomers with one or two double bonds [2-4, 11]. As it can be seen from Figure 5.42, the deterministic 1-D PDE and ODE models predicted the experimental behavior of the photopolymerization of SR256 resin quite accurately as the stochastic models. Thus, it may be concluded that the deterministic approach is particularly quite useful and productive for simulating the photopolymerization of monomers with fewer double bonds. The deterministic 1-D PDE and ODE models simulations for the photopolymerization of SR256 resin composed of monomers with one double bond shown in Figure 5.42 confirm this conclusion.

5.5 Validation of Stochastic Monte Carlo Model

Further to validate the SMCM, FTIR and DSC measurements were also conducted. For this purpose, SR256 and SR494 resins were chosen for FTIR and DSC measurements, respectively.

5.5.1 Validation by FTIR measurements

The degree of conversion of a photopolymerization process can be determined FTIR measurement results [108]. In this study FTIR experiments was performed to measure the double bond conversion during the photopolymerization of the SR256 resin. For this set of experiments, photoinitiator loading concentration of 1%, 5%, and 10% by weight percentage were used. As mentioned previously, each SR256 monomer has one carbon-carbon double bond in its vinyl group, which has a stretching frequency of 1640 cm^{-1}. As example, Figure 5.43 shows three different FTIR spectra of SR256 resin with the photoinitiator loading concentration of 5% by weight percentage. The highest curve in this figure represents the FTIR spectrum of the uncured resin and the lower two curves represent the FTIR spectra taken at the end of 4 s and 15 s curing times respectively.

As can be seen from Figure 5.43, the absorption peak from the C=C stretching mode at 1640 cm^{-1} has almost disappeared from the lowest curve corresponding to measurements done after curing for 15 s, indicating that allmost all of the C=C bonds have been broken during the photopolymerization process after 15 s of curing. This set of experiments was repeated at eight different UV light exposure times.

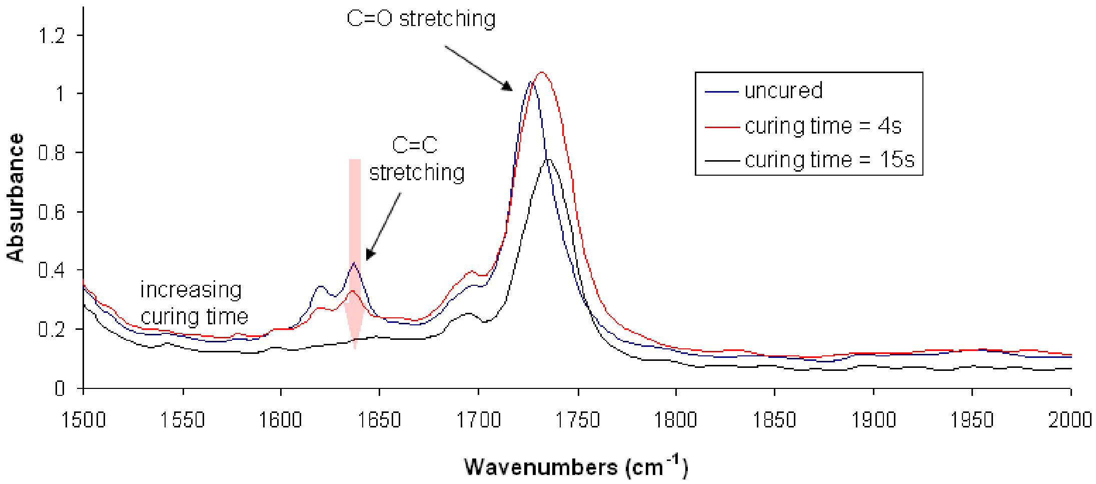

Figure 5.43: FTIR Spectrum of Cured and Uncured SR256 Resin ($[S]_0$=5%)

At the end of each experiment, the area under the C=C stretching peak at 1640 cm^{-1} was calculated automatically by the FTIR spectrometer using the OPUS software package. The results of these experiments are shown in Figure 5.44.

In Figure 5.44, the diamonds represent area under the 1640 cm^{-1} peak area after a given time period of UV exposure, also known as the Peak Area (PA). The scale of the PA is shown on the left vertical axis. The squares are monomer conversion percentages calculated from the ratio of the PA after curing to the PA before curing. The scale for the monomer conversion is shown on the right-hand vertical axis. The relationship between the monomer conversion and the PA is:

$$\text{Monomer Conversion} = 1 - \frac{\text{PA}(t)}{\text{PA}(t=0)} \qquad \textbf{(5.63)}$$

The error bars shown in Figure 5.44 for PA were calculated from repeating each UV exposure time experiment four times.

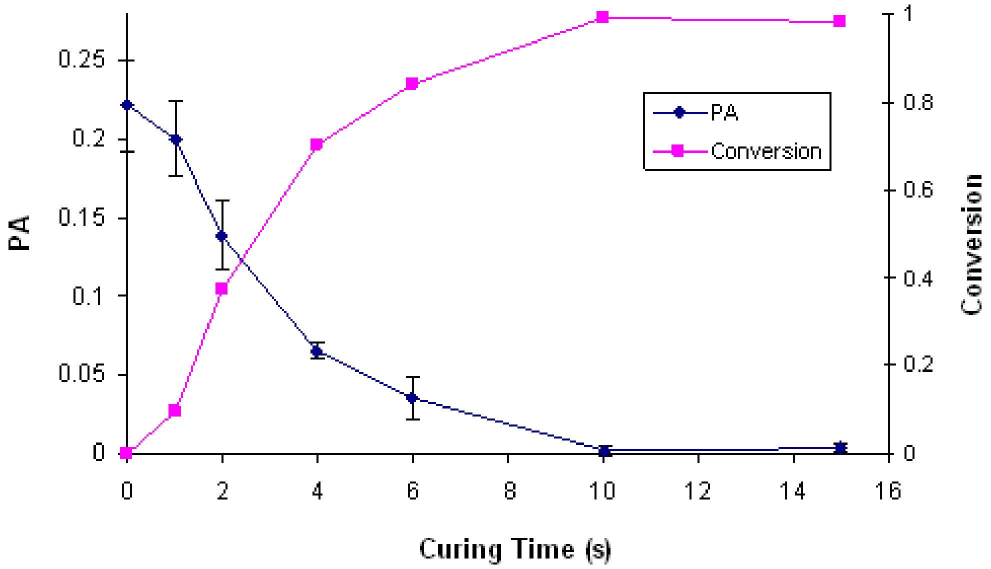

Figure 5.44: Monomer Conversion as a Function of Reaction Time for SR256 ($[S]_0$=5%)

Figure 5.45 compares the experimental and predicted double bond conversions as a function of the exposure time where the photoinitiator loading concentration was 1% by weight percentage. In this figure, points marked with diamonds and squares represent the experimental measurements and the predictions of the SMCM, respectively. The other two sets of experiments were done with photoinitiator loading concentrations of 5% and 10% by weight percentage. Figures 5.46 and 5.47 show the results from FTIR experiments along with the results from the corresponding SMCM simulations for photoinitiator loading concentrations of 5% and 10%, respectively. As can be seen from, Figures 5.45 and 5.46, the agreement between experimental results and the model predictions for the 1% and 5% photoinitiator loading concentrations are quite remarkable given the complexity of the problem.

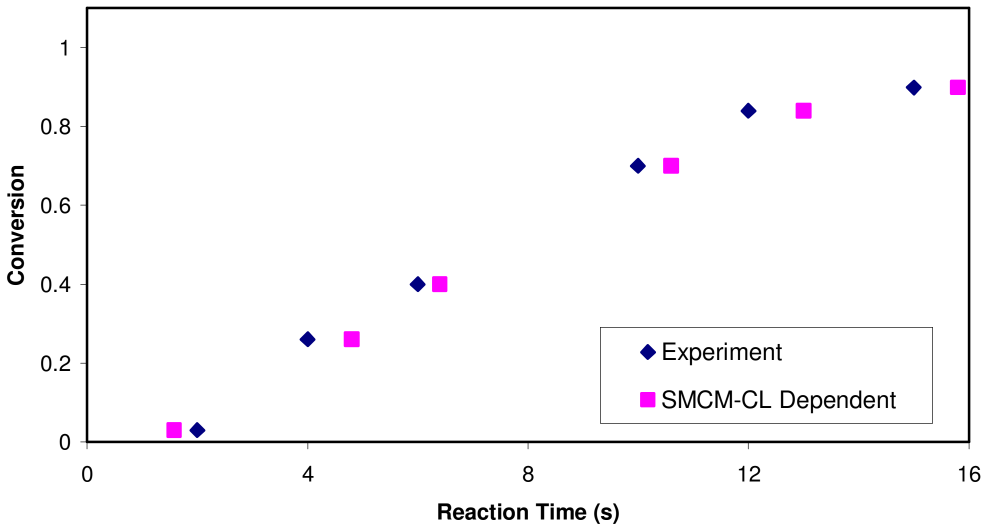

Figure 5.45: Comparison of Experimental and Predicted Conversion Values of SR256 Resin For 1% Photoinitiator Loading Concentration

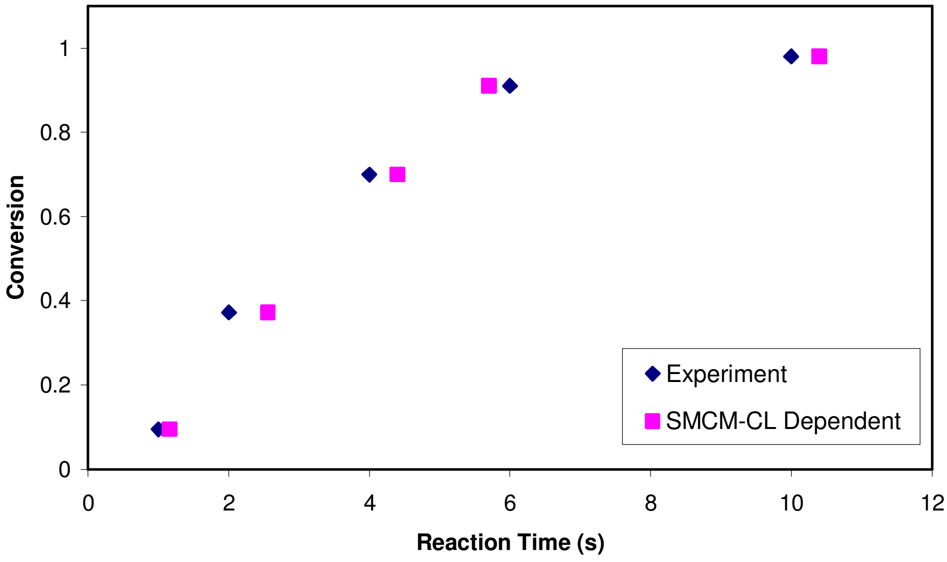

Figure 5.46: Comparison of Experimental and Predicted Conversion Values of SR256 Resin for 5% Photoinitiator Loading Concentration

For the 10% photoinitiator loading concentration, the model predictions for the conversion times at the highest double conversion values (or longer conversion times) are somewhat smaller than those experimentally measured (Figure 5.47). The overall behavior of the simulation and experimental curves, however, are still remarkably similar. For longer curing times, larger amounts of heat are produced in the reaction volume by the photopolymerization process; the resulting increase in temperature is not included in the determination of the reaction probabilities in the simulations. This might be the reason for these discrepancies. These figures also clearly show the sharp increase in the conversion rate—that is, the slope of the double bond conversion curves in these graphs—as the photoinitiator loading concentration increases.

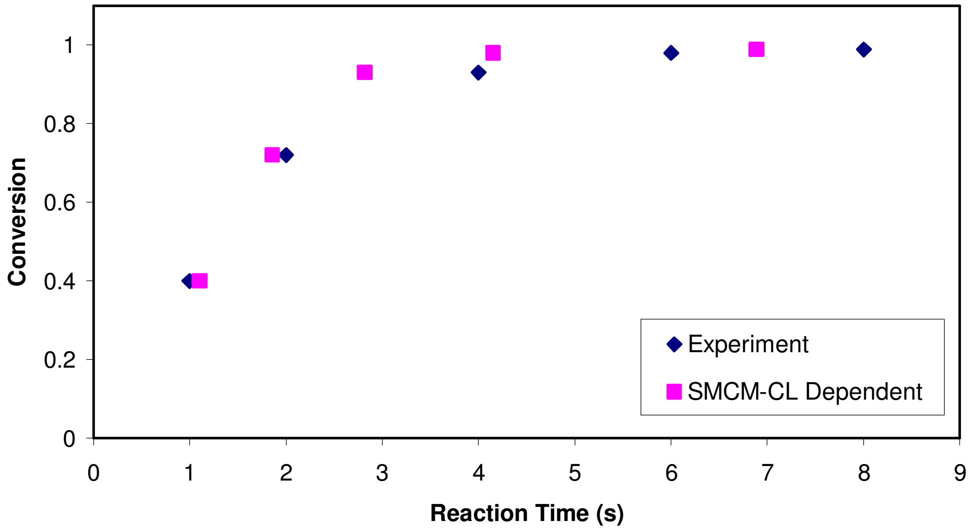

Figure 5.47: Comparison of Experimental and Predicted Conversion Values of SR256 Resin for 10% Photoinitiator Loading Concentration

The gelation times obtained from the FTIR measurements are found to be very close to the gelation times determined from the passive microrheology experiments. For example, the gelation times obtained from the FTIR and passive microrheology experiments conducted for SR256 resin with 1% photoinitiator loading concentration in the absence of oxygen gave 15 s and 16.2 s, respectively. For the 5% photoinitiator loading concentration the same measurement gave 6 s and 4.8 s, respectively. It should be noted that Flory predicts 1 as the critical conversion for the photopolymerization of monomers with one double bond which indicates 100% conversion. In reality, there is never 100% conversion in a finite amount of time as seen from FTIR experiments. Thus, the gelation times determined by the SMCM simulations for SR256 resin corresponds to 95% conversion rather than 100% conversion as predicted by Eq. (5.25) [100].

The conversion versus time curves obtained from the SMCM simulations given in Appendices G clearly show the increase in the speed of conversion as reflected by the curves in Figures 5.45-5.47 as a function of increasing photoinitiator loading concentration. The SMCM correctly predicts the behavior of conversion as a function of reaction time with different photoinitiator loading concentrations in the photopolymerizing resin. The success of the predictions of the SMCM based on the SSA seen in these last three figures holds promise for its potential to treat a variety of interesting chemical problems with complex reaction mechanisms.

5.5.2 Validation by DSC measurements

In these experiments the normalized heat flow signal obtained from the DSC apparatus as a function of the reaction time was integrated to get the total heat generated by the photopolymerization reaction at four different reaction temperatures. The heat flow signals from the DSC as a function of reaction time at 303 K, 343 K, 383 K, and 403 K are shown in Figure 5.48. The double bond conversion values were then calculated by dividing the area under the heat flow signal curves by the total heat of the photopolymerization process, which is assumed to be the amount of heat generated when all the monomer double bonds have been broken via photopolymerization [109, 110].

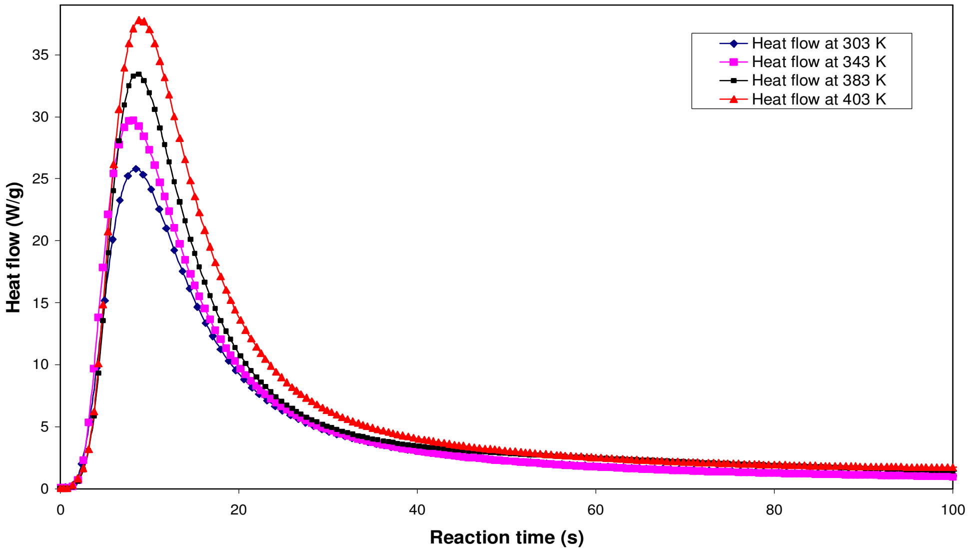

Figure 5.48: DSC Curves Obtained for the Photopolymerization of SR494 at 303K, 343 K, 383 K, and 403 K

The SMCM simulation results obtained for the photopolymerization of SR494 resin with photoinitiator loading concentration of 0.02% by weight percentage at reaction temperatures of 303 K, 343 K, 383 K, and 403 K are compared with the corresponding experimentally measured conversions values in Figures 5.49-5.52.

SR494 thermally polymerizes at temperatures of 413 K and above; all the temperatures in these DSC experiments were less than this critical temperature [71]. Therefore, the increase in the conversion values as a function of temperature is apparent in these curves. Yet, an increase can be seen in the conversion as a function of reaction time. This may be due to the thermal energy distribution, which makes it possible for some resin molecules to possess sufficient thermal energy to excite and eventually become polymeric radicals. As can be seen in Figures 5.49-5.52, the simulations also predict the same behavior and shows a clear rise in the conversion as a function of temperature.

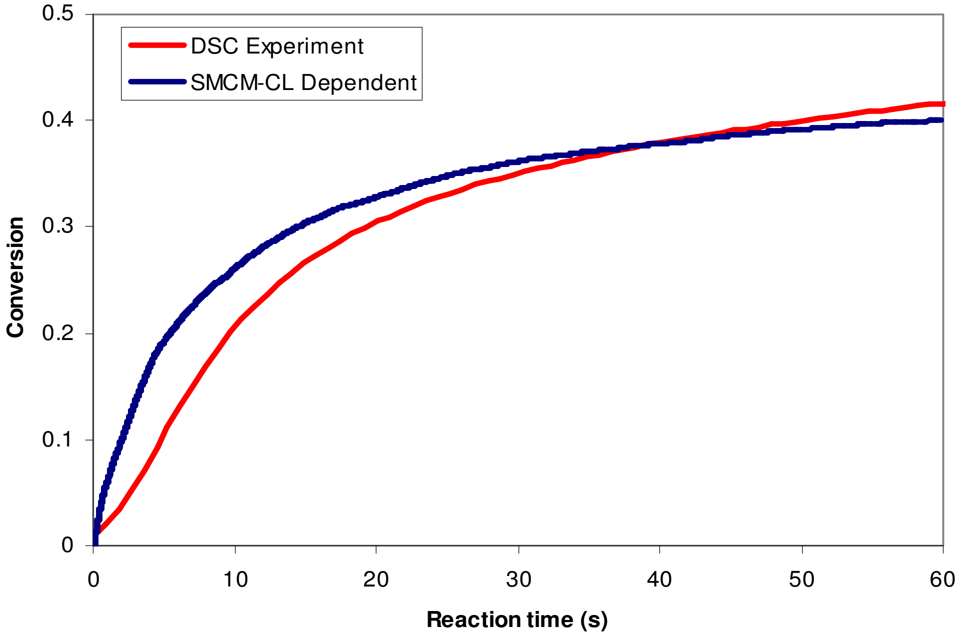

Figure 5.49: Comparison of Experimental and Predicted Conversion Values of SR494 Resin Photopolymerized at 303 K

As can be seen from these figures the agreement between the SMCM simulations and the experiments are very good at all temperatures. The temperature effect in the simulations are represented by multiplying the reaction propensities by an Arrhenius factor as given in Eq. (5.37). These results further validate the stochastic Monte

Carlo model as a reliable method to make predictions about the photopolymerization of resins composed of multifunctional monomers.

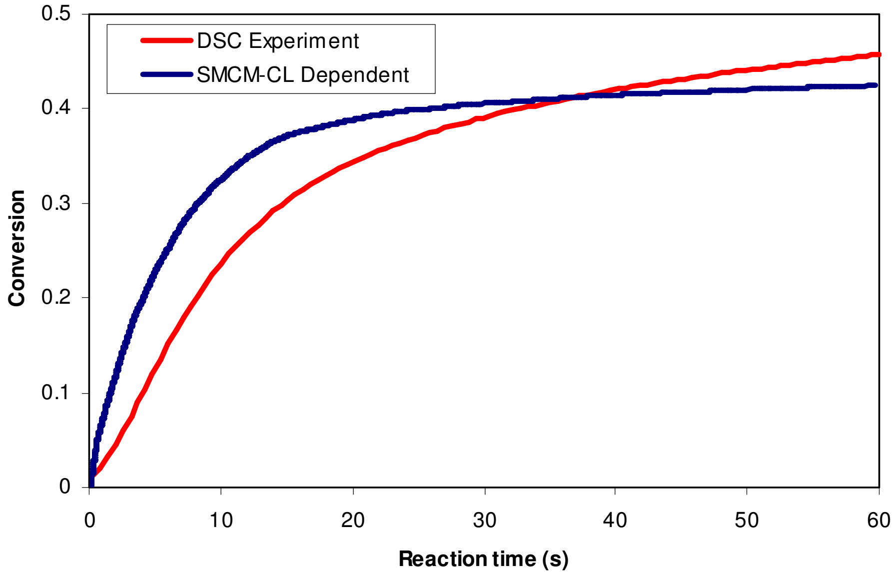

Figure 5.50: Comparison of Experimental and Predicted Conversion Values of SR494 Resin Photopolymerized at 343 K

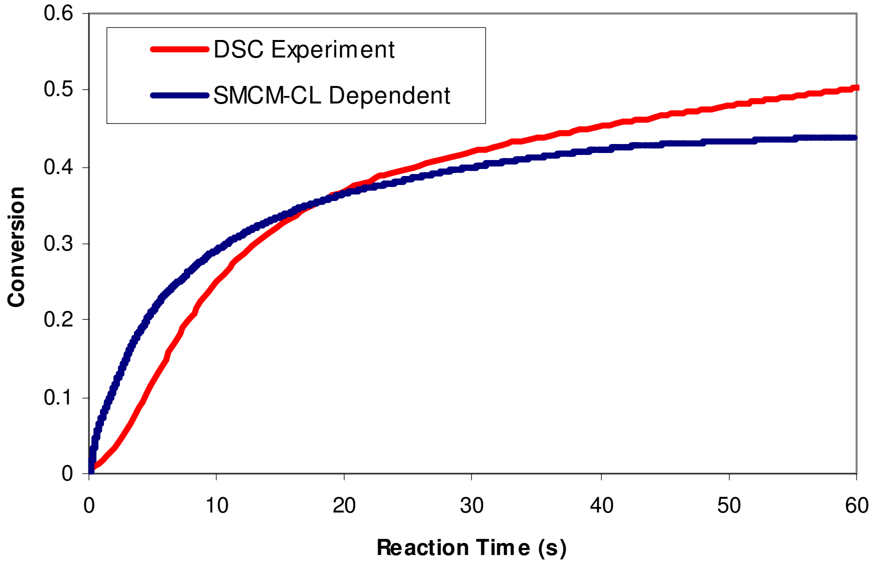

Figure 5.51: Comparison of Experimental and Predicted Conversion Values of SR494 Resin Photopolymerized at 383 K

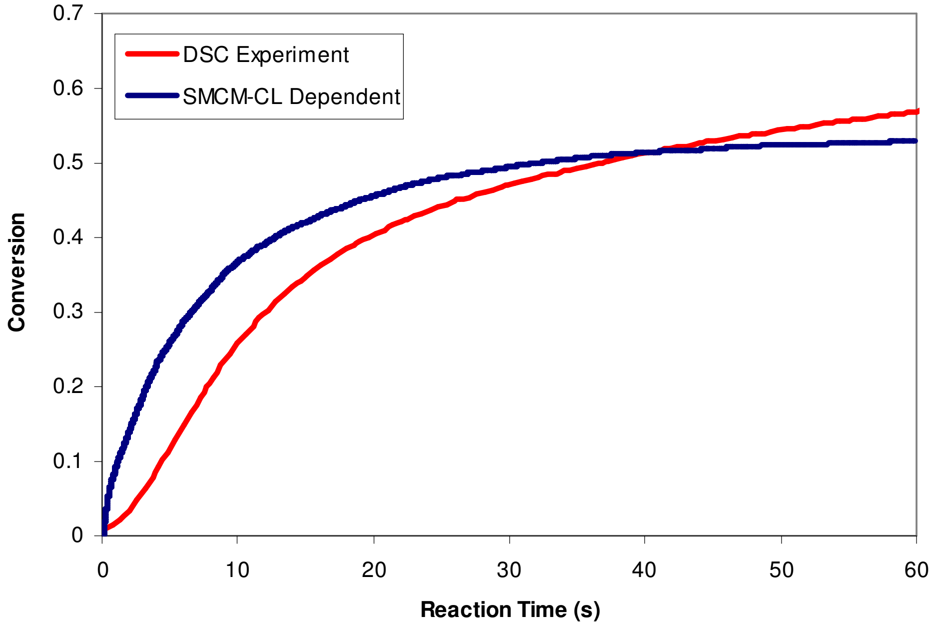

Figure 5.52: Comparison of Experimental and Predicted Conversion Values of SR494 Resin Photopolymerized at 403 K

6. CONCLUSIONS AND RECOMMENDATIONS

6.1 Conclusions

The most important goal of this thesis was to develop a mathematical model which predicts the characteristic behavior of the photopolymerization process of different functional monomers conducted at various conditions. The results presented in the thesis can be summarized as follows.

1. The scanning speed of UV light source illuminating the resin surface was found to have a critical effect on the final shape of the parts to be produced using SLA.

2. The parts produced in SLA at lower UV light scanning speed of 1.18×10^{-2} m/s have higher dimensions then parts produced at 2.27×10^{-2} m/s. This trend is also successfully simulated with the 2-D PDE model solved with COMSOL programme packege in this study.

3. There was no visible contour obtained for the scanning speeds of the UV light source at 2.27×10^{-1} m/s due to oxygen inhibition reactions.

4. Simulations with 2-D PDE model indicates that 85% of the total conversion in SL takes place during the UV light exposure time of 0.02 s which indicates most of the radicals are produced during the UV light exposure time.

5. Since photopolymerization process is an exotermic reaction, the highest temperature change was observed in SL simulations for the lower UV light scanning speed.

6. SL simulation showed that the degree of conversion is higher near the surface of the resin at all UV light scanning speeds.

7. The 2-D PDE model reasonably predicted the geometry of the parts as contours of a 2-D cross section of the cured region in the *y-z* plane. The shape of the contour reflects the intensity profile of the illuminating UV light source.

8. The 2-D PDE model contour curves corresponding 10% conversion as a function of geometry showed much better agreement with experiment than the ones corresponding to 5% and 15% conversions.
9. The errors in the simulated part dimensions decreased as the UV light scanning speed decreases.
10. The critical conversion of SR494 resin was predicted approximately as 10% by the 2-D PDE model simulations.
11. The agreement between the results of 1-D PDE model and the experimental measurements for the dependence of the gelation time on the UV light penetration depth for the photopolymerization of SR494 resin was seen to be quite remarkable. However, this agreement was found to be acceptable for SR351 and SR272.
12. The gelation time of different functional resins were found to increase as the UV light penetration depth increases. Also, the gelation time increased as the functionality of the monomers composing the resin decrease. In addition, as the functionality of the monomer increased, the difference between the gelation times at minimum and maximum UV light penetration depths were decreased.
13. The gelation time increased as the wavelength of the illuminating UV light changed from 356 nm to 248 nm for SR494 resin.
14. The gelation time increased as the intensity of the UV light decreased for SR494 resin.
15. Both simulation and experimental results displayed a linear dependence of the gelation time on the UV light penetration depth for all resin.
16. The agreement between the results of 1-D PDE model simulation and experimental measurements worsened with decreasing intensity of the UV light.
17. The rate of the decrease in the gelation time as a function of the photoinitiator loading concentration was quite large initially; but, decreased considerably and

became almost zero after the photoinitiator concentration reached a value of approximately 4.0% by weight for SR494 resin in the presence of oxygen.

18. The photoinitiator loading concentrations between 0.25% and 2 % by weight had the most dramatic effect on the gelation time for SR494 in the absence of oxygen.

19. The gelation times for the photopolymerization of SR494 resin in the absence of oxygen at photoinitiator loading concentration greater than 2% by weight could not be measured experimentally in this study.

20. The agreement between 1-D PDE model simulation and experiment for photopolymerization of SR494 resin in the presence of oxygen was found to be quite remarkable. The experimental curves of the gelation time as a function of the photoinitiator loading concentration in the presence of oxygen were all linear in plots with logarithmic scales on both axes and the associated simulations also produced very similar linear behavior for different functional resins.

21. The predictions of 1-D PDE model for the gelation time as a function of photoinitiator loading concentration for the photopolymerization of the SR494 resin in the absence of oxygen did not follow the experimental trend.

22. For the same photoinitiator loading concentrations the gelation time increased as the functionality of the monomers of the corresponding photopolymerizing resins decreased. The 1-D PDE simulations reproduced this linear behavior quite well and their predictions agree closely with the experimental measurements.

23. For different resins the change of the gelation time as a function of the photoinitiator loading concentration in the absence of oxygen were found to be nonlinear in plots with logarithmic scales on both axes. The 1-D PDE model failed to predict this nonlinear behavior.

24. The gelation time as a function of the photoinitiator loading concentration in the absence of oxygen became increasingly nonlinear as the functionality of the monomers of the corresponding photopolymerizing resins increases. The 1-D PDE model simulations failed to predict this increasingly nonlinear behavior as a function of increasing monomer functionality.

25. The deviation between the 1-D PDE model simulation and experimental results decreased with decreasing monomer functionality.

26. The failure of the deterministic 1-D PDE model in predicting the highly nonlinear behavior of the gelation time as function of the photoinitiator loading concentration in the absence of oxygen was the main motivation to search for other models of the simulation of photopolymerization process. For this purpose, another deterministic kinetic approach based on ODEs was employed.

27. ODEs are solved numerically by using an implementation of the 4th order Runga-Kutta method written in FORTRAN 90 for this study and solved to simulate the relation between the gelation time and photoinitiator loading concentration for the deoxygenated photopolymerization of multifunctional monomers.

28. While the experimental results showed pronounced nonlinear behavior in a logarithmic plot, in contrast, ODE models simulations showed linear behavior.

29. The results for experiments conducted in the absence of oxygen showed that the deterministic 1-D PDE and ODE models were insufficient for the description of the behavior of multifunctional monomers' photopolymerization process.

30. The considerable deviation between the actual experimental results and the predictions of the deterministic 1-D PDE and ODE models in the absence of oxygen underscored the need for a new model that takes into account the noncontinuous, discrete nature of chemical reactions. For this purpose, SMCM which is based on probabilistic approach, was developed to simulate these experimental data.

31. In this study, first successfull implementation of the SMCM was achieved to simulate the photopolymerization of a homogenous and wellmixed system to determine the relationship between the gelation time and the photoinitiator loading concentration.

32. A programme in FORTRAN 90 was written to implement the SMCM in this thesis.

33. The SMCM simulations were first performed for binary propagation and termination reactions using chain-length-independent rate constants, then the simulations were repeated by using chain-length-dependent rate constants and allowing primary cyclization reactions.

34. The simulation data from the SMCM were obtained with ten different runs with different seed values used to generate the pseudorandom numbers; the plotted gelation times are an arithmetic average of the gelation times predicted by the ten individual runs.

35. The results from the SMCM using chain-length-independent rate constants displayed the same nonlinear behavior as the experimental results showed for the predictions of gelation times for lower photoinitiator loading concentrations.

36. At higher photoinitiator loading concentrations, the predictions of the SMCM using chain-length-independent rate constants for both propagation and termination reactions deviated somewhat from the experimental results.

37. To remedy the deviation of the SMCM using chain-length-independent rate constants for both propagation and termination reactions, the model was altered to include the effect of the chain lenght dependence in propagation and termination rate constants and to allow polymeric radicals to undergo primary cyclization reactions.

38. The agreement between the SMCM using chain lenght dependence in propagation and termination rate constants and to allow primary cyclization reactions simulations and the experimental measurements were very remarkable.

39. The relatively good agreement between experimental results and the predictions of the current SMCM based on the SSA was mostly attributed to the fact that the time evolution of the photopolymerization process was treated probabilistically rather than deterministically.

40. Dependence of the gelation times on the photoinitiator loading concentrations in the absence of oxygen predicted by both sets of SMCM simulations gave the similiar nonlinear behavior.

41. For all resins investigated in this study as the photoinitiator loading concentration increased, the stochastic model's predictions agreed with the trend of the experimental measurements. In contrast, with the deterministic 1-D PDE and ODE models the agreement worsened as the photoinitiator loading concentration increased.

42. The overall qualitative agreement between experiment and the deterministic 1-D PDE and ODE model simulation results was much better for SR351, SR272, and SR256 resins than for SR494 at lower photoinitiator loading concentrations.

43. Validation of the SMCM was performed by FTIR and DSC measurements by using SR256 and SR494 resins, respectively.

44. The agreement between experimental FTIR results and the SMCM predictions for the 1% and 5% photoinitiator loading concentrations were quite remarkable given the complexity of the problem. For the 10% photoinitiator loading concentration, the model predictions for the conversion times at the highest double conversion values (or longer conversion times) were somewhat smaller than those experimentally measured.

45. The close agreement between the FTIR measurements and the microrheology experiments to determine the gelation time was a strong evidence for the integrity of these experiments.

46. The SMCM correctly predicted the behavior of conversion as a function of reaction time with different photoinitiator loading concentrations in the photopolymerizing resin.

47. An increase in the degree of conversion as a function of temperature was observed in DSC measurements due to the thermal energy distribution, which makes it possible for some resin molecules to possess sufficient thermal energy to excite and eventually become polymeric radicals.

48. The simulations of SMCM also showed a clear rise in the degree of conversion with increasing temperature which is in agreement with DSC experimental results.

49. The predictions of the SMCM for the microreology, FTIR, and DSC experiments were found to be strongly compatible to each other.

50. The success of the predictions of the SMCM based on the SSA holds promise for its potential to treat a variety of interesting chemical problems with complex reaction mechanisms.

6.2 Recommendations

1. The SLA curing quality could be improved if the effects of spatial variations and oxygen diffusion or other inhibition agents on the photopolymerization process were better understood.

2. From the modeling point of view, an improved description of the boundary conditions in the application of the 1-D PDE model may improve its resulting predictions.

3. The SMCM could be improved by incorporating the effect of enthalpy changes during the exothermic photopolymerization process into the calculation of the propensities of the possible reactions at each step of the simulation; the current model calculates the propensities from the binary encounters modified by the stochastic rate constants for the propagation, termination, and cyclization reactions at a given temperature. Improved models can shed light on the analysis of the experiment results on many complex photopolymerization systems. The simulation results presented in this thesis hold promise for the value of using SMCM toward this end.

4. A further test of the SMCM simulation can come from comparing its predictions of the molecular weight distribution with those experimentally measured using gel permeation chromatography (GPC).

5. Using active microrheology to monitor the changes in the rheological properties of the polymerizing sample by externally manipulating the tracer particles embedded in the resin might provide further insight into the network forming photopolymerization process of multifunctional monomers.

6. In the current stochastic model, only the binary interactions between species have been considered. Thus, this method can be improved by considering ternary or higher interactions between reactant species.

REFERENCES

[1] **Lovestead, T. M., O'Brien, A. K., and Bowman, C. N.,** 2003. Models of multivinyl free radical photopolymerization kinetics, *J of Photochem. and Photobio., A: Chemistry,* **159,** 135–143.

[2] **Andrzejewska, E.,** 2001. Photopolymerization kinetics of multifunctional monomers, *Progress in Polymer Science,* **26,** 605-665.

[3] **Achilias, D. S.,** 2007. A review of modeling of diffusion controlled polymerization reactions, *Macromolecular Theory and Simulations,* **16,** 319-347.

[4] **Anseth, K. S., and Bowman, C. N.,** 1993. Reaction diffusion enhanced termination in polymerizations of multifunctional monomers, *Polymer Reaction Engineering,* **1,** 499-520.

[5] **Gillespie, D. G.,** 1976. A general method for numerically simulating the stochastic time evolution of coupled chemical reactions, *J. Comp. Phys.,* **22,** 403-434.

[6] **Fogler, H. S.,** 2001. Elements of chemical reaction engineering, Prentice Hall PTR, New Jersey.

[7] **Odian, G.,** 1981. Principles of polymerization, John Wiley and Sons Inc, New York.

[8] **Studer, K., Decker, C. Beck, E. and Schwalm, R.,** 2003. Overcoming oxygen inhibition in UV-curing of acrylate coatings by carbon dioxide inerting: Part II, *Progress in Organic Coatings,* **48,** 92-100.

[9] **Studer, K., Decker, C. Beck, E. and Schwalm, R.,** 2003. Overcoming oxygen inhibition in UV-curing of acrylate coatings by carbon dioxide inerting: Part I, *Progress in Organic Coatings,* **48,** 101-111.

[10] **Decker, C.,** 1994. Photoinitiated curing of multifunctional monomers, *Acto Polymer,* **45,** 333-347.

[11] **Goodner, M. D. and Bowman, C. N.,** 2002. Development of a comprehensive free radical photopolymerization model incorporating heat and mass transfer effects in thick films, *Chemical Eng.Sci.,* **57,** 887-900.

[12] **Fouassier, J. P., Rabek, J. F.,** 1993. Radiation curing in polymer science and technology volume III: polymerizations mechanisms, Elsevier Applied Science, London.

[13] **Kaur, M. and Srivastava, A. K.,** 2002. Photopolymerization: A review, *J Macromolecule Science-Polymer Reviews,* **4,** 481-512.

[14] **Koleske, J.,** 1982. Radiation curing of coatings, John Wiley and Sons Inc, New York.

[15] **Peppas, S. P.,** 1985. UV curing: science and technology volume II, CT: Technology Marketing Corporation, Norwalk.

[16] **Drobny, J. G.,** 2003. Radiation technology for polymers, CRC Press, London.

[17] **Roffey, C. G.,** 1982. Photopolymerization of surface coatings, John Wiley and Sons Inc, New York.

[18] **Allock, H. R. and Lampe, F. W.,** 1990. Contemporary polymer chemistry. Prentice Hall, New Jersey.

[19] **http://www.zeusinc.com/pdf/Zeus_Coloring.pdf,** http://www.zeusinc.com/pdf/Zeus_Coloring.pdf, accessed at 24/02/2008.

[20] **Lovestead, T. M., Berchtold, K. A., and Bowman, C. N.,** 2002. Modeling the Effects of Chain Length on the Termination Kinetics in Multivinyl Photopolymerizations, *Macromol. Theory Simul.*, **11,** 729–738.

[21] **Additives,** http://www.sigmaaldrich.com/Area_of_Interest/Chemistry/Materials_Science/Polymerization_Tools/Additives.html#Chain%20transfer%20agents, accessed at 24/02/2008.

[22] **Moad, G. and Solomon, D. H.,** 2006. The chemistry of radical polymerization, Elsevier, Oxford.

[23] **Matyjaszewski, K. and Davis, T. P.,** 2002. Handbook of radical polymerization, John Wiley and Sons Inc, New Jersey.

[24] **Skoog, D. A. and Leary, J. J.,** 1992. Principles of instrumental analysis, Saunders College Publishing, Fort Worth.

[25] **Harris, D. C.,** 1991. Quantitative chemical analysis, W. H. Freeman and Company, New York.

[26] **Groenenboom, H. J., Hageman, T., Overeem, T., and Weber, A. J. M.,** 1982. Photoinitiators and photoinitiation, 3a. Comparison of the photodecompositions of a methoxy- and a.a-dimethoxydeoxybenzoin in 1,1- diphenylethylene as model substrate, *Macromol. Chem. and Phys.,* **183,** 281-292.

[27] **Kloosterboer, J. G., Van de Hei G. M. M. and Boots, H. M. J.,** 1984. Inhomogeneity curing the photopolymerization of diacrylates: DSC experiments and percolation theory, *Polymer Commun,* **25,** 354-357.

[28] **Bowman, C. N. and Anseth, K. S.,** 1995. Microstructural evolution in polymerizations of tetrafunctional monomers, *Macromol. Symp.*, **93,** 269-276.

[29] **Russell, G. T.,** 2002. The kinetics of free-radical polymerization: fundamental aspects, *Aust. J. Chem.*, **55,** 399-414.

[30] **Benson, S. W and North, A. M.,** 1962. The kinetics of free radical polymerization under conditions of diffusion controlled termination, *J. Amer. Chem. Soc.*, **84,** 935-940.

[31] **Benson, S. W and North, A. M.,** 1959. A simple dilatometric method od determining the rate constants of chain reactions. II. The effect of the viscosity on the rate constants of polymerization reactions, *J. Amer. Chem. Soc.*, **81,** 1339-1345.

[32] **Marten, F. L and Hamielec, A. E.,** 1979. High Conversion diffusion-controlled polymerization. In Polymerization Reactors and Processes, *J. Amer. Chem. Soc. Symp,* **104,** 43-70.

[33] **Marten, F. L and Hamielec, A. E.,** 1982. High-converion diffusion-controlled polymerization of Styrene I, *J.Appl.Poly. Sci.,* **27,** 489-505.

[34] **Bowman, C. N and Peppas, N. A.,** 1991. Coupling of kinetics and volume relaxation during polymerizations of multiacrylates and multimethacrylates, *Macromolecules,* **24,** 1914-1920.

[35] **Goodner, M. D, Lee, H. R. and Bowman, C. N.,** 1997. Method for determining the kinetic parameters in diffusion-controlled free-radical homopolymerizations, *Ind. Eng. Chem. Res.*, **36,** 1247-1252.

[36] **Zhu, S. and Hamielec, A. E.,** 1989. Chain length dependent termination for free radical polymerization, *Macromolecules,* **22,** 3093-3098.

[37] **Masaro, L. and Zhu, X. X.,** 1999. Physical models of diffusion for polymer solutions, gels and solids, *Prog. Poly. Sci.*, **24,** 731-775.

[38] **Soh, S. K. and Sundberg, D. C.,** 1982. Diffusion-controlled vinyl polymerization. I. The gel effect, *J Polym. Sci. Polym.Chem.,* **20,** 1299-1313.

[39] **Stickler, M.,** 1983. Free-radical polymerization kinetics of metylmethacrylate at very high conversions, *Makromol. Chem.,* **184,** 2563-2579.

[40] **Davidson, R. S.**, 1993. The role of amines in UV-curing, in: Radiation curing in polymer science and technology, Elsevier, London.

[41] **Becker, H. and Vogel, H.,** 2006. The role hydroquinone monomethyl ether in the stabilization of acrylic acid, *Chem. Eng. Tech.,* **29,** 1227-1231.

[42] **Nguyen, K. T., and West, J. L.,** 2002. Photopolymerizable hydrogels for tissue engineering applications, *Biomaterials,* **23,** 4307–4314.

[43] **Chowdhury, S. M., and Hubbell, J. A.,** 1996. Adhesion prevention with ancrod released via a tissue-adherent hydrogel, *J Surg Res,* **61,** 58–64.

[44] **Peppas N. A., Keys KB, Torres-Lugo, M. and Lowman, A. M.,** 1999. Poly(ethylene glycol)-containing hydrogels in drug delivery, *J Controlled Rel,* **62,** 81–7.

[45] **An, Y., and Hubbell, J. A.,** 2000. Intraarterial protein delivery via intimally adherent bilayer hydrogels, *J Controlled Rel,* **64,** 205–15.

[46] **Schacht, E.,** 2003. Biodegradable Polymers for Biomedical Applications, *European Cells and Materials,* **5,** 58.

[47] **Lin, Y. and Stansbury, J.,** 2001. Application of FT-NIR spectroscopy for monitoring the kinetics of photoinitiated methacrylate/vinyl ether copolymerizations, *Am. Chem. Soc., Polym Prepr.,* **42,** 809-810.

[48] **Nelson, E. and Scranton, A.,** 1996. In situ Raman spectroscopy for cure monitoring of cationic photopolymerizations of divinyl ethers, *J Raman Spect.*, **27,** 137-144.

[49] **Puskas, J.,** 2003. In-situ spectroscopy of monomer and polymer synthesis, Kluwer Academic/Plenum Publishers, New York.

[50] **Alfassi, Z. B.,** 1999. General Aspects of the Chemistry of Radicals, Wiley, New York.

[51] **Bower, D. L. and Maddams, W. F.,** 1989. The vibrational spectroscopy of polymers, Cambridge University Press, New York.

[52] **Gallagher, P. K.,** 1998. Handbook of thermal analysis and calorimetry, Elsevier, New York.

[53] **Decker, C. and Moussa, K.,** 1988. A New Method for Monitoring Ultra-Fast Photopolymerizations By Real-Time Infrared Spectroscopy (RTIR), *Makrol. Chem.,* **189,** 2381-2394.

[54] **Clark, S., Hoyle, C., Jonsson, S., Morel, F., and Decker, C.,** 1999. Photopolymerization of acrylates using N-aliphaticmaleimides as photoinitiators, *Polymer,* **40,** 5063-5072.

[55] **Verney, V. and Michel, A.,** 1989. Representation of the rheological properties of polymer melts in terms of complex fluidity, *Rheologica Acta,* **28,** 54-60.

[56] **Breedveld, V., and Pine, D. J,** 2003. Microrheology as a tool for high-throughput screening, *J Mater Sci,* **38,** 4461-4470.

[57] **Mason, T. G., Ganesan, J. H., Wirtz, D., and Kuo, S. C.,** 1997. Particle Tracking Microrheology of Complex Fluids, *Phys. Rev. Lett.,* **79,** 3282-3285.

[58] **Nikam, P. E.,** 2000. Application of subtractive rapid prototyping to the design and manufacture of rapid solidification process tooling, *MSc Thesis,* Cleveland State University, Cleveland, OH.

[59] **Jacobs, P, F.,** 1992. Rapid prototyping and manufacturing: fundamentals of stereolithography, Soc of Manufturing Engineers, Dearborn, MI.

[60] **Howwstuffworks "How Stereolithography (3-D Layering) Works"**, http://computer.howstuffworks.com/stereolith2.htm, accessed at 02/12/2007.

[61] **Zhou, J. G., Herscovici D., and Chen C. C.,** 1999. Parametric Process Optimization to Improve the Accuracy of Rapid Prototyped Stereolithography Parts, *J Mach. Tools and Manuf.,* **40,** 1-17.

[62] **Onuh, S. O. and Hon, K. K.,** 1998. Optimising build parameters for improved surface finish in stereolithography, *International Journal of Tools Manufact.,* **38,** 329-342.

[63] **Hur, S, S., Lee, J. H. and Youn, J. R.,** 2000. Thermal deformation of a photo-cured polymer for the analysis of stereolithography, *Polymer-Plastic Tech. Eng.,* **39,** 651-666.

[64] **Slopek, R. P., McKinley H. K., Henderson C. L. and Breedveld V.,** 2006. In situ monitoring of mechanical properties during photopolymerization with particle tracking microrheology, *Polymer,* **47,** 2263-2268.

[65] **Satio, K.,** 1993. Study on development of stereo-lithography method of solid form, *Ministry of Education Report,* **No.03555022,** Japan.

[66] **Nagamori, S., and Yoshizawa, T.,** 2002. Research on solidification of resin in stereolithography: comparison between measured and estimated shapes of solidified resin, and manufacturing accuracy of photo-cured model, Proc. *SPIE, The International Society for Optical Engineering,* **4556,** 47-57.

[67] **Nagamori, S., and Yoshizawa, T.,** 2003. Research on shape of solidified resin in stereolithography, *Optical Eng,* **42,** 2096-2103.

[68] **Perry, M. F. and Young, G. W.,** 2005. A mathematical model for photopolymerization from a stationary laser light source, *Macromol. Theory and Simul.,* **14,** 26-39.

[69] **Flach, L. and Chartoff, R. P.,** 1995. A process model for nonisothermal photopolymerization with a laser light source. I: Basic model development, *Polymer Eng. And Sci,* **35,** 483-492.

[70] **Flach, L. and Chartoff, R. P.,** 1995. A process model for nonisothermal photopolymerization with a laser light source. II: Behavior in the vicinity of a moving exposed region, *Polymer Eng. And Sci,* **35,** 493-498.

[71] **Tang, Y.,** 2005. Stereolithography cure process modeling, *PhD thesis,* Georgia Tech, New York.

[72] **Esch, J., Blumenstock, T. and Eyerer, P.,** 1999. Comparison of the curing process of epoxy and acrylate resins for stereolithography by means of experimental investigations and FEM- simulation, The 10th *Solid Freeform Fabrication Symposium,* Austin, Texas, USA, August 19-13.

[73] **Dufaud, O, and Corbel, S.,** 2002. Oxygen diffusion in ceramic suspensions for stereolithography, *Chemical Eng. J.,* **92,** 55-62.

[74] **Lee, J. H., Prud'homme, R. K. and Aksay, I. A.,** 2001. Cure depth in photopolymerization: experiments and theory, *Journal of Mater. Res.,* **16,** 3536-3544.

[75] **Chockalingam, K., Jawahar, N. and Ramanathan, K. N., and Banerjee, P. S.,** 2006. Optimising of stereolithography process parameters for part strength using design of experiments, *International Journal of Adv. Manuf. Technol,* **29,** 79-88.

[76] **Bartolo, P., Jardini, A. and Scaparo, M.,** 2004. Stereolithographic processes: materials, techniques and applications, *10thEuropean Forum on Rapid Prototyping, Rapid Prototyp. Manuf.,* Courbevoie, France, September 14-15.

[77] **Maffezzolli, A., and Terzi, R.,** 1998. Effects of irradiation intensity on the isothermal photopolymerization kinetics of acrylic resins for stereolithography, *Thermochimica Acta,* **321,** 111-121.

[78] **Schaub, D. A., Chu, K. R. and Montgomery, D. C.,** 1997. Optimising stereolithography throughput, *Journal of Manuf. Systems,* **16,** 290-303.

[79] **Banerjee, P. S., Sinha, A. and Banerjee, M. K.,** 2001. A study on effect of variation of SLA process parameters over strength of built model, *Proceedings of the 2nd National Symposium on Rapid Prototyping and Rapid Tooling Technologies,* Bangalore, India, November 2001, 79-84.

[80] **Chockalingam, K., Jawahar, N. and Vijaybabu, E. R.,** 2003. Optimization of process parameters in stereolithography using genetic algorithm, *Smart Materials, Structures, and Systems,* **5062,** 417-424.

[81] **Cho, H. S., Park, W. S., Choi, B. W. and Leu, M. C**., 2000. Determining optimal parameters for stereolithography process via genetic algorithm, *Journal of Manuf. Systems,* **19,** 18-27.

[82] **Onuh, S. O., and Hon, K. K.,** 1998. Applications of the taguchi method and new hatch styles for quality improvement in stereolithography, *Proc. of the Institution of Mech. Eng, Part B, J Eng Manuf,* **212,** 461-472.

[83] **Jayanthi, S., Keefe, M. and Garhiulo, E. P.,** 1994. Studies in stereolithography: influence of process parameters on curl distortion in photopolymer models, *Solid Freeform Fabrication Symposium Proceedings,* Austin, Texas, USA, August 8-10, 250-258.

[84] **Gittes F., Schnurr B., Olmsted P. D., Mackintosh F. C. And Schmidt C. F.,** 1997. Microscopic viscoelasticity: shear moduli of soft materials determined from thermal fluctuations., *Phys. Rev. Lett.,* **79,** 3286-3289.

[85] **Waigh T. A.,** 2005. Microscopic viscoelasticity: shear moduli of soft materials determined from thermal fluctuations., *Rep.Prog.Phys.,* **68,** 685-742.

[86] **Mason, T. G.,** 2000. Estimating the viscoelastic moduli of complex fluids using the generalized Stokes-Einstein equation, *Rheol. Acta.,* **39,** 371–378.

[87] **Mason, T. G. and Weitz, D. A.**, 1995. Optical measurements of frequency-dependent linear viscoelastic moduli of complex fluids, *Phys. Rev. Lett.,* **74**, 1250-1253.

[88] **Brau, R. R., Ferrer, J. M., H Lee, H., Castro, C. E., Tam, B. K., Tarsa, P. B., Matsudaira, P., Boyce, M. C., Kamm, R. D., and Lang, M. J.**, 2007. Passive and active microrheology with optical tweezers, *J. Opt. A: Pure Appl. Opt.,* **9**, S103–S112.

[89] **Winter, H. H. and Chambon, F. J.**, 1986. Analysis of linear viscoelasticity of a crosslinking polymer at the gel point, *J Rheology,* **30**, 367-382.

[90] **Tung, C. M. and Dynes, P. J.**, 1982. Relationships Between Viscoelastic Properties and Gelation. in Thermosetting Resins, *J. Appl. Polym. Sci.,* **27**, 569-574.

[91] **Scanlan, J. C., and Winter H. H.**, 1991. Composition dependence of. the viscoelasticity of end-linked poly(dimethylsiloxane), *Macromolecules,* **24**, 47-54.

[92] **Rodd, A. B., Cooper-White, J. J., Dunsten, S. E., and Boger D. V.**, 2001. Gel point studies for chemically modified biopolymer networks using small amplitude oscillatory rheometry, *Polymers,* **42**, 185-198.

[93] **Ross-Murphy, S.B**., 1995. Structure-property relationships in food biopolymer gels and solutions, *J. Rheol.,* **39**, 1451–1463.

[94] **Winter, H. H. and Mours, M.**, 1997. Rheology of polymers pear liquid-solid transitions, *Advances in Polymer Science,* **134**, 1-70.

[95] **Sartomer,** http://www.sartomer.com/proddetail.asp?plid=1&sgid=5&prid=SR494, accessed at 10/12/2007.

[96] **Ciba®IRGACURE®,** http://www.ciba.com/irgacure_651_2?pageid=10029&mode=P&prod=987&attribs=33, accessed at 30/07/2007.

[97] **Bird, R. B., Stewart, W. E., and Lightfood, E. L.**, 2002. Transport Phenomena, John Wiley and Sons Inc., New York.

[98] **O'Brian, A. K,. Cramer, N. B., and Bowman, C. N.**, 2006. Oxygen inhibition in thiol-acrylate photopolymerizations, *Polymer Chem,* **44**, 2007-2017.

[99] **Hu, X., Fan, J., and Yoe, C. Y.,** 2001. Rheological study of crosslinking and gelation in bismaleimide/cyanate ester interpenetratin polymer network, *J Appl. Poly. Sci.,* **80,** 2437-2445.

[100] **Flory, P. J.,** 1953. Principles of Polymer Chemistry, Cornell University Press, Ithaca, NY.

[101] **Russel, G. T.**, 1994. On exact and approximate methods of calculating an overall termination rate coefficient from chain length dependent termination rate coefficients,*Macromol. Theory Simul.,* **3**, 439-468.

[102] **Terazima, M., and Hirota, N.**, 1991. Measurements of the quantum yield of triplet formation and short triplet lifetimes by the transient grating technique, *J Chem. Phys,* **95**, 6490-6495.

[103] **Terazima, M., Tenma, S., Watanabe, H., and Tomhagab, T.**, 1996. Translational diffusion of chemically stable and reactive radicals in solution, *J. Chem. Soc., Faraday Trans.,* **92**, 3057-3062.

[104] **Gillespie, D. G.,** 1977. Exact stochastic simulationof coupled chemical reactions, *J Phys Chem,* **81,** 2340-2361.

[105] **Wen, M., Scriven, L. E., McCormick**, **A. V.,** 2003. Kinetic gelation modeling: kinetics of cross-linking polymerization, *Macromolecules,* **36,** 4151-4159.

[106] **Smith, G. B., Russell, G. T., Yin, M., and Heuts**, **J. P. A.,** 2005. The effects of chain length dependent propagation and termination on the kinetics of free-radical polymerization at low chain lengths, *European Polymer Journal,* **41**, 225-230.

[107] **Smith, G. B., Russell, G. T., and Heuts, J. P. A.**, 2003. Termination in dilute-solution free-radical polymerization: a composite model, *Macromol. Theo Simul.,* **12**, 299-314.

[108] **Houbenz, R., Domann, G., Schulz, J., Olsowski, B., Frohlich, L., and Kim, W-S.**, 2004. Impact of photoinitiators on the photopolymerization and the optical properties of inorganic–organic hybrid polymers, *App Phys Lett.,* **84**, 1105-1107.

[109] **Cook, W. D.,** 1993. Photopolymerization kinetics of oligo(ethylene oxide) and oligo(metylene) oxide dimetyacrylates, *J Poly. Sci.,* **31,** 1053-1067.

[110] **Cook, W. D.,** 1992. Thermal aspects of the kinetics of dimetyacrylates, *Polymer,* **33,** 2152-2161.

APPENDIX

APPENDIX-A

Table A.1 The Parameters Used for to Simulate the Photopolymerization Process of SR351 [11, 71, 95]

	Parameters	Symbols	Values	Units
Model Parameters	Parameter for propagation rate	A_p	4	-
	Parameter for termination rate	A_t	4	-
	Pre-exponential factor	A_{Ep}	28.378	m^3/mol-s
	Pre-exponential factor	Aet	8916	m^3/mol-s
	Activation energy	E_p	1626	J/mol
	Activation energy	E_t	2102	J/mol
	Reaction diffusion constant	R_{rd}	0.0011	m^3/mol
	Thermal convection coefficient	h	4.18	W/m^2-K
	Chamber temperature	Ta	300.48	K
Laser Parameters	Wavelength	λ	356	nm
	Beam radius	w_o	1.1x10^{-4}	m
Material Properties	Thermal conductivity	k	0.142	W/m-K
	Heat of polymerization	ΔH_P	20x10^4	J/mol
	Absorptivity (initiator)	ε	0.15	m^3/mol-m
	Initiation quantum yield	ϕ_i	0.6	-
	Diffusion coefficient (monomer)	D_M	1x10^{-3}	m^2/s
	Diffusion coefficient (radical)	$D_{P\cdot}$	1	m^2/s
	Diffusion coefficient (initiator)	D_S	1	m^2/s
	Diffusion coefficient (oxygen)	D_O	49x10^{-7}	m^2/s
	Coefficient of thermal expansion (monomer)	α_M	0.00177	1/K
	Coefficient of thermal expansion (polymer)	α_P	0.00012	1/K
	Glass transition temperature (monomer)	Tg_M	212.15	K
	Glass transition temperature (polymer)	Tg_P	335.15	K
	Heat capacity (monomer)	C_{PM}	$C_{P,M} = 5.6 \times T(K) + 218.6$	J/kg-K
	Heat capacity (polymer)	C_{PP}	$C_{P,P} = 9.1 \times T(K) - 1535.5$	J/kg-K
	Heat capacity (curing system)	C_P	$C_P = C_{P,M}(1-X) + C_{P,P}X$	J/kg-K
	Density (monomer)	ρ_M	$1109/(1+\alpha_M(T-298))$	kg/m^3
	Density (polymer)	ρ_P	$1200/(1+\alpha_P(T-308))$	kg/m^3
	Density (curing system)	ρ	$\rho = \rho_M \phi_M + \rho_P(1-\phi_M)$	kg/m^3
Resin Composition	Monomer concentration	[M]	3746	mol/m^3
	Initiator concentration	[S]	0.25-8.0	wt%
	Oxygen concentration	[O]	1x10^{-3}	mol/m3

Table A.2: The Parameters Used for to Simulate the Photopolymerization Process of SR272 [11, 71, 95]

	Parameters	Symbols	Values	Units
Model Parameters	Parameter for propagation rate	A_p	2	-
	Parameter for termination rate	A_t	2	-
	Pre-exponential factor	A_{Ep}	1600	m^3/mol-s
	Pre-exponential factor	Aet	3600	m^3/mol-s
	Activation energy	E_p	18230	J/mol
	Activation energy	E_t	2940	J/mol
	Reaction diffusion constant	Rrd	0.002	m^3/mol
	Thermal convection coefficient	h	4.18	W/m^2-K
	Chamber temperature	Ta	300.48	K
Laser Parameters	Wavelength	λ	356	nm
	Beam radius	w_o	$1.1x10^{-4}$	m
Material Properties	Thermal conductivity	k	0.142	W/m-K
	Heat of polymerization	ΔH_P	$50x10^3$	J/mol
	Absorptivity (initiator)	ε	0.15	m^3/mol-m
	Initiation quantum yield	ϕ_i	0.6	-
	Diffusion coefficient (monomer)	D_M	$1x10^{-3}$	m^2/s
	Diffusion coefficient (radical)	$D_{P.}$	1	m^2/s
	Diffusion coefficient (initiator)	D_S	1	m^2/s
	Diffusion coefficient (oxygen)	D_O	$49x10^{-7}$	m^2/s
	Coefficient of thermal expansion (monomer)	α_M	0.0005	1/K
	Coefficient of thermal expansion (polymer)	α_P	0.000075	1/K
	Glass transition temperature (monomer)	Tg_M	213.15	K
	Glass transition temperature (polymer)	Tg_P	351.15	K
	Heat capacity (monomer)	C_{PM}	$C_{P,M} = 5.6 \times T(K) + 218.6$	J/kg-K
	Heat capacity (polymer)	C_{PP}	$C_{P,P} = 9.1 \times T(K) - 1535.5$	J/kg-K
	Heat capacity (curing system)	C_P	$C_P = C_{P,M}(1-X) + C_{P,P}X$	J/kg-K
	Density (monomer)	ρ_M	$1109/(1+\alpha_M(T-298))$	kg/m^3
	Density (polymer)	ρ_P	$1200/(1+\alpha_P(T-308))$	kg/m^3
	Density (curing system)	ρ	$\rho = \rho_M\phi_M + \rho_P(1-\phi_M)$	kg/m^3
Resin Composition	Monomer concentration	[M]	4298	mol/m^3
	Initiator concentration	[S]	0.25-8.0	wt%
	Oxygen concentration	[O]	$1x10^{-3}$	mol/m3

Table A.3: The Parameters Used for to Simulate the Photopolymerization Process of SR256 [11, 71, 95]

	Parameters	Symbols	Values	Units
Model Parameters	Parameter for propagation rate	A_p	0.66	-
	Parameter for termination rate	A_t	1.2	-
	Pre-exponential factor	A_{Ep}	1600	m^3/mol-s
	Pre-exponential factor	Aet	3600	m^3/mol-s
	Activation energy	E_p	18230	J/mol
	Activation energy	E_t	2940	J/mol
	Reaction diffusion constant	R_{rd}	0.002	m^3/mol
	Thermal convection coefficient	h	4.18	W/m^2-K
	Chamber temperature	Ta	300.48	K
Laser Parameters	Wavelength	λ	356	nm
	Beam radius	w_o	1.1×10^{-4}	m
Material Properties	Thermal conductivity	k	0.142	W/m-K
	Heat of polymerization	ΔH_P	50×10^3	J/mol
	Absorptivity (initiator)	ε	0.15	m^3/mol-m
	Initiation quantum yield	ϕ_i	0.6	-
	Diffusion coefficient (monomer)	D_M	1×10^{-3}	m^2/s
	Diffusion coefficient (radical)	$D_{P\cdot}$	1	m^2/s
	Diffusion coefficient (initiator)	D_S	1	m^2/s
	Diffusion coefficient (oxygen)	D_O	49×10^{-7}	m^2/s
	Coefficient of thermal expansion (monomer)	α_M	0.0005	1/K
	Coefficient of thermal expansion (polymer)	α_P	0.000075	1/K
	Glass transition temperature (monomer)	Tg_M	219.15	K
	Glass transition temperature (polymer)	Tg_P	451.15	K
	Heat capacity (monomer)	C_{PM}	$C_{P,M} = 5.6 \times T(K) + 218.6$	J/kg-K
	Heat capacity (polymer)	C_{PP}	$C_{P,P} = 9.1 \times T(K) - 1535.5$	J/kg-K
	Heat capacity (curing system)	C_P	$C_P = C_{P,M}(1-X) + C_{P,P}X$	J/kg-K
	Density (monomer)	ρ_M	$1013/(1+\alpha_M(T-298))$	kg/m^3
	Density (polymer)	ρ_P	$1115/(1+\alpha_P(T-308))$	kg/m^3
	Density (curing system)	ρ	$\rho = \rho_M \phi_M + \rho_P(1-\phi_M)$	kg/m^3
Resin Composition	Monomer concentration	[M]	5389	mol/m^3
	Initiator concentration	[S]	0.25-8.0	wt%
	Oxygen concentration	[O]	1×10^{-3}	mol/m3

APPENDIX-B

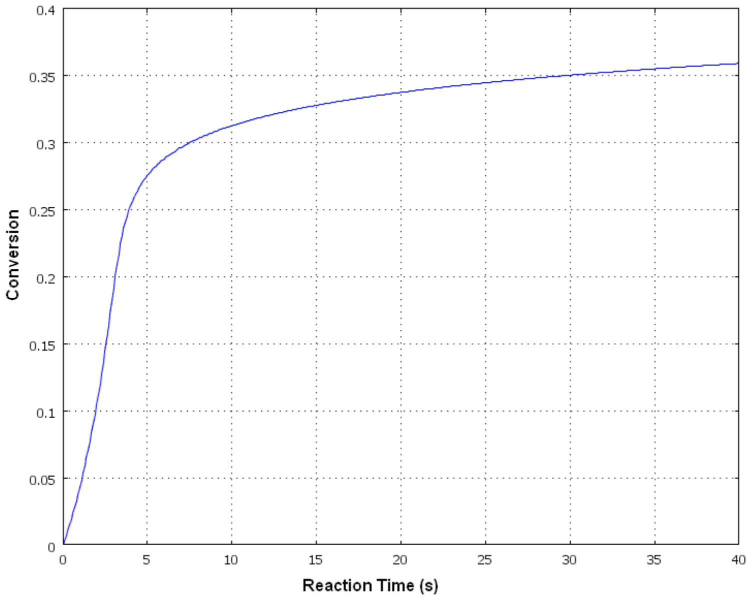

Figure B.1: Conversion Versus Time Curve for the Oxygenated Photopolymerization of SR494 Obtained from the 1-D PDE Model at 60 µm UV Light Penetration Depth ($[S]_0$=5%)

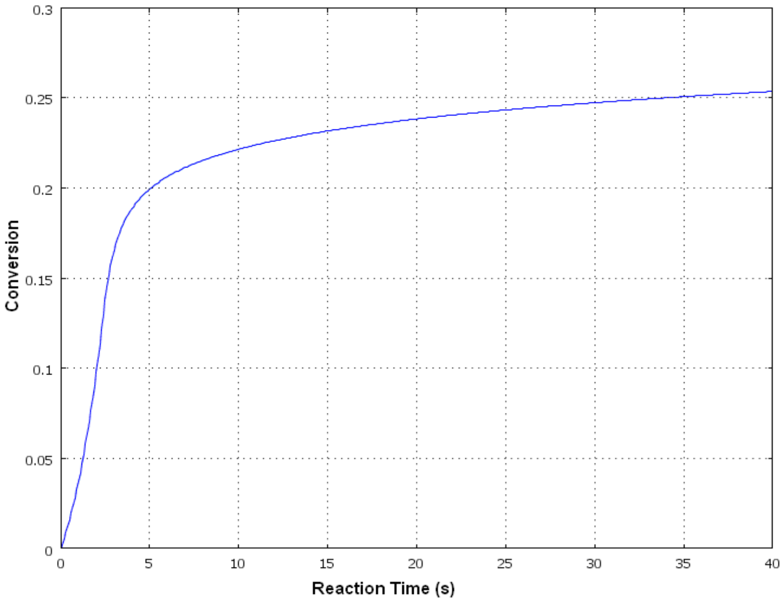

Figure B.2: Conversion Versus Time Curve for the Oxygenated Photopolymerization of SR351 Obtained from the 1-D PDE Model at 60 µm UV Light Penetration Depth ($[S]_0$=5%)

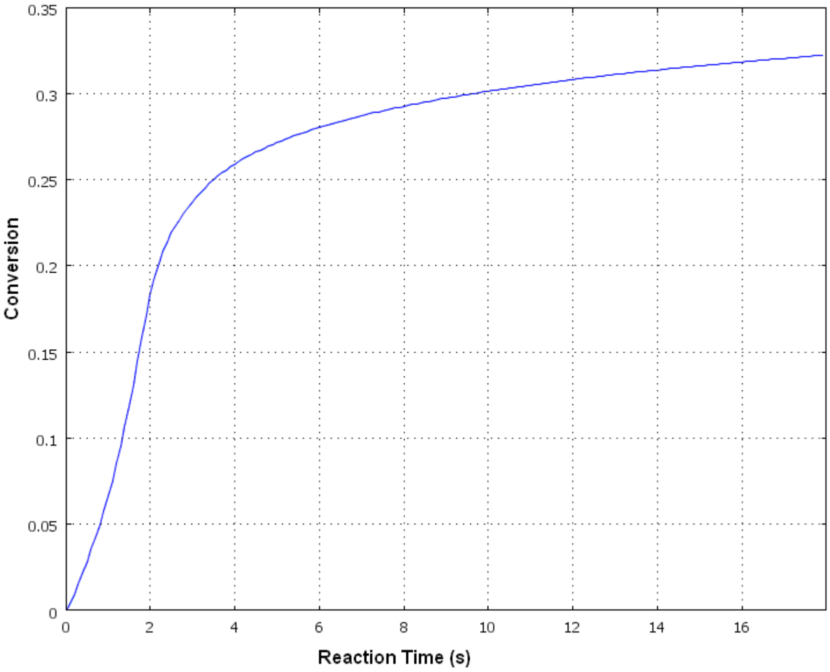

Figure B.3: Conversion Versus Time Curve for the Oxygenated Photopolymerization of SR272 Obtained from the 1-D PDE Model at 60 µm UV Light Penetration Depth ($[S]_0$=5%)

APPENDIX-C

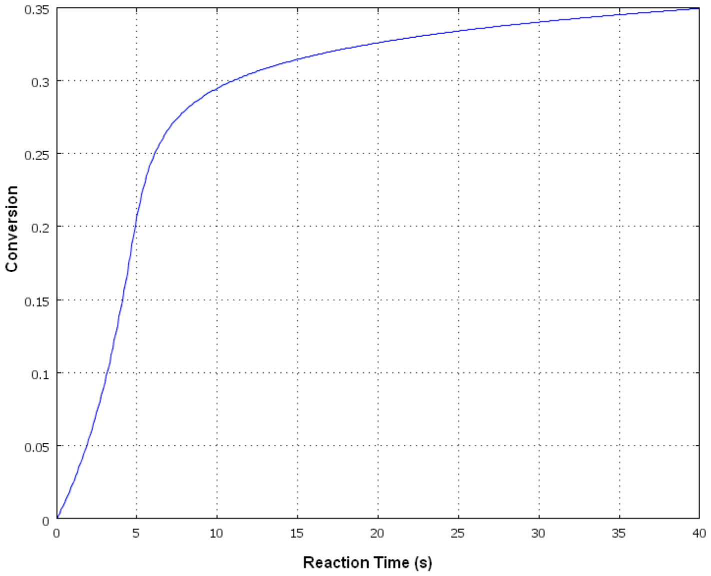

Figure C.1: Conversion Versus Time Curve for the Oxygenated Photopolymerization of SR494 Obtained from the 1-D PDE Model at 60 µm UV Light Penetration Depth ($[S]_0$=2%)

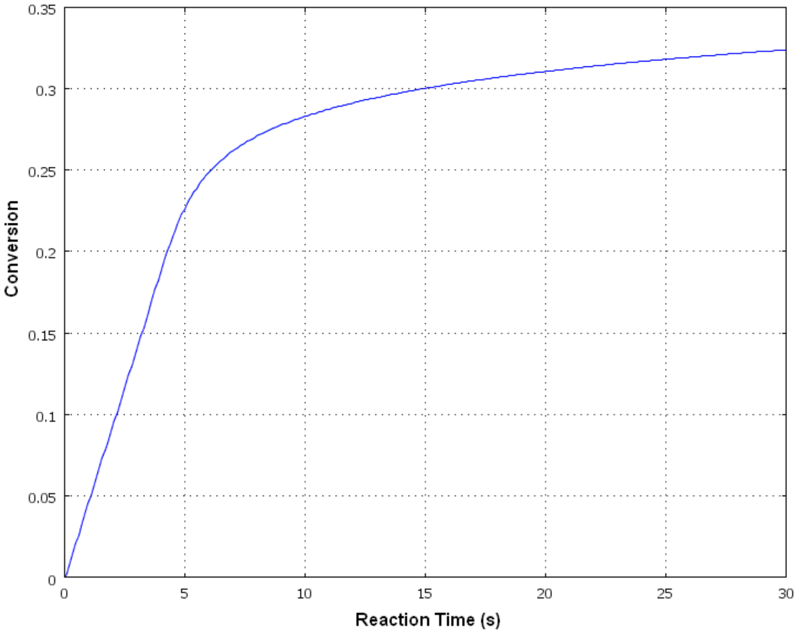

Figure C.2: Conversion Versus Time Curve for the Deoxygenated Photopolymerization of SR494 Obtained from the 1-D PDE Model at 60 µm UV Light Penetration Depth ($[S]_0$=2%)

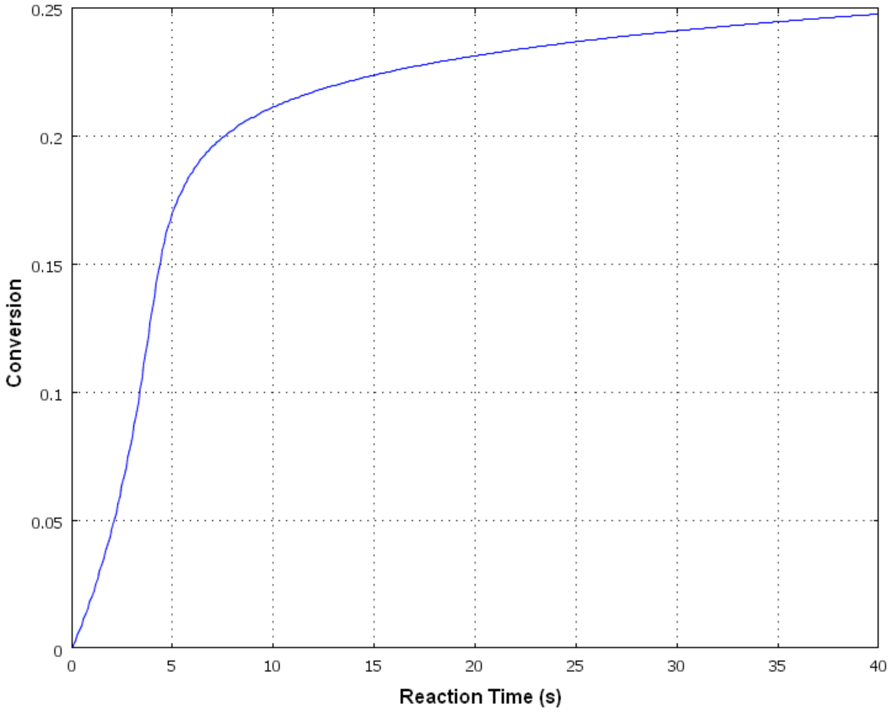

Figure C.3: Conversion Versus Time Curve for the Oxygenated Photopolymerization of SR351 Obtained from the 1-D PDE Model at 60 μm UV Light Penetration Depth ($[S]_0=2\%$)

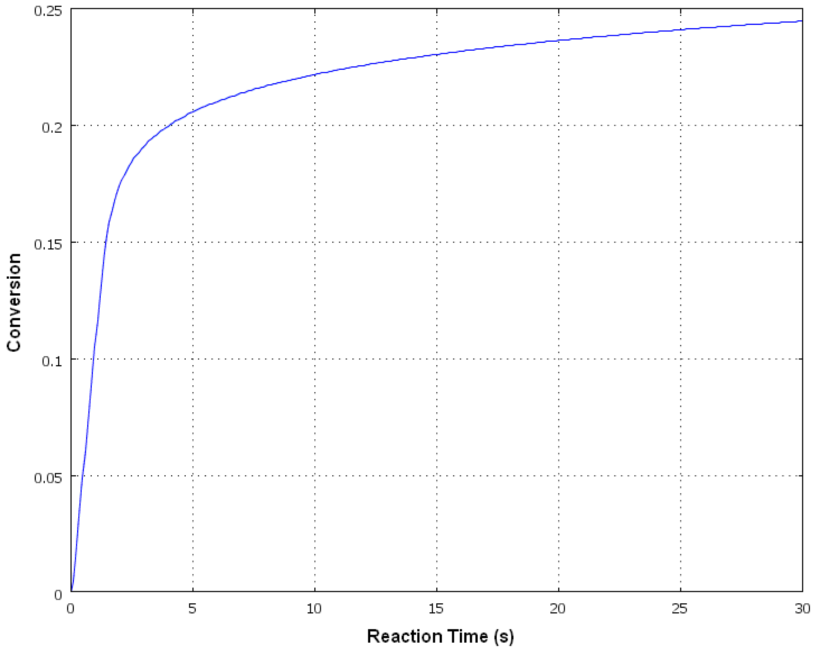

Figure C.4: Conversion Versus Time Curve for the Deoxygenated Photopolymerization of SR351 Obtained from the 1-D PDE Model at 60 μm UV Light Penetration Depth ($[S]_0=2\%$)

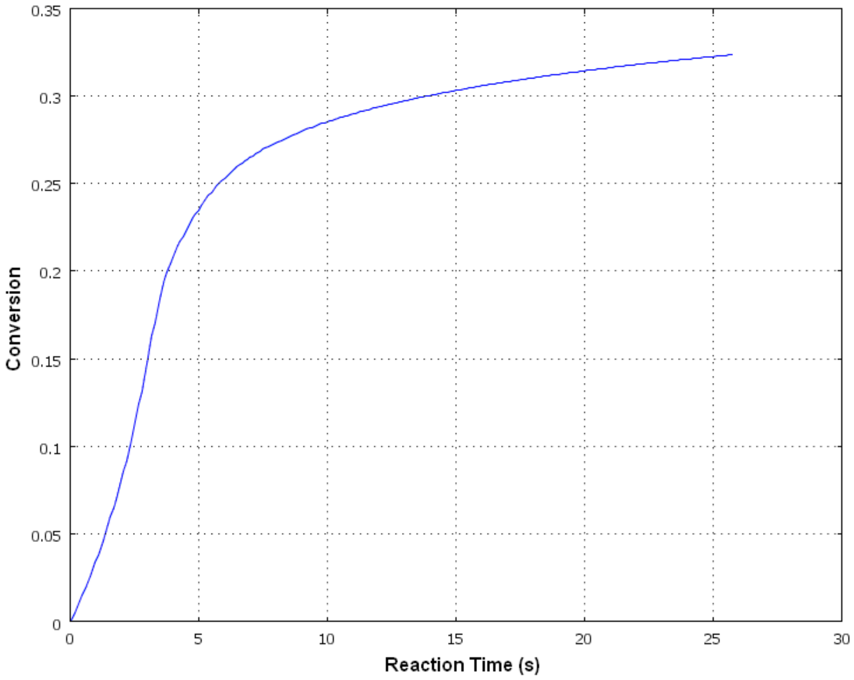

Figure C.5: Conversion Versus Time Curve for the Oxygenated Photopolymerization of SR272 Obtained from the 1-D PDE Model at 60 µm UV Light Penetration Depth ($[S]_0$=2%)

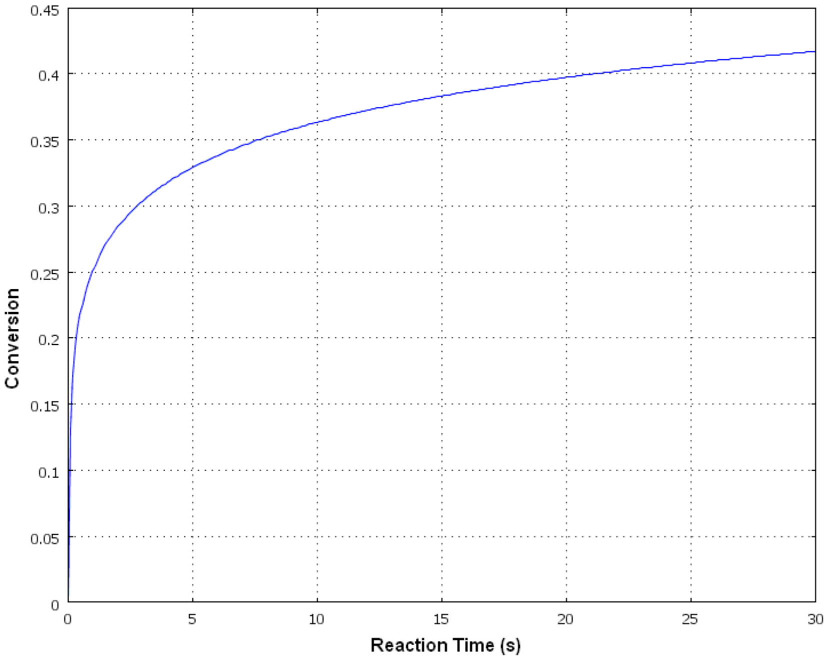

Figure C.6: Conversion Versus Time Curve for the Deoxygenated Photopolymerization of SR272 Obtained from the 1-D PDE Model at 60 µm UV Light Penetration Depth ($[S]_0$=2%)

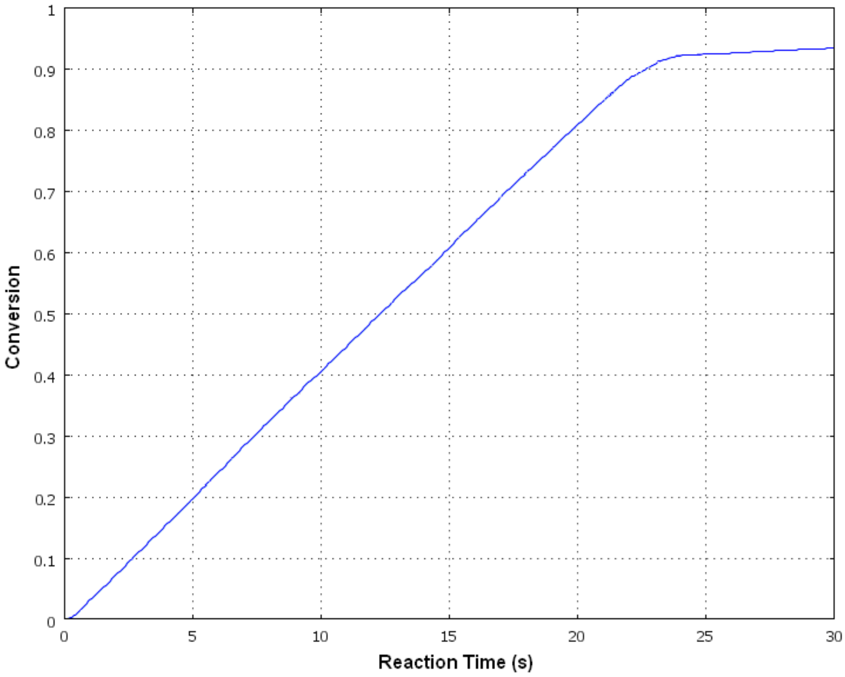

Figure C.7: Conversion Versus Time Curve for the Oxygenated Photopolymerization of SR256 Obtained from the 1-D PDE Model at 60 µm UV Light Penetration Depth ($[S]_0$=2%)

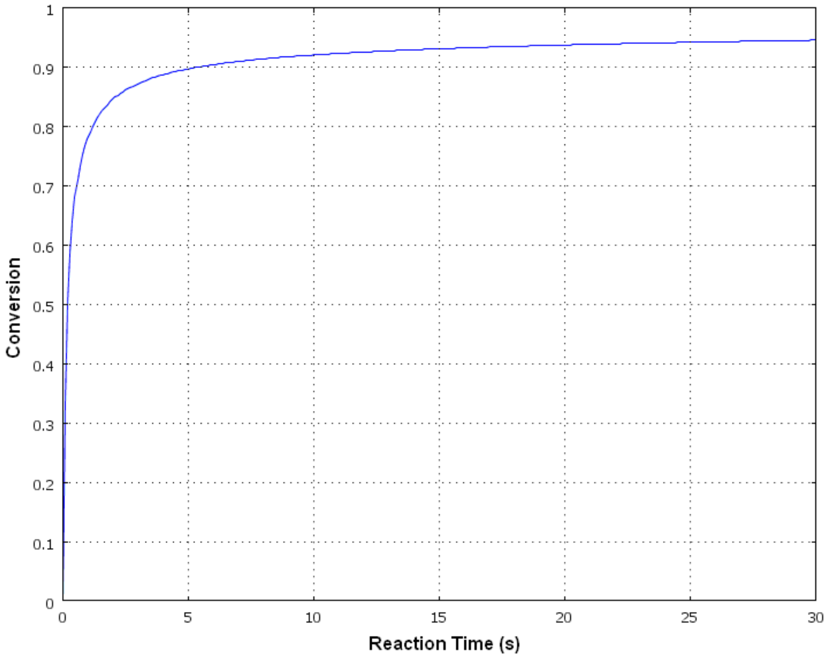

Figure C.8: Conversion Versus Time Curve for the Deoxygenated Photopolymerization of SR256 Obtained from the 1-D PDE Model at 60 µm UV Light Penetration Depth ($[S]_0$=2%)

APPENDIX-D

```
PROGRAM CLDT
   implicit none
   integer,parameter ::ngrp=1,neqn=100,gp=5
integer(I4B) :: it,itN
  real(DP) :: Iinc,wtCT,Ski,rhom,rhop,rhocta
  real(DP) :: kt0,kp0,kclc,ktp,Mo,Lambda,MWinit,eff,eps0,Tgm,Tgp,Temp
  real(DP) :: wtpct,a,gamma,kct1,Ap,At,fcp,fct,alpham,alphap
  real(DP) :: RDP,q,MWMon;I0,eps,t,dt,TT,kpavga,kpavgb,kpavg,ktavg,Rp
  real(DP) :: dtd,kpread1,kpread2,kpread,Rtotd1,Conva,Convb,Conv
  real(DP) :: Rtotd2,Rtotd,Mon2d,Mond;Rtota,Rtotb,Rtot,Rptot,Rttot
  real(DP) :: kdis,SIo2,SIa,SIb,SI,Ri0,Ria,Rib,Ri,Mona,Monb,Mon
  real(DP) :: ffva,ffvb,ffv,ffvm,ffvp,phima,phimb,phim,DeaMin
  real(DP) :: invffva,invffvb,invffv,Sumdis,Right,Artir,dumb
  real(DP) :: R1inva,R1invb,R1inv,R2inva,R2invb,R2inv
  real(DP),dimension(ngrp,neqn) :: Ra,Rb,R;Terma,Termb,Term,Disp,kcla,kclb,kcl
  real(DP),dimension(ngrp,neqn) :: RGa,RGb,RG;kpa,kpb,kp,Gelprb,Poly
  read(*,*) TT,dt,Iinc,Ski,rhom,rhop,a,gamma
  read(*,*) kt0,kp0,kclc,ktp,Mo,Lambda
  read(*,*) MWinit,eff,wtpct,eps0,Ap,At,fcp,fct
  read(*,*) Tgm,Tgp,Temp,RDP,q,MWMon,alpham,alphap
   SIo2 = (wtpct*rhom*10.00)/MWinit;I0=(Iinc*Lambda*1.0D-9)/(0.11960*1000.00)
   ffvm=0.0250+alpham*(Temp-Tgm;ffvp=0.025d0+alphap*(Temp-Tgp)
   Mon=Mo;eps=2.3030*eps0;kdis=1000.00*eps*I0;Right=0.05;Artir=1.0d0
   Ri0=2000.00*eff*eps*I0;SI=SIo2;Ri=Ri0*SI*(exp(-1.0d0*kdis*t))**q
DO IR =1,ngrp
 DO IC = 1,neqn
  R(ig,ie)=0.0d0;Ra(ig,ie)=0.0d0;Rb(ig,ie)=0.0d0;RG(ig,ie)=0.0d0
  kcl(ig,ie)=0.0d0;kcla(ig,ie)=0.0d0;kclb(ig,ie)=0.0d0;RGa(ig,ie)=0.0d0
  Poly(ig,ie)=0.0d0;Disp(ig,ie)=0.0d0;RGb(ig,ie)=0.0d0
  enddo
enddo
kp(1,1)=kp0;kpavg=kp(1,1);kpavga=kpavg;kpavgb=kpavg
Rtot=0.0d0;Rptot=0.0d0;Rttot=0.0d0;Rtota=0.0d0;Rtotb=0.0d0
t=0.0d0;dumb=1.0d0;itN=int(TT/dt)
DO it=1,itN
t=t+dt
Mona = Mon
CALL RKcalc (dt,kpavga,kpavgb,kpavg,Rtota,Rtotb,Rtot,Monb,Mon)
      SIa = SI
CALL RKcalc (dt,kdis,kdis,kdis,dumb,dumb,dumb,SIb,SI)
            IF (q.eq.1) then
              Ria=Ri0*SIa;Rib=Ri0*SIb;Ri=Ri0*SI
            ELSEIF (q.eq.0) THEN
              Ria=Ri0*SIo2;Rib=Ri0*SIo2;Ri=Ri0*SIo2
            ENDIF
Conva=(Mo-Mona)/Mo;Convb=(Mo-Monb)/Mo;Conv=(Mo-Mon)/Mo
phima=(1.0d0-Conva)/((1.0d0-Conva)+(rhom*Conva/rhop))
phimb=(1.0d0-Convb)/((1.0d0-Convb)+(rhom*Convb/rhop))
phim=(1.0d0-Conv)/((1.0d0-Conv)+(rhom*Conv/rhop))
ffva=(ffvm*phima)+((ffvp)*(1.0d0-phima));ffvb=(ffvm*phimb)+((ffvp)*(1.0d0-phimb))
ffv =(ffvm*phim) +((ffvp)*(1.0d0-phim))
invffva = 1.0d0/ffva;invffvb=1.0d0/ffvb;invffv=1.0d0/ffv
   CALL KPcalc (kp0,kclc,fcp,Ap,gamma,ffva,ffvb,ffv,kpa,kpb,kp)
R1inva=RDP*kpavg*Mona;R1invb=RDP*kpavg*Monb;R1inv =RDP*kpavg*Mon
 R2inva=kt0*(exp(-At*((1.0d0/ffva)-(1.0d0/fct))))
 R2invb=kt0*(exp(-At*((1.0d0/ffvb)-(1.0d0/fct))))
```

```
R2inv=kt0*(exp(-At*((1.0d0/ffv)-(1.0d0/fct))))
DO IR= 1,ngrp
  DO IC=1,neqn
         Term(ig,ie)=0.0d0;Terma(ig,ie)=0.0d0;Termb(ig,ie)=0.0d0
           ENDDO
         ENDDO
CALL KTcalc (R1inv,R1inva,R1invb,R2inva,R2invb,R2inv,kt0,a,dt,&
         Ra,Rb,R,kcla,kclb,kcl,Terma,Termb,Term)
Sumdis = 0.0d0
CALL RAdcal(dt,kct,Ria,Rib,Ri,ktp,Mona,Monb,Mon,&
        Ra,Rb,R,Terma,Termb,Term,kpa,kpb,kp,Disp,Sumdis,&
        Poly,Rtota,Rtotb,Rtot)
CALL Prob (conv,ski,Gelprb)
         Rtot=0.0d0;Rptot=0.0d0;Rtota=0.0d0;Rtotb = 0.0d0
CALL Birth (Mon,kp,Ra,Rb,R,RGa,RGb,RG,Poly,Gelprb,&
           Rtota,Rtotb,Rtot,Rptot)
Rp = kp(1,1)*Mon*Rtot;kpavga = kpavg;kpavg = Rptot/Mon/Rtot
kpavgb=(kpavg+kpavga)/2.0d0;ktavg=Rttot/Rtot/Rtot
IF (t.ge.(Right*Artir)) THEN
        write(46,77)t,Conv
        write(47,77)Conv,Rp
         Artir = Artir + 1
77    format(8(1pe20.10))
END IF
ENDDO
STOP
END
Subroutine RKcalc(dtd,kpread1,kpread2,kpread,Rtotd1,Rtotd2,Rtotd,Mon2d,Mond)
   implicit none
   real(DP) :: dtd,Rtotd1,Rtotd2,Rtotd,Mon2d,Mond
   real(DP) :: kpread1,kpread2,kpread,Monad,Monbd,Moncd,Mondd
   Monad=dtd*(-1.0d0*kpread1*Mond*Rtotd1)
   Monbd=dtd*(-1.0d0*kpread2*(Mond+Monad*0.5d0)*Rtotd2)
   Moncd=dtd*(-1.0d0*kpread2*(Mond+Monbd*0.5d0)*Rtotd2)
   Mondd=dtd*(-1.0d0*kpread*(Mond+Moncd)*Rtotd)
   Mon2d=Mond+(Monad+(2.0d0*Monbd)+(2.0d0*Moncd)+Mondd)/12.0d0
   Mond =Mond+(Monad+(2.0d0*Monbd)+(2.0d0*Moncd)+Mondd)/6.0d0
Return
END
   Subroutine KPcalc(kp0,kclc,fcp,Ap,gamma,ffva,ffvb,ffv,kpa,kpb,kp)
    implicit none
    integer(I4B) :: IR,IC
    real(DP) :: kp(ngrp,neqn),adder,kpa(ngrp,neqn),kpb(ngrp,neqn)
    real(DP) :: kp0,Ap,kclc,ffv,ffva,ffvb,fcp,gamma,man,i
    adder = 0.0d0
DO IR = 1,ngrp
 DO IC = 1,neqn
   man = gp**(IR-1);i=IC*man+adder
kp(IR,IC)=kp0/ man/(1.0d0+  &
  ((1+(1.0d0*kclc)/i)**gamma*exp(Ap*((1.0d0/ffv)-(1.0d0/fcp)))))
kpa(IR,IC)=kp0/ man/(1.0d0 +  &
((1+(1.0d0*kclc)/i)**gamma*exp(Ap*((1.0d0/ffva)-(1.0d0/fcp)))))
kpb(IR,IC)=kp0/ man/(1.0d0 +  &
  ((1+(1.0d0*kclc)/i)**gamma*exp(Ap*((1.0d0/ffvb)-(1.0d0/fcp)))))
 ENDDO
         adder = i
   ENDDO
RETURN
END
 Subroutine Prob (conv,ski,Gelprb)
```

```
    implicit none
    integer(I4B) :: IR,IC,i
    real(DP) :: Gelprb(ngrp,neqn),conv,FAout,ski,board,gig,geal
    FAout = 3.0d0
    IF (conv.gt.0.0d0) THEN
    FAout = ((1.0d0-ski) /ski/conv) + 0.25d0
    END IF
    IF (FAout.lt.2.0d0) THEN
    board=((sqrt(FAout)-0.50d0)**2+((1.0d0-conv)/conv))&
                /(((1.0d0-conv)/conv) + 1.0d0 )
          geal = 0
          DO IR = 1,ngrp
            DO IC= 1,neqn
               gig = gp**(IR-1);i = IC*gig + geal
               Gelprb(IR,IC) = 1.0d0 - board**i
             ENDDO
                  geal = i
           ENDDO
    endif
    Return
    END
Subroutine KTcalc (R1inva,R1invb,R1inv,R2inva,R2invb,R2inv,&
             kt0,a,dt,Ra,Rb,R,kcla,kclb,kcl,Terma,Termb,Term)
  implicit none
real(DP) :: adder,adder2;Term(ngrp,neqn),Terma(ngrp,neqn),Termb(ngrp,neqn)
real(DP) :: kcl(ngrp,neqn),R(ngrp,neqn),Ra(ngrp,neqn),Rb(ngrp,neqn)
real(DP) :: kcla(ngrp,neqn),kclb(ngrp,neqn),R2inv,R1inv,i,j
real(DP) :: R1inva,R1invb,R2inva,R2invb,kt0,a,dt,tar,alt
integer(I4B) :: IR,IR1,IC,IC1
adder = 0.0d0;adder2 = 0.0d0
DO IR = 1,ngrp
  DO IC= 1,neqn
     alt = gp**(IR-1);i = IC*alt + adder
           DO IR1 = 1,ngrp
             DO IC1 = 1,neqn
                     tar = gp**(IR1-1)
                     j = IC1*tar + adder2
kcla(IR1,IC1) = Ra(IR1,IC1)*(1.0d0/((1.0d0/kt0)+(1.0d0/(R1inv+(R2inv* &
             0.5d0*((1.0d0/(i**a))+(1.0d0/(j**a))))))))
kclb(IR1,IC1) = Rb(IR1,IC1)*(1.0d0/((1.0d0/kt0)+(1.0d0/(R1inv+(R2inv* &
             0.5d0*((1.0d0/(i**a))+(1.0d0/(j**a))))))))
kcl(IR1,IC1) = R(IR1,IC1)*(1.0d0/((1.0d0/kt0)+(1.0d0/(R1inv+(R2inv* &
             0.5d0*((1.0d0/(i**a))+(1.0d0/(j**a))))))))
Term(IR,IC)=Term(IR,IC)+kcl(IR1,IC1);Terma(IR,IC)=Terma(IR,IC)+kcla(IR1,IC1)
Termb(IR,IC)=Termb(IR,IC)+kclb(IR1,IC1)
             ENDDO
           adder2 =  j
           ENDDO
           adder2 = 0.0d0
      ENDDO
           adder = i
    ENDDO
Return
END
Subroutine CTpcal (Poly,Disp,Sumdis)
implicit none
real(DP) :: Disp(ngrp,neqn),Poly(ngrp,neqn),bigz,leafz,Sumdis,i
integer(I4B) :: IR,IC
leafz = 0.0d0
  DO IR = 1,ngrp
```

```
    DO IC= 1,neqn
         bigz = gp**(IR-1);i=IC*bigz+leafz
         Disp(IR,IC)=Poly(IR,IC)*i;Sumdis = Sumdis + Disp(IR,IC)
       ENDDO
         leafz = i
     ENDDO
Return
END
Subroutine RAdcal(dt,kct,Ria,Rib,Ri,ktp,Mona,Monb,Mon,Poly,Rtota,&
        Ra,Rb,R,Terma,Termb,Term,kpa,kpb,kp,Disp,Sumdis,Rtotb,Rtot)
implicit none
real(DP) :: Ra(ngrp,neqn),Rb(ngrp,neqn),R(ngrp,neqn),Poly(ngrp,neqn)
real(DP) :: Terma(ngrp,neqn),Termb(ngrp,neqn),Term(ngrp,neqn),IR,IC
real(DP) :: kpa(ngrp,neqn),kpb(ngrp,neqn),kp(ngrp,neqn),Disp(ngrp,neqn)
real(DP) :: Sumdis,dt,ktp,Ria,Rib,Ri,Mona,Monb,Mon,Rtota,Rtotb,Rtot
real(DP) :: R1,R2,R3,R4,R5,R6,R7,R8,R9,R10,R11,R12,R13,R14,R15,R16
real(DP) :: D1,D2,D3,D4,D5,D6,D7,D8,D9,D10,D11,D12,D13,D14,D15,D16
real(DP) :: P1,P2,P3,P4,P5,P6,P7,P8,P9,P10,P11,P12,P13,P14,P15,P16
real(DP) :: RT1,RT2,RT3,RT4,RT5,RT6,RT7,RT8,RT9,RT10,RT11,RT12,RT13
real(DP) :: RT14,RT15,RT16
DO IR = 1,ngrp
  DO IC= 1,neqn
         Ra(IR,IC) = R(IR,IC)
         IF ((IR.eq.1).AND.(IC.eq.1)) THEN
          D1 = dt*((ktp*R(IR,IC)*Sumdis)-(ktp*Disp(IR,IC)*Rtota))
          P1 = dt*Terma(IR,IC)*R(IR,IC)
          R1=dt*(Ria-(kpa(IR,IC)*Mona*R(IR,IC)))-P1-D1
          D2 =dt*((ktp*(R(IR,IC)+R1*0.5d0)*Sumdis)-(ktp*Disp(IR,IC)*Rtotb))
          P2 = dt*Termb(IR,IC)*( R(IR,IC)+R1*0.5d0)
          R2 = dt*(Rib+ -(kpb(IR,IC)*Monb*(R(IR,IC)+R1*0.5d0)))-P2-D2
          D3 = dt*((ktp*(R(IR,IC)+R2*0.5d0)*Sumdis)-(ktp*Disp(IR,IC)*Rtotb))
          P3 = dt*Termb(IR,IC)*(R(IR,IC)+R2*0.5d0)
          R3 = dt*(Rib -(kpb(IR,IC)*Monb*(R(IR,IC)+R2*0.5d0)))-P3-D3
          D4 = dt*((ktp*(R(IR,IC)+R3)*Sumdis)-(ktp*Disp(IR,IC)*Rtot))
          P4 = dt*Term(IR,IC)*(R(IR,IC)+R3)
          R4 = dt*(Ri- (kp(IR,IC)*Mon*(R(IR,IC)+R3)))-P4-D4
    Poly(IR,IC)=Poly(IR,IC)+((P1+2.0d0*P2+2.0d0*P3+P4)/6.0d0)
    Rb(IR,IC)= R(IR,IC)+((R1+2.0d0*R2+2.0d0*R3+R4)/12.0d0)
    R(IR,IC) = R(IR,IC)+((R1+2.0d0*R2+2.0d0*R3+R4)/6.0d0)
    ELSE IF ((IR.eq.ngrp).AND.(IC.eq.neqn)) THEN
          D5 = dt *((ktp*R(IR,IC)*Sumdis)-(ktp*Disp(IR,IC)*Rtota))
          P5 = dt*Terma(IR,IC)*R(IR,IC)
          R5 = dt*(kpa(IR,IC)* Mona*Ra(IR,IC-1) )-P5-D5
          D6 = dt*((ktp*(R(IR,IC)+R5*0.5d0)*Sumdis)-(ktp*Disp(IR,IC)*Rtotb))
          P6 = dt*Termb(IR,IC)*(R(IR,IC)+R5*0.5d0)
          R6 = dt*( kpb(IR,IC)*Monb*Rb(IR,IC-1) )-P6-D6
          D7 = dt*((ktp*(R(IR,IC)+R6*0.5d0)*Sumdis)-(ktp*Disp(IR,IC)*Rtotb))
          P7 = dt*Termb(IR,IC)*(R(IR,IC)+R6*0.5d0)
          R7 = dt* ( kpb(IR,IC)* Monb*Rb(IR,IC-1) )- P7 - D7
          D8 = dt*((ktp*(R(IR,IC)+R7)*Sumdis)-(ktp*(Disp(IR,IC))*Rtot))
          P8 = dt*Term(IR,IC)*(R(IR,IC)+R7)
          R8 = dt*( kp(IR,IC)*Mon*Rb(IR,IC-1))-P8-D8
     Poly(IR,IC) = Poly(IR,IC)+((P5+2.0d0*P6+2.0d0*P7+P8)/6.0d0)
     Rb(IR,IC) = R(IR,IC)+((R5+2.0d0*R6+2.0d0*R7+R8)/12.0d0)
     R(IR,IC) = R(IR,IC)+((R5+2.0d0*R6+2.0d0*R7+R8)/6.0d0)
         ELSE IF ( IC.eq.1 ) THEN
          D9 = dt*((ktp*(R(IR,IC))*Sumdis)-(ktp*Disp(IR,IC)*Rtota))
          P9 = dt*Terma(IR,IC)*R(IR,IC)
      R9 = dt*((kpa(IR-1,neqn)*Mona*Ra(IR-1,neqn))-(kp(IR,IC)*Mona*R(IR,IC)))-P9-D9
                   D10 = dt*((ktp*(R(IR,IC)+R9*0.5d0)*Sumdis)-(ktp*Disp(IR,IC)*Rtotb))
```

```
                    P10 = dt*Termb(IR,IC)*(R(IR,IC)+R9*0.5d0)
R10=dt*((kpb(IR-1,neqn)*Monb*Rb(IR-1,neqn))-kp(IR,IC)*Monb*(R(IR,IC)+R9*0.5d0)))-P10-D10
                    D11 = dt*((ktp*(R(IR,IC)+R10*0.5d0)*Sumdis)-(ktp*Disp(IR,IC)*Rtotb))
                    P11 = dt*Termb(IR,IC)*(R(IR,IC)+R10*0.5d0)
R11=dt*((kpb(IR-1,neqn)*Monb*Rb(IR-1,neqn))-kp(IR,IC)*Monb*(R(IR,IC)+R10*0.5d0)))-P11&
-D11
                   D12 = dt*((ktp*(R(IR,IC)+R11)*Sumdis)-(ktp*Disp(IR,IC)*Rtot))
                   P12 = dt*Term(IR,IC)*(R(IR,IC)+R11)
          R12 = dt*((kp(IR-1,neqn)*Mon*R(IR-1,neqn))-(kp(IR,IC)*Mon*(R(IR,IC)+R11)))-P12-D12
               Poly(IR,IC) = Poly(IR,IC)+((P9+2.0d0*P10+2.0d0*P11+P12)/6.0d0)
               Rb(IR,IC) = R(IR,IC)+((R9+2.0d0*R10+2.0d0*R11+R12)/12.0d0)
             R(IR,IC) = R(IR,IC)+((R9+2.0d0*R10+2.0d0*R11+R12)/6.0d0)
                             ELSE
                   D13 = dt*((ktp*(R(IR,IC))*Sumdis)-(ktp*Disp(IR,IC)*Rtota))
                   P13 = dt*Terma(IR,IC)*R(IR,IC)
                   R13=dt*(kpa(IR,IC)*Mona*(Ra(IR,IC-1)-R(IR,IC)))-P13-D13
                   D14 = dt*((ktp*(R(IR,IC)+R13*0.5d0)*Sumdis)-(ktp*Disp(IR,IC)*Rtotb))
                   P14 = dt*Termb(IR,IC)*(R(IR,IC)+R13*0.5d0)
                   R14=dt*((kpb(IR,IC)*Monb*(Rb(IR,IC-1)-(R(IR,IC)+R13*0.5d0))))-P14 -D14
                   D15 = dt*((ktp*(R(IR,IC)+R14*0.5d0)*Sumdis)-(ktp*Disp(IR,IC)*Rtotb))
                   P15 = dt*Termb(IR,IC)*(R(IR,IC)+R14*0.5d0)
                   R15=dt*((kpb(IR,IC)*Monb*(Rb(IR,IC-1)-(R(IR,IC)+R14*0.5d0))))-P15-D15
                   D16 = dt*( (ktp*(R(IR,IC)+R15)*Sumdis)-(ktp*Disp(IR,IC)*Rtot))
                   P16 = dt*Term(IR,IC)*(R(IR,IC)+R15)
                   R16 = dt*((kp(IR,IC)*Mon*(R(IR,IC-1)-(R(IR,IC)+R15))))-P16-D16
              Poly(IR,IC) = Poly(IR,IC)+((P13+2.0d0*P14+2.0d0*P15+P16)/6.0d0)
              Rb(IR,IC) =R(IR,IC)+((R13+2.0d0*R14+2.0d0*R15+R16)/12.0d0)
              R(IR,IC) =R(IR,IC)+((R13+2.0d0*R14+2.0d0*R15+R16)/6.0d0)
                             END IF
            ENDDO
          ENDDO
          Return
          END
          Subroutine RTcalc (a,kt0,R1inv,R2inv,R,Rttot)
          implicit none
          real(DP) :: kcl6(ngrp,neqn);R(ngrp,neqn),Rttot,R1inv,R2inv,a
          real(DP) :: gig,geal,adder,adder2,kt0,i,j
          integer(I4B) :: IR,IC,IR1,IC1
          adder = 0.0d0;adder2 =0.0d0
          DO IR = 1,ngrp
            DO IC= 1,neqn
                   gig = gp**(IR-1);i=IC*gig + adder
               DO IR1 = 1,ngrp
                 DO IC1 = 1,neqn
                      geal = gp**(IR1-1);j=IC1*geal + adder2
          kcl6(IR1,IC1)=((R(IR,IC)*R(IR1 ,IC1)*(1.0d0/((1.0d0/kt0)+(1.0d0/(R1inv+(R2inv* &
                                0.5d0*((1.0d0/(i**a))+(1.0d0/(j**a))) )))))))
                             Rttot = Rttot + kcl6(IR1,IC1)
                              ENDDO
                     adder2 = j
                        ENDDO
                   adder2 = 0.0d0
               ENDDO
          adder =  i
             ENDDO
          Return
          END
```

APPENDIX-E

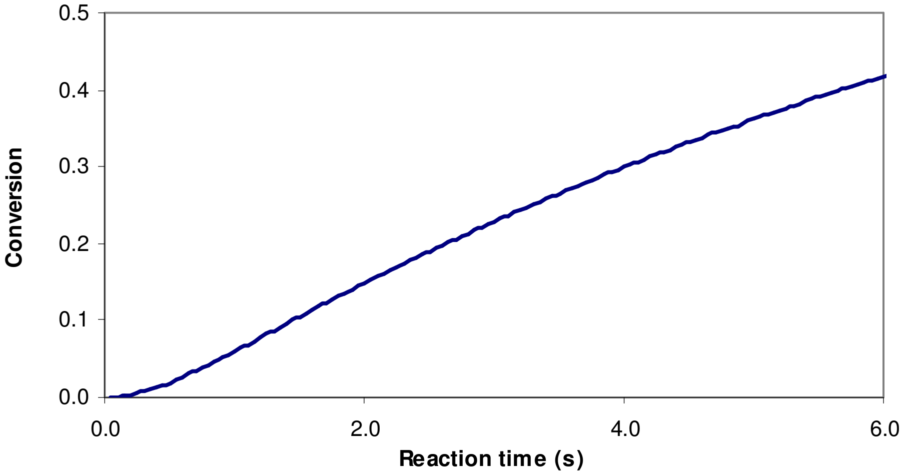

Figure E.1: Conversion Versus Time Curve for the Deoxygenated Photopolymerization of SR494 Obtained from the ODE Model ($[S]_0$=2%)

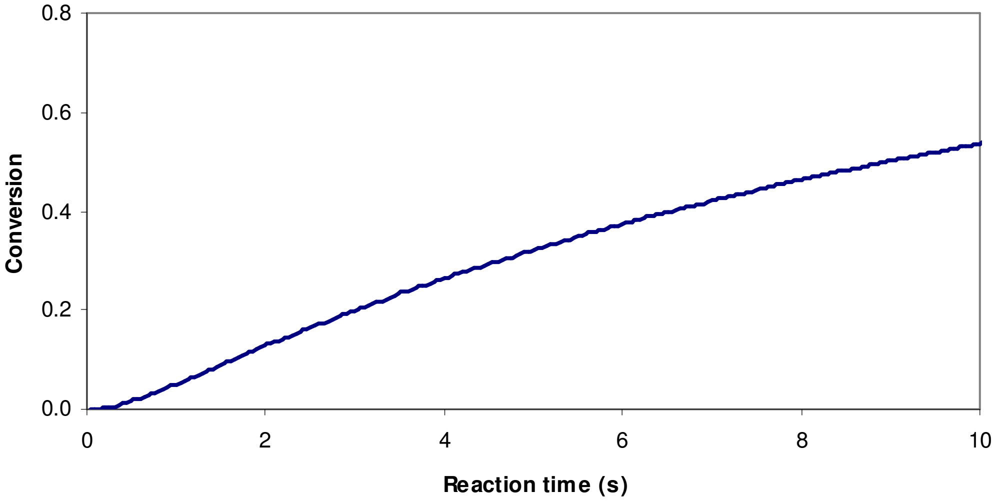

Figure E.2: Conversion Versus Time Curve for the Deoxygenated Photopolymerization of SR351 Obtained from the ODE Model ($[S]_0$=2%)

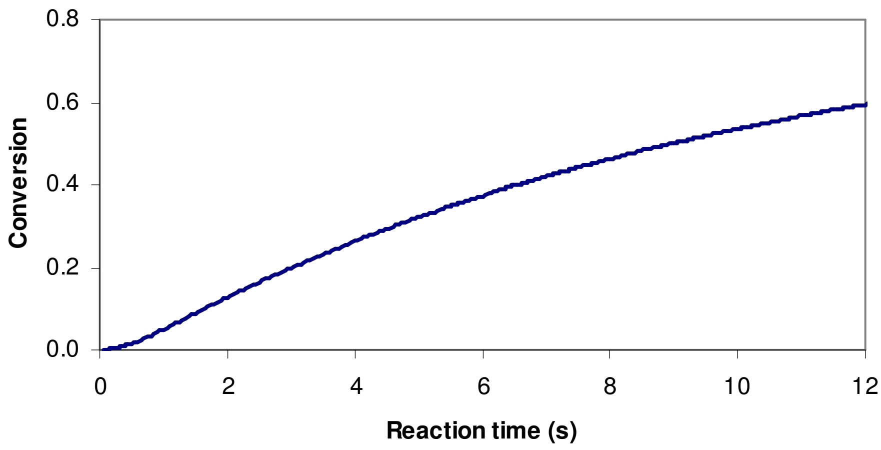

Figure E.3: Conversion Versus Time Curve for the Deoxygenated Photopolymerization of SR272 Obtained from the ODE Model ($[S]_0$=2%)

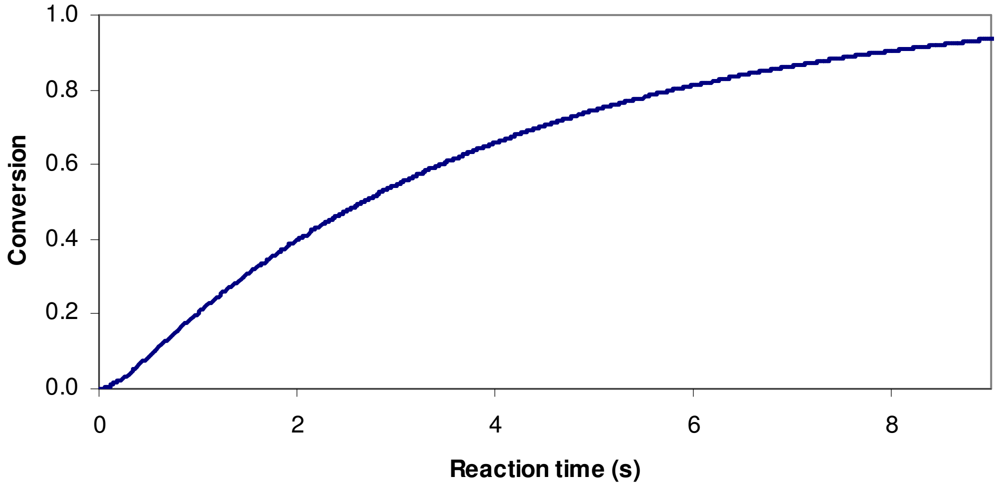

Figure E.4: Conversion Versus Time Curve for the Deoxygenated Photopolymerization of SR256 Obtained from the ODE Model ($[S]_0$=2%)

APPENDIX-F

```
program SMCM
!Main    program    calculates    the    conversion    values    of
!photopolymerization reaction as a function of reaction time with
!the stochastic Monte Carlo model.
        IMPLICIT NONE
     INTEGER, PARAMETER :: I4B = SELECTED_INT_KIND(9)
     INTEGER, PARAMETER :: DP = KIND(1.0D0)
     INTEGER, PARAMETER :: I2B = SELECTED_INT_KIND(4)
     INTEGER, PARAMETER :: I1B = SELECTED_INT_KIND(2)
     INTEGER, PARAMETER :: SP = KIND(1.0)
     INTEGER(I4B), PARAMETER :: MAX_MON=5000,MAX_INFO=10
     INTEGER(I4B), PARAMETER :: MAX_REAC_NUM=800000
     REAL(DP), PARAMETER :: R=8.314
     INTEGER(I4B), PARAMETER :: MAX_TUR=20000
     INTEGER(I4B) :: MON_LEFT,MAX_PR,md0,nbi,idn1,idn2,Initiator
     INTEGER(I4B) :: actrxn,rxnnum,i,j,k,ndsp,ndspy
     INTEGER(I4B) ::  i1,j1,k1,l1,n1,m1,i2,j2,k2,l2,rtyp,iia,iib
     INTEGER(I4B) ::  ymn,ydbn,yrn,mdbs,zero,one,two,three,BIN
     INTEGER(I4B) ::  ii,jj,ij,kk,iq,cyclnum,runsay,sumr,sumspn,rprb
     REAL(DP) ::  kpg,ktg,rkpg,kp,kt,rc,wbdr,greg1,greg2,greg
     REAL(DP) ::  R_TIME,kpg1,kpg2,pair,sumd,tempsum,mconv,dconv
     INTEGER(I4B),dimension(MAX_TUR) ::  mn,dbn,rn,spn,iseed
     INTEGER(I4B),dimension(MAX_TUR) ::  mnd,dbnd,rnd,spnd
     REAL(DP),dimension(1000) :: bt
     REAL(DP) :: M0,MWM,MWI,RouM,INITPER,INC,rand,xran,srand
     REAL(DP) :: AEp,AEt,Ep,Et,TEMP,kp0,kt0,RT,RST,dumy
     REAL(DP) :: rannumber1,rannumber2,ki,dn1,t1,dt1,tdbn
     REAL(SP),dimension(1000) :: rnmi
     REAL(DP),dimension(MAX_REAC_NUM,MAX_INFO) :: rxn
            read(8,*) R_TIME,mdbs,rc,ki,M0,MWM,MWI,RouM,INITPER
                  read(8,*) BIN,AEp,AEt,Ep,Et,TEMP,iseed,iq
                 zero=0;one=1;two=2;three=3
           kp0=AEp*exp(-Ep/(R*TEMP));kt0=AEt*exp(-Et/(R*TEMP))
      INC=(INITPER/MWI)*(RouM/(100-INITPER))*1000000.
      MAX_PR=nint((INITPER*MWM*MAX_MON)/((100.0-INITPER)*MWI        +
INITPER*MWM))
      do i=1,MAX_REAC_NUM
              do j=1,MAX_INFO
          rxn(i,j)=zero
              enddo
      enddo
             ndsp=two
             ki=ki*(1.0d0*MAX_PR/(mdbs*MAX_MON))
             BIN=one;nbi=BIN;mn(1)=one;dbn(1)=mdbs-one;rn(1)=one
             spn(1)=2*nbi;mn(2)=one;dbn(2)=mdbs;rn(2)=zero
             spn(2)=(MAX_MON-MAX_PR)-spn(1)
      do i=3,MAX_TUR
                 mn(i)=zero;dbn(i)=zero;rn(i)=zero;spn(i)=zero
             enddo
             do i=1,(MAX_PR-nbi-1)
                bt(i)=(log(((MAX_PR-nbi)*1.0d0)/(MAX_PR-nbi-i)))/ki
             enddo
             md0=0
             Do i=1,ndsp
             md0=md0+spn(i)*dbn(i)
      End do
             t1=bt(1);RST=t1;RT=0;iia=1;iib=iia+1
```

```
             xran=srand(iseed)
      cyclnum=0
      DO WHILE (RST<=R_TIME)
      cyclnum=cyclnum+1
      rxnnum=0
             do ii=1,ndsp
               do jj=ii,ndsp
                 if(  (spn(ii).eq.zero).or.(spn(jj).eq.zero)  )  goto
730
                     if( (ii.eq.jj).and.(spn(ii).eq.one) ) goto 730
           kpg1=kp*(1.0d0+15.8*exp(-1.0*log(2.0)*(mn(ii)-1)/(1.12)))
           kpg2=kp*(1.0d0+15.8*exp(-1.0*log(2.0)*(mn(jj)-1)/(1.12)))
                             if(ii.eq.jj) then
                             pair=0.5d0*spn(ii)*(spn(jj)-1)
                             else
                             pair=1.0d0*spn(ii)*spn(jj)
                             endif
                  if( (((rn(ii).ge.one).and.(dbn(jj).ge.one)).or. &
                      ((dbn(ii).ge.one).and.(rn(jj).ge.one))) ) then
                  rxnnum=rxnnum +1
                  rxn(rxnnum,1)=mn(ii)
                  rxn(rxnnum,2)=dbn(ii)
                  rxn(rxnnum,3)=rn(ii)
                  rxn(rxnnum,4)=spn(ii)
                  rxn(rxnnum,5)=mn(jj)
                  rxn(rxnnum,6)=dbn(jj)
                  rxn(rxnnum,7)=rn(jj)
                  rxn(rxnnum,8)=spn(jj)
                       rxn(rxnnum,9)=1

wbdr=1.0d0*(rn(ii)*dbn(jj)*kpg1+dbn(ii)*rn(jj)*kpg2)/  &

(rn(ii)*dbn(jj)+dbn(ii)*rn(jj)+rn(ii)*rn(jj)+rn(ii)*dbn(ii))
                     rxn(rxnnum,10)=1.0d0*wbdr*pair
                  endif
                  if( ((rn(ii).ge.one).and.(dbn(ii).ge.one)).and. &
                      (mdbs.gt.one) ) then
                  rxnnum=rxnnum +1
                  rxn(rxnnum,1)=mn(ii)
                  rxn(rxnnum,2)=dbn(ii)
                  rxn(rxnnum,3)=rn(ii)
                  rxn(rxnnum,4)=spn(ii)
                  rxn(rxnnum,5)=zero
                  rxn(rxnnum,6)=zero
                  rxn(rxnnum,7)=zero
                  rxn(rxnnum,8)=zero
                       rxn(rxnnum,9)=3
                wbdr=1.0d0*(rn(ii)*dbn(ii)*kpg1*rc)/ &

(rn(ii)*dbn(jj)+dbn(ii)*rn(jj)+rn(ii)*rn(jj)+rn(ii)*dbn(ii))
                     rxn(rxnnum,10)=1.0d0*wbdr*spn(ii)
                  endif
                  if( (rn(ii).ge.one).and.(rn(jj).ge.one) ) then
                    if( (mn(ii).le.100) ) then
                         greg1=kt*mn(ii)**(-0.5)
                    else
                         greg1=kt*(100)**(-0.34)*mn(ii)**(-0.16)
                    end if
                    if( (mn(jj).le.100) ) then
                         greg2=1.0d0*kt*mn(jj)**(-0.5)
                    else
```

```
                         greg2=1.0d0*kt*(100)**(-0.34)*mn(jj)**(-
0.16)
                    endif
                         ktg=sqrt(greg1*greg2)
                  rxnnum=rxnnum +1
                  rxn(rxnnum,1)=mn(ii)
                  rxn(rxnnum,2)=dbn(ii)
                  rxn(rxnnum,3)=rn(ii)
                  rxn(rxnnum,4)=spn(ii)
                  rxn(rxnnum,5)=mn(jj)
                  rxn(rxnnum,6)=dbn(jj)
                  rxn(rxnnum,7)=rn(jj)
                  rxn(rxnnum,8)=spn(jj)
                       rxn(rxnnum,9)=2
                 wbdr=1.0d0*(rn(ii)*rn(jj))/ &

(rn(ii)*dbn(jj)+dbn(ii)*rn(jj)+rn(ii)*rn(jj)+rn(ii)*dbn(ii))
                       rxn(rxnnum,10)=1.0d0*ktg*wbdr*pair
                       endif
      730     continue
             enddo
           enddo
      sumd=0
             if(rxnnum.eq.0) goto 999
      do i=1,rxnnum
      sumd=sumd+rxn(i,10)
      enddo
             rannumber1=rand(0)
             rannumber2=rand(0)
             rannumber2=rannumber2*sumd
             RT=(1.0/sumd)*log(1.0/rannumber1)
      tempsum=0
      do i = 1, rxnnum
           tempsum=tempsum+rxn(i,10)
        if(tempsum>=rannumber2) then
            actrxn=i
           exit
        end if
      enddo
           i1=int(rxn(actrxn,1))
           j1=int(rxn(actrxn,2))
           k1=int(rxn(actrxn,3))
           l1=int(rxn(actrxn,4))
           i2=int(rxn(actrxn,5))
           j2=int(rxn(actrxn,6))
           k2=int(rxn(actrxn,7))
           l2=int(rxn(actrxn,8))
           rtyp=int(rxn(actrxn,9))
           rprb=rxn(actrxn,10)
           if(rxn(actrxn,9).eq.three) then
              do i=1,ndsp
                if( (mn(i).eq.i1).and.(dbn(i).eq.j1).and. &
                   (rn(i).eq.k1) ) then
                   spn(i)=spn(i)-1
                  goto 160
                endif
              enddo
           endif
             do i=1,ndsp
               if( (mn(i).eq.i1).and.(dbn(i).eq.j1).and. &
                  (rn(i).eq.k1).and. &
```

```
             (i1.eq.i2).and.(j1.eq.j2).and. &
             (k1.eq.k2) ) then
             spn(i)=spn(i)-2
             goto 160
          endif
        enddo
        do i=1,ndsp
         if( (mn(i).eq.i1).and.(dbn(i).eq.j1).and. &
             (rn(i).eq.k1) ) then
             spn(i)=spn(i)-1
             goto 250
         endif
        enddo
250    continue
        do i=1,ndsp
         if( (mn(i).eq.i2).and.(dbn(i).eq.j2).and. &
            (rn(i).eq.k2) ) then
            spn(i)=spn(i)-1
            goto 160
         endif
        enddo
160    continue
 if (rtyp.eq.three) then
           ymn=nint(rxn(actrxn,1))
           ydbn=nint(rxn(actrxn,2))-1
           yrn=nint(rxn(actrxn,3))
        endif
 if (rtyp.eq.one) then
           ymn=nint(rxn(actrxn,1))+nint(rxn(actrxn,5))
           ydbn=nint(rxn(actrxn,2))+nint(rxn(actrxn,6))-1
           yrn=nint(rxn(actrxn,3))+nint(rxn(actrxn,7))
      endif
 if (rtyp.eq.two) then
           ymn=nint(rxn(actrxn,1))+nint(rxn(actrxn,5))
           ydbn=nint(rxn(actrxn,2))+nint(rxn(actrxn,6))
           yrn=nint(rxn(actrxn,3))+nint(rxn(actrxn,7))-2
        endif
         do kk=1,ndsp
             if((ymn.eq.mn(kk)).and.(ydbn.eq.dbn(kk)).and. &
                (yrn.eq.rn(kk))) then
                   spn(kk)=spn(kk)+1
                 go to 220
             end if
         enddo
              ndsp=ndsp+1
              mn(ndsp)=ymn
              dbn(ndsp)=ydbn
              rn(ndsp)=yrn
              spn(ndsp)=spn(ndsp)+1
220    continue
              if( spn(ndsp).gt.MAX_MON ) then
                 goto 999
              endif
 write(9+iq,*)'cycle #=',cyclnum
          ndspy=0
          do kk=1,ndsp
            if(spn(kk).gt.zero) then
                ndspy=ndspy+1
           mnd(ndspy)=mn(kk)
                dbnd(ndspy)=dbn(kk)
                rnd(ndspy)=rn(kk)
```

```
                     spnd(ndspy)=spn(kk)
           endif
               enddo
               do kk=1,ndspy
                     mn(kk)=mnd(kk)
                     dbn(kk)=dbnd(kk)
                     rn(kk)=rnd(kk)
                     spn(kk)=spnd(kk)
               enddo
               do kk=ndspy+1,ndsp
               mn(kk)=zero;dbn(kk)=zero;rn(kk)=zero;spn(kk)=zero
               enddo
         sumr=zero;sumspn=zero;MON_LEFT=zero;tdbn=0.0d0
             do kk=1,ndspy
              write
(9+iq,*)'mdr(',mn(kk),dbn(kk),rn(kk),')=',spn(kk)
              sumspn=sumspn+spn(kk)*mn(kk)
                     sumr=sumr+rn(kk)*spn(kk)
                     tdbn=tdbn+dbn(kk)*spn(kk)
               if((mn(kk).eq.one).and.(dbn(kk).eq.mdbs).and. &
                  (rn(kk).eq.zero)) then
                       MON_LEFT=spn(kk)
                   goto 270
               else
               endif
      270         continue
             enddo
     dconv=(md0-tdbn)/md0;mconv=1.0*(MAX_MON-MON_LEFT)/MAX_MON
     ndsp=ndspy;RST=RST+RT
             if(nbi.gt.(MAX_PR-1)) goto 790
              idn1=zero
       do kk=iia+1,(MAX_PR-BIN-1)
               if ( RST.ge.bt(kk) ) then
                  idn1=idn1+1;iib=kk
               endif
              enddo
              if (idn1.gt.zero) then
                iia=iib;nbi=nbi+idn1;idn2=idn1*2
                    do kk=1,idn2
                       rnmi(kk)=rand(0)
                    enddo
            endif
      790   continue
          if(
(sumr.eq.zero).or.ndsp.le.one.or.sumspn.gt.MAX_MON).or. &
                     (RST.gt.R_TIME) ) then
                      goto 999
          endif
             write(19+iq,150)RST,dconv
             write(49+iq,150)RST,mconv
      150    format(f20.8,3x,f20.8)
      ENDDO
     999     continue
     ! this the end of the DO WHILE LOOP
      stop
      end program SMCM
```

APPENDIX-G

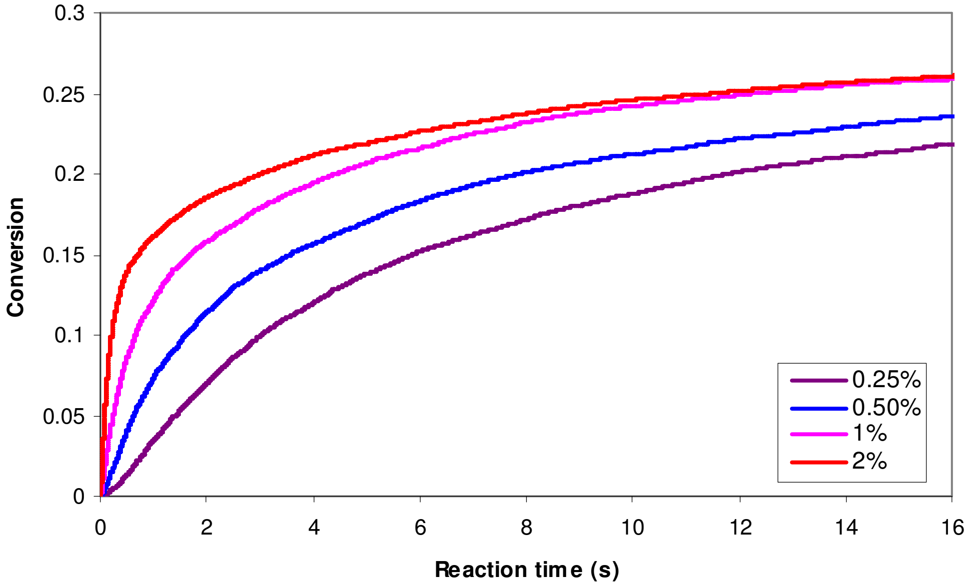

Figure G.1: Conversion Versus Time Curves for the Deoxygenated Photopolymerization of SR494 Obtained from the SMCM

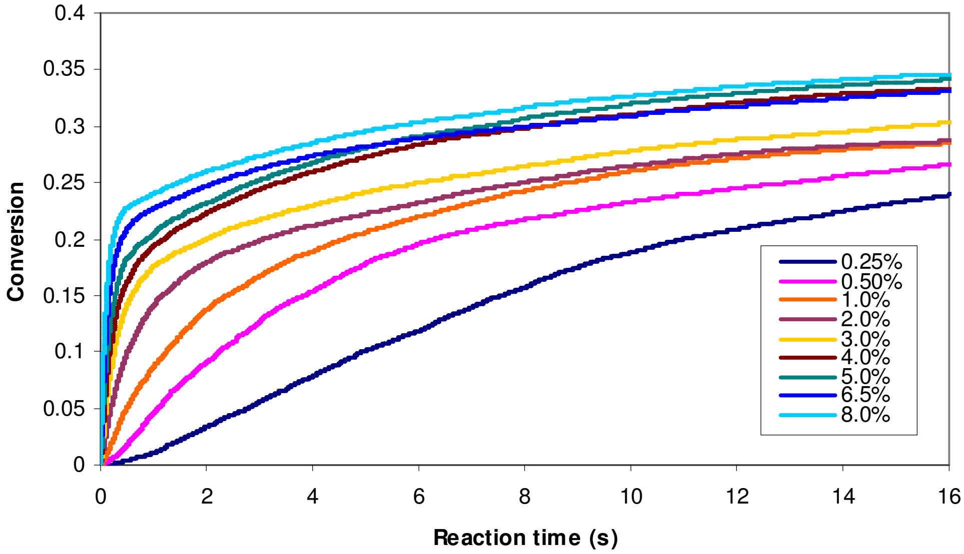

Figure G.2: Conversion Versus Time Curves for the Deoxygenated Photopolymerization of SR351 Obtained from the SMCM

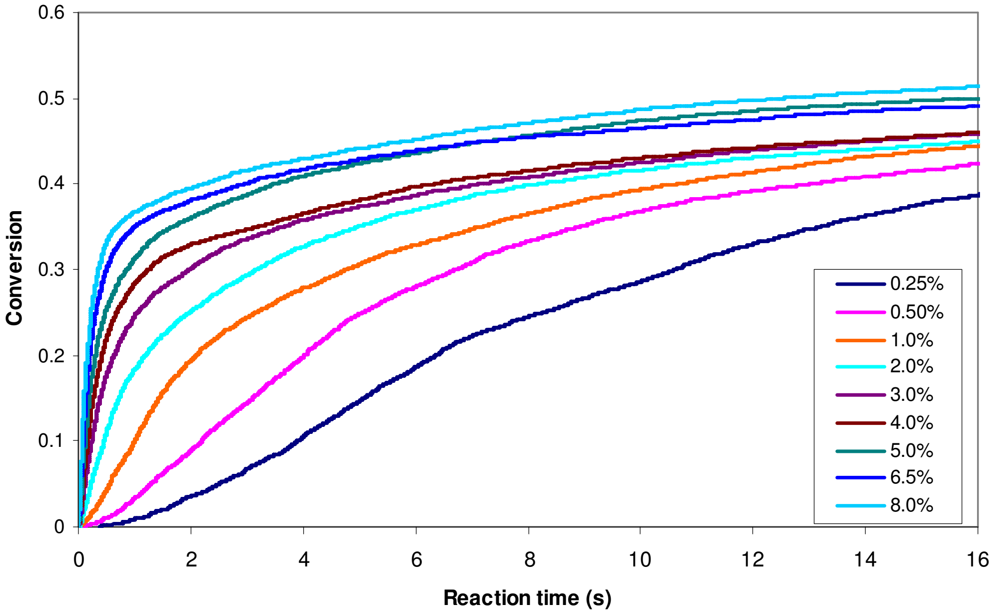

Figure G.3: Conversion Versus Time Curves for the Deoxygenated Photopolymerization of SR272 Obtained from the SMCM

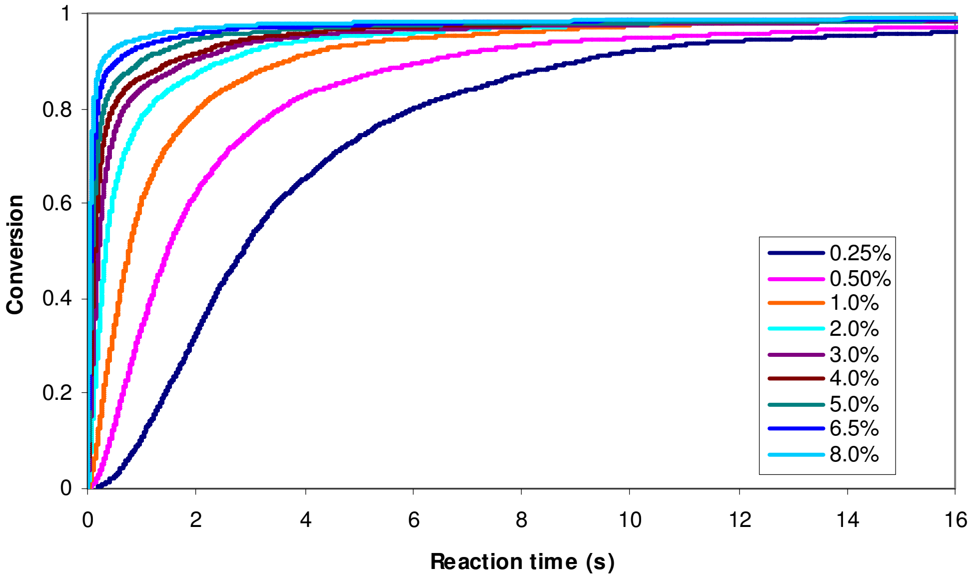

Figure G.4: Conversion Versus Time Curves for the Deoxygenated Photopolymerization of SR256 Obtained from the SMCM

CURRICULUM VITEA

Gökçen Alev ALTUN-ÇİFTÇİOĞLU was born on April 2, 1979 in Charlottesville, Virginia, USA. After finishing her high school degree at Kadıköy Anatolian Highschool, she received her bachelor's degree (B.S.) from the Department of Chemical Engineering of Yıldız Technical University in İstanbul and her master's (M.S.) degree from the Department of Chemical Engineering of İstanbul Technical University (İTU), Turkey in 2002. She holds another M.S. degree from the Department of Management Science and Engineering of İstanbul Technical University. Currently, she is a PhD. candidate at the Chemical Engineering Department of İTU. She has also been working as a research and teaching assistant at the Chemical Engineering Department at Marmara University, İstanbul, Turkey, since 2002.